

# Microfluidic culture platforms for *C. elegans* bacterial interaction and digestion studies at single-organism resolution

Présentée le 5 juillet 2021

Faculté des sciences et techniques de l'ingénieur  
Laboratoire de microsystemes 2  
Programme doctoral en microsystemes et microélectronique

pour l'obtention du grade de Docteur ès Sciences

par

**Vittorio VIRI**

Acceptée sur proposition du jury

Prof. L. G. Villanueva Torrijo, président du jury  
Prof. M. Gijs, Dr T. Lehnert, directeurs de thèse  
Prof. X. Casadevall i Solvas, rapporteur  
Prof. P. Rezai, rapporteur  
Dr N. Dhar , rapporteur



*“...ridatemi il cervello che basta alle mie mani.”*  
Fabrizio de André, “Il bombarolo”





# Acknowledgements

I would like to express my sincere gratitude to all the people who contributed to this thesis work.

First of all, I would like to deeply thank my scientific advisor Prof. Martin Gijs, for offering me the great chance to work in LMIS2 laboratory in these years. Martin allowed me to pursue my PhD with freedom and to find my own path, yet he patiently showed me the roadmap all the times I was losing my bearings. I sincerely admired his gentle but decisive leadership, his broad interdisciplinary knowledge, his way of looking at problems from a simple, but far from obvious, perspective and, last but not least, his witty sense of humor. Thank you Martin.

I am equally grateful to my co-advisor, Dr. Thomas Lehnert, who was always available for scientific discussions and helping me to disentangle often intricate data. Thank you Thomas for your extraordinary competence, patience and for the lessons I hope to have learned from you.

I also would like to express my sincere gratitude to my master thesis advisor Prof. Domenico Caputo. His support and motivation during the preliminary steps of my PhD journey were fundamental to me. I would like to thank Prof. Guillermo Villanueva, Prof. Pouya Rezai, Prof. Xavier Casadevall i Solvas, Dr. Neeraj Dahar for accepting to be the jury members of this thesis and for their insightful comments to my work. I thank Prof. McKinney at LMIC laboratory for the fruitful collaboration. Thank you Melis and Lucie for managing all the administrative issues, I would have been lost without your help. I want to express my gratitude to Jalil for his kind support for the teaching activities in cleanroom.

I am deeply thankful to all the former and current members of LMIS2 and the people met during this time at EPFL, I was glad to share a part of this journey with all of you.

Thanks to Greg for welcoming me in the lab and for all the amazing hikes we had in the Swiss Alps, Baris for always making worktime more relaxed with his chilled mood, Daniel for constantly involving me in stimulating scientific and non-scientific projects with his innate positive attitude, Roger for his kindness (and for that tube amp too!), Yang for climbing together the rugged PhD mountain, Raphaël, Cristina, Jonas, Tuan, Xiaopeng, Pahram and Li. Thanks to Farzad, Muaz and “brother” Lin. I truly wish all of you the best in your studies. I am sincerely thankful to Nagi Bioscience’s members : Matteo and Laurent for their helpful advices on *C. elegans* and microfluidics topics and Fabien, for his suggestions about all the best bike tracks in the Lausanne area. Thanks to Soham, for being a true friend.

Thanks to Maël, I really appreciated the dedication you put in the project we carried out and I wish the best for your PhD. I am also thankful to all Center of Microtechnology staff for their help with machine trainings and the microfabrication processes.

I am grateful to my “musical advisor” Jesus Gomez. Playing with you after work helped me to overcome the Blues due to failed experiments and long days in the lab. A special thanks goes to my outstanding ski/skateboard instructor, flatmate and friend Pascal.

Thanks to my old friends Elena, Mario, Pietro and Tommaso and all the “Piazza Cina lads” for always being there each time I came back to Rome. Also, a huge thanks goes to Cornacchia Bros. and Fabio for the crazy Skype talks we had in this weird last period of pandemic. You made these tough times way easier to bear. I am profoundly grateful to Gianmarco, Greta and Cemile. I can’t thank you enough.

Finally, I would like to express my deepest gratitude and dedicate this work to my father and my mother, who gave me the tools and the support to get to this point, and to my sister Francesca, who will go even further on her own road.

Vittorio

Lausanne, 17 June 2021

# Abstract

*Caenorhabditis elegans* (*C. elegans*) is a free-living nematode residing in the soil and feeding on bacterial food. *C. elegans* has emerged as an important model organism for biology and biomedical research, since many biological pathways and genes are shared among this nematode and humans. In recent years, in the broader field of human health-related research, particular attention has been given to the gut microbiota. Beyond its primary function of food processing and nutrient digestion, the intestine more and more appears to play a central role in important biological phenomena common to most animals, such as stress response, aging and neurophysiological processes. In this context, *C. elegans*, as a microbivorous organism, has emerged as an informative and experimentally accessible model organism for microbiome-related research. Many interesting studies have already been proposed, exploring, for instance, the effect of specific microbial diets on the worms' life span and phenotypic expression. Another important field of interest are infection assays that focus on the study of innate immune response induced by bacterial pathogens in the worms' gut.

In this thesis we present innovative worm and bacteria imaging protocols taking advantage of custom-developed microtechnology/microfluidic-based approaches. In particular, our work focused on (i) time-lapse *in vivo* monitoring and analysis of bacterial transit in the *C. elegans* gut, (ii) a study of the bacterial load, intestine-bacteria interactions and digestion processes in *C. elegans*, and (iii) on a microfluidic method to enhance detection of fluorescent bacteria by integrating BaTiO<sub>3</sub> dielectric microspheres acting as lenses in PDMS membranes. The different projects are described in more detail in the following.

(i) In the first part of the thesis, we report a new method for the analysis of *C. elegans* food transit in a microfluidic chip. In particular we studied the dynamics of the transit of *Escherichia coli* bacteria through the worms' intestine. For this purpose, we fabricated a chip for alternating *C. elegans* culture and immobilization, enabling periodic high-resolution time-lapse imaging at single-worm level over several days. We introduced a novel 'digestion phenotype' of *C. elegans* based on dynamic measurements of the bacterial intestinal content. Reversible immobilization using arrays of tapered channels was compatible with normal feeding protocols and suitable for assay parallelization. Feeding behavior and *E. coli* intestine transit were characterized in an automated way over the first 3 days of worm adulthood. Measurements on the worms were performed under confined and free-swimming conditions. On-chip worm culture and observation revealed diminishing gut efficiency as the worms aged. In addition, we studied the bacterial load transit cycle periodicity. Comparison between intestinal dynamic patterns in N2 and the pharyngeal pumping-defective mutant *eat-2 (ad465)* represented a first validation of our analytical technique. In particular, we observed a rather stable bacterial accumulation in the hindgut of the *eat-2* mutants. As a further proof-of-concept, the effect of a food intake modulation on the bacterial load in the worm intestine, induced by the 5-hydroxytryptamine hydrochloride (5-HT) neurotransmitter, was examined. We observed an increase of the bacterial load in the gut of treated worm populations.

(ii) In the second part, we present a microfluidic platform for *in vivo* studies of the fate of fluorescent bacterial strains in the gut of *C. elegans* worms. In particular, we studied the digestion process of *E. coli* in the

worms' intestine. We fabricated a PDMS microfluidic device based on a design principle that enabled long-term immobilization of young adult (YA) and adult worms by means of passive elastomer structures without interposed transfer into on-chip culture chambers. By this means, we characterized the transit and chemical digestion of non-pathogenic *E. coli* bacteria based on measurements of fluorescent signals of different nature in the worm intestine. In order to validate our approach, we first examined *in vivo* the properties of *E. coli* bacteria fluorescently labeled with pH-sensitive (GFP) and pH-insensitive (RFP) reporters. We monitored the bacterial load time evolution in immobilized N2 worms fed with fluorescently marked *E. coli* OP50-RFP, starting from the YA stage over 30 h. By detecting the decay of the diffuse signal originating from disrupted bacteria in the worm gut, we could estimate the time constant for enzymatic digestion in YA *C. elegans*. The cyclic peristaltic intestinal load dynamics was further characterized by feeding N2 YA nematodes with fluorescently marked indigestible microbeads. Moreover, we analyzed the bacterial load in the worms' intestine in the presence pathogenic *M. marinum* bacteria and measured the expression of mitochondrial stress response in *C. elegans hsp-6::gfp* mutants.

(iii) Finally, we report a study on BaTiO<sub>3</sub> microspheres partially embedded in thin polymeric membranes of mismatched refractive index. In particular, we assessed the improvement of detection performances observed for a low-magnification objective paired with polymeric membrane/dielectric sphere assembly (PMDSA). We computed the transformation that PMDSA mediates on the light originating from the sample towards the optical detector and showed its enhanced-detection potential. We fabricated microfluidic chips with custom designs and precise location of such dielectric spheres relative to the microfluidic structures. Detection of fluorescent living bacteria, either flowing in aqueous medium or immobilized in hydrodynamic traps was accomplished by coupling the PMDSA with a low-magnification objective. The contrast gain provided by the PMDSA for short exposure was quantified. We compared the performances of our optical system with a high-magnification objective, also showing that our device is suitable for long-term imaging.

In summary, this thesis is reporting different microfluidic methods for optimizing the time-lapse image acquisition of live organisms (nematodes and bacteria) using conventional microscopy techniques. These methods were applied to perform *in vivo* studies concerning the processing of the intestinal bacterial load in *C. elegans* under diverse experimental conditions, and the detection of fluorescently marked bacteria in liquid solutions.

**Keywords:** *Caenorhabditis elegans*, *Escherichia coli*, microfluidics, lab-on-a-chip, worm trapping, fluorescence microscopy, *in vivo* imaging, worm intestine, peristalsis, digestion process, bacterial load, pathogenic gut colonization, dielectric beads.

# Sommario

Il *Caenorhabditis elegans* (*C. elegans*) è un nematode fasmidario, comunemente presente nel suolo, che si ciba di batteri. Esso si è dimostrato essere un importante organismo modello in sia ambito biologico che per la ricerca biomedica, dal momento che numerose vie metaboliche e geni sono comuni sia ai *C. elegans* che all'essere umano. Negli ultimi anni, nel vasto campo della ricerca relativo alla salute umana, si è dato particolare interesse allo studio della flora intestinale. Oltre alla sua primaria funzione di decomposizione del cibo e di digestione dei nutrienti, l'intestino sembra ricoprire sempre di più un ruolo centrale in importanti fenomeni biologici presenti nella maggioranza degli animali, come ad esempio la risposta allo stress, l'invecchiamento ed i processi neurofisiologici. In tale contesto, il *C. elegans*, nutrendosi di batteri, si è rivelato essere un organismo modello utile e sperimentalmente accessibile per la ricerca riguardante il microbioma. Ad esempio, è stata proposta una serie di interessanti studi che analizzano nei *C. elegans* i diversi effetti dovuti al consumo di diete a base di ceppi batterici differenti sulla durata della vita media e sull'espressione di alcuni fenotipi. Un altro importante settore d'interesse è costituito dalle analisi infettive che si focalizzano sullo studio della risposta immunitaria innata causata dai batteri patogeni nell'intestino dei *C. elegans*. In questa tesi vengono presentati dei protocolli innovativi per l'imaging di vermi e batteri, tramite un approccio basato su tecniche di microtecnologia e microfluidica. Nello specifico, abbiamo incentrato il nostro lavoro (i) sul monitoraggio time-lapse *in vivo* e sull'analisi del transito batterico nell'intestino dei *C. elegans*, (ii) sullo studio del carico batterico, delle interazioni tra batteri e intestino e dei processi digestivi nei *C. elegans* e (iii) sullo sviluppo di un metodo microfluidico per migliorare il rilevamento di batteri fluorescenti tramite l'integrazione di microsferiche dielettriche in BaTiO<sub>3</sub>, agenti da lenti, in una membrana polimerica. Qui di seguito i vari progetti vengono descritti in maggior dettaglio. (i) Nella prima parte della tesi, viene riportato un nuovo metodo microfluidico per l'analisi del transito di cibo nell'intestino dei *C. elegans*. In particolare, abbiamo studiato le dinamiche di transito di batteri *Escherichia coli* attraverso l'apparato digerente dei vermi. A tal proposito, è stato fabbricato un dispositivo microfluidico per alternare coltura e immobilizzazione dei *C. elegans*, permettendo un'acquisizione periodica di immagini in time-lapse ad alta risoluzione di singoli vermi nel corso di alcuni giorni. Abbiamo introdotto un nuovo 'fenotipo di digestione' per i *C. elegans* basato su misure dinamiche del contenuto intestinale di batteri. L'immobilizzazione reversibile attuata tramite una serie di microcanali rastremati è risultata compatibile con i convenzionali protocolli di alimentazione dei vermi e adatta per la parallelizzazione dei test. Il comportamento alimentare ed il transito intestinale di *E. coli* sono stati caratterizzati in maniera automatica lungo i primi 3 giorni dell'età adulta dei vermi. Le misure sui vermi sono state effettuate sia in condizioni di immobilità che di movimento dei vermi. La coltura e l'osservazione dei vermi in ambiente microfluidico hanno rivelato una riduzione dell'efficienza intestinale legata all'invecchiamento nei vermi. In aggiunta, abbiamo studiato la periodicità ciclica del transito batterico. I confronti tra le dinamiche intestinali degli N2 e dei mutanti *eat-2* (*ad465*) con limitata funzionalità della faringe hanno rappresentato una prima validazione della nostra tecnica analitica. In particolare, abbiamo osservato un'accumulazione batterica piuttosto stabile nel tratto intestinale posteriore dei mutanti *eat-2*. Come ulteriore convalida sperimentale, è stato esaminato l'effetto della modulazione di consumo di cibo, indotta dal neurotrasmettitore 5-idrossitriptamina (5-HT), sul carico batterico intestinale nei vermi. Abbiamo osservato un incremento del carico batterico nelle popolazioni di

vermi soggette al trattamento. (ii) Nella seconda parte, presentiamo una piattaforma microfluidica per studi *in vivo* riguardanti la sorte di ceppi di batteri fluorescenti ingeriti e metabolizzati dall'apparato digerente dei *C. elegans*. In particolare, abbiamo studiato il processo digestivo degli *E. coli* nell'intestino dei vermi. Abbiamo progettato e fabbricato un dispositivo microfluidico in PDMS che permettesse l'immobilizzazione e la coltura di vermi a partire dal principio dell'età adulta (stadio YA) su un lungo periodo tramite l'uso di strutture elastomeriche passive senza necessità di trasferimento dei vermi in apposite camere di coltura. Quindi, abbiamo caratterizzato il transito e la digestione chimica dei batteri non patogeni *E. coli* basandoci su misure di segnali di fluorescenza di diversa natura, ottenute nell'intestino dei vermi. Per validare il nostro approccio, abbiamo inizialmente esaminato *in vivo* le proprietà di batteri *E. coli* marcati con fluorocromi sensibili (GFP) e non sensibili (RFP) al pH. Abbiamo monitorato l'evoluzione del carico batterico in vermi N2 immobilizzati e nutriti con *E. coli* OP50-RFP fluorescenti, a partire dallo stadio YA per 30 ore. Rilevando la progressiva riduzione del segnale diffuso generato dai batteri disgregati nell'intestino dei vermi, abbiamo potuto stimare la costante di tempo per la digestione enzimatica nei *C. elegans* allo stadio YA. Le dinamiche cicliche della peristalsi intestinale sono state ulteriormente caratterizzate alimentando i vermi N2 YA con microsfere fluorescenti non digeribili. Inoltre, abbiamo analizzato il carico batterico nell'intestino dei vermi in presenza del batterio patogeno *M. marinum* e misurato l'espressione genica legata allo stress mitocondriale nei mutanti di *C. elegans hsp-6::gfp*. (iii) Infine, presentiamo uno studio sulle microsfere in BaTiO<sub>3</sub> parzialmente integrate in una sottile membrana polimerica con indice di rifrazione non adattato. In particolare, abbiamo valutato il miglioramento di prestazioni di rilevamento osservate per un obiettivo a basso ingrandimento combinato con un assemblaggio di membrane e sfere dielettriche (PMDSA). Abbiamo calcolato la trasformazione realizzata dal PMDSA sulla luce proveniente dal campione verso il rilevatore ottico e abbiamo mostrato il miglioramento di detezione introdotto. Abbiamo fabbricato dei dispositivi microfluidici con un design su misura e con un preciso posizionamento delle sfere dielettriche rispetto alle strutture microfluidiche. L'individuazione *in vivo* di batteri fluorescenti, sia presenti in un fluido acquoso in moto sia immobilizzati in trappole idrodinamiche, è stata realizzata abbinando PDMSA e un obiettivo a basso ingrandimento. In seguito, è stato quantificato il guadagno in contrasto prodotto dal PDMSA per brevi tempi d'esposizione. Abbiamo messo a confronto le prestazioni del nostro sistema ottico con un obiettivo ad elevato ingrandimento, mostrando che il nostro dispositivo è adatto per l'imaging a lungo termine.

In sintesi, questa tesi presenta diversi metodi microfluidici per ottimizzare l'acquisizione di immagini di organismi viventi (nematodi e batteri) in time-lapse utilizzando convenzionali tecniche di microscopia. Tali metodi sono stati applicati per eseguire studi *in vivo* relativi alla digestione del carico batterico intestinale nei *C. elegans* in diverse condizioni sperimentali, e al rilevamento di batteri fluorescenti nei liquidi.

**Parole chiave:** *Caenorhabditis elegans*, *Escherichia coli*, microfluidica, lab-on-a-chip, intrappolamento vermi, microscopia a fluorescenza, acquisizione di immagini *in vivo*, intestino, peristalsi, processi digestivi, carico batterico, colonizzazione intestinale, sfere dielettriche.

# Contents

Acknowledgements .....	v
Abstract .....	vii
Sommario .....	ix
List of Figures.....	xiv
List of Tables.....	xvii
<b>Chapter 1 Introduction .....</b>	<b>19</b>
<b>1.1 <i>Caenorhabditis elegans</i> .....</b>	<b>19</b>
1.1.1 A nature's gift to science .....	19
1.1.2 General description of <i>C. elegans</i> .....	20
<b>1.2 Bacteria and <i>C. elegans</i>.....</b>	<b>22</b>
<b>1.3 Microfluidics for lab-on-a-chip .....</b>	<b>23</b>
1.3.1 Basics of microfluidics .....	23
1.3.2 Microfluidic systems for <i>C. elegans</i> based studies .....	24
<b>1.4 Thesis outline .....</b>	<b>27</b>
<b>Chapter 2 State of the art.....</b>	<b>29</b>
<b>2.1 Conventional approaches for <i>C. elegans</i>-bacteria interaction studies .....</b>	<b>30</b>
2.1.1 Bacterial food processing in the <i>C. elegans</i> intestine.....	30
2.1.2 <i>C. elegans</i> digestion studies .....	31
<b>2.2 Microfluidic platforms for <i>C. elegans</i> culturing, immobilization and imaging .....</b>	<b>35</b>
<b>2.3 Microfluidic platforms for <i>C. elegans</i>-bacteria interaction studies .....</b>	<b>41</b>
<b>Chapter 3 Microfluidic chip fabrication, materials and system integration .....</b>	<b>45</b>
<b>3.1 Microfluidic chip fabrication.....</b>	<b>45</b>
3.1.1 Mask for photolithography .....	45
3.1.2 Fabrication of single-layer and double-layer Si/SU-8 molds .....	47
3.1.3 Fabrication of a polymeric membrane/dielectric sphere assembly .....	48
<b>3.2 Materials and chemicals .....</b>	<b>49</b>
<b>3.3 <i>C. elegans</i> and bacteria preparation .....</b>	<b>50</b>
<b>3.4 Experimental setup of the microfluidic platforms .....</b>	<b>50</b>
3.4.1 Platform for <i>C. elegans</i> studies .....	50

	3.4.2 Platform for bacterial imaging based on a PMDSA .....	50
<b>Chapter 4</b>	<b>Bacterial transit dynamics in the <i>C. elegans</i> intestine .....</b>	<b>53</b>
4.1	Introduction .....	54
4.2	Microfluidic platform and imaging protocols.....	55
4.2.1	Microfluidic chip design .....	55
4.2.2	Operation of the microfluidic platform .....	56
4.2.3	Imaging of the worms and of the bacterial load in the intestine .....	58
4.3	Microbial assays and results .....	61
4.3.1	Dynamics of microbial food ingestion and peristalsis cycles of free-swimming N2 worms .....	61
4.3.2	Bacterial food transit time in the gut of adult N2 worms .....	65
4.3.3	Bacterial transit dynamics in <i>C. elegans eat-2</i> mutants .....	66
4.3.4	Serotonin effects on the <i>C. elegans</i> bacterial transit dynamics .....	68
4.4	Discussion.....	70
<b>Chapter 5</b>	<b>Long-term on chip worm immobilization for peristalsis, digestion and pathogen interaction studies .....</b>	<b>73</b>
5.1	Introduction .....	74
5.2	Microfluidic platform for long-term <i>in vivo</i> worm intestine imaging.....	75
5.2.1	Microfluidic chip design .....	75
5.2.2	Operation of the microfluidic platform .....	77
5.2.3	Imaging protocols of the worm intestine.....	78
5.3	Evaluation of <i>in vivo</i> bacterial imaging conditions in the worm intestine .....	79
5.3.1	Discriminating intact and disrupted bacteria in the worm gut .....	79
5.3.2	pH sensitivity of different microbial fluorescent markers .....	80
5.3.3	Intact vs disrupted bacteria in the intestine of wild-type <i>C. elegans</i> and <i>eat-2</i> mutants.....	83
5.3.4	Peristalsis dynamics and biochemical digestion of bacterial food .....	84
5.3.5	Analysis of peristalsis patterns and bacterial absorption by high-resolution imaging .....	88
5.3.6	Infection assay on <i>M. marinum</i> accumulation and <i>hsp6::gfp</i> expression .....	92
5.4	Discussion.....	95
<b>Chapter 6</b>	<b>Bacteria detection enhanced by dielectric microbeads .....</b>	<b>97</b>
6.1	Introduction .....	97
6.2	PMDSA modeling, imaging protocols and chip design.....	98
6.2.1	Analytical modeling of the PMDSA.....	98
6.2.2	Image acquisition and processing .....	99
6.2.3	Data Analysis .....	100
6.2.4	Microfluidic chip design .....	100
6.3	Optical performance of the PMDSA chip .....	102
6.3.1	Contrast enhancement of a low-magnification system.....	102
6.3.2	Comparison with a high-magnification system .....	103



6.4	Discussion.....	104
Chapter 7	Conclusions and outlook .....	107
7.1	Work and results presented in this thesis .....	107
7.2	The future of <i>C. elegans</i> – microbial assays .....	109
References.....		111
Curriculum Vitae .....		124

# List of Figures

<b>Figure 1.1</b> - Brightfield microscopy image of an adult <i>C. elegans</i> .	20
<b>Figure 1.2</b> – Schematic representation of the <i>C. elegans</i> development cycle at 22 °C.	22
<b>Figure 1.3</b> – <i>C. elegans</i> colonized by <i>Staphylococcus aureus</i> expressing GFP.	23
<b>Figure 1.4</b> – Schematic representations of microfluidic systems designed for investigating worm motion, analyzing sensory response of immobilized worms and worms culturing and imaging.	25
<b>Figure 1.5</b> – Microfluidic platforms for <i>C. elegans</i> studies.	26
<b>Figure 2.1</b> - (a) Schematic representation of a hermaphrodite adult <i>C. elegans</i> worm showing main features of the entire gut. (b) Differential interference contrast micrograph of an adult worm. (c) Autofluorescent birefringent gut granules.	30
<b>Figure 2.2</b> - The active cytoplasm of <i>C. elegans</i> enterocytes.	31
<b>Figure 2.3</b> - Two techniques for food intake measurements in <i>C. elegans</i> nematodes.	33
<b>Figure 2.4</b> - Colonization assays with <i>C. elegans</i> .	34
<b>Figure 2.5</b> - Adult transgenic worms carrying a <i>lys-1::GFP</i> reporter construct that induces an increased resistance to <i>S. marcescens</i> .	35
<b>Figure 2.6</b> - <i>C. elegans</i> microfluidic platforms for whole-organism screening.	36
<b>Figure 2.7</b> - Different approaches for <i>C. elegans</i> on-chip immobilization techniques.	38
<b>Figure 2.8</b> - Examples of devices taking advantage of immobilization techniques by physical constriction.	40
<b>Figure 2.9</b> - Microfluidic platforms for <i>C. elegans</i> -bacteria interaction studies.	42
<b>Figure 3.1</b> – Microfluidic device designs.	46
<b>Figure 3.2</b> - Cr photomask fabrication process.	46
<b>Figure 3.3</b> - Fabrication process of a single-layer Si/SU-8 mold and the PDMS microfluidic chip.	47
<b>Figure 3.4</b> - Schematic of the fabrication procedure a polymeric membrane/dielectric sphere assembly (PMDSA), comprising a PDMS membrane with partially embedded BaTiO <sub>3</sub> dielectric spheres.	48
<b>Figure 3.5</b> – Experimental setup of the microfluidic platforms.	51
<b>Figure 4.1</b> - Microfluidic device for bacterial transit studies in <i>C. elegans</i> .	56
<b>Figure 4.2</b> - On-chip imaging of an immobilized worm.	57
<b>Figure 4.3</b> - Monitoring of development parameters of N2 worms and <i>eat-2 (ad465)</i> mutants for on-chip and agar plate culture.	58
<b>Figure 4.4</b> - Monitoring of the fluorescence signal expressed by HT155 GFP-labeled (a) and OP50 RFP-labeled (b) <i>E. coli</i> bacteria in order to assess photo-bleaching of the fluorophores.	59
<b>Figure 4.5</b> - Monitoring of fluorescence expressed by HT155 GFP-labeled (a) and OP50 RFP-labeled (b) <i>E. coli</i> bacteria suspended in buffer solutions ranging from pH 3.776 to 6 in order to assess the fluorophore sensitivity to pH.	59
<b>Figure 4.6</b> - Principle of measuring the bacterial load in <i>C. elegans</i> worms.	60
<b>Figure 4.7</b> - Analysis of the bacterial load in free-swimming wild-type worms.	62
<b>Figure 4.8</b> - Bacterial transit cycle.	62

<b>Figure 4.9</b> - Average fluorescence signal corresponding to the hindgut region for 4 representative worms fed with <i>E. coli</i> HT115 GFP bacteria..	63
<b>Figure 4.10</b> - Average fluorescence signal corresponding to the hindgut region for 4 representative worms fed with <i>E. coli</i> OP50 RFP bacteria..	64
<b>Figure 4.11</b> - Fast Fourier Transform (FFT) magnitude computed for the fluorescence signal sequences corresponding to the worms' hindgut region for worms fed with <i>E. coli</i> HT115 GFP and <i>E. coli</i> OP50 RFP.	64
<b>Figure 4.12</b> - Analysis of the bacterial load in wild-type worms immobilized on the chip.....	65
<b>Figure 4.13</b> - Bacterial transit process of <i>E. coli</i> HT115 for an <i>eat-2 (ad465)</i> mutant.....	67
<b>Figure 4.14</b> - Bacterial load in adult N2 <i>C. elegans</i> worms. ....	68
<b>Figure 4.15</b> - 5-hydroxytryptamine (5-HT)-induced modulation of the bacterial transit process in N2 worms. ....	69
<b>Figure 4.16</b> - (a) Time-lapse images of free-swimming adult N2 worms, without and with 5-HT exposure, emphasizing increasing bacterial load upon treatment. Scale bars = 300 $\mu$ m. (b) Fluorescence signal averaged over the total length of the worm gut for treated and untreated worms. ....	70
<b>Figure 4.17</b> - High-resolution brightfield/fluorescence (40x) time-lapse images of an immobilized N2 <i>C. elegans</i> worm fed with <i>E. coli</i> HT115 GFP.....	71
<b>Figure 5.1</b> - Microfluidic device for <i>C. elegans</i> immobilization and intestinal bacterial load imaging.	76
<b>Figure 5.2</b> - Fluorescent images of the pharyngeal lumen of an N2 adult worm filled with RFP expressing OP50 <i>E. coli</i> bacteria, recorded with double-light exposure (white and 545 nm green light) (a), and with 545 nm green light excitation only (b).....	78
<b>Figure 5.3</b> - Automated image analysis for fluorescence measurements of the bacterial load in the worm's gastrointestinal tract.....	79
<b>Figure 5.4</b> - Analysis of the bacterial load in immobilized adult N2 <i>C. elegans</i> worms fed with fluorescently marked <i>E. coli</i> bacteria.....	81
<b>Figure 5.5</b> - Comparison between the bacterial load measured by fluorescence of the gut of immobilized and free-swimming worms in adult N2 fed with <i>E. coli</i> HT115 GFP (a) and <i>E. coli</i> OP50 RFP (b) over 30 h.82	
<b>Figure 5.6</b> - Intact vs disrupted bacteria in the <i>C. elegans</i> intestine. ....	83
<b>Figure 5.7</b> - Analysis of the bacterial digestion and transit of indigestible microbeads in the worm intestine. ....	85
<b>Figure 5.8</b> - Evaluation of the periodicity of the intestinal load motion due to peristaltic activity.....	87
<b>Figure 5.9</b> - Brightfield time-lapse recording of the posterior worm section of a gravid N2 <i>C. elegans</i> recorded over 60 s, showing multiple peristaltic contractions of the intestinal lumen.....	88
<b>Figure 5.10</b> - Analysis of transit patterns and bacterial nutrient absorption in the intestine of N2 <i>C. elegans</i> worms by high-resolution brightfield/fluorescence imaging (50x).....	89
<b>Figure 5.11</b> - Fluorescent signal corresponding to the hindgut region for 4 representative worms fed with rhodamine B-marked melamine microbeads. ....	90
<b>Figure 5.12</b> - Fluorescence signal corresponding to the hindgut region for 4 representative worms fed with <i>E. coli</i> OP50 RFP. ....	91
<b>Figure 5.13</b> - Analysis of bacterial accumulation and UPR <sup>mt</sup> response in <i>C. elegans</i> nematodes induced by pathogenic <i>M. marinum</i> bacteria..	93
<b>Figure 5.14</b> - Analysis of UPR <sup>mt</sup> response in <i>C. elegans</i> <i>hsp-6::gfp</i> mutants induced by the antibiotic tetracycline..	94
<b>Figure 6.1</b> - PMDSA model. ....	100

<b>Figure 6.2</b> - Structure and operation of the microfluidic PMDSA chip.....	101
<b>Figure 6.3</b> - Imaging of fluorescent bacteria. ....	102
<b>Figure 6.4</b> - Quantitative assessment of the optical enhancement with the PMDSA chip. ....	104
<b>Figure 7.1</b> - Microfluidic tools developed in the frame of this thesis for <i>C. elegans</i> and bacteria imaging.....	108

# List of Tables

**Table 6.1** - Summary of the main features of the low- and high-magnification objectives used in this study.  
.....104



# Chapter 1 Introduction

## 1.1 *Caenorhabditis elegans*

### 1.1.1 A nature's gift to science

In the mid-sixties, Sydney Brenner adopted the free-living nematode *Caenorhabditis elegans* (*C. elegans*) as a model organism with the intent to address a broad spectrum of classical problems in molecular biology. Brenner recognized that research based on *C. elegans* would bring about significant progress in developmental and neurobiology studies. In 1974 he presented his results in "The genetics of *Caenorhabditis*", initiating the establishment of this nematode as a major model organism [1]. Brenner's research work on *C. elegans*, together with John Sulston and Robert Horvitz, was awarded with the Nobel Prize in Physiology or Medicine in 2002. Today, *C. elegans* has become a well established model organism that is actively studied in the frame of various research fields in biology and biomedical sciences. For instance, *C. elegans* research contributed to important advancements in genomics, aging studies, developmental biology, microbiology, neurobiology and human disease studies [2, 3, 4].

*C. elegans* is a relatively simple and well characterized organism. The *C. elegans* genome was fully sequenced in 1998 [5]. Its simple nervous system, composed of 302 neurons, has been extensively studied. Remarkably, it was demonstrated by genomic comparison between humans and *C. elegans* that many human disease genes and pathways are also present in the worms. Approximately 60 - 80 % of human genes, of which about 40 % are related to human diseases, have orthologs in the *C. elegans* genome [6, 7]. This genetic correspondence has further increased the use of this nematode as a versatile tool of investigation for a number of neurodegenerative diseases, including amyotrophic lateral sclerosis and age-associated diseases, such as Alzheimer's, Parkinson's and Huntington's disease [8]. Metabolic diseases and muscle-associated disorders, in particular *diabetes mellitus* and Duchenne muscular dystrophy, and cardiovascular diseases have been found to have orthologs in the *C. elegans* genome as well [9, 10, 11]. Furthermore, *C. elegans* has been extensively used to study mitochondrial dysfunction, oxidative stress and aging [12]. Moreover, use of *C. elegans* for drug discovery and drug screening has been proposed [13]. Even though the mouse (*Mus musculus*) as classic model vertebrate presents higher genetic similarities with humans, implementing *C. elegans* in the drug screening pipeline may have numerous benefits. In particular, *C. elegans* can be an effective biological model in the early stage of the drug discovery process [13, 14]. Eventually, the tremendous cost of current drug screening campaigns could be significantly reduced. Unlike many other model organisms, nematodes pose no ethical issue, thus these organisms can be utilized for experimentation without particular restrictions or regulations.

As an established genetic model, the bacteriovorus *C. elegans* has also been increasingly used in the recent years for studies on host-microbiota interactions [15]. In the context of human health, there is an increasing awareness that the composition of the gut flora has an important influence on general health conditions. At present, it has been demonstrated that gut flora has major functions in metabolic activities, such

as absorption of nutrients, trophic effects on the intestinal tissue and protection against infections by pathogenic bacteria. Further and deeper understanding of microbiota functions could elucidate its role in the development of certain diseases [16]. In this context, *C. elegans* is emerging as an interesting research tool for microbiota-related studies. The nematode appears to be an effective model to investigate how the presence of viable or inactivated bacteria in the intestine influences the organism's health and development. For example, recent works utilized *C. elegans* as a model in order to study the intricate network of signaling pathways known as the gut-brain axis [17]. The interaction of pathogenic or probiotic bacteria with the nematode and the resulting effects on life span and health span are currently subjects targeted by multiple works.

*C. elegans* has demonstrated to be a very powerful tool to effectively address a large number of biological questions. *In vivo* studies on this organism constitute a valuable alternative to cell or tissue models and enable the evaluation of responses on a whole-organism level.

### 1.1.2 General description of *C. elegans*

*C. elegans* is a small nematode present in numerous parts of the world. In its natural habitat, this round-worm lives in rotten fruit, feeding on microbes. Small size, relatively short life cycle, compact genome, stereotypical development, ease of culturing and reproduction are some of the features that make this animal a practical organism for laboratory studies. *C. elegans* is usually maintained and cultured at room temperature on dedicated nematode growth medium (NGM) agar plates, seeded with a thin lawn of *Escherichia coli* (*E. coli*) OP50 bacteria as a food source [1, 18]. *C. elegans* has a transparent body, which greatly facilitates cell tracking and the observation of biological processes *in vivo* by optical microscopy. The length of newly born larvae is approximately 0.25 mm and adult worms normally grow to about 1 mm. A brightfield microscopy image of an adult N2 wild-type *C. elegans* is shown in Fig. 1.1.



**Figure 1.1** - Brightfield microscopy image of an adult *C. elegans* with the mouth/pharyngeal region oriented to the left and the tail to the right. The intestine lumen expanding through the whole worm body can be identified. Embryos can be distinguished in the worm mid body region. Scale bar = 200  $\mu$ m.

The developmental life cycle from the embryo to the egg laying adult stage is around 3 days under optimal conditions, and the total life span is approximately 2 weeks. Such a short development time allows fast data acquisition of different phenotypes in a matter of days, unlike other model organisms (*e.g.* mouse, zebrafish, etc.) for which the adult reproductive stage is reached only after weeks or even months. A sche-



matic of the life cycle from embryo to egg laying adult stage is shown in Fig. 1.2. Developmental times in between stages correspond to a culture temperature of 22 °C. After embryo hatching, the nematode goes through four larval stages (L1 - L4) separated by successive molting events, before reaching the adult stage [19]. In case of starvation, overcrowding or exposure to harsh environmental conditions during late L1 stage, *C. elegans* can arrest its normal growth process and enter the dauer stage [20]. During the dauer stage, the worm's mouth is occluded by an internal plug and the pharynx does not pump. The nematode can remain in the dauer stage up to 4 months. Otherwise, in favorable environmental conditions, the nematode develops normally through the 4 larval stages (L1 - L4) and the young adult (YA) stage after the last molting event. The adult stage, defined by the onset of the capability to generate progeny, is reached after about 46 h. *C. elegans* presents two sexes, males and hermaphrodites. The existence of a hermaphrodite sex constitutes a significant advantage for *C. elegans* maintenance and culturing in laboratory. In fact, the hermaphrodites are self-fertilizing females able to reproduce in the absence of male individuals. Males can be only rarely (0.1 %) produced from spontaneous non-disjunction events in the hermaphrodite germ line or, with higher incidence (50 %), as a result of mating between hermaphrodites and males [21]. Over the entire life span, a single hermaphrodite produces around 300 progenies.

At the adult stage, *C. elegans* consists of only 959 somatic cells and 1000 - 2000 germ cells [22]. Complete cell lineage has been traced in *C. elegans* [22]. An important feature of *C. elegans* is the tissue differentiation in this small animal. Despite its simplicity, *C. elegans* not only has an epidermis but also fully developed muscular, nervous, digestive, excretory and reproductive systems [19]. All internal structures are arranged almost concentrically in the body of the nematode. However, *C. elegans* does not have a respiratory system and oxygen uptake occurs by diffusion through the tissues into the mitochondria [23]. A wide variety of mutant strains, either overexpressing certain genes or with suppressed ones, have been generated. Activation or silencing of selected genes is particularly relevant in the analysis of the genetic origin of specific nematode phenotypes. Actually, it is relatively easy in *C. elegans* to access a broad range of scorable phenotypes induced by genetic manipulation [6].

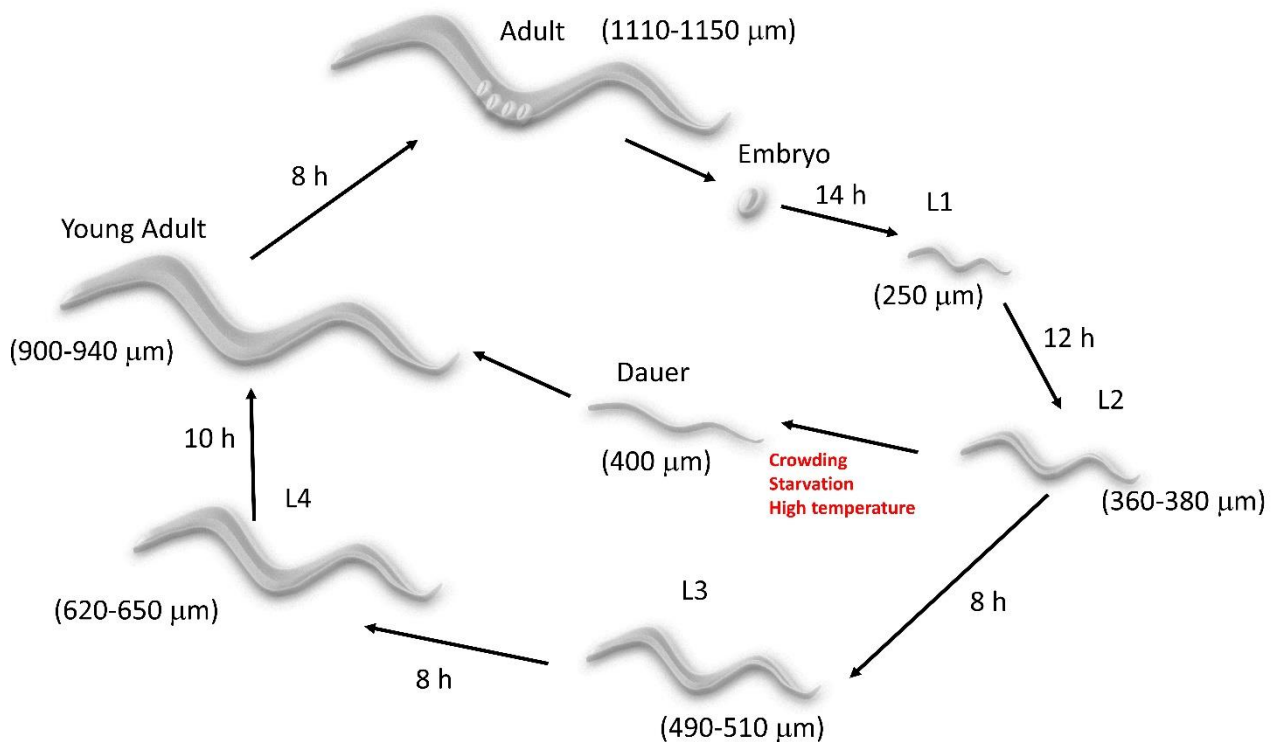


**Figure 1.2** – Schematic representation of the *C. elegans* development cycle at 22 °C. The developmental duration of successive stages and the average length of the worms at each larval stage are noted. In case of unfavorable conditions the L1 larvae enter into dauer stage.

## 1.2 Bacteria and *C. elegans*

Bacteria are the main nutrition source for *C. elegans*. In its natural environment *C. elegans* is proliferating on a microbe-rich soil or rotten fruits, and feeding on live bacteria is fundamental for the nematodes' developmental processes and overall health [24]. In nature, *C. elegans* is exposed to and capable to survive on a range of different bacterial strains. For instance, on rotten apples, being a typical *C. elegans* habitat, four main bacterial phyla are present (Proteobacteria, Bacteroidetes, Firmicutes and Actinobacteria). Interestingly, it has been demonstrated that the abundance of a specific type of Proteobacteria correlates with enhanced growth of the worms [24]. Depending on the specific type, bacteria supply *C. elegans* with varying amounts of carbohydrates, lipids and proteins. Behavioral studies of *C. elegans* on different bacterial strains unraveled the nematodes' dietary preference. Attraction or avoidance were observed depending on nutrition source. Unlike other more complex organisms, this nematode can be easily grown under axenic or monoaxenic conditions [25], and viable *C. elegans* embryos can be maintained in the absence of any bacteria. In laboratory conditions *C. elegans* has been cultured on monoaxenic lawns of *E. coli* OP50 bacteria for many years. The main reason for using *E. coli* as food source resides in the high availability of this strain. These particular feeding features are a prerequisite for controlling and manipulating the microbial exposure of the organism. However, bacteria do not solely represent a food source to this nematode. For instance, by feeding the worms with genetically manipulated *E. coli*, genetic interference can be achieved and expression of selected genes of the nematode can be silenced in order to assess specific pathways, interactions or phenotypes [26].

Over the past decades, *C. elegans* has evolved as a versatile model for investigating host-microbiota interaction mechanisms. Interaction of worms and bacteria can be assessed by observation of many well-characterized *C. elegans* phenotypes, such as longevity, size or the measurement of fluorescent reporters for specific processes in mutant strains. Bacteria produce metabolites that may modulate *C. elegans* life history traits, such as extending or decreasing nematodes' life span [27]. It has been demonstrated that nematodes fed on live bacteria may show life span extension [28]. Interestingly, a specific diet based solely on inactivated bacteria can also have beneficial effects on worms' longevity [29, 30]. In multiple studies, researchers focused on nematode-pathogen interactions. Microbial pathogens may accumulate or colonize the worms' gut. This bacterial load in the *C. elegans* gut can be readily observed by optical microscopy thanks to the transparency of its body. In many cases, fluorescently tagged bacteria are used for tracking and imaging the microbial colonies inside the worm. An example of *C. elegans* colonized by *Staphylococcus aureus* expressing green fluorescent protein (GFP) is shown in Fig. 1.3. Specific pathogenic strains may generate infections of the intestine and other parts of the organism, such as the epidermis, which in many cases eventually leads to death of the nematode [31]. Different ways of killing the host organism have been identified, such as killing mediated by toxins or by intestinal pathogenic proliferation [32]. On the other hand, some probiotic bacterial strains have beneficial effects on the worms' health, inducing life span extension, for instance [33]. In addition, different bacterial types can induce mitochondrial stress response in worms [34].

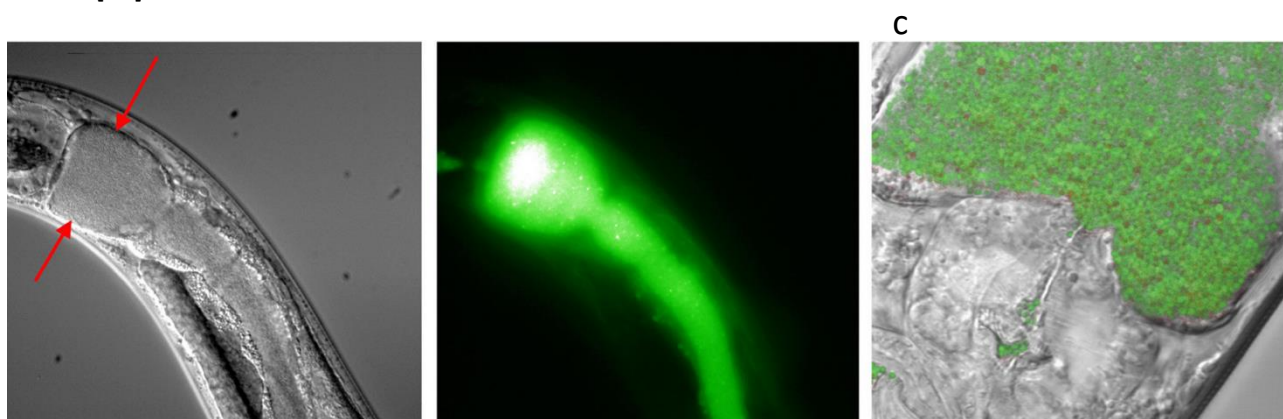


**Figure 1.3** – *C. elegans* colonized by *Staphylococcus aureus* expressing GFP. (a) The anterior intestine is distended to its full width by microbial proliferation (red arrows, left). (b) Epifluorescence image of the bacterial load in the intestine (middle). (c) High-magnification brightfield and epifluorescence imaging resolving individual bacteria (right). Reproduced and adapted from [35].

## 1.3 Microfluidics for lab-on-a-chip

### 1.3.1 Basics of microfluidics

Microfluidic systems are increasingly used in multiple areas of experimental science, in particular bringing along many technical advantages to bioanalytical applications. Lab-on-a-chip and integrated microfluidic systems, taking advantage from implementing different features of microfluidics, electronics and material science, have been proposed for a wide range of applications, including genetic analysis, DNA amplification, point-of-care diagnostics, drug discovery, organisms and organoids analysis, molecules and nanomaterial synthesis [36]. Microfluidic tools present advantages, such as reducing the time of analysis, eliminating or minimizing sample handling steps and, in many cases, enable higher throughput by assay multiplexing and parallelization. High design flexibility is a relevant feature of microfluidic devices, which makes them easily

adaptable to diverse applications. As a direct consequence of the microliter flow regime, sample and reagent volumes, as well as waste production, may be considerably reduced with respect conventional techniques. Consequently, the overall cost per assay is low, which is beneficial in view of commercial applications.

Development of microfluidic systems has been supported by the fact that the underlying physical processes are more easily controllable at a micrometer scale than at macroscale. Specifically, due to miniaturization and small volumes, a laminar flow regime is established for fluid motion in microfluidic devices. In general the velocity field  $\mathbf{v}$  of a viscous liquid is described by Navier-Stokes equations

$$\rho(\partial_t \mathbf{v} + (\mathbf{v} \cdot \nabla) \mathbf{v}) = -\nabla p + \eta \nabla^2 \mathbf{v} + \rho \mathbf{g}$$

where  $p$  is the pressure,  $\eta$  is the dynamic viscosity,  $\rho$  is the mass density and  $\mathbf{g}$  the gravitational acceleration. The Navier-Stokes equations are a set of 3 differential equations, one for each component of the velocity field  $\mathbf{v}$  vector. In the Navier-Stokes equations, the change of momentum density is set equal to the sum of the forces densities applied to the fluid, namely the pressure force density  $-\nabla p$ , the viscous force density  $\eta \nabla^2 \mathbf{v}$  and the gravitation force density  $\rho \mathbf{g}$ . They express the conservation of linear momentum in any point of the flow field and can thus be considered as Newton's second law applied to fluids. In microfluidic applications, inertial forces can be neglected, consequently viscous forces are dominant. The Reynolds number  $Re$  of a given system allows to predict the flow regime, either turbulent or laminar, depending on the ratio of inertial and viscous forces.  $Re$  is defined as

$$Re = \frac{\rho V_0 L_0}{\eta}$$

where  $V_0$  is the mean flow velocity and  $L_0$  is a characteristic linear dimension of the system. For fluids in microfluidic channels,  $Re$  is generally  $\ll 100$ . Under this condition, no turbulences occur and laminar flow is observed. Under laminar flow conditions, the trajectory of fluid particles is predictable, allowing to exert high control on fluid manipulations, for instance based on robust automated fluidic protocols and device operation by means programmable syringes pumps. Since inertial forces can be generally neglected in microfluidic channels, the Navier-Stokes equations reduce to a simpler form, known as the Stokes equations

$$0 = -\nabla p + \eta \nabla^2$$

which is valid in the range of small  $Re$ , i.e. for sufficiently low flow velocities, small channel dimensions or high viscosity conditions.

### 1.3.2 Microfluidic systems for *C. elegans* based studies

*C. elegans* research based on microfluidic systems has considerably expanded over the past years. In comparison to conventional methods, microfluidic devices provide a number of advantages in terms of worm manipulation, phenotyping and worm imaging. Additionally, microfluidic assays are suitable for automation of the experimentation, parallelization and increasing throughput. Almost every branch of *C. elegans* research may benefit from microfluidic integration, including behavioral and developmental studies, worm sorting and trapping, neurobiological studies or microsurgery on worms [37]. High-throughput drug screen-

ing based on *C. elegans* platforms can also be envisioned [38]. Some different concepts for microfluidic investigation systems are shown in Fig. 1.4.

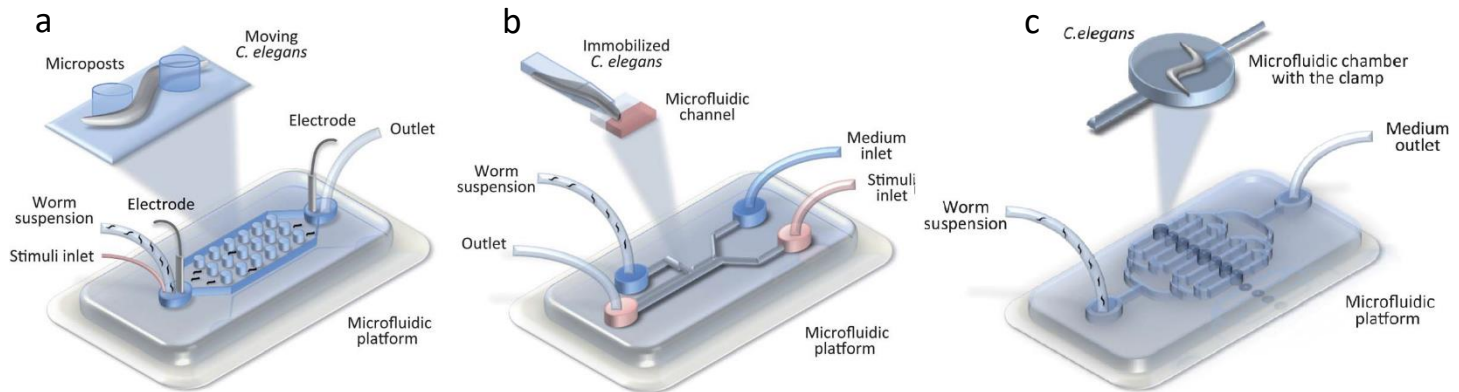


**Figure 1.4** – Schematic representations of microfluidic systems designed for (a) investigating worm motion through specific patterns and in response to electrical fields, (b) analyzing sensory response of immobilized worms and (c) worms culturing and imaging. Reproduced and adapted from [37].

More specific representative examples for microfluidic *C. elegans* platforms and studies are shown in Fig. 1.5. For example, Le *et al.* have developed an automated microfluidic-based platform for longitudinal behavioral monitoring during health span studies (Fig. 1.5a) [39]. Their platform allows culturing and monitoring a large population of nematodes (up to 1400) under controlled temperature and fluidic conditions. Each worm is isolated in a dedicated culture chamber, enabling precise longitudinal tracking and phenotyping of single animals, from L4 stage until death. In their work, versatility and robustness of the platform was assessed by longevity and health span data of established long-living (*daf-2*) and short-living (*daf-16*) mutants. Moreover, impact of dietary restriction and culture temperature on worm aging were evaluated. Cornaglia *et al.* developed a microfluidic platform to perform long-term high-resolution imaging of individual *C. elegans* embryos (Fig. 1.5b) [40]. Arraying and phenotyping of *C. elegans* embryos was achieved by integrating micro-incubators for embryo trapping in a serpentine-shaped microfluidic channel. Initially, the microfluidic protocol enabled reliable positioning and convenient alignment of up to 20 embryos in the incubator array. The authors employed the platform to investigate morphogenesis and mitochondrial biogenesis during the entire embryonic development. Atakan *et al.* demonstrated that such embryo arrays are particularly useful for high-throughput platforms [41]. They extended the previous concept and developed a microfluidic platform for screening up to 800 embryos. The system was validated by measuring the developmental lag and mitochondrial stress response in embryos treated with glucose and NaCl. In a different study, Rezai *et al.* utilized a microfluidic approach to analyze the innate response of *C. elegans* in the presence of a DC electric field, inducing oriented swimming patterns, also known as electrotaxis (Fig. 1.5c) [42]. They demonstrated that electrotaxis is directional, fully penetrant and highly sensitive. This behavioral response is mediated by neuronal activity in worms.



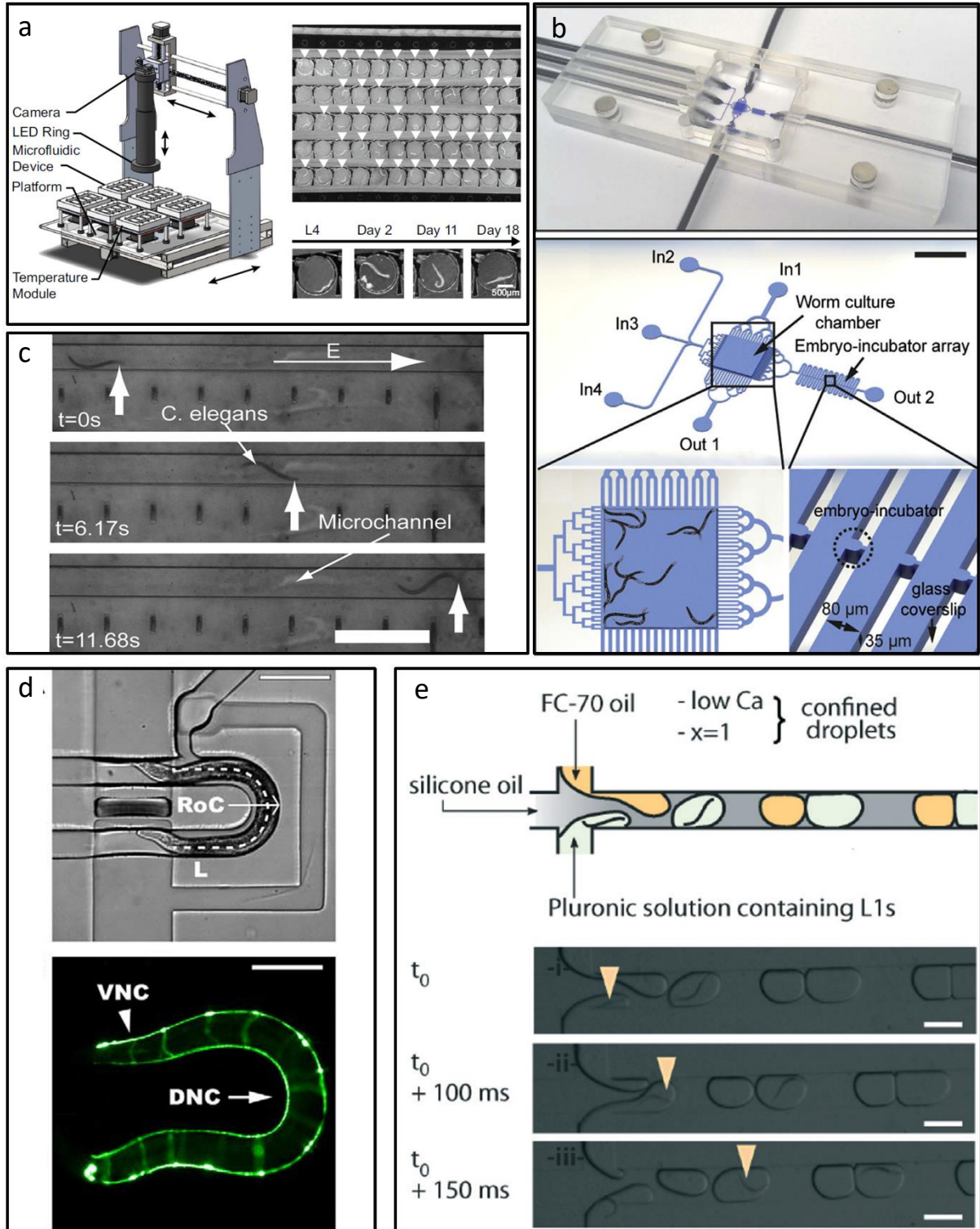


**Figure 1.5** – Microfluidic platforms for *C. elegans* studies. (a) Automated platform for monitoring long-term behavior and health span in *C. elegans* (reproduced and adapted from [39]). (b) Microfluidic chip featuring two distinct sections for worm culture and for capture/incubation of embryos, respectively. Scale bar = 2 mm (reproduced and adapted from [40]). (c) Electrotaxis of *C. elegans* in a microfluidic channel. Scale bars = 1 mm (reproduced from [42]). (d) *C. elegans* positioning with lateral orientation for microfluidic-operated neurodegeneration studies. Scale bars = 200  $\mu\text{m}$  (reproduced and adapted from [43]). (e) Microfluidic platform for immobilizing early larval *C. elegans* in hydrogel droplets, intercalated by oil spacer plugs to avoid coalescence. The sequence of images (i–iii) shows the process of worm encapsulation (indicated by arrows) (reproduced from and adapted [44]). Scale bar = 200  $\mu\text{m}$ .

Microfluidic tools were also successfully applied for neurobiological studies and for the analysis of neurodegenerative diseases. In this frame, Cáceres et al. presented a microfluidic device for imaging of *C. elegans* morphological features along its dorso-ventral body axis (Fig. 1.5d) [43]. In their device, loading, confinement and sorting of worms was operated at a rate of 500 animals per hour. The platform was utilized for the inspection of D-type motor neurons. In general, downscaling of microfluidic structures to the size of small larvae is challenging. Aubry *et al.* addressed this issue by encapsulating worms at the L1 larva stage within droplets of a thermosensitive Pluronic hydrogel (Fig. 1.5e) [44]. A schematic view of the droplet production unit and images of the worm-containing droplet sequence are shown. The microfluidic platform was used for high-resolution imaging of a transgenic strain that expressed GFP in coelomocytes or URX sensory neurons.

In summary, microfluidics can bring about a considerable technical improvement compared to traditional protocols for worm manipulation, culturing and for long-term studies on single worms. Parallelization and automation appear to be valuable characteristics of microfluidic based platforms, well-suited for substantially increasing the throughput and the information content of *C. elegans* studies.

## 1.4 Thesis outline

In this thesis, different microfluidic-based devices for *in vivo* imaging and analysis of *C. elegans* and bacteria are presented. In particular, the main focus of this work was to develop microfluidic tools for optimizing studies related to the interaction between *C. elegans* and bacteria. Novel approaches for evaluating the bacterial load, transit dynamics and the kinetics of nutrient absorption in the nematodes' intestine are presented. Moreover, an innovative method for imaging bacteria in liquid will be discussed.

Chapter 1 constitutes the introduction of this thesis that describes basic concepts that are relevant for the frame of the presented work. The nematode *C. elegans* is briefly introduced, followed by more a specific focus on aspects of nematode-bacteria interaction. The basics of microfluidics is outlined and some representative examples of microfluidic tools applied for *C. elegans* research are presented.

Chapter 2 in its first part is dedicated to a review of the state of the art of biological studies related to techniques for evaluating the bacterial load in the worms' intestine and food intake measurements, performed with conventional protocols. In a second section, microfluidic-based devices for worm and bacteria imaging are presented. A third section focuses on microfluidic tools and studies related to worms-bacteria interaction (food intake assays, colonization assays, etc.).

Chapter 3 presents materials, methods and common experimental protocols use for the present work. Standard microfabrication techniques for realizing the microdevices are discussed, in particular microstructuring of SU-8 or Si for mold fabrication. Protocols for nematodes and bacteria culturing and other standard techniques for worm manipulation are presented. Microfluidic device integration in the experimental is discussed.

Chapter 4 presents an *in vivo* microfluidic study for analyzing the dynamics of the bacterial transit in the *C. elegans* intestinal lumen. A dedicated microfluidic platform was developed for reversible worm on-chip immobilization. The new method takes advantage of tracking fluorescently labeled *E. coli* bacteria in the worm's gut. We utilized a microfluidic chip to perform worm culturing and imaging over three days. Addi-

tionally, we characterized modifications of the intestinal bacterial load kinetics in worms exposed to the neurotransmitter serotonin.

Chapter 5 is mainly dedicated to an *in vivo* microfluidic study of chemical digestion in *C. elegans*, based on the previously developed imaging techniques for monitoring bacterial transit. A microfluidic device for ergonomic on-chip confinement of several worms is proposed. We utilized *E. coli* bacteria expressing either pH-sensitive or pH-insensitive fluorescent reporters and indigestible microbeads to perform digestion assays and peristalsis monitoring. High-resolution imaging enabled *in vivo* characterization of the chemical digestion process of mechanically disrupted bacteria in the worm intestine. Additionally, we studied intestinal accumulation of pathogenic *Mycobacterium marinum* bacteria and characterized the mitochondrial stress response in mutants.

Chapter 6 presents a new cost-effective way of fabricating a microfluidic chip for empowering a low-end microscopy system. We fabricated a microfluidic device integrating BaTiO<sub>3</sub> dielectric microspheres and hydrodynamic traps for bacteria confinement, in order to perform time-lapse imaging and detection of fluorescently marked *E. coli* in liquids. We assessed the performance of our device by comparing it with a high-end detection system.

Chapter 7 summarizes the results achieved in this thesis and provides main conclusions. Also an outlook on possible future directions in the research fields addressed in this thesis will be given.



## Chapter 2 State of the art

Simple model organisms represent valuable tools for host-bacteria interactions studies. Over the past decades, *C. elegans* has emerged as a powerful model to analyse interplays between life and health span and bacteria, considered both as a nutritional source and as a symbiotic (or parasitic) organism. More recently, development of microfluidic technologies has brought important advancements for *C. elegans* analytical methods and for biological studies in general. Microfluidic platforms remarkably allowed improving the nematodes' culturing and imaging techniques, introducing innovative tools featuring higher levels of automation and higher throughput with respect to the conventional techniques. In particular, *in vivo* immobilization and imaging techniques of nematodes were positively affected by adoption of microfluidic devices for *C. elegans* research [45]. Microfluidics was applied to *C. elegans* studies ranging from neurobiological to behavioral assays [37]. Despite the effectiveness of microfluidics in biological research, on-chip studies of the *C. elegans*-bacteria interaction are still limited. This chapter aims to provide a brief review of the related biological and technological frame. The first section starts with a reminder of the main features of the *C. elegans* intestine. Then some biological studies of the *C. elegans* intestinal bacterial load based on conventional methods will be presented. Different aspects of dietary studies using *C. elegans* as a model organism are discussed. Particular emphasis is given to nutrients absorption, digestion processes and intestinal infection in nematodes caused by pathogens. In a second section, an outline of microfluidic tools enabling on-chip worm immobilization and imaging will be given. Reliable worm immobilization, ideally under physiological conditions, is a prerequisite for on-chip monitoring of the worm intestine over extended time spans. Finally, microfluidic platforms for *C. elegans*-bacteria interaction studies, mainly related to pathogenic colonization assays and measurements of expression of intestinal infection-induced genetic reporters, are described.

## 2.1 Conventional approaches for *C. elegans*-bacteria interaction studies

### 2.1.1 Bacterial food processing in the *C. elegans* intestine

The gut is one of the largest organs in *C. elegans* with multiple functions, that in more complex organisms, are specific to distinct organs [46] (Fig. 2.1). These functions include food digestion, chemical absorption of nutrients, synthesis and storage of macromolecules, and activation of immune response in presence of pathogenic agents [47, 48, 49, 50]. More generally, three major adjacent anatomical regions are easily identifiable in the digestive tract of *C. elegans*: the pharynx, the intestine (or midgut) and the rectum (or hindgut). After ingestion, the bacterial load is first processed by the grinder in the pharyngeal terminal bulb. The pharyngeal grinder disrupts the cell walls and bacterial membranes [50]. Rhythmic pumping and isthmus peristalsis movements, correlated to food presence, results in crushing ingested bacteria and initiates digestion. After grinding, the microbial food is pushed through the pharyngeal intestinal valve into the posterior intestinal regions [51]. The intestine has the primary function of processing and biochemically digesting microbial fragments to enable absorption of nutrients. The intestine of *C. elegans* is composed of 20 epithelial cells arranged as tubular structure, thus forming an internal lumen that extends from the mouth to the anus of the nematode (Fig. 2.2). The intestinal cells can be subdivided in nine distinct rings. Finally residues are expelled from the gut.

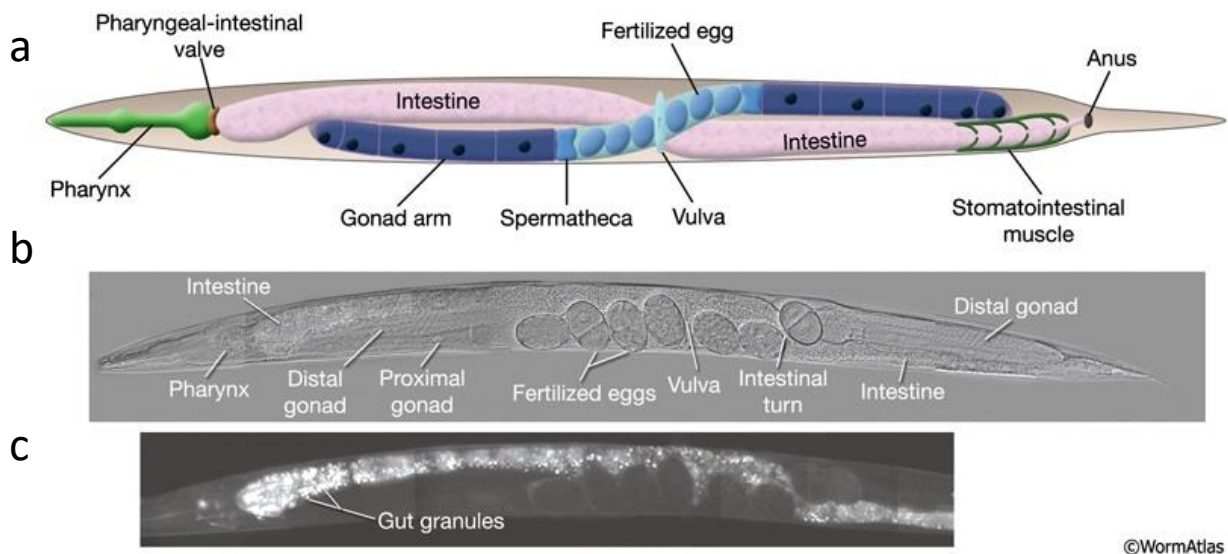


**Figure 2.1** - (a) Schematic representation of a hermaphrodite adult *C. elegans* worm showing main features of the entire gut, namely the pharyngeal region and the intestine. The reproductive apparatus is also indicated. (b) Differential interference contrast micrograph of an adult worm (length  $\approx 1$  mm). The intestinal lumen running parallel to the reproductive apparatus can be distinguished. Embryos are visible (magnification 400x). (c) Autofluorescent birefringent gut granules are present in the intestine throughout its whole length. Same animal as in (b). Reproduced from [52].

In the intestine, food is transformed by digestive enzymes secreted by the cells composing the intestinal lumen. Enzymes are not only responsible of further breakage of food into simpler constituents, but they also may represent a defense against pathogens. It has been demonstrated that antimicrobial effectors in *C. elegans* have digestive as well as defensive function [53]. Enzymatic breakdown of macromolecules is mostly occurring in intestinal regions with low pH value. Chauhan *et al.* have characterized the pH of the pharyngeal and the intestinal lumen of *C. elegans* in real time by using pH-sensitive fluorescent nanosensors [54]. In their work, *in vivo* measurement of the intestinal pH was performed and a pH gradient from the pharyngeal to the hindgut lumen was found, ranging from 5.96 to 3.59, respectively. They demonstrated that non-viable nematodes were not able to maintain a pharyngeal and intestinal lumen gradient. In another work, a periodical process of intestinal acidification was observed along the *C. elegans* gut [55]. A compartment of high acidity is transferred from the hindgut to the anterior region of the intestine, and visa-versa. In fact, the intestine of *C. elegans* presents oscillations of acidity values over time and gut regions, with some spots characterized by a highly acidic environment.

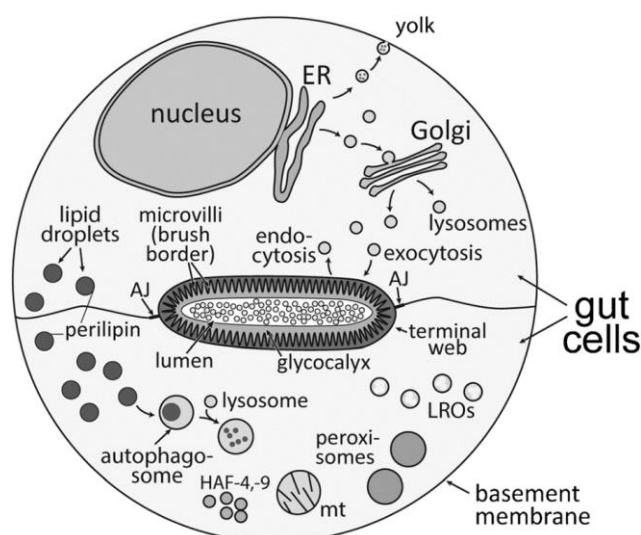


**Figure 2.2** - The active cytoplasm of *C. elegans* enterocytes. The worm gut consists of cells arranged as rings around the intestinal lumen. A transversal schematic section of two epithelial gut cells that are part of the same ring is shown. Diverse structures and processes found in the intestinal cells are represented. Reproduced from [46].

It is known for the time being that digestion in *C. elegans* depends on periodical chemical and physiological changes in the intestinal tract. However, analysis of digestion in worms still presents numerous blind spots. For instance, a current challenge is to obtain experimental data about the subcellular compartmentalization of digestion in nematodes. One of the issues in this context is the high autofluorescence of the worm gut, making precise protein localization difficult.

### 2.1.2 *C. elegans* digestion studies

*C. elegans* became a relevant model for dietary studies. Multiple works used this nematode to investigate correlations between diet, lipids storage, autophagy and life span [56, 57]. For instance, it was demonstrated that dietary restriction (DR) during the larval stages induces slower worm development and increases the life span [58]. Bishop *et al.* showed that the SKN-1 transcription factor mediates longevity induced by

DR in *C. elegans* [59]. In their work, food intake was limited by culturing the worms in liquid medium solution with a significantly diluted bacterial concentration ( $2.5 \times 10^7$  CFU/ml). Caloric restriction studies involving mutants have demonstrated that autophagy and reduced food intake cause life span extension in *C. elegans*. Specific *C. elegans* mutants, such as the *eat-2* mutant that displays a low pharyngeal pumping frequency resulting in reduced food intake with respect to wild-type nematodes, are effective tools for analysis of DR in worms. Gelino *et al.* used *eat-2* mutants to monitor autophagy in worms [60], showing the contribution of intestinal autophagy in the health span of DR conditioned *C. elegans*. The influence of different bacterial strains used as a nutrition source on the fat storage in *C. elegans* has also been investigated. Brooks *et al.* analyzed the fat storage of fixed nematodes by fat staining and biochemical lipid analysis. Worms have been fed on various *E. coli* strains, in particular OP50, DA837, HB101 and HT115 [61]. They observed that the dimension and the fluorescent intensity of stained lipid droplets depends on the *E. coli* strain.

In the context of dietary studies, reliable techniques for quantification of food intake are of considerable importance. Apparently, the amount of food ingested by the worms can be directly correlated to the pharyngeal pumping frequency [51]. Pharyngeal pumping consists of two distinct actions, namely pumping and isthmus peristalsis, and is sensitive to the environmental conditions surrounding the nematode. Several studies focused automated methods for measurements of pharyngeal pumping [62] and specific approaches for evaluating food intake were developed (Fig. 2.3). Gomez-Amaro *et al.* presented two different methods for *C. elegans* food intake measurements [63]. The first is a bacterial clearing assay consisting in the measurement of the variation of the bacterial optical density (OD600) over time caused by the worms' feeding activity. This assay was performed on a microtiter plate (Fig. 2.3a). A second method was based on measurements of food absorption by metabolic labeling coupled with quantitative mass spectroscopy. Ding *et al.* used a bioluminescent *E. coli* strain for the quantification of food consumption by *C. elegans* nematodes cultured on Nematode Growth Media (NGM) plates (Fig. 2.3b) [64]. Their method was based on the measurement of the bioluminescence signal that is sensitive to the metabolic activity of the bacteria. Actually, only living bacteria are capable of bioluminescent emission, and the observed signal loss can thus be related to ingestion and killing by the worms. This technique was employed to quantify microbial food uptake, both in wild-type (N2) worms and different mutants (*eat-2* and *npr-1*).

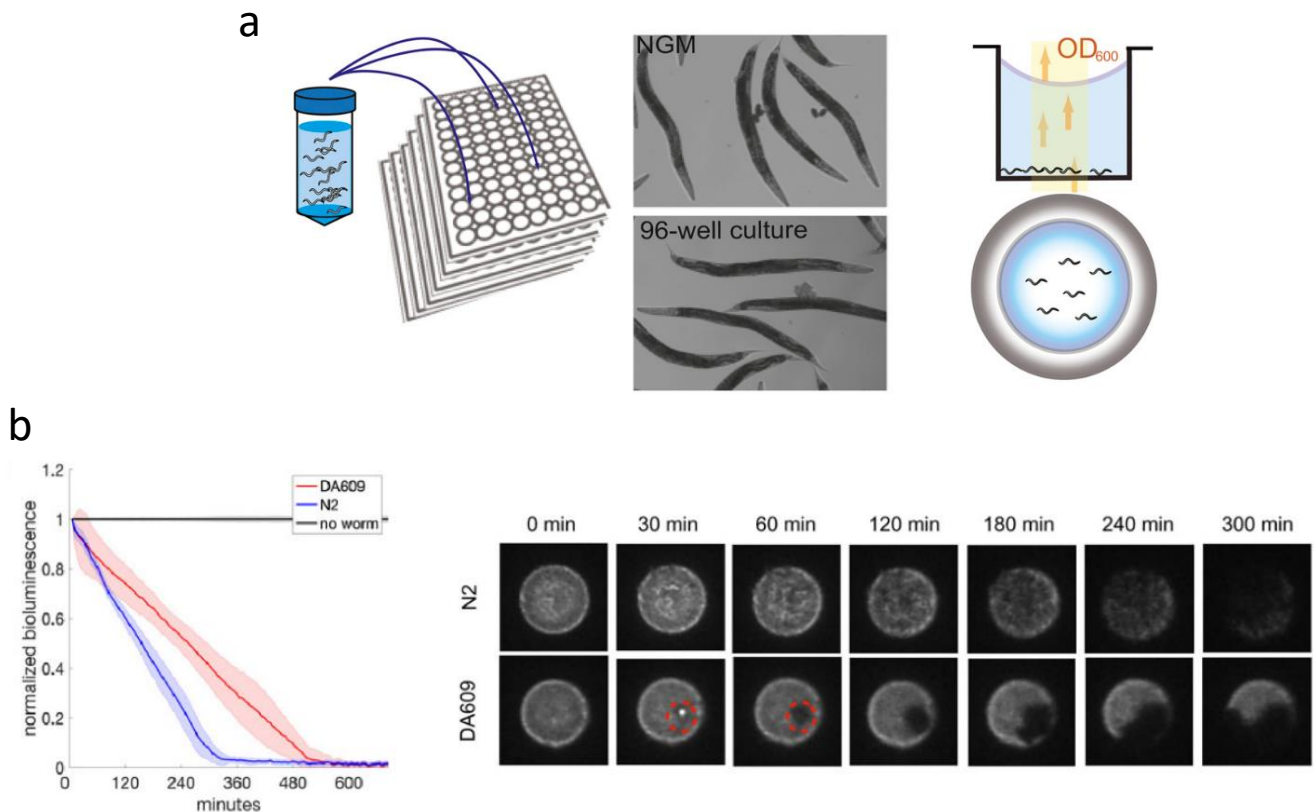


**Figure 2.3** - Two techniques for food intake measurements in *C. elegans* nematodes. (a) Schematic of a bacterial clearance assay with *C. elegans* in a 96-well liquid culture format. Worms are placed in wells and bacterial concentrations are monitored by optical density measurements at 600 nm (OD<sub>600</sub>). The microscopy images compare adult N2 worms grown on NGM plates and in liquid culture. No significant morphological difference was observed. (b) Bioluminescence from feeding experiments on NGM plates of N2 worms and of the *npr-1* aggregation mutant DA609. The graph shows the decreasing signals for N2 worms (blue) and DA609 (red), as well as a control (black). DA609 has a lower feeding rate. A series of images comparing the spatial pattern of food depletion in N2 (top) and DA609 (bottom) population feeding experiments. Reproduced and adapted from [63, 64].

So far, mechanisms related to digestion and feeding have been discussed. On the other hand, bacterial accumulation in the intestine represents an important phenotype in *C. elegans*-bacteria interactions studies. Stable bacterial presence in the gut is related to multiple causes, associated both to the colonizing capability of ingested bacteria, in particular of some pathogenic strains, and to the receptivity of the nematode itself. Bacterial load measurements are often performed by feeding the nematodes with bacteria expressing fluorescent protein markers. The fluorescence signal measured along the intestine is used as indicator of bacterial presence. This method for bacterial imaging has been well-established over a few decades and allows to identify intestinal regions that are particular sensitive to bacterial accumulation. Tan *et al.* observed mechanisms of infection and killing of *C. elegans* related to the opportunistic pathogen *Pseudomonas aeruginosa* (*P. aeruginosa*) [65]. Depending on the composition of the medium on which *P. aeruginosa* is grown, two different killing modalities were identified. Killing of nematodes occurring over several days, indicated as 'slow killing', was observed when bacteria were cultured on minimal medium. On the

contrary, worms fed with bacteria cultured on high-osmolarity medium were subjected to ‘fast killing’, occurring over a time frame of several hours. Fig. 2.4a compares worms presenting infection by *P. aeruginosa* and worms exposed to normal feeding conditions with non-pathogenic *E. coli*.

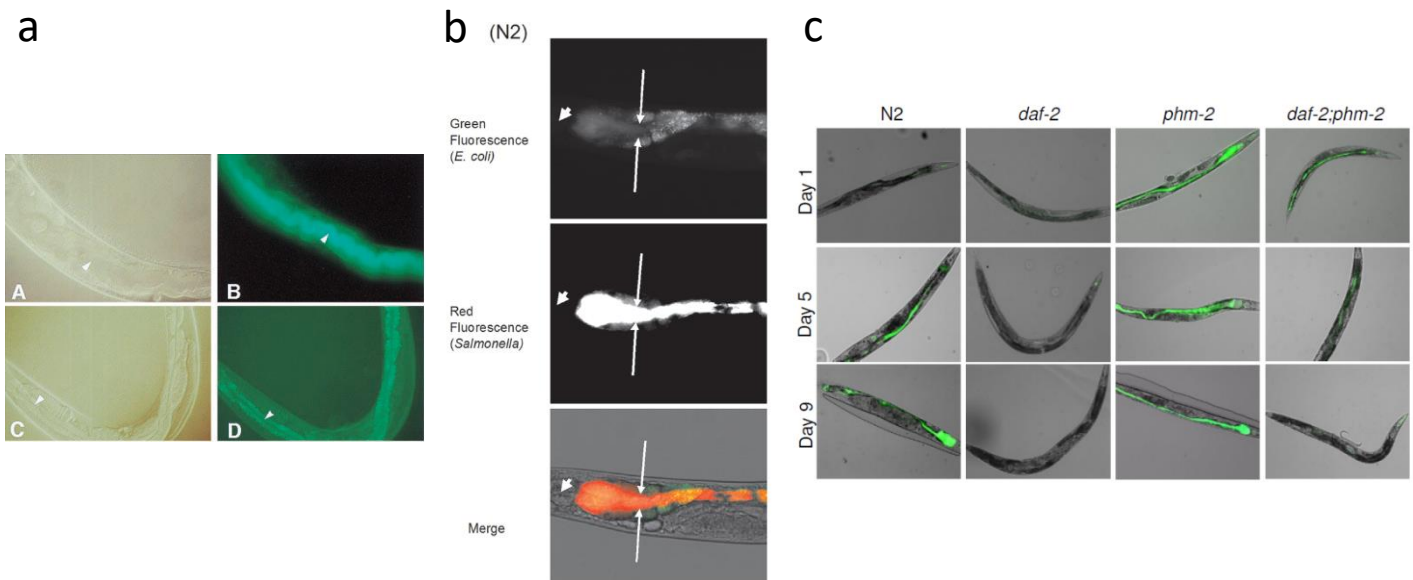


**Figure 2.4** - Colonization assays with *C. elegans*. (a) Worms fed with the *P. aeruginosa* strain PA14/GFP or with the *E. coli* DH5 $\alpha$ /GFP strain imaged under Nomarski phase contrast (A, C) and corresponding fluorescence micrographs (B, D). Fluorescent images show accumulation of pathogenic PA14/GFP (B) and normal intestine load with non-pathogenic *E. coli* (D), respectively. (b) Fluorescence microscopy images (40x) of *C. elegans* N2 after feeding on mixed lawns of *E. coli* OP50 and pathogenic *S. typhimurium*. Arrowheads indicate the pharyngeal grinder. The GFP channel shows *E. coli* inside the gut lumen, and the RFP channel shows *S. typhimurium* fluorescence. The merged image indicates bacterial colocalization (yellow). (c) Fluorescence images of N2, *daf-2* and *phm-2* single *C. elegans* mutants, and a *daf-2;phm-2* double-mutant showing different bacterial loads and accumulation patterns upon feeding on GFP-expressing *E. coli*. Reproduced and adapted from [65, 66, 67].

In other works, multiple fluorescently marked bacterial strains were simultaneously imaged in the gut of *C. elegans*. Porthal-Celhay *et al.* investigated the competition between founder and introduced bacteria in wild-type nematodes and mutants (*daf-2* and *daf-16*). In the assay, *C. elegans* were preliminarily grown on low-pathogenic *E. coli* OP50 bacteria expressing green fluorescent protein (GFP). Subsequently, the worms were exposed to highly pathogenic *Salmonella enterica* serovar *typhimurium* (*S. typhimurium*), labeled with red fluorescent protein (RFP) (DsRed) [66]. Worms were fixed by exposure to sodium azide for imaging. The authors demonstrated that, both in N2 nematodes and in mutants, very few active colonies of *Salmonella* substantially outcompeted *E. coli* (*i.e.* at a concentration ratio of 1:100). Through fluorescent imaging of the nematodes' gut, clusters of GFP marked *E. coli* were observed in the anterior gut region, while RFP marked *Salmonella* was present throughout the full intestine (Fig. 2.4b). In a separate study, Porthal-Celhay *et al.* demonstrated that several *C. elegans* genotypes show a reduced capability of controlling the bacterial presence in the intestine during adulthood [67]. Moreover, an inverse correlation between bacterial accumulation and worms' lifespan in different genotypes was observed. Measurements of bacterial load and

viability of the nematodes were performed over several days. Bacterial presence in the intestine was evaluated by imaging of GFP-labeled bacteria (Fig. 2.4c).

Pathogenic infection can induce the activation of multiple defense mechanism in *C. elegans*, including unfolded protein response (UPR<sup>mt</sup>) and the generation of reactive oxygen species [68, 69]. Activation of innate immune response in *C. elegans* can be correlated to upregulation of the expression of specific genes. For instance, Mallo *et al.* showed that *C. elegans* infected by the gram-negative bacterium *Serratia marcescens* (*S. marcescens*) provoked upregulation of genes encoding for lectins and lysozymes (Fig. 2.5). They demonstrated that *dbl-1* mutants presented a reduced resistance to infection, while overexpression of the lysozyme gene *lys-1* induced an increased resistance to *S. marcescens*.

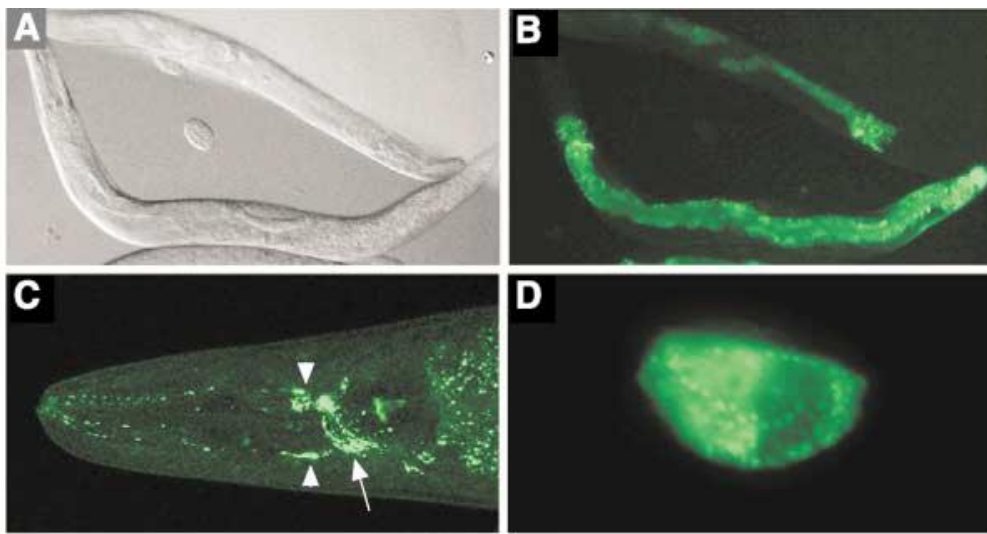


**Figure 2.5** - Adult transgenic worms carrying a *lys-1::GFP* reporter construct that induces an increased resistance to *S. marcescens*. (A) Worm morphology observed by Nomarski interference. (B) Worm showing *lys-1::GFP* expression throughout the intestine as revealed by fluorescence microscopy. (C) A confocal image of the head of a worm showing *lys-1::GFP* expression in the IL1 and IL2 neurons (arrowheads) and in the nerve ring (arrow). (D) *lys-1::GFP* concentration in vesicles in a single posterior intestinal cell. Reproduced and adapted from [68, 69].

## 2.2 Microfluidic platforms for *C. elegans* culturing, immobilization and imaging

One of the most attractive features offered by microfluidics is the efficiency of worm manipulation. Groups of several worms or single organisms can be conveniently handled on-chip. For operating a microfluidic system, worms are generally suspended in liquid culturing medium (such as S-medium) and loaded into dedicated microfluidic channels. A large number of different designs, adapted for a specific application, have been proposed. A rough classification of microfluidic tools for *C. elegans* analysis can be made between on-chip culturing devices, in which worms are freely moving in chambers of suitable size, and devices enabling immobilization of single worms for imaging specific worm features. In general, such microfluidic devices take advantage of an array format. As an example for an application based on free-swimming worms, the microfluidic platform developed by Letizia *et al.* is shown in Fig. 2.6. This platform was designed for efficient multi-parametric testing on *C. elegans* [70]. The microfluidic chip consists of eight independent parallel channels. Each channel comprises a linear arrangement of six culture chambers separated by a set



of size-selective filters for L1 larvae. A specific fluidic protocol allowed loading of a single L1 worm in each chamber (Fig 2.6a). In this study, the influence of the culture temperature, the amount of bacterial food and the exposure to antibiotics on the developmental time of L1 larvae to adulthood was examined by means of a design-of-experiment approach. On-chip imaging and long-term monitoring of the different worm developmental stages was performed (Fig 2.6b). Automated setups and protocols enabled tracking of worms in each chamber of the chip array. In another study, Chung *et al.* developed a microfluidic platform for fast whole-organism behavior-based chemical screening [71]. Their device consists of an array of 48 circular chambers connected by a serpentine-shaped microchannel (Fig 2.6c and Fig. 2.6d). Each chamber is designed to host a single free-swimming worm that can be loaded through an optimized inclined inlet channel. Investigating free-swimming worms allowed to evaluate motility-related phenotypes (*i.e.* number of body bends per second). Behavioral response of individual worms to drugs and sex pheromones in hermaphrodite-conditioned medium was analyzed. The microfluidic design enabled precise chemical delivery to the worms and liquid exchanges with high temporal precision.

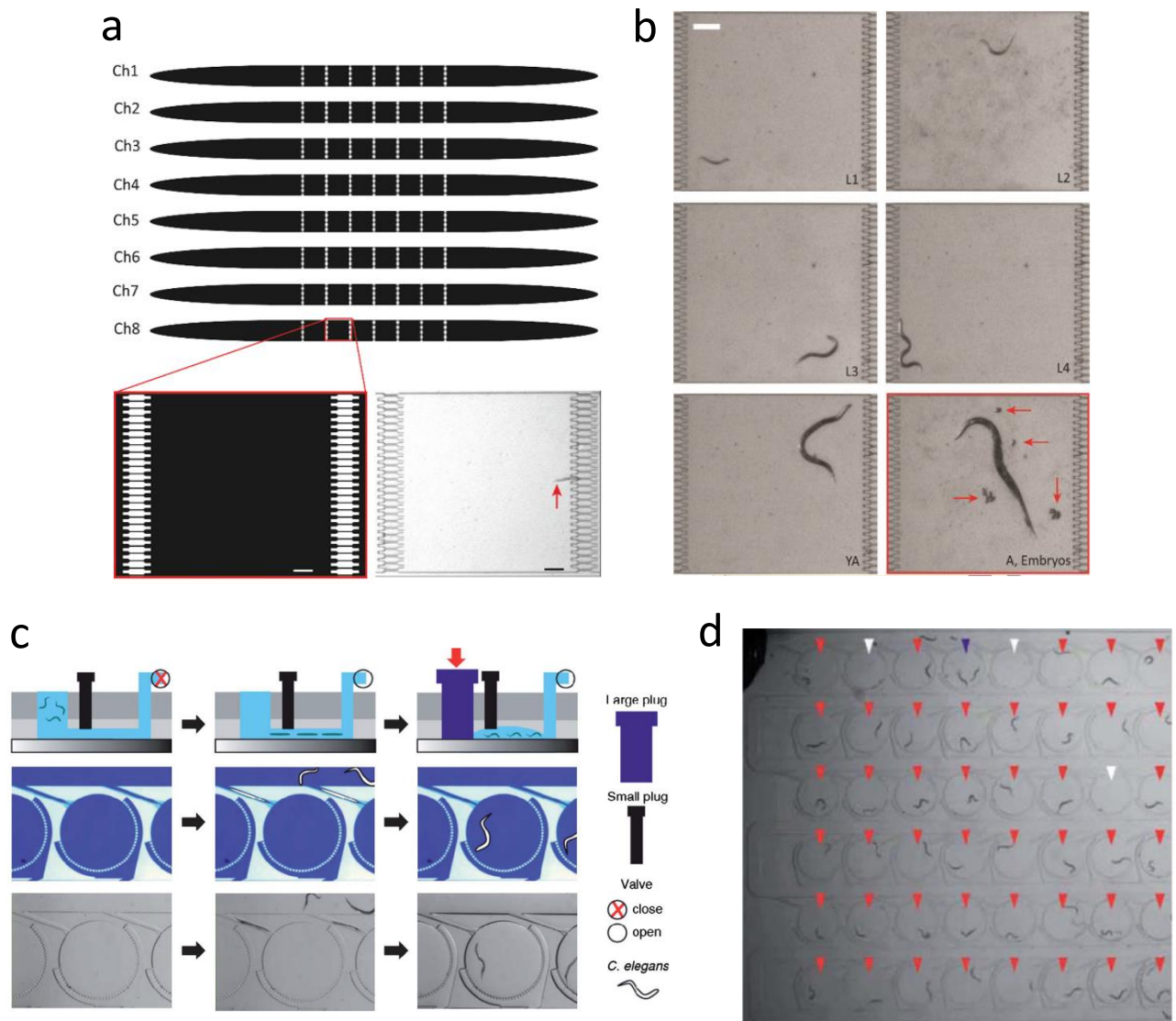


**Figure 2.6** - *C. elegans* microfluidic platforms for whole-organism screening. (a) Schematic of a microfluidic device for multi-parametric drug testing featuring 8 independent parallel channels with adjacent worm chambers. The chambers are separated by filter structures allowing selective worm transfer. (b) Illustration of the time-lapse bright field imag-



ing process in a selected chamber. A worm may be monitored over the whole life span starting from early larval stage. Scale bar = 200  $\mu\text{m}$ . Reproduced and adapted from [70]. (c) A microfluidic platform for fast whole-organism behavior-based chemical screening. The device operation process for worm capture and release in the circular culture chamber is shown: schematic cross-section of the device (top), illustration of single chamber (middle), optical micrographs of worm transfer into a single circular chamber (bottom). (d) Optical photographs of *C. elegans* loaded (red arrows) in the array of 48 circular chambers connected by a serpentine-shaped microchannel. Reproduced and adapted from [71].

Over the past years, multiple on-chip immobilization techniques for imaging of *C. elegans* have been developed. The most important principles are summarized in Fig. 2.7 and some related applications are discussed here. Physical immobilization methods are based on worm confinement. This can be obtained by actuation of a pneumatic valve-like structure similar to the so-called Quake's valves [72]. Trapping of the worm is achieved through deflection of a thin polydimethylsiloxane (PDMS) membrane by pressure application through a control layer, providing secure and reversible immobilization that can be effectively used for high-resolution imaging (Fig. 2.7a). However, the two-layer structure generally requires a more time-consuming fabrication process. A somewhat simpler physical restriction method was initially proposed by Hulme *et al.*. The method permits *C. elegans* immobilization by confinement of worm in a tapered microchannel simply through application of flow (Fig. 2.7b) [73]. Release of the worms simply occurs by interruption of the flow. The authors developed a microfluidic device integrating an array of 128 worm clamps and validated the device by trapping and imaging of adult nematodes. Additionally, they monitored the survival rate over 30 days of released worms that underwent immobilization and demonstrated that this type of physical restriction does not significantly damage the worms. An alternative worm immobilization technique is creating a  $\text{CO}_2$  micro-environment to stop worm's motion (Fig. 2.7c). The  $\text{CO}_2$  micro-environment may be generated by perfusing  $\text{CO}_2$  into a control layer from where it diffuses through a PDMS membrane into the microchannels hosting the worms. The method thus takes advantage of the PDMS gas permeability. A study by Chokshi *et al.* demonstrated that this technique allowed immobilization of nematodes for a duration of 1-2 hours [74].

Gelation of a thermosensitive hydrogel (*e.g.* Pluronic F127) was also employed for hindering worms' movement. Upon cooling down this polymer, a reversible sol-gel transition occurs and the solution together with the worm suspension can be loaded into the chip. Gelation takes place at room temperature and it was demonstrated that the high viscosity of the gel phase is sufficient to effectively immobilize adult *C. elegans* nematodes (Fig. 2.7d) [75]. Cornaglia *et al.* developed a platform for *in vivo* observation of biomolecules and automated analysis of protein aggregation in a *C. elegans* model for amyotrophic lateral sclerosis (ALS) [76]. In their work, gelation of Pluronic solution was utilized to immobilize worms during all the developmental stages for high-resolution imaging. Gel immobilization was used by Dong *et al.*, for instance, for immobilizing nematodes by a hydrogel-bead matrix interposed between a glass slide and a coverslip [77]. They successfully applied this technique for high-resolution imaging of the mitochondrial morphology in worm body wall muscle cells. Additionally, long-term quantitative measurements of number and size of specific protein aggregates in multiple *C. elegans* models for neurodegenerative diseases were carried out. Another original method was developed by Chung *et al.* using low temperature-based immobilization in a microfluidic system for high-throughput and high-resolution sorting of *C. elegans* (Fig. 2.7e) [78]. Immobilization was achieved by cooling worms to  $\sim 4^\circ\text{C}$  by means of an integrated local temperature-control system. They applied this method for screening of worms based on cellular and subcellular phenotypes. Individual nematodes were automatically sorted after a classification based on evaluation of the specific phenotypes. Imaging of immobilized worms was also required to measure gene-expression patterns in mutants.

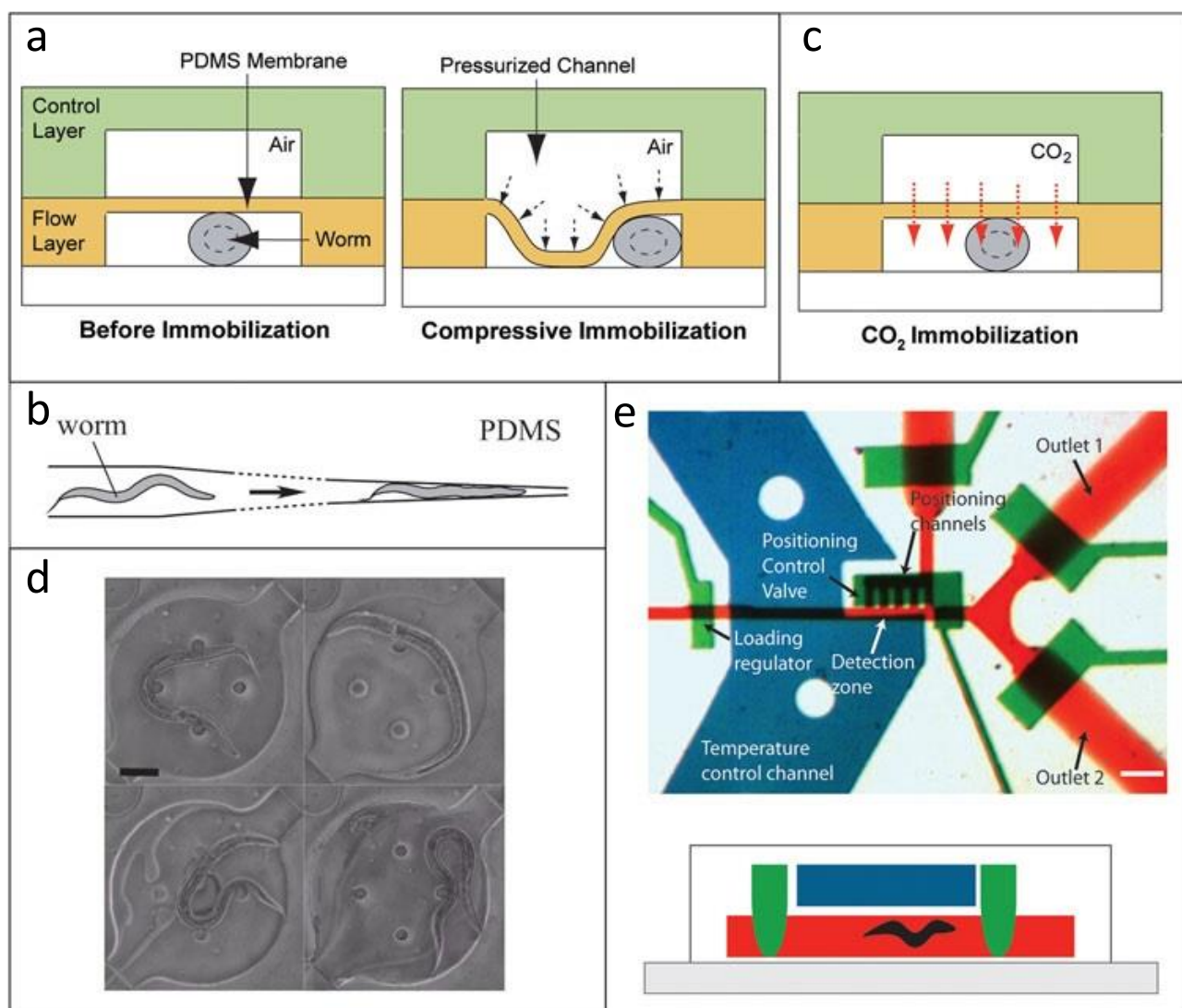


**Figure 2.7** - Different approaches for *C. elegans* on-chip immobilization techniques. (a) Physical constriction of the microchannel by a deflecting thin PDMS membrane. The PDMS membrane is deflected by pressure exerted from the control layer on top, resulting in the confinement and compression of the worm on the side of the microchannel. (b) Physical restriction of worms in a tapered channel. The applied flow (arrow) gently pushes the worm into the trap. Interruption of the flow allows the nematode to exit the trap by itself. (c) Chemical immobilization by CO<sub>2</sub> gas diffusing through the gas-permeable PDMS membrane. Worms are immobilized by temporary anaesthesia. (d) Worm immobilization in a thermosensitive gel (Pluronic F127). Gelation may efficiently limit movements of the nematode. Scale bar = 60  $\mu\text{m}$ . (e) Immobilization by cooling. Worm's motility is significantly reduced by exposure to low temperature controlled by the liquid medium in a dedicated channel. Prior to cooling, the worm is positioned on the channel sidewall by suction through a specific channel. Reproduced and adapted from [45].

An example of a device using by the deflection of a thin PDMS membrane for physical worm immobilization, as explained in Fig. 2.7a, is shown in Fig. 2.8a. Based on this approach, Gilleland *et al.* presented a microfluidic chip for immobilization of *C. elegans* worms from the L4 larval to the adult stage [79]. Single worms were loaded in a chamber and aligned in an elongated position in close contact to an on-chip filter structure. By pressurizing a control layer on top of the chamber, the worm was pushed further towards the filter wall and securely immobilized. The worm was released by depressurization of the control layer. This device was used for a range of applications, including *in vivo* imaging of dynamic cellular processes, laser microsurgery and 3D microscopy. In many devices, separate compartments for free-swimming and worm immobilization are implemented side-by-side on the same chip. As an example, Atakan *et al.* developed a device with eight independent microchannels, featuring four separate worm compartments in each channel (Fig 2.8b) [80]. Such a chamber presents both a region for worm growth and one for immobilization. Immobilization, imaging and high-content phenotyping of developing *C. elegans* from L1 larval stage to adulthood was achieved by taking advantage of the tapered shape of worm clamps. The microfluidic chip was validated by observing the effect of feeding the nematodes with different bacterial concentrations on the expression of a neurodegenerative disease marker in a specific *C. elegans* mutant.

Long-term on-chip observation of *C. elegans* is generally done by successive and reversible immobilization and release of the worms in order to maintain physiological and normal worm development conditions. This fact, however, requires control of specific actuation protocols over the whole assay duration, in particular for adjusting on-chip fluidic or pressure conditions. Kopito *et al.* addressed this issue and presented a microfluidic system for imaging of worms within an optimized worm trap, named WormSpa (Fig 2.8c) [81]. In this work, trapping channels were ergonomically designed for hosting adult *C. elegans* for long-term immobilization (24 h). Each chamber consisted of a trapping area and an egg-collection area. An important feature of this device are the lateral openings on the side of the worm traps that allow the physiological egg-laying process occurring in adult hermaphrodites. The number of embryos laid, the pharyngeal pumping frequency and quantification of stress-mediated genetic expression have been considered as indicators of the health condition of immobilized worms. No damage by long-term confinement in the WormSpa was observed. The microfluidic device used in the *C. elegans*-bacteria interaction assays presented in Chapter 4 and 5 of this thesis was inspired by the WormSpa.

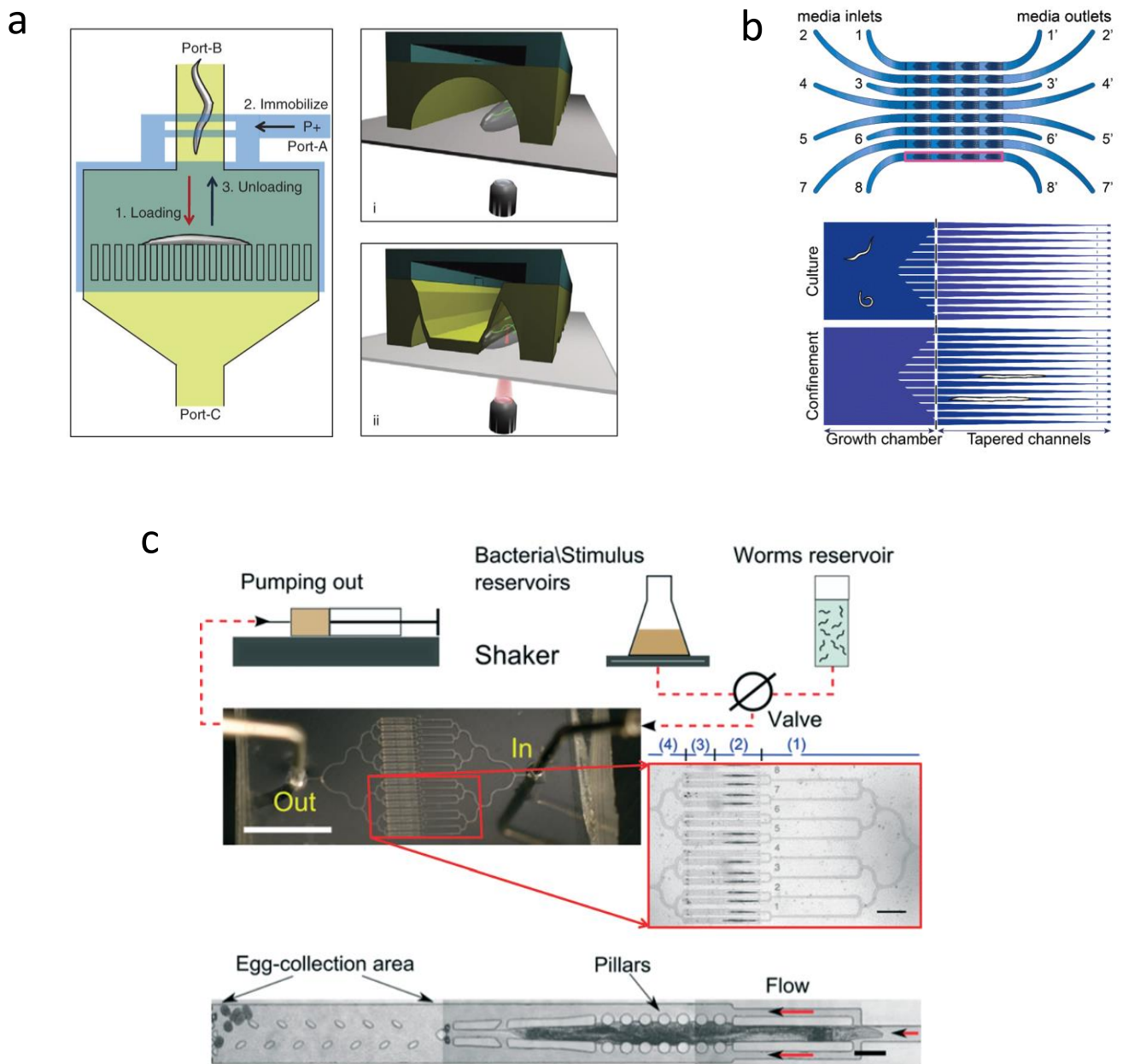


**Figure 2.8** - Examples of devices taking advantage of immobilization techniques by physical constriction. (a) A system based on the pneumatic valve approach. The device first linearly orients the worm, and then completely restrains its motion by pressing a flexible PDMS membrane against the animal. The diagrams indicate *C. elegans* loading/unloading sequences into the flow layer (yellow) and worm confinement by a narrow channel array. Immobilization by pressurizing the compression layer (blue) is indicated. The cross-sections of the chip schematically explain how laser microsurgery through the cover glass may be performed after worm immobilization. Reproduced and adapted from [79]. (b) Microfluidic platform for automated high-content phenotyping of *C. elegans*. Schematic representation of the microfluidic chip with 8 independent lanes, having each 4 chambers with two specific sections. Two operation modes are possible: "culture" mode with free-swimming worms and "confinement" mode in tapered channels for imaging and phenotyping. Reproduced and adapted from [80]. (c) WormSpa for long-term *C. elegans* on-chip immobilization. The worm is confined in an ergonomically designed microchannel. Laid embryos are present in the egg-collection area (indicated by arrows, bottom image). Design and schematic representation of a WormSpa experiment (top image). The inlet of the device can be selectively connected to worms or bacteria/stimulus reservoirs for loading or feeding

operations, respectively. Flow is induced by suction through a syringe pump connected to the outlet. Reproduced and adapted from [81].

## 2.3 Microfluidic platforms for *C. elegans*-bacteria interaction studies

Microfluidic techniques for *in vivo* imaging of *C. elegans* have reached a certain degree of maturation, allowing effective trapping of worms at any development stage, high-resolution imaging and high-throughput analysis. However, for the time being, only a few studies took advantage of microfluidics in order to investigate bacterial presence in the nematodes' intestinal lumen and to perform pathogenicity assays. Yang *et al.* presented one of the first studies that used a microfluidic platform to observe pathogenic colonization of *C. elegans* [82]. The system was designed to perform on-chip compound screening for evaluating possible antimicrobial properties. The device comprises a central worm dispenser from where worms are distributed into a surrounding concentric arrangement of 32 trapping chambers (Fig. 2.9a). Worms were exposed to pathogenic *Staphylococcus aureus* or the mildly pathogenic *E. coli* OP50 strain and maintained on-chip for 6 h at 25 °C to induce infection in worms' intestine. After washing out the bacteria suspension, nematodes in the incubation chambers were exposed to a drug/buffer medium solution. Thanks to four on-chip microfluidic concentration gradient generators connected to the chambers, 32 different conditions could be tested simultaneously. A range of potential antimicrobial molecules (aloe-emodin, rhein and emodin) was tested and the antimicrobial activity was compared to a well-established bactericidal antibiotic (amoxillin). In a separate study, Lee *et al.* adopted the WormSpa platform, already described in the previous section (Fig. 2.8c), to perform on-chip infection of individual *C. elegans* young adult worms with pathogenic bacteria. The dynamics of immune response genes and egg-laying events were monitored [83]. An array of the ergonomic WormSpa confinement structures was used for that purpose to align individual nematodes side-by-side. A bacterial suspension of *P. aeruginosa* was continuously perfused to the channels for 10 h and simultaneously time-lapse images of worms were acquired. Worms' response to infection was monitored by measuring the expression of infection-induced fluorescent genetic reporters (Fig. 2.9b). In particular, the activity of the immune response gene *irg-1* was evaluated, which is strongly expressed in the intestine at early stages of *P. aeruginosa* infection. In addition, laid embryos were counted over the entire experiment. Hu *et al.* proposed a different design of an integrated microfluidic device for *in vivo* analysis of *C. elegans* immune response and antibiotic effectiveness on infected worms [84]. The platform consisted of a two-layer microfluidic chip enabling pneumatic compression of the culture chambers for worm reversible immobilization (Fig. 2.9c). Expression of the *irg-1* gene was measured by time-lapse image acquisition in worms infected by pathogenic *P. aeruginosa* (strain PA14). The study indicated that *irg-1* gene expression possibly responds to the presence of *P. aeruginosa* in a dose-dependent fashion. In another study, Yang *et al.* developed a pneumatic microfluidic chip (pChip) for *in vivo* screening of antibacterial compounds at single-nematode resolution (Fig. 2.9d) [85]. The device comprises a worm sampler and a drug dispenser, both connected to an array of incubation chambers that can be individually isolated by pneumatic action. A dedicated side channel allowed loading single worms into each chamber. The chip was validated by testing multiple antibiotic compounds on nematodes infected and colonized by *P. aeruginosa*. Lee *et al.* presented the so-called HandKChip (Hands-free killing assay on a chip) as alternative microfluidic method to standard nematode killing assays based on agar plates (Fig. 2.9e) [86]. In particular, the microfluidic chamber was constructed with a hexagonal array of micropillars that supported worm motility, thus simulating properties of solid media used for conventional assay substrates. The worms were exposed up to 40 h and infected with *P. aeruginosa* PA14 bacteria. High-content automated phenotyping was achieved by simultaneous quantification of multiple indicators, including intestinal bacterial load, fluorescent gene (*irg-1*) expression, worm's body color and motility (Fig. 2.9f).



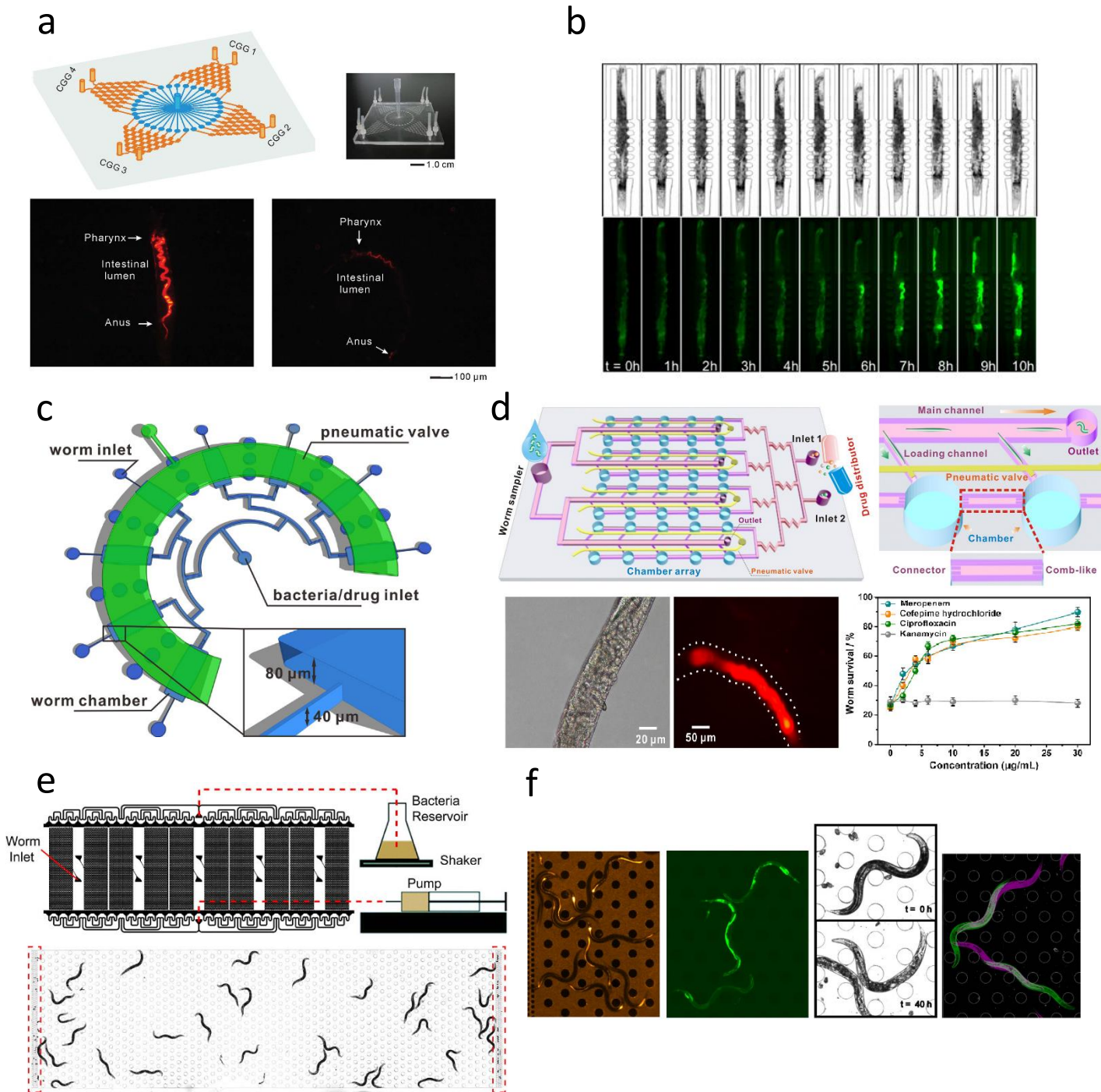


**Figure 2.9** - Microfluidic platforms for *C. elegans*-bacteria interaction studies. (a) Schematic of a microfluidic device for antimicrobial compound screening assays. The chip presents two functional units: a radial worm dispenser with 32 deep-sunken trap chambers and 4 multiple gradient generators. A photograph of the chip with fluidic connections is also shown. Fluorescence photomicrographs (below) enabled tracing the infection patterns of worms after feeding for 6 h on *S. aureus* (on the left) and *E. coli* OP50 (on the right), respectively. (b) WormSpa confinement structure for long-term on-chip monitoring. Time-lapse bright field and GFP fluorescent images of a representative *irg-1* mutant acquired over 10 h after the onset of *P. aeruginosa* infection. Increasing pathogenic colonization of the worm's intestine can be observed. The image at  $t = 0$  was taken just before the pathogen was introduced. (c) Schematic of the microfluidic device for real-time monitoring of *C. elegans* pathogen-induced immune response. The two-layer microfluidic chip was designed for worm culture and immobilization by pneumatic compression. (d) Schematic representations of the pChip for antibacterial screening (top). The device has three functional units: a worm sampler, a drug distributor, and the chamber array with channels for dispensing worms individually. The enhanced view indicates single-worm loading

and pneumatic isolation of each chamber (top). Bright field and fluorescence micrographs of a worm infected after on-chip exposure for 6 h with fluorescently labeled *P. aeruginosa* (lower left side). Survival rate of *P. aeruginosa* infected worms after treatment with meropenem, cefepime hydrochloride, ciprofloxacin and kanamycin for 4 days (lower right side). (e) HandKAchip for worms killing assays compatible with standard assays on solid media. A schematic of the microfluidic worm chambers and the experimental scheme is represented (top). The bright field image shows a single chamber hosting a population of crawling worms. Lateral worm filters (marked by red dashed boxes) prevent adult worms from escaping while allowing progenies and liquid to pass through (bottom). (f) Representation of the four infection-related phenotypes measured with the HandKAchip platform: *P. aeruginosa* PA14 RFP intestinal bacterial load, *irg-1::GFP* fluorescent gene expression, nematode body color and motility (left to right). Reproduced and adapted from [82, 83, 84, 85, 86].





## Chapter 3 Microfluidic chip fabrication, materials and system integration

This chapter describes common methods, materials and microfluidic system integration aspects used for the projects carried out in the frame of this thesis. First, two dedicated fabrication protocols for the PDMS microfluidic chips that were used for *C. elegans*-bacteria interaction assays and intestine imaging (Chapters 4 and 5) will be explained in detail. This PDMS microfluidic chip technology is based on conventional fabrication methods, involving the design and realization of a Cr mask for the photolithography process, fabrication of Si/SU-8 molds for single- or double-layer PDMS devices and PDMS soft lithography. A somewhat different protocol was adopted in the frame of the project for bacterial imaging (Chapter 6), where a polymeric membrane/dielectric sphere assembly (PMDSA) was realized. Furthermore, the preparation techniques for *C. elegans* and bacterial samples will be outlined. In the final section of this chapter, microfluidic device integration will be described, comprising the experimental setups for fluidic manipulation and optical imaging.

### 3.1 Microfluidic chip fabrication

#### 3.1.1 Mask for photolithography

Mold fabrication for the microfluidic PDMS devices requires a photolithographic process for transferring the design patterns into a photosensitive SU-8 negative resist layer. The following standard protocol for mask fabrication is applicable for all photomasks used in this thesis. Initially, the design layout of the microfluidic chip was drawn by using CleWin editor. Functional elements, such as worm or bacteria trapping structures and worm filters, were integrated in the on-chip microchannels (Fig. 3.1a and b). The geometrical features of the microfluidic structures were defined according to the specific requirements of the application of interest. Use of conventional photolithographic techniques allowed accurate replication of the computer-designed chip layouts on the fabricated devices (Fig. 3.1c and d).

A blank mask is a 5" × 5" quartz substrate covered by a Cr layer and a thin positive photoresist layer. The chip design was transferred into the resist layer by laser beam exposure and chemical development. The uncovered parts of the Cr layer were chemically etched, thus opening defined transparent areas on the mask for subsequent SU-8 exposure. Finally, photoresist remaining on the mask was removed. Figure 3.2 describes the mask fabrication process.

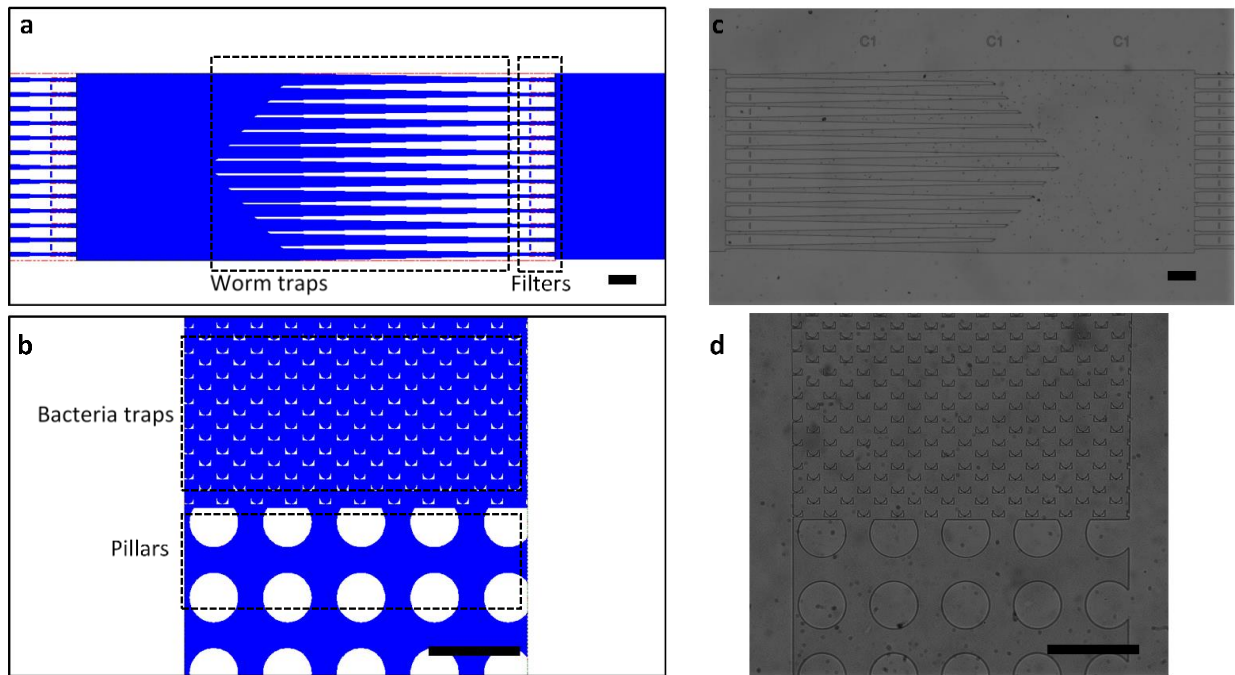


**Figure 3.1** – Microfluidic device designs. (a-b) Mask designs used for dynamic bacterial load measurements in *C. elegans* (a) and for enhancement of bacteria detection, presented in Chapter 4 and Chapter 6, respectively. Functional structures (white) integrated in the microchannels (blue) are highlighted by dashed rectangles. (c-d) Micrographs of the fabricated devices for dynamic bacterial load measurements in worms (c) and for enhancement of bacteria detection (d), respectively. Scale bars = 200  $\mu\text{m}$ .

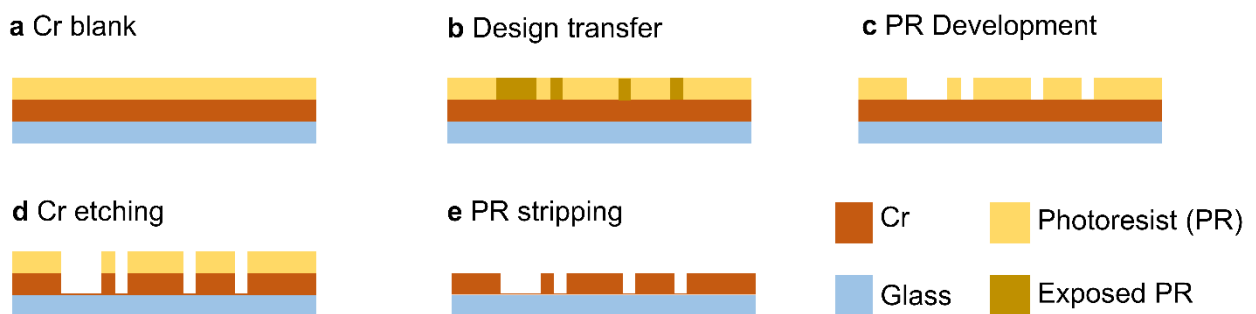


**Figure 3.2** - Cr photomask fabrication process. (a) 5"  $\times$  5" Cr/quartz blank with a thin positive photoresist layer. (b) The microfluidic chip design was transferred into the positive photoresist layer by means of a laser writer. (c) Exposed photoresist was developed. (d) Chemical etching of the Cr layer. (e) Non-exposed photoresist was stripped with solvents.

### 3.1.2 Fabrication of single-layer and double-layer Si/SU-8 molds

The microfluidic device was conceived as a PDMS layer on a glass coverslip. Microfluidic chips were prepared by soft lithography using SU-8 molds on 4-inch Si wafers. Conventional photolithography was used to pattern either a single SU-8 photoresist layer or a double-layer SU-8 layer, the latter requiring two exposure steps. The single-layer protocol is illustrated in Fig. 3.3. Si wafers were first coated with an 80  $\mu\text{m}$  thick SU-8 layer by spin-coating, which was subjected to a prebaking step and then exposed by UV light through a Cr photomask for transferring the microfluidic design. Development removes not polymerized unexposed areas of the negative SU-8 resist and reveals the mold structure. In the case of the double-layer process, a 20  $\mu\text{m}$  thick SU-8 layer was spin-coated on the Si wafer and exposed by means of a first photomask. Subsequently a 40  $\mu\text{m}$  thick SU-8 layer was deposited on top and exposed through a second photomask. This protocol allows fabricating a microfluidic device with different structure heights. Chlorotrimethylsilane (TMCS) treatment of the Si/SU-8 mold was carried out to avoid PDMS adhesion to the wafer/mold surface during the final demolding operation. For fabricating the microfluidic chips, a PDMS mixture (10:1 base to crosslinker weight ratio) was degassed, poured onto the mold and cured at 100  $^{\circ}\text{C}$  for 1h. After PDMS demolding, fluidic inlets and outlets were punched into the material and the chip was bonded by air plasma-activation onto a 150  $\mu\text{m}$  thick glass slide. Finally, the chip was connected to external tubing.

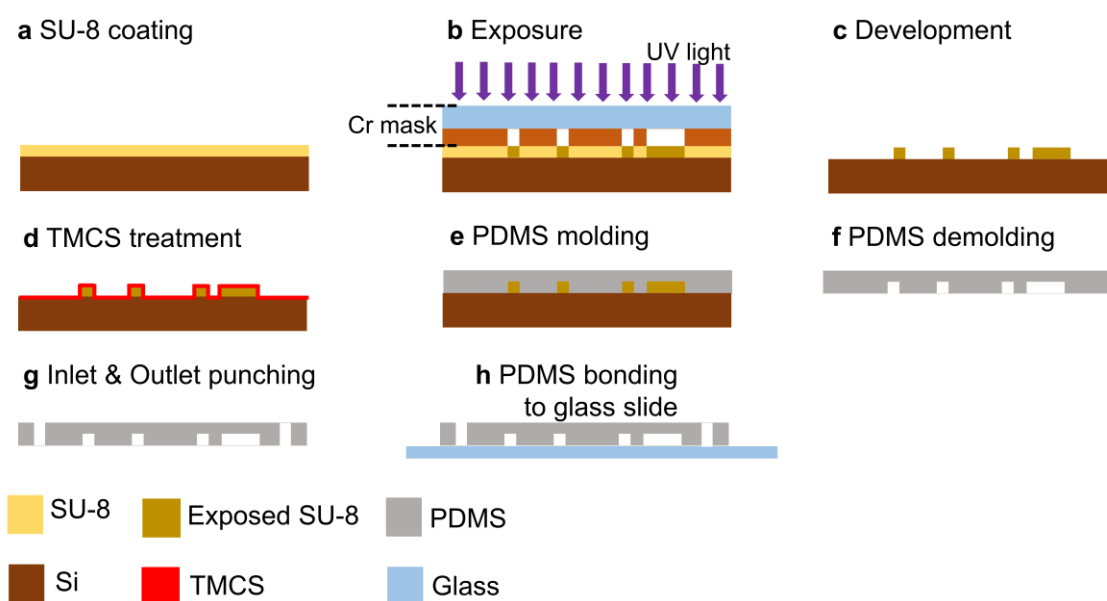


**Figure 3.3** - Fabrication process of a single-layer Si/SU-8 mold and the PDMS microfluidic chip. Standard photolithography techniques were utilized to (a) deposit an 80  $\mu\text{m}$  thick SU-8 layer, (b) expose it by UV light and (c) remove unexposed patterns. In the case of the double-layer mold, steps (a) and (b) were performed twice. (d) The molds were treated with TMCS under vacuum to prevent PDMS adhesion upon demolding. (e) PDMS was poured and cured on the wafer. (f) The microstructured PDMS block was peeled off, (g) inlets and outlets were punched, and (h) the PDMS chip and a glass slide were bonded together by air plasma treatment.

The fabrication process allows fast prototyping. Before each experiment, the microfluidic chip was filled with Pluronic F-127 and incubated overnight. This coating avoids clogging of the PDMS channels by minimizing bacterial adhesion and biofilm formation. Then the microfluidic device was flushed with 1 mL of 70 % ethanol and dried with an air gun.

### 3.1.3 Fabrication of a polymeric membrane/dielectric sphere assembly

For the fabrication of the polymeric membrane/dielectric sphere assembly (PMDSA), we utilized a procedure to create PDMS membranes featuring custom-defined microfluidic structures and embedded millimeter-sized spheres to increase bacterial imaging resolution and sensitivity (Fig. 3.4). The microfluidic design comprises larger channels with supporting pillars and micrometer-sized structures for hydrodynamic bacteria trapping and position control. For this process, the mold structure for casting the PDMS membrane was

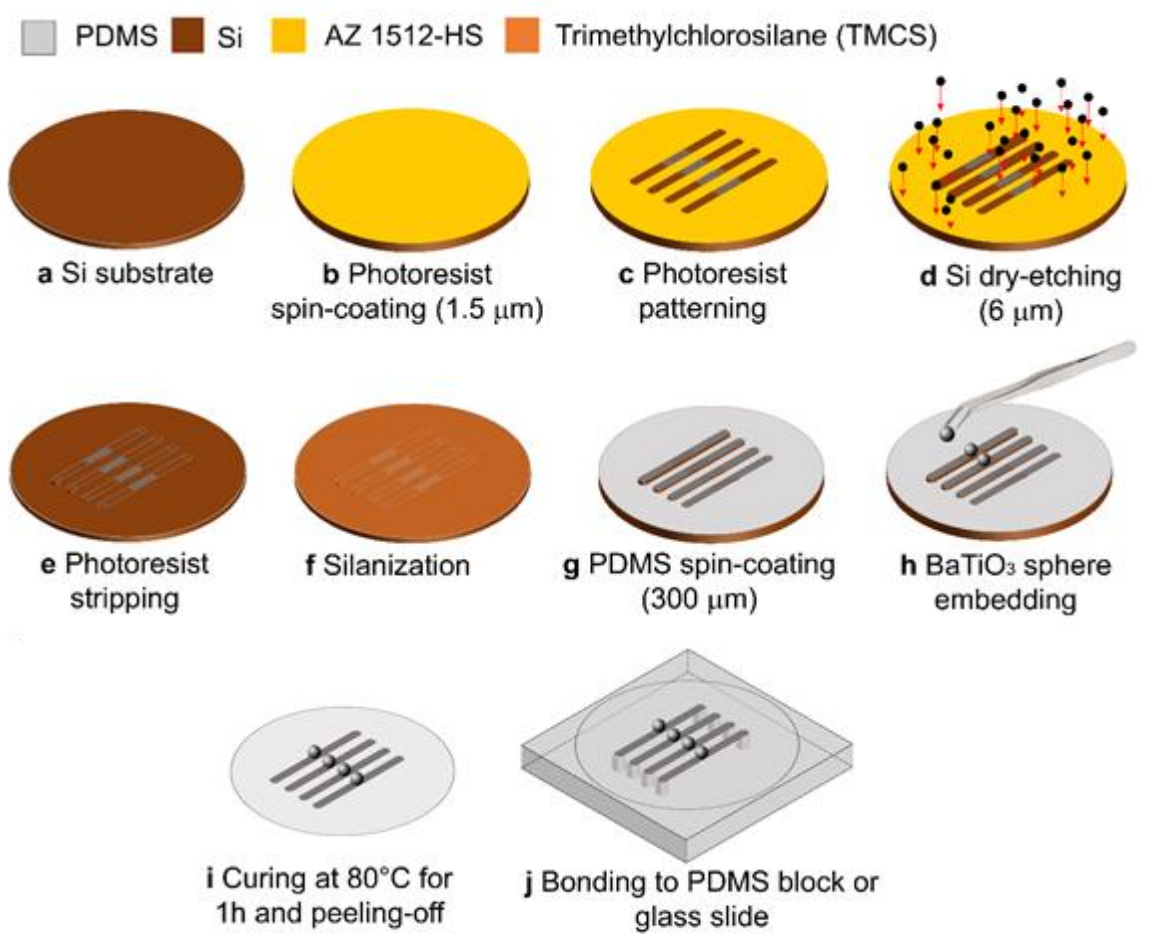


**Figure 3.4** - Schematic of the fabrication procedure a polymeric membrane/dielectric sphere assembly (PMDSA), comprising a PDMS membrane with partially embedded BaTiO<sub>3</sub> dielectric spheres. (a-e) Channels and trapping structures are patterned on a Si wafer by photolithography and dry etch processing. (f) Silanization of the Si mold to prevent PDMS from sticking to the wafer. (g-h) PDMS prepolymer is spin-coated and BaTiO<sub>3</sub> dielectric spheres are manually placed at positions corresponding to the microfluidic structures. (i-j) The whole wafer is heated to 80 °C for PDMS curing, then the membrane with integrated spheres is peeled off and bonded to a PDMS block or to a glass slide.

directly realized in a Si wafer. Conventional photolithography was used to pattern a 1.5  $\mu\text{m}$  thick AZ9260 positive photoresist layer on the Si wafer. Subsequently, the blank parts of the Si substrate were dry etched to a depth of 6  $\mu\text{m}$  and the remaining protective photoresist layer was stripped. For dry etching, a standard Bosch process at 25°C (etching rate  $\sim 3.5 \mu\text{m}/\text{min}$ ) was applied. The Si mold surface was silanized in order to prevent sticking of the PDMS membrane on the substrate when peeled off. The 300  $\mu\text{m}$  thick PDMS membrane was formed by spin-coating (10:1 prepolymer to curing ratio) on top of the microstructured Si wafer. To create the final PMDSA, millimeter-sized  $\text{BaTiO}_3$  spheres were positioned on the PDMS film at the desired locations. Finally the PDMS was cured (80 °C for 1 h) and peeled off the Si mold. Pillars and hydrodynamic traps should be located underneath the dielectric spheres for bacterial imaging. These structures were therefore distributed over the microfluidic channels in dense arrays, so that no particular accuracy in positioning of the spheres was required. The latter step could then be easily performed manually with tweezers by visual inspection under a stereomicroscope. The full chip was assembled by bonding the PMDSA to a thick flat PDMS block by air plasma activation. Fluidic inlets and outlets were manually punched into the PDMS and sealed on one side by bonding to a glass slide, before connecting the chip to external tubing. Embedding of the  $\text{BaTiO}_3$  spheres directly in the patterned PDMS membrane highly improved the precision of the location of the spheres relative to the microfluidic structures. Spheres could be accurately reversibly positioned before the PDMS curing step. An alternative method would be to bond a membrane with embedded dielectric spheres onto a patterned PDMS block. However, in this case alignment is extremely critical because it must be done very quickly after plasma activation of the PDMS surfaces and the bonding is irreversible.

### 3.2 Materials and chemicals

4-inch 550  $\mu\text{m}$  thick Si wafers and 5-inch Cr/quartz glass masks were obtained from the EPFL Center of MicroNanoTechnology (Lausanne, Switzerland). SU-8 3050 negative epoxy photoresist was purchased from micro resist technology GmbH (Berlin, Germany). PDMS Sylgard 184 was acquired from Dow Silicones Deutschland GmbH (Wiesbaden, Germany).  $\text{BaTiO}_3$  spheres were acquired from Cospheric LLC (Santa Barbara, United States). Microline ethyl vinyl acetate tube (0.51 mm inner and 1.52 mm outer diameter) was bought from Fisher Scientific AG (Wohlen, Switzerland). Corning® (75 mm  $\times$  50 mm, thickness 960  $\mu\text{m}$ ) microscope slides were purchased from Sigma-Aldrich Chemie GmbH (Buchs, Switzerland). Pluronic F-127 solution with a concentration of 0.4 wt.% was used. Buffer solutions (pH 3.776, 4, 5, 6) were purchased from Roth AG (Arlesheim, Switzerland). S-medium for worm culture was prepared with 1 L of S-Basal, 10 mL 1 M potassium citrate (pH 6), 10 mL trace metals solution, 3 mL 1 M  $\text{CaCl}_2$  and 3 mL 1 M  $\text{MgSO}_4$ . S-Basal and L-Broth were sterilized by autoclaving. Lysogeny Broth (LB) for *E. coli* bacteria liquid culture, 5-hydroxytryptamine hydrochloride, tetracycline, ampicillin and kanamycin, and 1  $\mu\text{m}$ -size rhodamine B marked melamine resin microparticles were purchased from Sigma-Aldrich (Buchs, Switzerland). Middlebrook 7H9 broth for *M. marinum* culture was obtained from the EPFL Laboratory of Microbiology and Microtechnology (EPFL-LMIC, Lausanne, Switzerland).

### 3.3 *C. elegans* and bacteria preparation

*C. elegans* N2 worms, DA465 *eat-2(ad465)* II and SJ4100 *zcls13[hsp-6::gfp]* mutants were provided by the Caenorhabditis Genetics Center (University of Minnesota). In order to obtain synchronized *C. elegans* populations, embryos were extracted from gravid adult worms by a standard bleaching protocol and cultured at 20 °C on NGM agar plates seeded with *E. coli* strain OP50. At L4 stage or young adult (YA) stage depending on the study, worms were collected from the agar plates. After embryos hatching, L4 larvae and YA worms were obtained after approximately 28 h and 50 h of on plate culturing, respectively. Subsequently, worms were suspended in S-medium and loaded into the microfluidic device. Different bacterial samples were used as food source for the on-chip assays. *E. coli* OP50 expressing red fluorescent protein (RFP) was constructed by transformation with plasmid vector *pRZT3::dsRED* using standard methods. *pRZT3* also contains a sequence for tetracycline resistance. Unlabeled *E. coli* OP50 were grown in LB and *E. coli* OP50 RFP in LB with 25 µg/mL tetracycline. The GFP expressing *E. coli* HT115 strain (RRID:WB-STRAIN:HT115) was inoculated in LB with 100 µg/mL ampicillin and 10 µg/mL kanamycin. All *E. coli* bacteria were cultured overnight in a shaker at 37 °C. *M. marinum* bacteria (unlabeled or GFP labeled) were inoculated in Middlebrook 7H9 broth and grown for 2 days at 30 °C. After culture, bacterial suspensions were centrifuged, bacteria pellets were resuspended in filtered S-medium and diluted to a concentration of  $4 \times 10^9$  cells/mL. Bacterial samples were freshly prepared for each experiment and the concentration was measured prior to each experiment with a WPA CO 8000 Biowave Cell Density Meter (Biochrom Ltd., UK). *E. coli* OP50 and HT115 GFP strains were provided by the EPFL Laboratory of Integrative Systems Physiology (EPFL-LISP) and *E. coli* OP50 RFP by the *C. elegans* Ageing Laboratory (University College London). *M. marinum* strains were provided by the EPFL Laboratory of Microbiology and Microtechnology (EPFL-LMIC).

### 3.4 Experimental setup of the microfluidic platforms

In the following sections, a brief illustration of the microfluidic system integration including optical and fluidic instrumentation is given. Experimental protocols and operation modes of the microfluidic platforms are described more in detail in the dedicated chapters.

#### 3.4.1 Platform for *C. elegans* studies

The microfluidic device was mounted on an upright microscope (Zeiss Axio Imager 2) equipped with a sCMOS pco.edge 4.2 LT camera (PCO AG, Germany) and two illumination systems for brightfield and fluorescence imaging, respectively. Low-resolution (Zeiss Plan-APOCHROMAT 10× NA 0.45 and Zeiss LD Plan-NEOFLUAR 20× NA 0.4) and/or high-resolution objectives (Zeiss 50× NA 0.55) were utilized for image acquisition, depending on the assay. The microfluidic chip was connected to a 12-port rotary valve placed on a Kloehn V6 48K Syringe drive pump (IMI Precision, United States). A Python script was used to control and the syringe pump via serial port commands. In experiments involving use of liquid suspensions of pathogenic bacteria, in particular *M. marinum*, a neMESYS syringe pump (Cetoni GmbH, Germany) was used. The motorized computer-controlled xyz-stage (Visitron Systems GmbH, Germany) enabled automated time-lapse image acquisition. VisiView® imaging software (Visitron, Germany) was used for this purpose. An illustration of the experimental setup is shown in Fig. 3.5a.

#### 3.4.2 Platform for bacterial imaging based on a PMDSA

The microfluidic chip was mounted on an Axio Imager M2 upright microscope, equipped with a SOLA light engine SOLA SE 5-LCR-VB (Lumencor). A filter cube Filter Set 43 HE (Zeiss, Germany) was placed in the opti-

cal path for fluorescence imaging. We used an air objective EC Epiplan-Neofluar 10x/0.25 DIC M27 and LD EC Epiplan-Neofluar 100x/0.75 DIC M27 (Zeiss, Germany). Images were recorded with a sCMOS camera pco.edge 4.2 LT (PCO AG, Germany) in 2x2 binning mode with variable exposure, depending on the condition of the specific experiment. In order to automate the acquisition, the microfluidic chip was fixed on a motorized xyz-stage (Visitron, Germany) of an upright microscope and connected to a neMESYS syringe pump (Cetoni GmbH, Germany). An illustration of the experimental setup is shown in Fig. 3.5b.

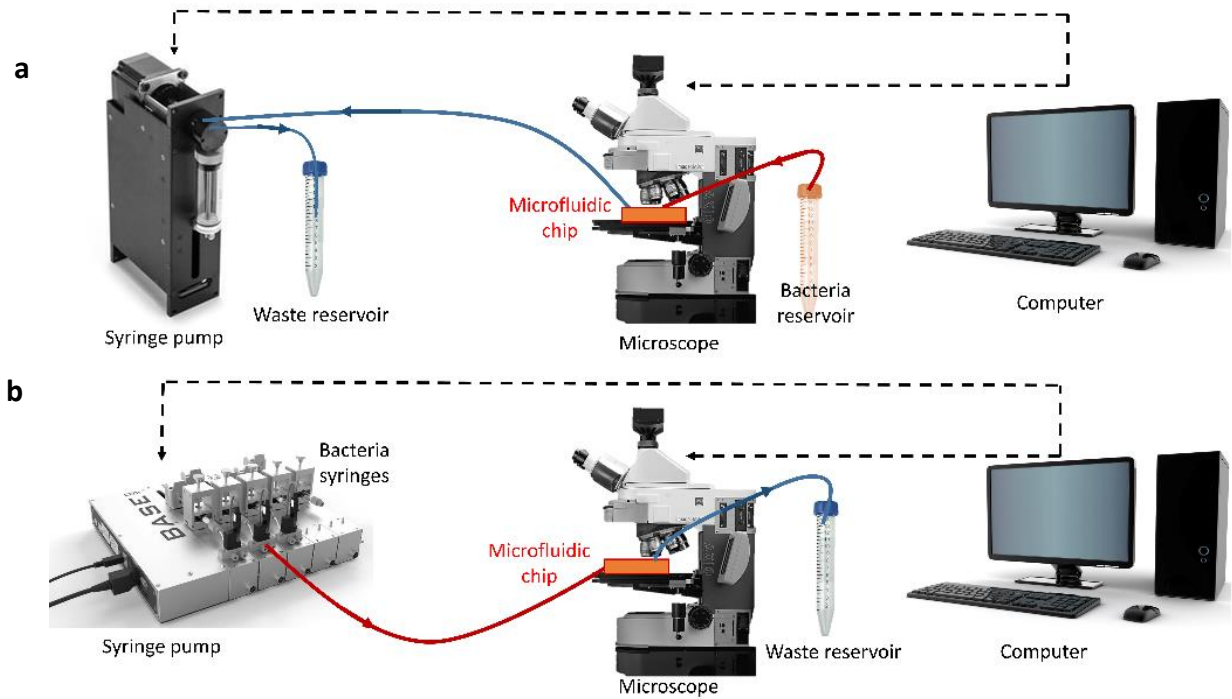


**Figure 3.5** – Experimental setup of the microfluidic platforms. Microscope and syringe pumps operations are computer-controlled (as indicated by dashed lines). (a) Typical setup used for the *C. elegans* analysis platforms. Fresh bacterial suspension is introduced into the microfluidic device by suction from a bacterial reservoir (indicated by the red line). For assays with non-pathogenic *E. coli*, a Kloehe syringe pump is used for this purpose (shown in the picture). For assays with pathogenic bacteria a neMESYS syringe pump is used, in order to prevent contamination of the user. For assay parallelization each microfluidic channel on the chip was connected independently to a dedicated reservoir. In this case the syringe pump was connected to the chip through a 12-port rotary valve (not shown). (b) Setup used for the PMDSA bacterial imaging platform. Fresh bacterial solution is injected into the microfluidic device by a neMESYS syringe pump (indicated by the red line). Each channel in the microfluidic device is connected to a dedicated syringe in this case.





## Chapter 4 Bacterial transit dynamics in the *C. elegans* intestine

*C. elegans* has gained importance as model organism for studying host-microbiota interactions and bacterial infections related to human pathogens. In this perspective, we introduce in this chapter a novel method for studying the dynamics of *E. coli* bacterial transit through the worm intestine. A microfluidic chip was designed for alternating *C. elegans* on-chip culture and immobilization, thereby enabling time-lapse imaging of the worm's gut and its bacterial load at single-worm resolution over several days. Immobilization was achieved in a reversible way using arrays of tapered channels suitable for assay parallelization. Dedicated *C. elegans* feeding protocols were applied. Two *E. coli* bacterial strains, HT115 and OP50, respectively labeled with green fluorescent protein (GFP) and red fluorescent protein (RFP), respectively, were used as food source and imaged with fluorescence microscopy techniques to measure relevant parameters of the bacterial transit process. Feeding behavior and *E. coli* transit dynamics in the whole intestinal tract of the worms were characterized in an automated way over the first 3 days of adulthood, revealing both fast transit phenomena and variations in microbial accumulation. In particular, we studied the bacterial food transit periodicity in wild-type and *eat-2 (ad465)* mutant *C. elegans* strains in both trapped and free-swimming conditions. In order to further demonstrate the versatility of our microfluidic platform, we also investigated drug-induced modifications of the bacterial transit by measuring the response of the worm intestine to the neurotransmitter serotonin.

---

This section was adapted from the following publications:

V. Viri, M. Cornaglia, H.B. Atakan, T. Lehnert, and M.A.M. Gijs, "An *in vivo* microfluidic study of bacterial transit in *C. elegans* nematodes", *Lab on a Chip*, 2020, **20**, 2696-2708.

V. Viri, M. Cornaglia, and M.A.M. Gijs, "An *in vivo* microfluidic method for study of bacterial digestion inside *C. elegans* roundworms", poster presentation, *MicroTAS 2018*, 11-15 November 2018, Kaohsiung, Taiwan.

V. Viri, T. Lehnert, and M.A.M. Gijs, "A microfluidic system for investigating the transit dynamics of live and heat-killed *E. coli* bacteria in *C. elegans*", poster presentation, *MicroTAS 2020*, 4-9 October 2020.

## 4.1 Introduction

Over the last decades, *C. elegans* has become an important model organism for investigating fundamental questions in genetics and neurobiology [87, 8, 88, 89]. More recently, in a context of increasing research efforts for elucidating gut microbiome effects on human health and in a more general sense to foster research on the gut-brain connection [90, 91, 92], this microbivorous nematode has drawn new attention as model organism for microbe-host interactions studies [35, 93, 94]. *E. coli* bacteria, which are processed and assimilated in the worm's intestine, are the common food source of *C. elegans*. In fact, all interactions between the organism and ingested bacteria are mediated by the worm's gut, comprising multiple concurrent processes, such as bacteria digestion and pathogenic colonization events [95, 96, 97]. Several research groups focused on the potential interdependence of the gut microbiota and innate immunity in *C. elegans*, thus contributing to the understanding of the molecular and genetic basis for aging and longevity, for instance [98, 99, 100, 101]. Other groups studied the impact of the microbial diet on the metabolism of *C. elegans* [102, 61]. Such biological assays often take advantage of compound-induced modulation of food intake and absorption of nutrients [103, 104]. In this context, reliable quantitative measurements of the bacterial load in the worm's gut of different worm genotypes are required to conduct studies on the organism's response to commensal or pathogenic bacterial exposure. For instance, Portal-Celhay *et al.* performed studies to determine the intestinal bacterial load in *C. elegans* and found a strong correlation between bacterial counts and lifespan [67]. The study was performed using conventional methods and assays on standard agar plates. Ghafouri *et al.* evaluated the bacterial residence time in the *C. elegans* gut. In this work, adult worms were fed with fluorescent polystyrene microbeads mixed with *E. coli* food in order to monitor intestinal clearance [105]. Ingestion of mildly pathogenic bacteria can be a causative factor of worm death, depending on the strain of the food source, intestinal region of accumulation and type of mutant used [106]. Alternative methods to standard agar plates, such as liquid culture in well plates, have been adopted for feeding assays or antimicrobial tests [107]. Gomez-Amaro *et al.* successfully performed nutrition assays on intestinal clearance in a 96-well microtiter plate-based assay that measured the food intake of *C. elegans* in liquid medium by quantifying the change in optical density of the bacteria suspension over time [63]. The bacterial food intake was characterized as a function of the worm development state and of their response to serotonin. However, such an approach presents some limitations related to the lack of active fluidic control, thus accurate control and maintenance of the concentration of the bacteria suspension and of the drug in the culturing medium cannot be guaranteed for long-term experiments. Indeed, fine control of bacteria suspension perfusion would be an important parameter for versatile food intake assays. More recently, a bioluminescence-based method for assessing the food intake and measuring compound-induced modulations in feeding behavior of *C. elegans* worms was developed [108].

In a context where various assay parameters may significantly alter the observed phenotype, microfluidic tools are particularly useful for generating controlled perturbations of the organism's microenvironment and for facilitating the observation of compound-induced effects. Microfluidic systems are now frequently used indeed for research involving *C. elegans* [37, 38, 109]. Phenotypic characterization could be significantly improved in studies on the single-cell level of multicellular tissues, not least because of the implementation of optimized and powerful on-chip imaging protocols [110, 40, 111, 112, 75]. As was outlined in Chapter 2 (Section 2.2), different lab-on-a-chip systems enabled worm sorting [78, 113] and worm immobilization [73, 114, 81]. In most cases, trapping of worms is obtained by pushing them into tailored immobilization microchannels or by actuation of integrated on-chip structures, based on the deformation of elastic membranes for gently squeezing of the worm body. For instance, Keil *et al.* proposed a valve-based approach for a cell development study on immobilized single nematodes by means of Nomarski and multi-

channel fluorescence microscopy [115]. Nevertheless, the added value of microfluidic systems for studying directly the interaction and impact of specific bacterial strains on *C. elegans*, *i.e.* dietary studies or worm gut colonization assays, is still underexplored. Previously, our group developed an automated system allowing confinement, trapping and fast phenotyping of *C. elegans* in order to observe the effects of dietary restriction on a worm mutant modeling Huntington's disease [80]. Other on-chip worm feeding studies investigated the influence of food concentration on the developmental response of antibiotic-treated worms [70], the feeding behavior in presence of anthelmintic drugs [116] or the incidence of different food concentrations on the lifespan of the organisms [117]. In a few works, devices were used to directly perform colonization assays. Lee *et al.* reported a 'hands-free killing assay', using a chip-based device featuring 10 to 20 separate microfluidic incubation chambers. The assay was based on monitoring of ~30 worms per chamber, where pathogenic bacteria *Pseudomonas aeruginosa* were continuously perfused (see Chapter 2, Fig. 2.9e and 2.9f) [86].

In this work, we present an on-chip system and microfluidic method to characterize the transient properties of food intake and processing in *C. elegans* under different experimental conditions. The microfluidic chip is designed for long-term worm culture and on-demand immobilization of single organisms. We demonstrate that the device is suitable for monitoring and characterizing the bacterial transit process over several days, enabling both measurement of bacterial load in the worms' gut and live imaging of the organism. Phenotyping of immobilized worms was performed by means of automated fluidic and imaging protocols. We demonstrate the versatility of our method by monitoring both rapid and prolonged changes of the bacterial content in the gut during nutrient absorption. The method was further validated by unraveling the effect of food intake modulation induced by the 5-hydroxytryptamine hydrochloride (5-HT) neurotransmitter on the bacterial load within the worm intestine.

## 4.2 Microfluidic platform and imaging protocols

### 4.2.1 Microfluidic chip design

Micro-environmental conditions may have a significant influence on physiological processes during *C. elegans* development. Hence, on the one hand, the variability of assays has to be minimized in order to identify the response to specific assay parameters, and on the other hand, the experimental approach should be versatile. For these reasons, testing different experimental conditions in parallel on an adequate number of samples is of importance. We designed a chip that contains a set of 4 main channels for testing simultaneously up to 4 different conditions. Each channel comprises 5 successive chambers, which were optimized for culturing 1 to 3 worms, thus the number of worms within each chip is sufficiently high for data analysis with statistical significance. A schematic view of a single channel is shown in Fig. 4.1a. Each Y-shaped channel features two inlets (In 1 and In 2). In 1 is used for initial worm loading and for periodic bacterial food injection during an experiment and In 2 for rinsing the chambers with clean S-medium. Each chamber is delimited by a microfluidic filter structure on its upstream side, the geometry of which was specifically tailored for letting pass L4 larvae but not adult worms, by designing the pore size of the filters such that the PDMS post distance was 22  $\mu\text{m}$  (Fig. 4.1b). The pore size is large enough for efficient wash-out of embryos and L1 progeny. Each on-chip chamber comprises two sections, one for worm culturing and another one for immobilization and imaging of the worms. The immobilization section is formed by 13 parallel tapered traps for tight and secure confinement of the worms at different development stages. Tapered traps also have the advantage that worms can be reversibly immobilized by simply changing the sense of the flow. A

schematic view of a single chamber is provided in Fig. 4.1c and a photograph of the whole chip arrangement with fluidic connections is shown in Fig. 4.1d, respectively.

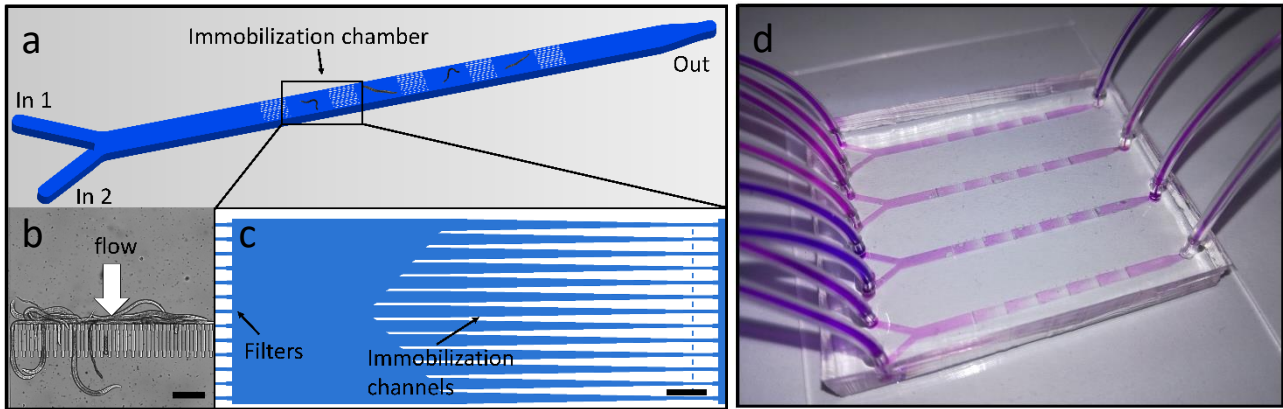


**Figure 4.1** - Microfluidic device for bacterial transit studies in *C. elegans*. (a) Chip design. Schematic view of the serial arrangement of 5 culture/immobilization chambers. The channel has two inlets (In 1 and In 2) for injecting worm/bacterial suspensions and clean S-medium, respectively, and a single outlet (Out). (b) Zoom on the passive PDMS filter structure in front of each culture chamber for selectively loading of L4 larvae. The image shows L4 worms passing through the filter, while adult worms are retained. Scale bar = 200  $\mu\text{m}$ . (c) Schematic view of an individual worm chamber (blue space is filled with liquid) comprising a larger free space for worm culture (left-hand side) and a parallel arrangement of tapered channels for worm immobilization and imaging (right-hand side). Scale bar = 500  $\mu\text{m}$ . (d) Photograph of the entire PDMS chip with tubing, featuring parallel channels for four independent assays.

#### 4.2.2 Operation of the microfluidic platform

The microfluidic chip was fixed on the motorized xyz-stage (Visitron, Germany) of an upright microscope and connected to a V6 Kloehn syringe pump (Kloehn, USA) through a 12-port rotary valve for fluidic control. Both were computer-controlled. A single-channel version of the experimental setup of the microfluidic platform was shown in Chapter 3 (Fig. 3.4a, without rotary valve). Each channel was linked by external tubing to one port of the rotary valve for selectively actuating loading and feeding protocols. We coupled each microfluidic channel (In 1) of the chip to a dedicated reservoir, containing a synchronized population of approximately 20 *C. elegans* L4 larvae suspended in 600  $\mu\text{L}$  S-medium solution. As was shown in Fig. 4.1b, L4 larvae were gently pushed towards the first filter barrier of each channel, where they accumulated. Then, the worms were distributed into the culture chambers until 1 to 3 of them could be found in each chamber. The whole loading process was operated by applying a custom command sequence to the syringe pump for controlling the flow rate and the resulting pressure build-up in the chip. Here we took advantage of the elastic properties of the PDMS filter posts, as L4 worms were able to pass the first and successive filter barriers because of the deformation that was provoked by the increasing fluidic pressure. However, a few adult worms that might potentially be present in the population, despite synchronization, could not cross the first line of filters. After worm loading, reservoirs were replaced with new ones containing 600  $\mu\text{L}$  of bacterial feeding suspension. Then, automated fluidic operation for on-chip worm culture and immobilization was started. A custom developed Python script was implemented for flow control via the syringe pump. A fluorescently labeled *E. coli* suspension was injected every hour for a duration of 30 min in all

chamber lanes for worm feeding (flow rate 5  $\mu\text{L}/\text{min}$ ). Reservoirs were refilled manually with bacterial suspension every 24 hours. During the subsequent 30 min lapse, the flow was stopped allowing proper worm feeding without perturbation. The automated protocol also included agitation of the bacterial suspension in the syringe by magnetic stirrers just before injection, thus preventing bacterial sedimentation and allowing dispensing a consistent amount of food to the worms. The platform was operated for 72 hours after L4 loading. In order to avoid overcrowding of the chambers due to progeny production, embryos and L1 larvae were automatically washed out after each feeding cycle and removed from the chip outlet. Moreover, the microchannels were rinsed every 24 hours during a long-term experiment by injecting S-medium through In 2.

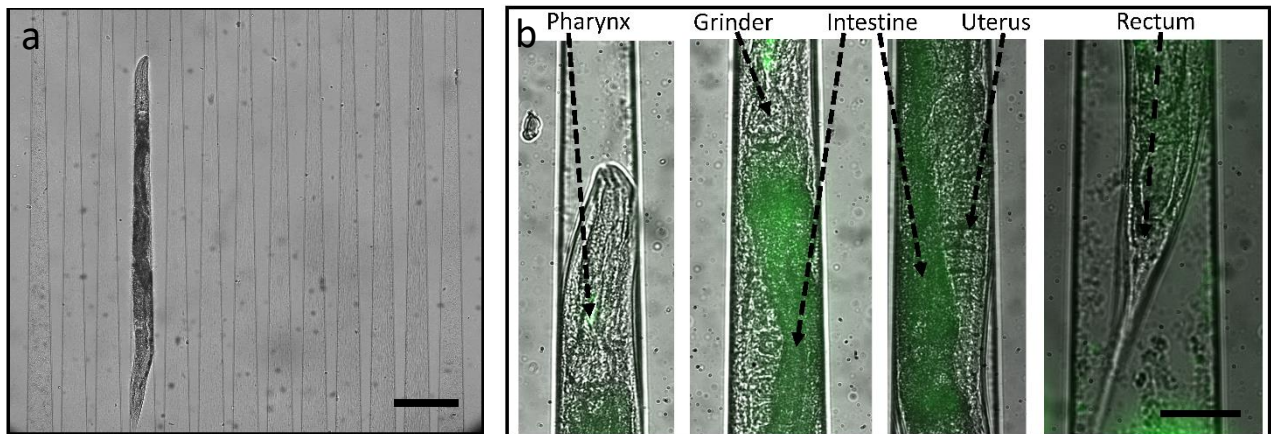


**Figure 4.2** - On-chip imaging of an immobilized worm. (a) Brightfield image of a wild-type adult *C. elegans* worm immobilized in one of the tapered traps. Scale bar = 200  $\mu\text{m}$ . (b) High-resolution brightfield/(auto-) fluorescence images of an adult N2 *C. elegans* worm highlighting different anatomical sections involved in bacterial food processing and bacterial transit. Scale bar = 50  $\mu\text{m}$ .

During this operation, bacteria aggregates accumulating in the filters were removed, thus avoiding flow disturbance and eventually clogging of the channels. The chamber clearing protocol was also performed in an automated way by applying repeated flow pulses (the In 1 tube was clamped manually during this operation). Worms were maintained in the culture chamber of the microfluidic chip most of the time, except for the immobilization period. During immobilization a moderate flow was applied (70  $\mu\text{L}/\text{min}$ ) for confining and maintaining the nematodes in the tapered channels. Worms moved back into the culture chamber by themselves when flow was stopped. Fig. 4.2a shows a brightfield image of the arrangement of tapered traps in a chamber with an immobilized wild-type adult *C. elegans* worm. The channel height was set to 80  $\mu\text{m}$  in order to avoid compression of the nematodes in the adult stage. At the same time, vertical movement of the worms is limited, thus maintaining the intestinal lumen in focus during imaging, a feature enabling high-resolution imaging. As an example, Fig. 4.2b shows high-resolution images of different anatomical sections relevant for studying bacterial food processing, taken on an immobilized adult worm.

Normal on-chip worm development was observed over the typical duration of an assay, as is confirmed by different physiological parameters shown in Fig. 4.3 for N2 worms and *eat-2* mutants (see section 4.3.3), respectively. Molting events, progeny production and worm size were considered as indicators for the state of development and revealed the good health of the worms (Fig. 4.3a and Fig. 4.3b). The pharyngeal pumping frequency was also recorded at different development stages (Fig. 4.3c).

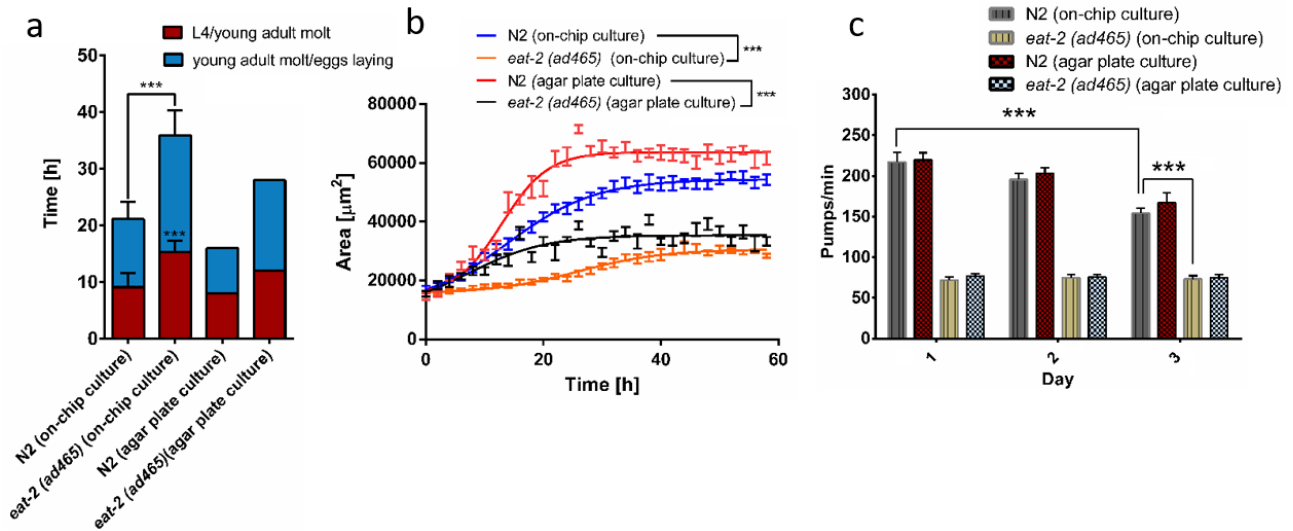


**Figure 4.3** - Monitoring of development parameters of N2 worms and *eat-2(ad465)* mutants for on-chip and agar plate culture. (a) Development time of N2 worms and *eat-2(ad465)* mutants for two different stages from L4 to adulthood. Free-swimming worms have been maintained in the culture part of the microfluidic chamber and were continuously perfused with *E. coli* HT115 ( $n = 17$ ). (b) Body area evolution over time (starting from L4 stage) for N2 worms and *eat-2(ad465)* mutants, measured by optical microscopy (data bars in the graphs express mean  $\pm$  SEM, \*\*\*  $p \leq 0.001$ ,  $n = 17$ ). (c) Pharyngeal pumping frequency recorded at Day 1, Day 2 and Day 3 after L4 stage (bar graphs are expressed as mean  $\pm$  SD, \*\*\*  $p \leq 0.001$ ,  $n = 10$ ).

#### 4.2.3 Imaging of the worms and of the bacterial load in the intestine

Prior to each experiment, the positions of the computer-controlled xyz-stage of the microscope (Zeiss Axio Imager 2) were acquired corresponding to each culture channel for automated time-lapse image acquisition. The microscope was equipped with a sCMOS camera (PCO AG, Germany). Automated image acquisition was performed with VisiView® software (Visitron, Germany) and ImageJ 1.51n software was used for image processing (<https://imagej.nih.gov/ij/>). We acquired images/video sequences, either in the culture part of the on-chip chamber, *i.e.* of freely moving worms, or in the immobilization section of the chip. For imaging immobilized worms, fluidic commands for worm trapping and start of video acquisition were synchronized. Two illumination systems were installed on the microscope for simultaneously acquiring bright-field images of whole worms and fluorescence images of the bacterial load in the worms' gut (Zeiss Plan-APOCHROMAT 10× NA 0.45 objective, 488 nm excitation wavelength for GFP and 545 nm for RFP). Bright-field and fluorescence images were recorded with an exposure time of 2 ms and 20 ms, respectively. By adopting this imaging protocol, we were able to identify the orientation of the worms, while keeping the autofluorescence signal of anatomic structures negligible with respect to the signal generated by fluorescently-labeled bacteria.

In order to evaluate the experimental assays conditions, we first characterized the impact of certain parameters on the fluorescence signal intensity emitted by GFP- and RFP-labeled *E. coli*. Fig. 4.4 shows that photo-bleaching due to excitation light exposure did not significantly affect the fluorescence signal of the bacteria. Furthermore, the intestine of viable worms represents an acidic environment with pH values rang-



ing from 5.96 in the pharynx to 3.59 in the posterior intestine [54]. We therefore simulated the *in vivo* acidic environment by buffer solutions with pH values that were selected accordingly. Fig. 4.5 shows that GFP-labeled *E. coli* revealed a higher sensitivity to pH with respect to OP50 RFP-labeled bacteria, whose fluorescence was not significantly affected by the pH variation.

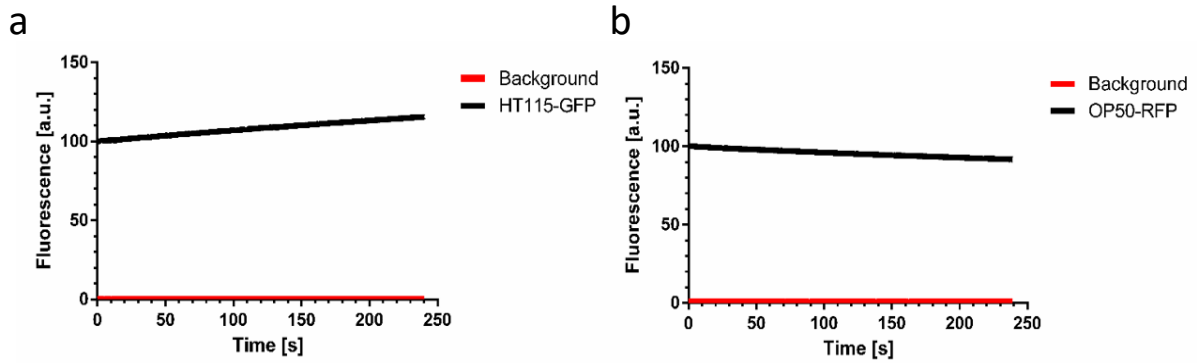


**Figure 4.4** - Monitoring of the fluorescence signal expressed by HT155 GFP-labeled (a) and OP50 RFP-labeled (b) *E. coli* bacteria in order to assess photo-bleaching of the fluorophores. Frames were acquired for a total duration of 240 s with a sampling interval of 200 ms. Excitation wavelengths selected for HT115 GFP and OP50 RFP *E. coli* bacteria are 488 nm and 545 nm, respectively. Photo-bleaching did not significantly affect the fluorescence signal expressed by the plasmid in both cases. Accordingly, the same parameters were selected to perform bacterial load measurements on worms.

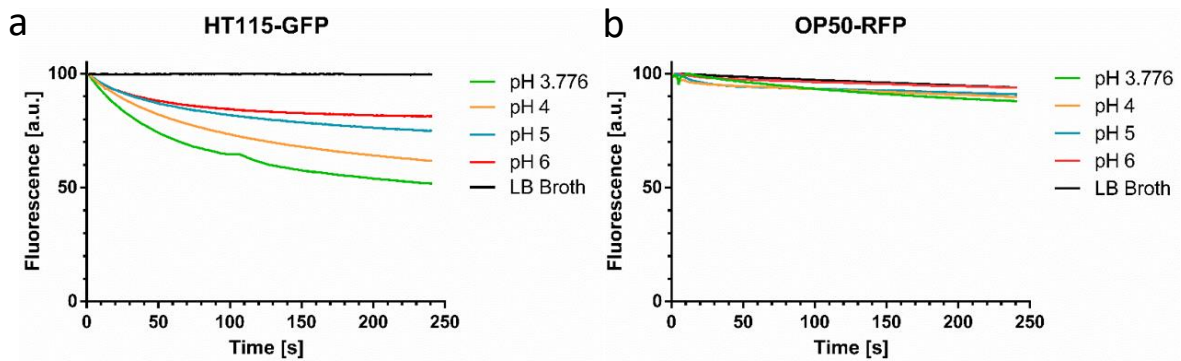


**Figure 4.5** - Monitoring of fluorescence expressed by HT155 GFP-labeled (a) and OP50 RFP-labeled (b) *E. coli* bacteria suspended in buffer solutions ranging from pH 3.776 to 6 in order to assess the fluorophore sensitivity to pH. 50  $\mu$ l of bacterial suspension was diluted and mixed in 1 ml of buffer solution with known pH value and fluorescence was measured over 240 s. In contrast to *E. coli* OP50 RFP, GFP-labeled bacteria clearly revealed pH sensitivity.

A typical example for imaging of an adult worm and its bacterial load of the gastrointestinal tract is shown in Fig. 4.6a (upper image). The fluorescence signal was measured along the clearly identifiable intestinal profile of the worm, and average values were computed over a width of 30  $\mu$ m, corresponding to the yellow line shown in Fig. 4.6a (lower image). For data monitoring and analysis the acquired signal sequences of the bacterial load were first translated into a graph representing the fluorescence amplitude over worm length, which was in turn presented as a color-coded scheme for better visual interpretation of the bacterial transit (Fig. 4.6b).

A custom Matlab script (Matlab R 2016b software, MathWorks, USA) was used to automatically process the data of immobilized worms. Furthermore, brightfield pictures were acquired every hour to monitor worm development. Pharyngeal pumping was analyzed through video sequences (duration 30 s) of adult worms and by visually counting the oscillation frequency of the grinder. Brightfield images were also processed to detect molting of the worms, progeny production and for size/body area measurements of the worms.

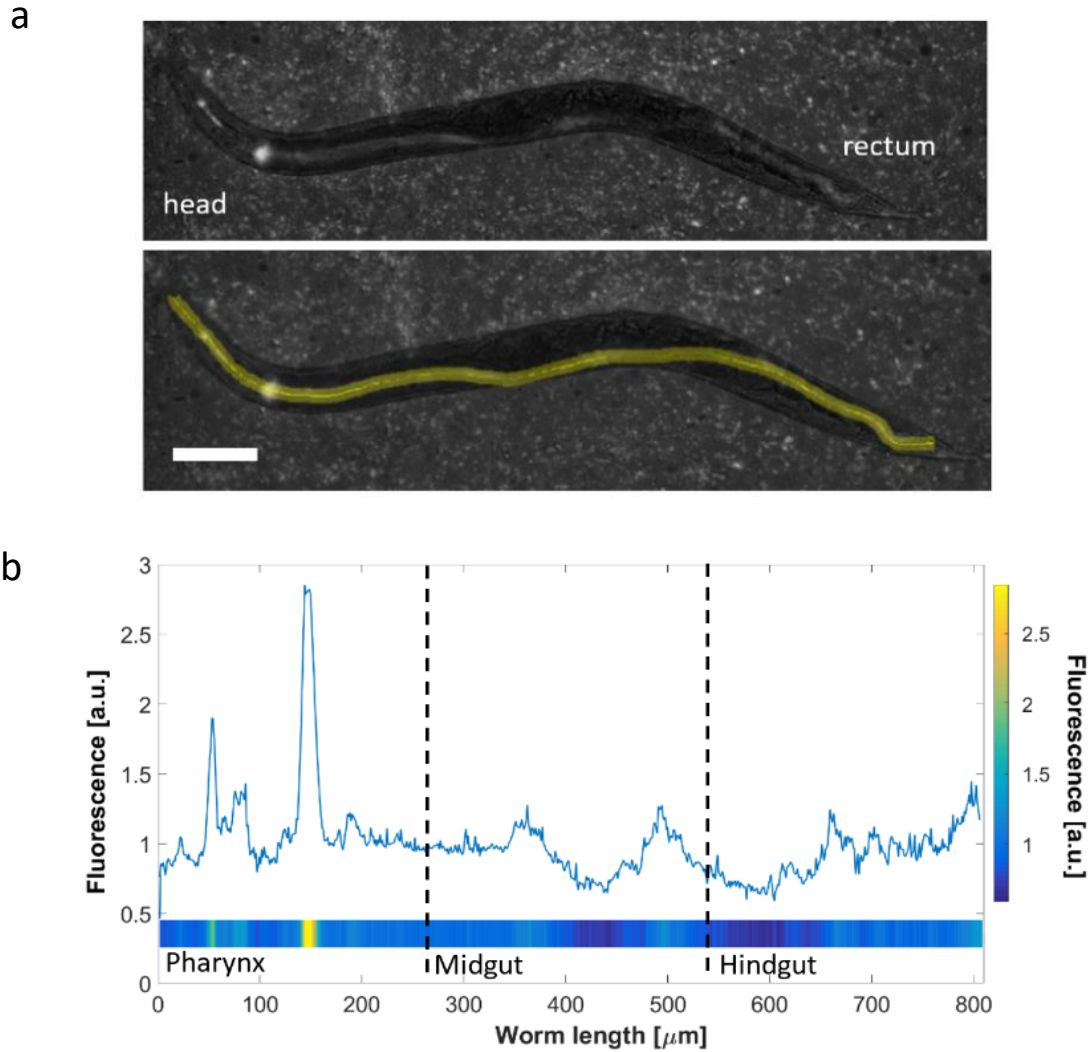


**Figure 4.6** - Principle of measuring the bacterial load in *C. elegans* worms. (a) Fluorescence microscopy image of an adult N2 worm fed with an *E. coli* HT115 bacteria strain expressing GFP. The fluorescence signal generated by the *E. coli* bacterial load of the worm's luminal gastrointestinal tract is visible. The signal was recorded along a manually defined line (averaged over a width of 12  $\mu\text{m}$ , as shown in the lower image). Scale bar = 100  $\mu\text{m}$ . (b) Fluorescence signal amplitude measured along the luminal tract over the whole worm length from the head region ( $l = 0$ ) to the tail region ( $l = 800 \mu\text{m}$  in this case,  $l_{\text{worm}} = 850 \mu\text{m}$ ). For analyzing bacterial load and transition, worms have been divided in three segments of equal length, indicated as pharynx, midgut and hindgut region, respectively. These regions are delimited by vertical dashed lines in the plot. The large peak at  $l \approx 150 \mu\text{m}$ , corresponding to the bright spot in the fluorescence microscopy image, indicates bacterial accumulation in the grinder region. The fluorescence signal graphs



have been transposed into a linear color code scheme for convenient visualization and analysis of the temporal evolution of bacterial transit processes (panel below the graph in Fig. 4.6b).

### 4.3 Microbial assays and results

#### 4.3.1 Dynamics of microbial food ingestion and peristalsis cycles of free-swimming N2 worms

Food ingestion and absorption in *C. elegans* is a surprisingly fast process [105]. However, to the best of our knowledge, no other study has directly and accurately measured the peristalsis in *C. elegans* nematodes. As a first application of our method, we analyzed the periodicity of normal eating events and subsequent food processing in Young Adult (YA) N2 worms. The worms considered for this analysis were free to move in the culture chamber of the chip, in order to avoid mechanical stress provoked by immobilization and to ensure physiological assay conditions. The dynamics of food intake, food processing and clearance is monitored and analyzed in Fig. 4.7. Brightfield images of a worm fed with *E. coli* HT115 GFP are shown, combined with the corresponding fluorescence images of the bacterial distribution in the gut (taken quasi-simultaneously by double illumination). Initially, ingested bacteria were pushed into the terminal bulb of the pharynx by two distinct serotonin-activated muscle movements, *i.e.* pharyngeal pumping and isthmus peristalsis [118], and bacteria accumulation can be observed in this part of the pharynx. We could track bacterial transit in *C. elegans* with high temporal resolution. Food processing by mechanical smashing of the bacteria by the grinder in the pharyngeal terminal bulb takes about 10 - 30 s. Subsequently, food is pushed through the pharyngeal-intestinal valve into the mid region of the intestine, and eventually expelled through the rectum [119]. This process repeats periodically, as soon as the worm ingests bacteria again. The color-coded map in Fig. 4.7 was compiled from time-lapse recordings of a representative food processing sequence, monitoring the fluorescence intensity of the bacterial load in the entire worm gut over a period of 220 s. In particular, we analyzed the periodicity of the fluorescence signal in the pharynx and hindgut, which are the two most relevant regions for characterizing the food transition.

Two representative examples for a YA N2 worm fed with *E. coli* HT115 GFP and OP50 RFP strains are shown in Fig. 4.8a and Fig. 4.8b, respectively. The lower fluorescence signal intensity measured in the hindgut of N2 worms fed with HT115 GFP *E. coli* compared to the one measured in the worms' pharynx in Fig. 4.8a can be explained by the sensitivity of the GFP fluorophore to acidic environments (see Fig. 4.5a). The time interval  $\Delta T$  corresponds to the time lapse between two consecutive maxima of the fluorescence signal in the pharynx and the hindgut region, respectively. The graphs indicate that a complete cycle, from bacterial ingestion to intestinal clearance until the onset of the following ingestion, takes approximately 70 to 90 s in the two specific cases shown in Fig. 4.8. The transient time  $\Delta t$  of processed *E. coli* from the pharynx terminal bulb to the hindgut can be estimated by the lag of the main peaks in the fluorescence signal plot. This parameter was found to be in the range of 10 to 20 s for free-swimming YA N2 worms (Fig. 4.8). This observation indicates that bacterial load transition through the midgut region and rectum is quite fast, possibly as a consequence of the increased constriction of the worm's intestine lumen with respect to the pharynx. Both intervals  $\Delta T$  and  $\Delta t$  appear not to be dependent on the specific *E. coli* strain used for feeding.

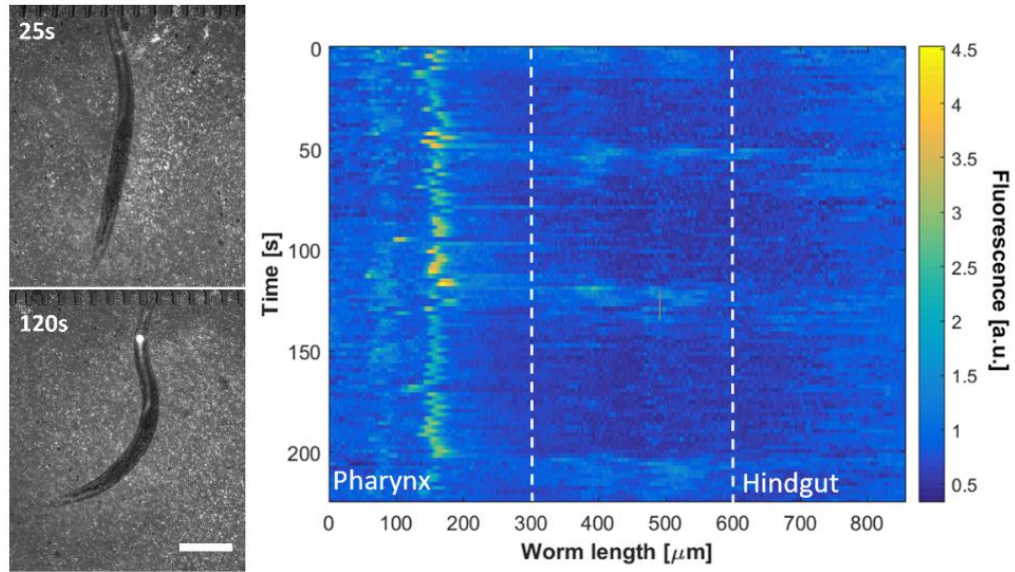


**Figure 4.7** - Analysis of the bacterial load in free-swimming wild-type worms. Time-lapse recordings (time interval 2 s) of the fluorescence intensity in the worm gut over worm length. A representative sequence is shown, indicating periodic bacterial accumulation in the grinder upon food uptake and subsequent release into the digestive tube. In this case, the worm is freely swimming in the microfluidic chamber filled with bacterial food suspension (*E. coli* HT115 expressing GFP). Vertical dashed lines delimit the pharynx region and the hindgut region, respectively ( $\Delta l_{\text{pharynx}} = [0 \mu\text{m}, 300 \mu\text{m}]$ ,  $\Delta l_{\text{hindgut}} = [600 \mu\text{m}, 900 \mu\text{m}]$ ,  $l_{\text{worm}} = 900 \mu\text{m}$ ). Two corresponding fluorescence images of the young adult N2 worm, taken at 25 s and 120 s, respectively, are also shown. Scale bar = 200  $\mu\text{m}$ .

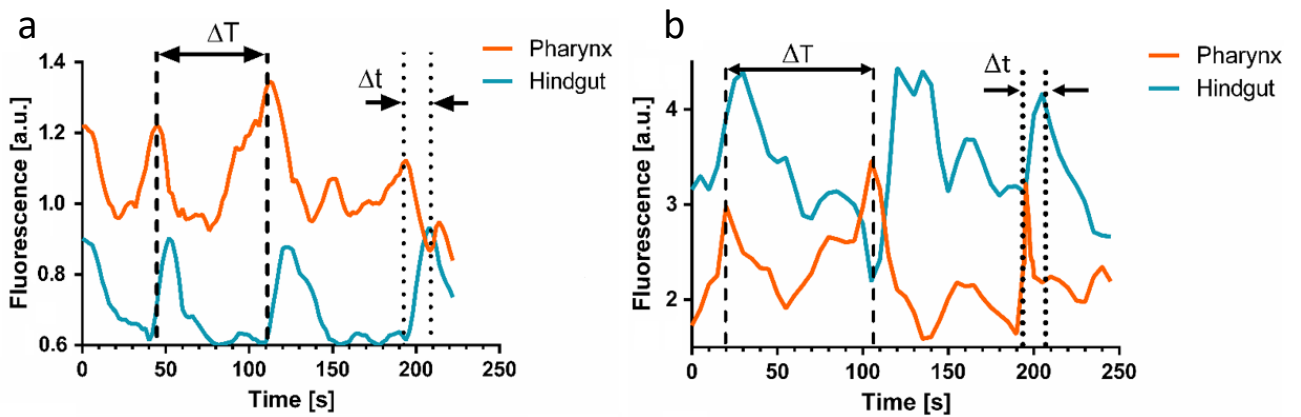


**Figure 4.8** - Bacterial transit cycle. (a) Fluorescence signal as a function of time of the worm shown in Fig 4.7, averaged over the pharynx region (orange curve) and the hindgut region (blue curve). The time interval  $\Delta T$  corresponding to food uptake/accumulation, as well as the time shift  $\Delta t$  corresponding to food transition through the intestinal track is indicated. (b) Fluorescence signal as a function of time of a single worm fed with *E. coli* OP50 expressing RFP, averaged over the pharynx region (orange curve) and the hindgut region (blue curve), respectively.

Four representative graphs of normalized time sequences, recorded in the hindgut of the worms, for nematodes fed with HT115 GFP and OP50 RFP strains are shown in Fig. 4.9 and Fig. 4.10, respectively. Based on these graphs, we attempted to perform a more systematic evaluation of the periodicity of the food processing and transition process by computing the Fast Fourier Transform (FFT) of peristalsis time sequences (Fig. 4.11). Comparison of the 4 graphs shows that the periodicity of food accumulation and clearance cannot always be clearly identified on the time scale and significant variations may occur. The FFT magnitude obtained for worms fed with *E. coli* HT115 GFP shows a distinct major peak at  $\sim 0.0135$  Hz (corresponding to  $\sim 74$  s), followed by smaller secondary peaks. Similarly for the *E. coli* OP50 RFP data set, the FFT magnitude shows major peak at  $\sim 0.0155$  Hz (corresponding to  $\sim 64.5$  s). We interpret these primary peaks as the average periodicity of the peristaltic process, corresponding to  $\Delta T_{\text{mean}} \approx 70$  s. This time lapse appears to be somewhat longer compared to previous studies that characterized the rhythmic  $\text{Ca}^{2+}$  oscillations controlling periodicity of peristaltic movements in the *C. elegans* intestinal tract, reporting that defecation occurs approximately once every 45-50 s [120, 121].

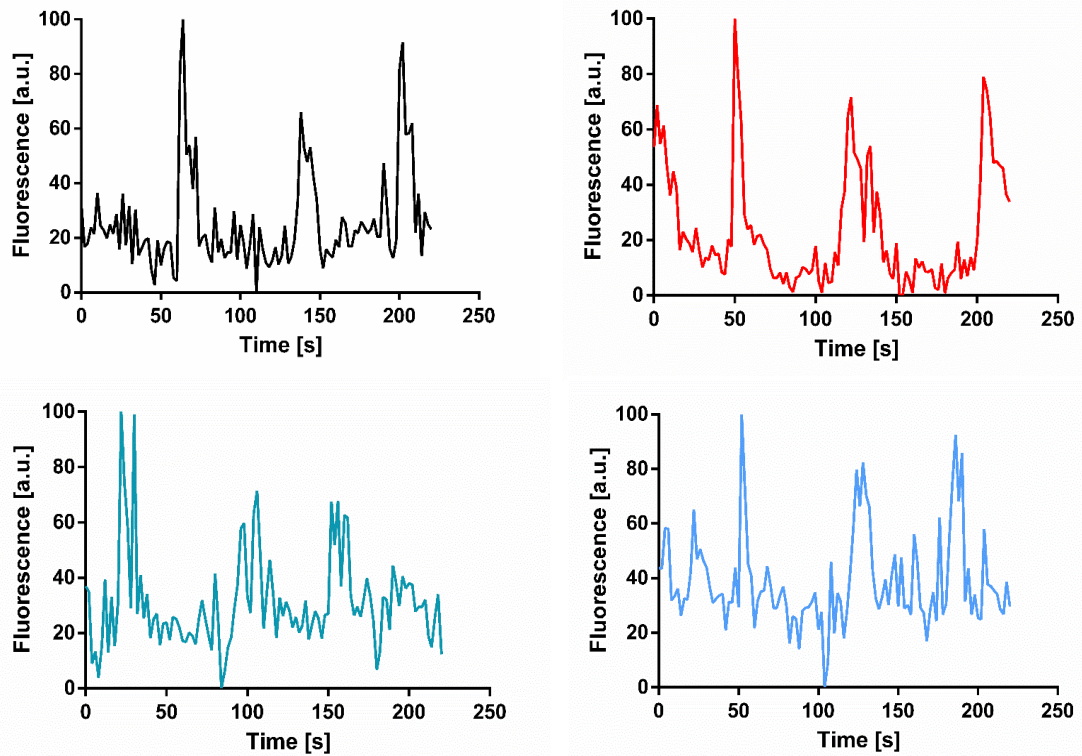


**Figure 4.9** - Average fluorescence signal corresponding to the hindgut region for 4 representative worms fed with *E. coli* HT115 GFP bacteria. The signals have been normalized for analyzing the periodicity by Fast Fourier Transformation (as shown in Fig. 4.11).

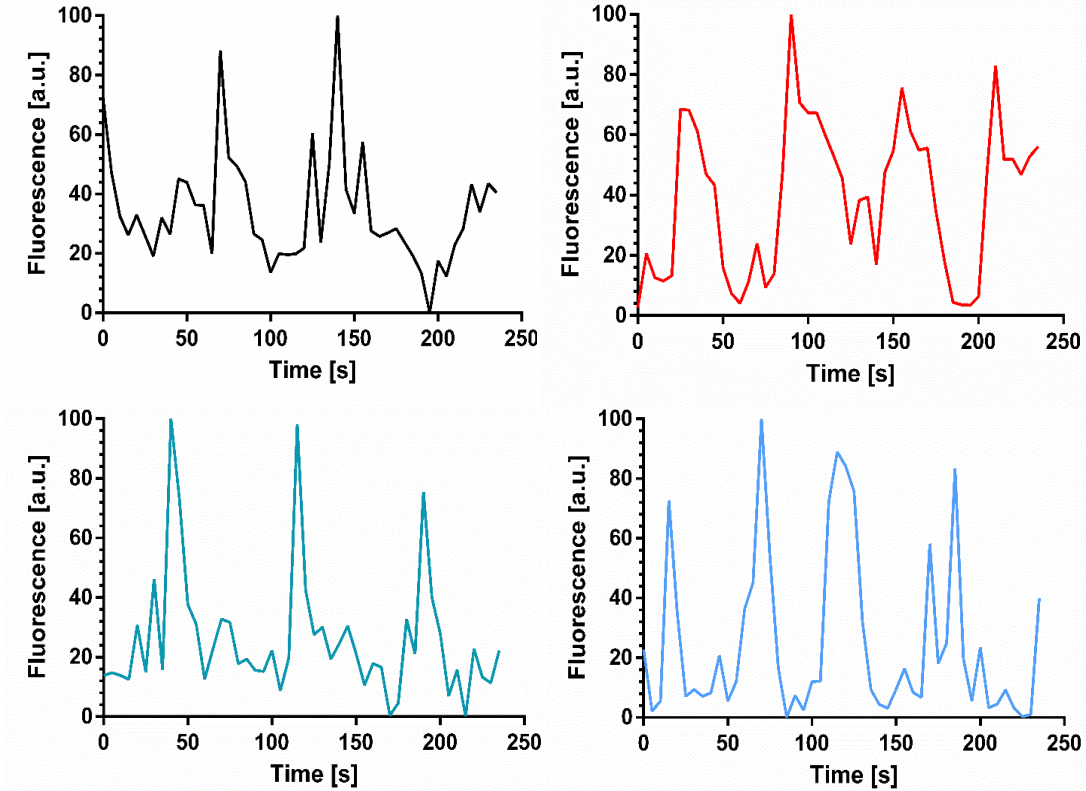


**Figure 4.10** - Average fluorescence signal corresponding to the hindgut region for 4 representative worms fed with *E. coli* OP50 RFP bacteria. The signals have been normalized for analyzing the periodicity by Fast Fourier Transformation (as shown in Fig. 4.11).

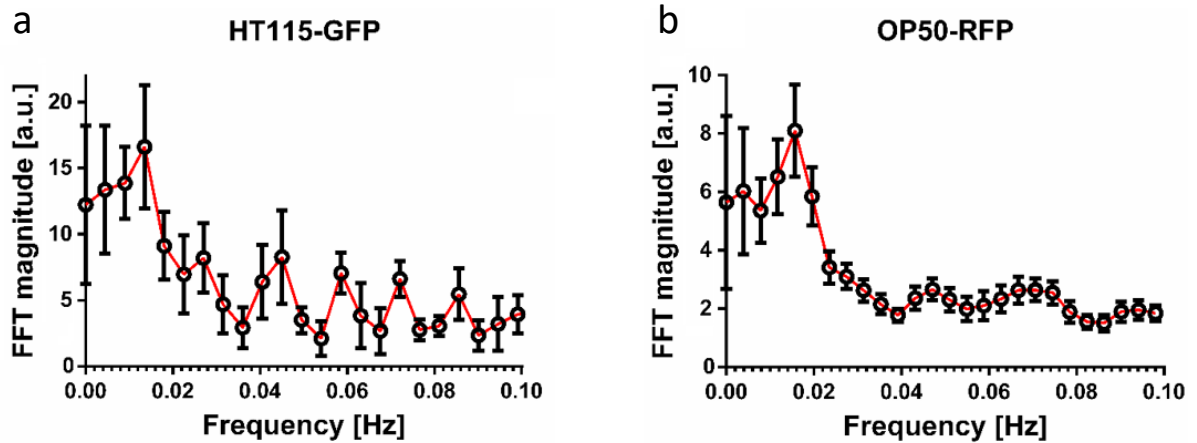


**Figure 4.11** - Fast Fourier Transform (FFT) magnitude computed for the fluorescence signal sequences corresponding to the worms' hindgut region for worms fed with *E. coli* HT115 GFP and *E. coli* OP50 RFP, shown in (a) ( $n = 4$ , based on Fig. 4.9) and (b) ( $n = 10$ , 4 graphs are shown in Fig. 4.10), respectively. The FFT magnitude shows a peak (at  $\approx 0.0135$  Hz for *E. coli* HT115 GFP and  $\approx 0.0155$  Hz for *E. coli* OP50 RFP), which correspond to the average primary periodicity of the bacterial transit process ( $\Delta T_{mean} \approx 70$  s).



## 4.3.2 Bacterial food transit time in the gut of adult N2 worms

After investigating periodic food ingestion and corresponding peristalsis cycles in the gut of free-swimming *C. elegans* worms, we evaluated further the time needed by the organism to push bacteria from the pharyngeal lumen into the adjacent sections of the intestine. In order to accomplish these measurements, nematodes were fed with *E. coli* HT115 GFP bacteria and confined in the tapered traps of the chip.

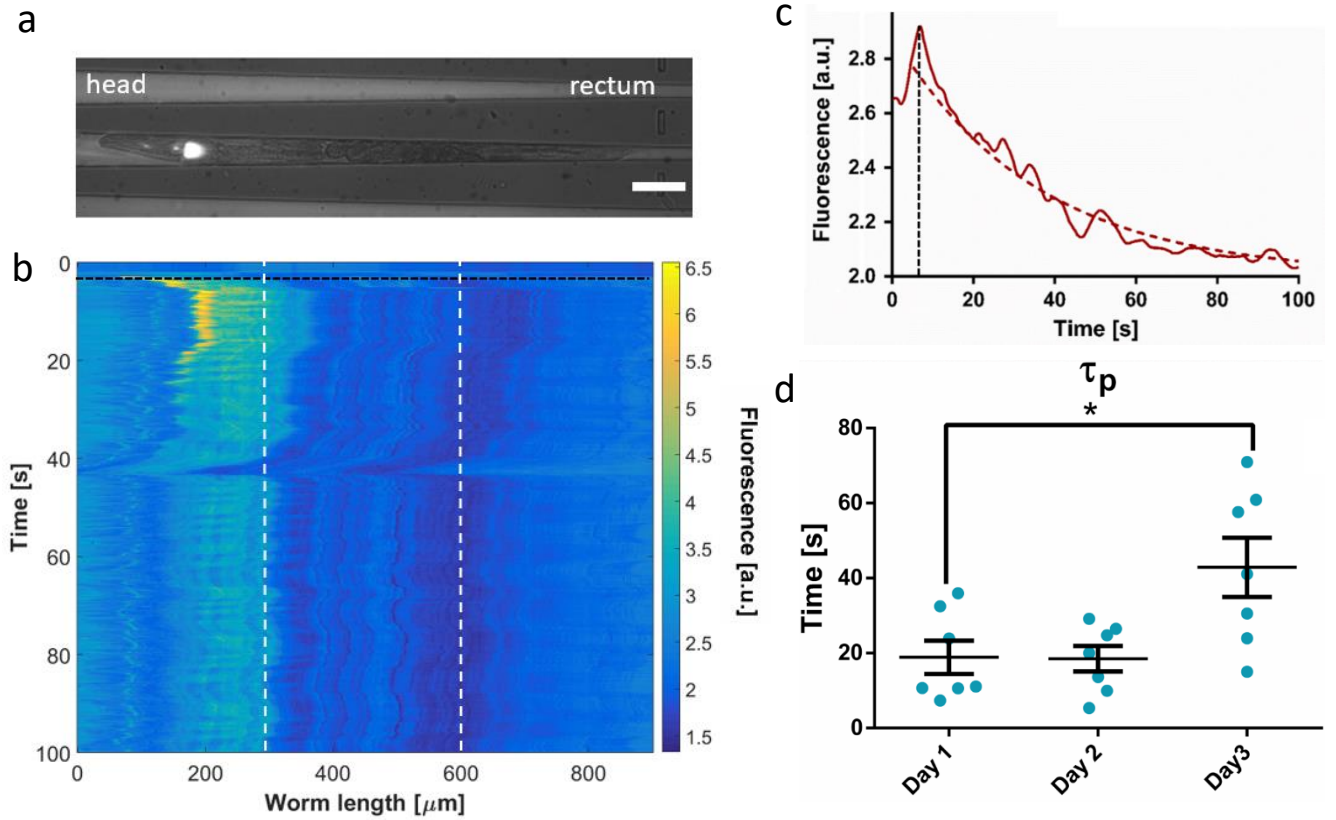


**Figure 4.12** - Analysis of the bacterial load in wild-type worms immobilized on the chip. (a) Representative fluorescence microscopy image of an adult N2 worm immobilized in a tapered channel fed with *E. coli* HT115 GFP strain, showing a strong signal due to bacterial accumulation in the grinder (YA, Day 1 after L4 loading). The picture was taken shortly after immobilization of the worm, *i.e.* after the last food uptake in the free-swimming state. Scale bar = 100  $\mu\text{m}$ . (b) Color-coded map of the fluorescence intensity in the worm gut over worm length showing the time evolution and distribution of the bacterial load ( $t = 0$  corresponds to full immobilization of the worm after the last food uptake, time interval 250 ms). Initially a maximum bacterial load (indicated by a black dashed line) was registered in the anterior portion of the gut, before the onset of food transit and/or release of the bacteria into the posterior portion of the gastrointestinal tract, corresponding to a single peristaltic event. Vertical dashed lines delimit the different subregions of the worm body. (c) Fluorescence signal recorded in the pharyngeal region of a single worm ( $\Delta l_{\text{pharynx}} = [0 \mu\text{m}, 300 \mu\text{m}]$ ,  $l_{\text{worm}} = 900 \mu\text{m}$ ). An exponential fit of the decay was used to determine the food transit time constant  $\tau_p$ . (d) Time constant  $\tau_p$  measured at Day 1 to 3 of adulthood. At Day 3 a significant deceleration of the bacterial transit through the intestinal tract could be observed (graphs are expressed as mean  $\pm$  SEM, \*  $p \leq 0.05$ ,  $n = 7$ ).

Fig. 4.12a shows an immobilized worm with a fluorescence image of the bacterial distribution in the gut. This image corresponds to a situation shortly after food intake, where bacteria accumulated in the grinder. Since worms were not able to eat while immobilized, we could precisely record the processing of a single

food intake event that took place just before trapping, when the worm was still swimming in the culture chamber. N2 worms initially filled the grinder region by a single peristaltic event and then quickly push the food without further accumulation of bacterial residues in the adjacent intestinal lumen. A color-coded map of the fluorescence intensity in the gut of an immobilized worm is shown in Fig. 4.12b. In this case, the sequence was acquired over a time lapse of 100 s, hereafter the worm was released into the culture chamber. The recording of the fluorescence signal measured over the pharynx of N2 worms could be well approximated by a 1<sup>st</sup> order exponential decay, as is shown in Fig. 4.12c. We determined the exponential time constant  $\tau_p$  each day over 3 days from the YA to adult stage. We observed an increase of  $\tau_p$  from ~20 s at Day 1 and Day 2 to ~40 s at Day 3 (Fig. 4.12d). This age-dependent increase is possibly related to a general weakening of the worms' intestinal muscle structure. The assumption is supported by a measurable decrease of the pharyngeal pumping frequency of N2 worms at Day 3 (Fig. 4.3c).

#### 4.3.3 Bacterial transit dynamics in *C. elegans eat-2* mutants

Dietary restriction (DR) studies have shown the benefits deriving from a reduced caloric intake, including lifespan increase and slowing down of aging effects in more than 20 model organisms [122]. DR in *C. elegans* may lead to a 10 - 30 % extension in lifespan [123]. The most commonly used model to investigate DR in *C. elegans* is the *eat-2* mutant, which is characterized by a defective pharynx. The EAT-2 nicotinic acetylcholine receptor subunit is necessary for the stimulation of the pharyngeal muscle, allowing the ingestion of bacterial food from the external environment [124]. If the *eat-2* gene is suppressed, the ligand-gated ion channel for pumping is not encoded and the pumping rate slows down [125]. In fact, *eat-2* mutants display an approximately 3 times slower pharyngeal pumping rate than the N2 wild-type strain. It has been demonstrated that the increase in lifespan of *eat-2* mutants is not related to the gene mutation itself, but to the lower amount of ingested food [126]. Moreover, longevity of *eat-2* mutants was explained by the activation of innate immune response triggered by bacterial accumulation in the gut [28]. Development parameters for agar plate and on-chip culture, respectively, as well as the pharyngeal pumping frequency have been provided in Fig. 4.3 for the *eat-2 (ad465)* mutants and N2 worms. We used our platform to characterize *E. coli* bacterial transit in *eat-2 (ad465)* mutants and compare the observations with N2 worms, in order to elucidate specific differences of food assimilation between the two strains. As in the previous assay, the feeding protocol was initiated after loading synchronized L4 mutant populations in the microfluidic device, and worms were cultured on-chip until the YA stage before starting the assay. Two channels of the chip were dedicated to each strain, providing good control and uniformity of all experimental conditions. After injection of fresh bacteria suspension and a short time lapse for normal feeding, worms were immobilized by hydrodynamic trapping for 150 s.

The most striking difference between N2 worms and *eat-2* mutants was bacteria accumulation in the hindgut for the latter worm type. The fluorescence image of the bacterial load in an immobilized *eat-2* mutant shown in Fig. 4.13a illustrates this fact. Time-lapse recordings of the fluorescence intensity plotted in Fig. 4.13b further emphasize accumulation and stagnation of bacterial transit in the hindgut region. It should be noted that, in principle, food accumulation in the grinder region after food intake could also be observed in *eat-2* mutants, similar to N2 worms. However, unlike the feeding behavior recorded in wild-type worms (Fig. 4.7), equally fast periodicity was not observed in *eat-2* mutants. As a consequence, since ingestion and the pharyngeal pumping

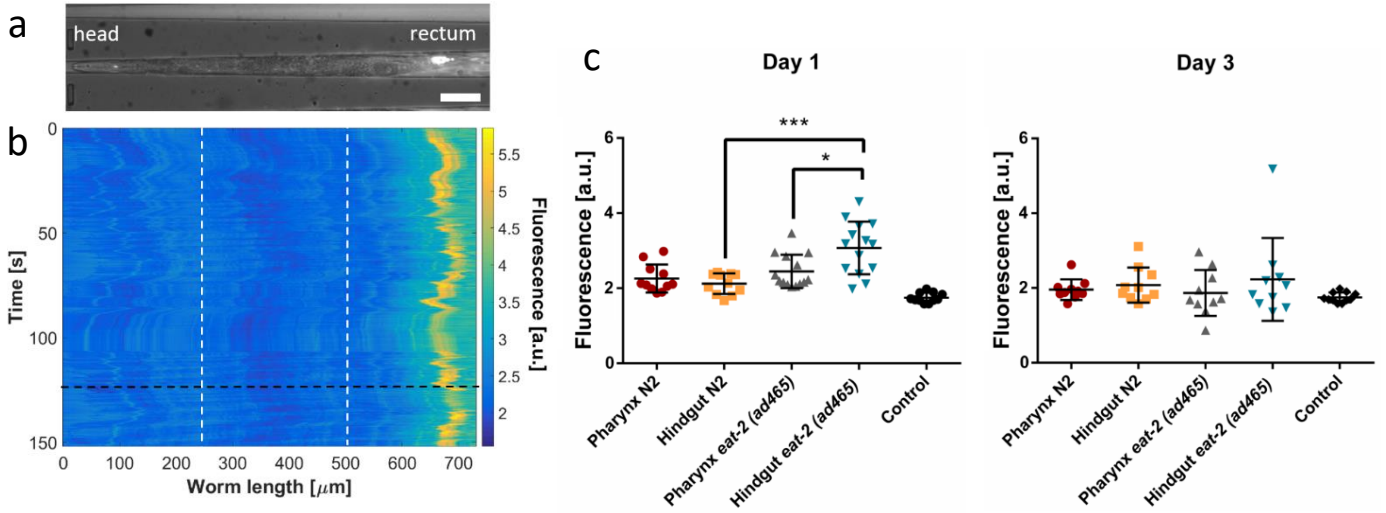


**Figure 4.13** - Bacterial transit process of *E. coli* HT115 for an *eat-2 (ad465)* mutant. (a) Representative fluorescence microscopy image of an *eat-2 (ad465)* mutant (YA, Day 1 after L4 stage) immobilized in a tapered channel, showing a strong signal due to bacterial accumulation in the hindgut. The picture was taken shortly after immobilization. Scale bar = 100 μm. (b) Corresponding color code maps of the fluorescence intensity in the worm gut monitoring the bacterial transit process. In contrast to N2 worms (Fig. 4.12), accumulation and stagnation of bacterial transit in the hindgut region was observed for *eat-2* mutants. The sequence was recorded shortly after the last food uptake by the worm in the free-swimming state. Vertical dashed lines delimit the pharynx and the hindgut region of the worm ( $\Delta l_{\text{pharynx}} = [0 \mu\text{m}, 230 \mu\text{m}]$ ,  $l_{\text{worm}} = 750 \mu\text{m}$ , *eat-2* mutants are shorter than N2 worms). (c) Bacterial load as measured by fluorescence of the worm gut in N2 and *eat-2 (ad465)* strains. The data points correspond to average values taken in the time interval [120 s - 150 s] after immobilization (indicated by a black dashed line in Fig. 4.13b). Control refers to values measured in starving worms. Reported loads refer to the pharyngeal section of the intestine and the hindgut. Measurements obtained for Day 1 and Day 3 are reported (graphs are expressed as mean ± SD, \*  $p \leq 0.05$ , \*\*\*  $p \leq 0.001$ ,  $n = 10$  to 12). Pharynx defective *eat-2 (ad465)* mutants showed a slower intestinal peristalsis with respect N2 *C. elegans*, resulting in persistent bacterial agglomerates in the rectal region of the gut at Day 1. This effect is strongly reduced at Day 3. Values for N2 worms do not show a significant difference with respect to control.

frequency are significantly slower in the mutants (Fig. 4.3), this signal could not always be captured in the initial phase of immobilization (as was the case in Fig. 4.13b). Moreover, a significant decrease in pharyngeal pumping rate was measured in older N2 worms (see Fig. 4.3). Fig. 4.13c shows mean fluorescence signals in the pharynx and hindgut region of several worms, recorded at Day 1 and Day 3 of adulthood for N2 worms and *eat-2* mutants. Considering only the stable bacterial accumulation in the gut, we evaluated the bacterial content by averaging the fluorescence intensity taken after 120 s of immobilization for a time lapse of 30 s. During the first day of culturing (Day 1), the majority of *eat-2* mutants displayed a consistent and stable bacterial accumulation in the ending section of the intestinal lumen, expressed by a significant increase of the average hindgut signal in Fig. 4.13c. In the following days, hindgut accumulation patterns became more irregular, with a broader distribution in more proximal portions of the intestine. Consequently, the average hindgut signal in Fig. 4.13c does not show a significant increase at Day 3. On the other hand, and consistent with our previous observations (Fig. 4.12c), the intestinal bacterial content in N2 strains vanished due to food assimilation and clearance at an earlier stage. Correspondingly, the average values for the pharynx and hindgut shown in Fig. 4.13c are close to control. During the measurement period of 3 days, no systematic overall increase of the bacterial content in the intestine was observed in both worm types, indicative of the low colonizing capability of the *E. coli* HT115 strain.

We acquired high-resolution images of ingested live and heat-killed bacteria (Fig. 4.14a-b), but both cases were indistinguishable, in agreement with results reported in a previous study [127]. It is therefore not possible to assess bacterial viability in *C. elegans* intestine solely by measurement of fluorescence.

However, stable accumulation in the hindgut can possibly be associated with the presence of viable bacteria colonizing the intestinal lumen. Also, the persistence of HT115 GFP fluorescence in the acidic environment of the worms' hindgut can be an indication for the presence of intact bacteria. In order to support this assumption, we measured the bacterial load in N2 worms fed with live and heat-killed *E. coli* OP50 RFP. This strain was used since it is only mildly pathogenic to *C. elegans* and has higher persistency in nematodes' gut with respect the HT115 GFP strain. Worms fed with live bacteria presented a higher and more stable fluorescence signal measured in the hindgut, as shown in Fig. 4.14 c-d and 4.14 e-f, respectively.

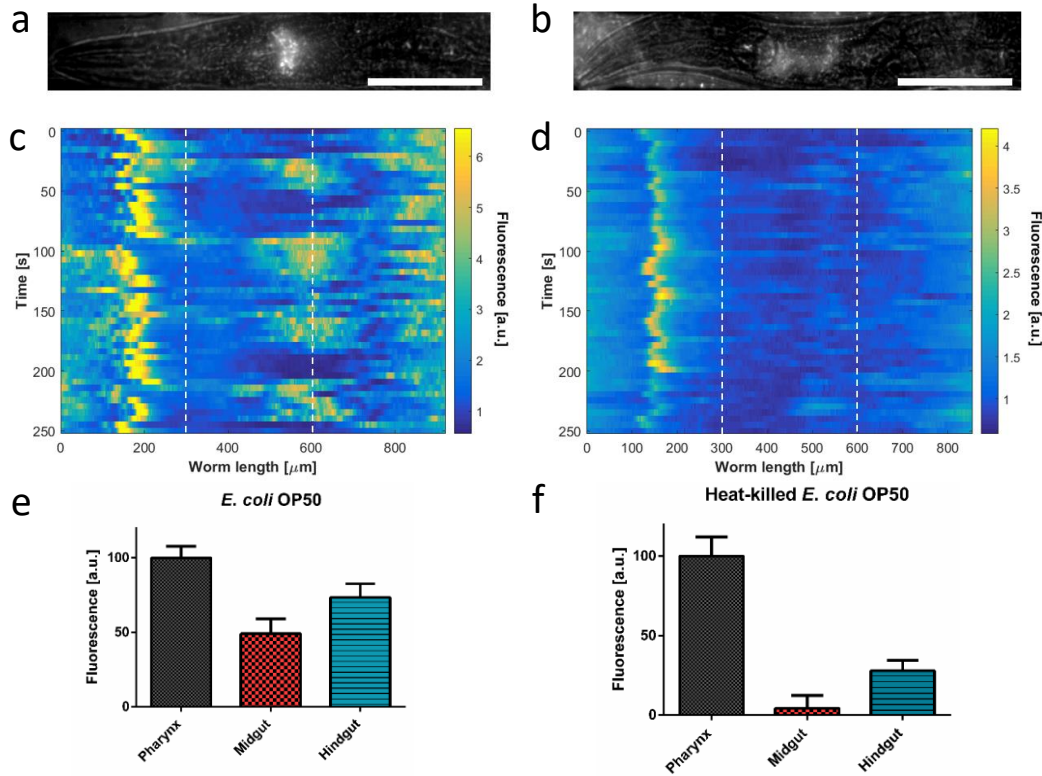


**Figure 4.14** - Bacterial load in adult N2 *C. elegans* worms. (a) High-resolution brightfield/fluorescence (40x) images of a worm (pharynx) fed with live (a) and heat-killed (b) *E. coli* OP50 RFP. Scale bar = 50 μm. (c-d) Time-lapse recordings of the fluorescence intensity in a representative single N2 worm over the whole gut. The worm was fed with live (c) and heat-killed (d) *E. coli* OP50 RFP, respectively. Pharynx, midgut and hindgut regions of the worms are delimited by vertical dashed lines in the plots ( $l_{\text{worm}} = 900 \mu\text{m}$ ). (e-f) Bacterial load as measured by fluorescence of the worm gut in adult N2 fed with live (e) and heat-killed (f) *E. coli* OP50 RFP. Bars correspond to average fluorescence values measured in the indicated intestine section, normalized with respect the maximum fluorescence value measured in the pharynx. Heat-killed *E. coli* OP50 RFP show a lower persistency in the posterior section of the worms' gut (graphs are expressed as mean  $\pm$  SD,  $n = 10$ ).

#### 4.3.4 Serotonin effects on the *C. elegans* bacterial transit dynamics

Serotonin, or 5-hydroxytryptamine hydrochloride (5-HT), is one of the biogenic amine neurotransmitters (such as dopamine, octopamine and tyramine) that can be detected in *C. elegans* extracts. These compounds appear to function as neurotransmitters or neuromodulators [128]. Serotonin induces dramatic behavioral effects in *C. elegans*, such as inhibition of locomotion and of the defecation motor program, but also stimulates egg laying [129]. In particular, 5-HT stimulates pharyngeal pumping and reduces enteric muscle contractions in worms [130]. In order to validate the efficacy of our method for testing of drug-dependent alteration of the worm feeding behavior, we observed the effects of 5-HT on the bacterial trans-



it in wild-type worms. We designed our study to obtain a direct and real-time measure of the increase of food content inside the gut, as caused by the compound-induced modulation of the intestine response.

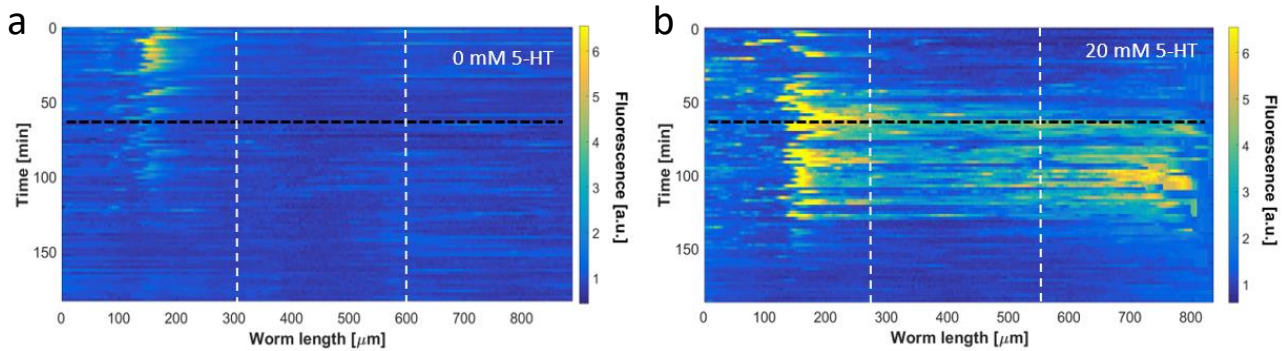


**Figure 4.15** - 5-hydroxytryptamine (5-HT)-induced modulation of the bacterial transit process in N2 worms. Representative color code maps of the bacterial load distribution in free-swimming N2 worms fed for 60 min with *E. coli* HT115 + 0 mM 5-HT (a) and with *E. coli* HT115 + 20 mM 5-HT (b), respectively. After 60 min flow was stopped (indicated by the black dashed lines). The bacterial load in the worm gut is strongly modified by 5-HT exposure, showing enhanced accumulation over an extended time span. In these experiments, the bacterial transit process was observed over a period of 3 hours. Vertical dashed lines indicate the different subregions of the worm body ( $l_{\text{worm}} = 900 \mu\text{m}$  in (a),  $l_{\text{worm}} = 850 \mu\text{m}$  in (b)).

First, one to three L4 N2 worms were loaded in each chamber of all 4 channels on the chip and fed with the same *E. coli* food solution until the YA stage. Then, for the control group, channels were filled with *E. coli* HT115 GFP diluted in S-medium to a concentration of  $2 \times 10^9$  cells/mL, and for the test group the same *E. coli* suspension was mixed with 5-HT to a final concentration of 20 mM, respectively. In order to minimize possible adverse effects due to instability of serotonin, the solutions were prepared freshly before the start of each experiment. We selected again *E. coli* HT115 GFP bacteria as food source because of the low colonizing aptitude of this strain, thus avoiding an increase of the bacterial load in the gut due to pathogenic effects. During an ongoing experiment, the culture chambers were refilled with fresh feeding suspension every 15 min, in order to provide a constant amount of food to the worms. Fluorescence images of the worms were recorded every 2 min. The feeding protocol was operated for 1 hour. After that, the flow was stopped and feeding suspensions were no longer dispensed to the worms. Worms treated with 5-HT 20 mM displayed an evident increase in the overall bacterial load in the intestine and defecation was strongly hindered. This is illustrated by comparing the color-coded plots for untreated and treated N2 worms shown in Fig. 4.15a and Fig. 4.15b. In particular, both the worms' pharynx and rectum featured highly-packed bacteria accumulation. Fluorescence images of treated and untreated worms shown in Fig. 4.16a indicate qualitatively the increase of the bacterial load over time and distribution modifications due to constipation as a consequence of the 5-HT treatment. Fig. 4.16b analyzes this assay quantitatively, showing that at  $\approx 30$  min after the onset of the experiment, the averaged bacterial GFP signal in the treated group, taken over the whole intestine, starts rising above that of the control group. A maximum was reached after  $\sim 60$  min (*i.e.* at the end of fresh food supply), where the signal is  $\sim 3.5$  times higher than for the control group. The average fluorescence signal of the control group remained constant because of a regular and fast clearance of the food on a time scale below  $\sim 2$  min.

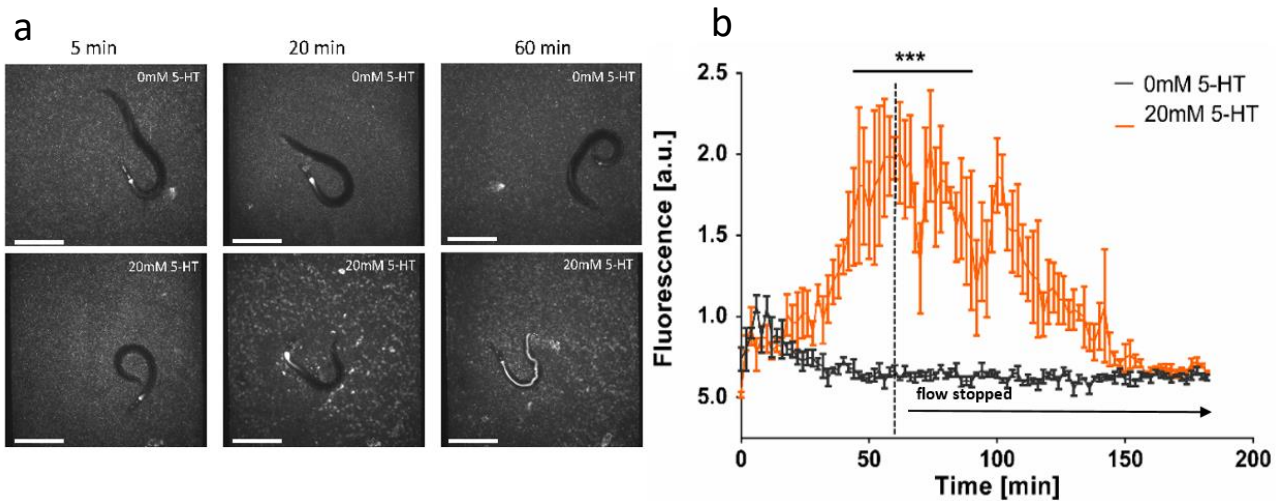


**Figure 4.16** - (a) Time-lapse images of free-swimming adult N2 worms, without and with 5-HT exposure, emphasizing increasing bacterial load upon treatment. Scale bars = 300  $\mu\text{m}$ . (b) Fluorescence signal averaged over the total length of the worm gut for treated and untreated worms, indicating increasing bacterial load up to 60 min in the latter case, followed by a slow decrease thereafter when the chamber was not replenished anymore. Increase of bacterial content in the gut is a consequence of increased food intake and reduced defecation rate caused by the 5-HT treatment (\*\*\*)  $p \leq 0.001$ , for data points in the interval indicated by the horizontal line,  $n = 10$ ).

## 4.4 Discussion

Our method offers an operative tool for direct and real-time investigation of the bacterial load in the *C. elegans* gut. An advantage of the present device is the implementation of simple microfluidic protocols for reversible immobilization of the worms. This features allows reliable imaging of entire worms, combined with on-chip culture over the whole lifespan. Observation of the bacterial transit in the worm's gut may therefore be analyzed for different feeding conditions, either for free-swimming worms or for immobilized worms. Unlike other immobilization techniques (*e.g.* based on pressure-controlled flexible membranes), the present approach relies on gentle fluidic capture of the worms without significant physical compression of the worm and its intestine.

Our imaging method is dedicated to the observation of transient features in the bacterial load in the worm's gut. Likewise, monitoring of bacterial accumulation in specific parts of the intestine (*e.g.* in the hindgut of *eat-2* mutants, Fig. 4.13) or possibly of full load of the gut (Fig. 4.16a, last image of the series) was demonstrated. Based on time-resolved imaging revealing the dynamics of the microbial load, it should be possible to distinguish between transient accumulation and permanent colonization. This features opens the way for direct monitoring the impact of non-pathogenic and pathogenic food sources. In this respect, a promising application of the present device could be the microfluidic implementation of worm infection assays for testing anti-infective activity or toxicity of potential drug candidates. Such assays are currently mainly carried out in liquid cultures in a microtiter well plate format [131]. Pathogenic microbial infection not only results in persistent colonization of the gut, but often also in a clear morphological impact, in particular the distention of the anterior intestine to the full width of the worm (as is shown in Fig. 1 of [8], for instance). In principle, such observations can be easily realized with our device, enabling to distinguish between infection and non-pathogenic features. In the frame of the study presented in this chapter, we used non-pathogenic or only mildly pathogenic bacteria, consequently such severe effects were not observed. Accurate monitoring of more subtle effects indeed requires higher magnification imaging, a feature that will be more specifically addressed in Chapter 5. Nevertheless, the worm immobilization technique pre-

sented here is suitable for high-resolution imaging. As a proof-of-concept, Fig. 4.17 shows image sequences of a few *E. coli* HT115 GFP bacteria persisting (“colonizing”) in a worm’s gut and a few transient bacteria, respectively.

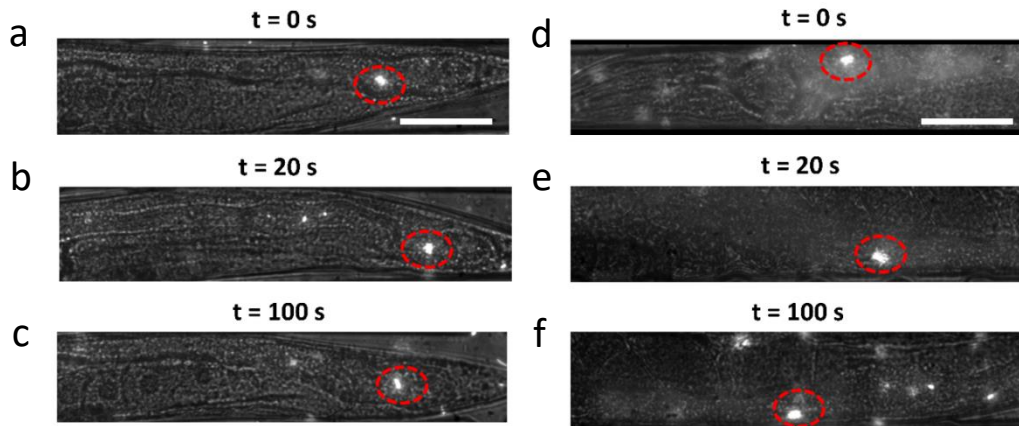


**Figure 4.17** - High-resolution brightfield/fluorescence (40x) time-lapse images of an immobilized N2 *C. elegans* worm fed with *E. coli* HT115 GFP. The image sequences show: (a-c) a few bacteria persisting in the region of the hindgut and (d-f) a few bacteria passing through the whole intestinal lumen, in particular the pharynx (d), the midgut (e) and the hindgut (f). Single bacteria are highlighted by red dashed circles. Scale bar = 50  $\mu\text{m}$ .

A limiting feature of the present device is efficient and fast clearing of the chip. Changing from a bacterial feeding condition to a clear buffer condition may take several minutes, as repeated rinsing steps have to be applied in order to completely remove bacterial residues, in particular from the on-chip bacterial filter structures. This issue can hinder the implementation of pulse-chase fluidic protocols for the time being. Further optimization of the microfluidic design should enable monitoring bacterial transit with enhanced accuracy and the implementation of more advanced fluidic assays, *e.g.* rapidly alternating worm exposure to bacterial food/no food conditions or the sequential application of various compounds.



## Chapter 5 Long-term on-chip worm immobilization for peristalsis, digestion and pathogen interaction studies

*C. elegans* is an interesting model for studying host-microbiota interactions. Assessing the fate of ingested bacteria in the worm's intestine is therefore of great interest. Based on the bacterial transit study presented in Chapter 4, we further developed on-chip worm immobilization and high-resolution imaging techniques for advanced *C. elegans*-bacteria interaction assays, enabling single-bacteria observation and assessing bacterial food absorption in the worm's intestine. In this chapter, in addition to more accurate studies of the intestinal microbial load dynamics, we focus on digestion kinetics and evaluate intestinal colonization by pathogens. Here, we report an *in vivo* study of bacteria in the *C. elegans* gut that takes advantage of a PDMS microfluidic device enabling passive immobilization of adult worms under physiological conditions. Non-pathogenic *E. coli* bacteria expressing either pH-sensitive or pH-insensitive fluorescence reporters, as well as fluorescently marked indigestible microbeads were used for the different assays. Dynamic fluorescence patterns of the bacterial load in the worm gut were conveniently monitored by time-lapse imaging. Cyclic motion of the bacterial load due to peristaltic activity of the gut was observed and biochemical digestion of *E. coli* was characterized by high-resolution fluorescence imaging of the worm's intestine. We could discriminate between individual intact bacteria and diffuse signals related to disrupted bacteria that can be digested. From the decay of the diffuse fluorescent signal, we determined a digestion time constant of  $14 \pm 4$  s. In order to evaluate the possibility to perform infection assays with our platform, immobilized *C. elegans* worms were fed with pathogenic *Mycobacterium marinum* (*M. marinum*) bacteria. We analyzed bacterial fate and accumulation in the gut of N2 worms and mitochondrial stress response in a *hsp-6::gfp* mutant.

---

This section was adapted from the following publications:

V. Viri, M. Arweiler, T. Lehnert, M. A. M. Gijs, "An *in vivo* microfluidic study of bacterial absorption in *C. elegans*", *Micromachines*, (submitted).

V. Viri, M. Arweiler, T. Lehnert, M. A. M. Gijs, "A microfluidic system for nematodes immobilization and bacterial colonization studies in *C. elegans*", poster presentation, MicroTAS 2019, 27-31 October 2019, Basel, Switzerland.

## 5.1 Introduction

Bacteria are the worms' natural food source and *C. elegans* develops a proper gut microbiome in their natural environment [94], whereas *E. coli* is used as the main food source in laboratory settings. In order to develop and sustain its physiological metabolism, a *C. elegans* worm needs to consume a considerable amount of bacteria over its lifespan, requiring highly efficient food processing and digestion mechanisms. Ingestion and pharyngeal transport of bacterial food are fast processes that have been monitored by high-speed video imaging using microparticles, for instance [132]. Advanced methods, including bacterial clearing assays, pulse-feeding assays with nitrogen isotope labeled bacteria or automated bioluminescence-based measurements, have also been used for food intake and nutrient absorption studies (see also Chapter 2, Section 2.1) [63, 64, 108]. As an example, Ding *et al.* used a bioluminescent *E. coli* strain seeded on NGM plates to quantify foraging and feeding of *C. elegans* N2 wild-type worms, *eat-2* mutants presenting a deficiency in pharyngeal pumping, and *npr-1* mutants [64]. As bioluminescence is coupled to living bacteria, food uptake could be quantified by the loss of signal after ingestion and digestion. After initial mechanical disruption of bacterial food in the pharyngeal grinder, small bacteria fragments were shown to transit into the gut for enzymatic digestion [50], where lysozymes and other enzymes may further break down membrane fragments and their lipid constituents [46]. Digestive hydrolase in *C. elegans*, including protease activity, relies on a finely regulated acidic environment in the gut [133, 134]. The pH variation in the *C. elegans* gut, which was determined by pH-sensitive fluorescence nanosensors, was found to range from  $5.96 \pm 0.31$  in the anterior pharynx to  $3.59 \pm 0.09$  in the posterior intestine [54]. Moreover, dynamic processes in the acidification profile of the intestinal lumen could be mapped in real-time and different oscillatory pH patterns have been reported [54, 55, 135]. For instance, during the defecation motor program, a spot of higher acidity rapidly moves periodically from the posterior to the anterior intestine every 45-50 s, with temporary localization for several seconds in the anterior region [55].

In the last years, *C. elegans* has become increasingly interesting as model for systems-level understanding of microbiota-host interactions [136]. Assays are generally based on assessing the worm's life/healthspan for different bacterial strains, gene expression analysis, or by evaluating intestinal bacterial proliferation [66, 67, 99, 137]. For instance, Stuhr *et al.* explored how the most commonly used *E. coli* strains and bacterial diet genera found in the natural environment of *C. elegans* affect multiple life history traits of the worms [137]. Interestingly, *C. elegans* is also a relevant model for human infectious disease research [138, 139, 140]. A range of tactics that pathogenic microbes apply to injure *C. elegans* has been identified, in many cases related to pathogen accumulation in the intestine [138, 141]. For instance, *Microbacterium nematophilum* was found to induce a distinctive swollen tail full of bacteria [142, 143]. Likewise *S. typhimurium* proliferates and fills the worm intestine with intact bacteria within 48 h [140]. On the other hand, beneficial bacteria or probiotics can prolong *C. elegans* survival. For instance, Donato *et al.* demonstrated that *Bacillus subtilis* biofilm germination in the worm intestine extends longevity of nematodes by down-regulation of the insulin-like signalling (ILS) pathway [144]. Moreover, pathogens can induce dysfunction of the physiological mitochondrial activity of *C. elegans* [68, 145], which leads to activation of mitochondrial repair, drug detoxification and pathogen response pathways [146, 147]. For instance, worm exposure to *Pseudomonas aeruginosa* induces mitochondrial dysfunction and the activation of the mitochondrial unfolded protein response (UPR<sup>mt</sup>) in *C. elegans* [34, 148].

In this context, advanced methods and protocols for monitoring the properties and dynamics of the bacterial load in the *C. elegans* intestine emerge as an important requirement to analyze directly specific features of the microbial-host interaction and the resulting physiological or morphological impact. Taking advantage of microfluidic approaches could be very beneficial to explore high-content digestion or infection studies,

based on accurate high-resolution imaging of the temporal and spatial evolution of the bacterial load. However, suitable microfluidic devices addressing related requirements, for instance long-term immobilization under physiological conditions, are not often used and optimized protocols still need to be implemented. Different approaches for on-chip worm immobilization have already been discussed in Chapter 2 (Section 2.2). Trapping by confinement in tapered microfluidic channels was one of the earliest techniques and is now used for different applications, including large-array imaging platforms [73, 80, 149, 150]. Immobilization based on active elements, in particular pneumatic valves on PDMS chips, has been successfully used for high-resolution worm imaging, however this option increases the complexity of the device, hinders easy access to food and exerts significant pressure on the worm body [79]. In the frame of the work presented in this thesis chapter, the microfluidic system (WormSpa) developed by Kopito *et al.* is of particular interest. In this system worms were confined individually in elongated ergonomic chambers. The authors showed that confined worms maintained normal physiological functions and were not stressed over periods of 24 h and longer [81]. Importantly, worms were capable to feed and to lay embryos during immobilization. More recently, Berger presented *et al.* a device for long-term immobilization of normally developing *C. elegans*, where worms are isolated by a set of on-chip valves in dedicated channel sections that perfectly match the worm body. The concept was validated by assessment of anchor cell invasion and distal tip cell migration in larval *C. elegans*, and germ cell apoptosis in adult *C. elegans* [151]. For the time being, only very few microfluidic worm infection assays have been proposed. In general, they focus on killing assays and gene expression, but not on imaging protocols of the bacterial load in the worm gut [82, 83, 85, 86].

Here, we present innovative dynamic imaging protocols of bacteria in the *C. elegans* intestinal track. We take advantage of a PDMS device comprising distinct microfluidic structures for worm culturing and long-term immobilization under physiological conditions. We monitored the transit of ingested bacteria, the spatial distribution and the dynamics of the intestinal bacterial load due to peristaltic activity over 30 h. Furthermore, we demonstrate that our microfluidic device is suitable for high-resolution imaging of fluorescently marked single bacteria persisting in the worm gut. Accurate discrimination between signals originating from intact and disrupted *E. coli* bacteria allowed determining the time constant of nutrient absorption in the gut during biochemical digestion. We further validated our method by monitoring the expression of the *hsp-6::gfp* stress reporter in *C. elegans* mutants exposed to pathogenic *M. marinum*.

## 5.2 Microfluidic platform for long-term *in vivo* worm intestine imaging

### 5.2.1 Microfluidic chip design

The bacterial digestion and colonization assays presented in this work take advantage of a monolithic PDMS microfluidic device comprising distinct adjacent microfluidic chambers for worm culturing and worm immobilization of *C. elegans*. The design for the microfluidic worm traps of our chip has been inspired by the WormSpa proposed by Kopito *et al.* that proved to provide physiological conditions for worm development during long-term confinement [81]. For the assays discussed in the present work, stress-free confinement in an ergonomic environment is of particular importance, for instance for maintaining normal peristaltic activity of the worm gut. In our device, we introduced additional design features that enabled worm immobilization merely by passive elements without application of continuous flow. A microfluidic assay unit on the chip comprises 4 larger



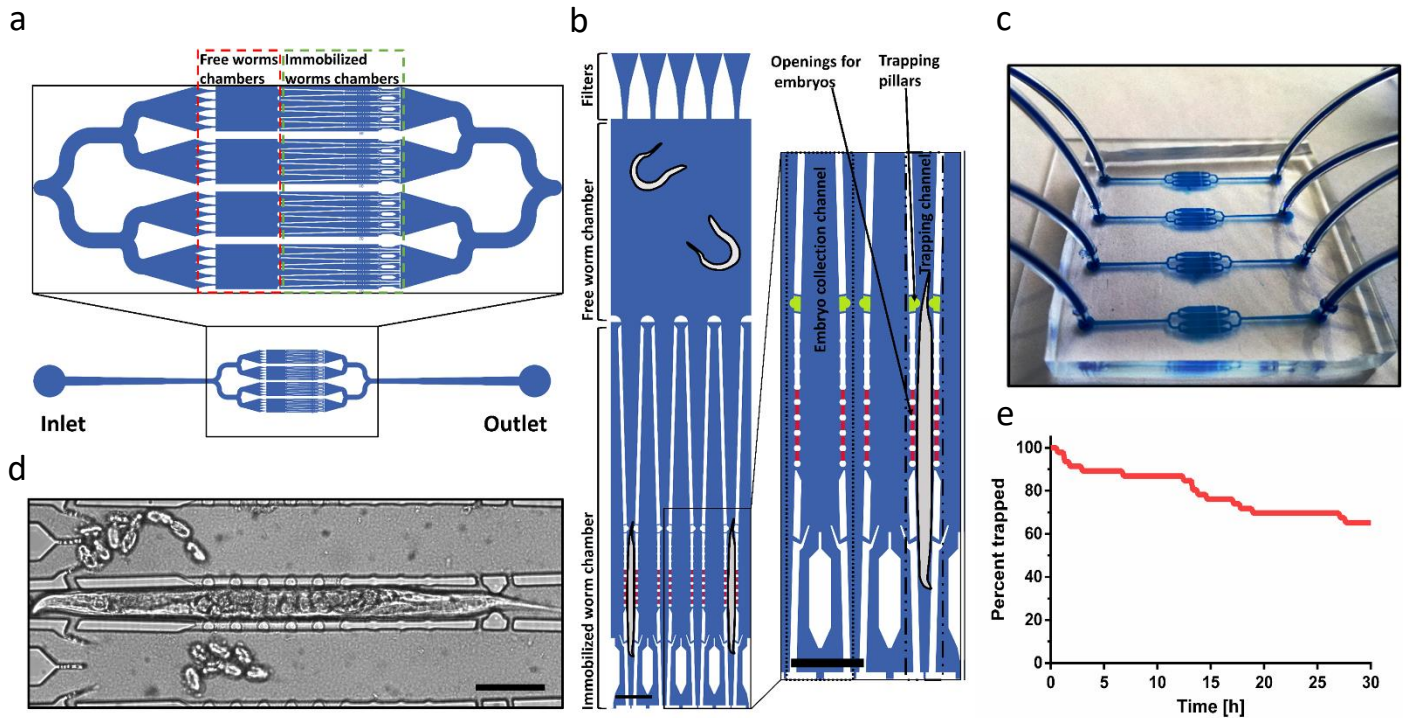


**Figure 5.1** - Microfluidic device for *C. elegans* immobilization and intestinal bacterial load imaging. (a) Schematic representation of an on-chip assay unit with 4 large channels comprising each a free-worm chamber ( $850\ \mu\text{m} \times 1200\ \mu\text{m}$ ,  $60\ \mu\text{m}$  high) and a section with 4 worm traps. (b) Schematic view of one of the channels. Passive PDMS filter structures (upper part of the figure) are located in front of each free-worm chamber to allow selective loading of YA worms. Smaller tapered channels guide the worms into the traps. Each trap has 2 opposite passive PDMS pillar structures for secured worm confinement (highlighted in green). Evacuation of embryos is possible through an arrangement of openings ( $20\ \mu\text{m} \times 25\ \mu\text{m}$ ,  $40\ \mu\text{m}$  high, highlighted in red) in the sidewalls of the traps. Feeding of immobilized worms independently from the body orientation is enabled by 2 lateral openings close to the end of the trap (see enlarged schematic view) and lateral openings at the location of the 2 trapping pillar structures (green). Scale bar =  $200\ \mu\text{m}$ . (c) Photograph of the PDMS chip with tubing, featuring parallel units for 4 independent assays. (d) Brightfield image of a N2 adult *C. elegans* worm immobilized with head-first position in one of the traps. Embryos laid by the worm were moving from the trap into the adjacent embryo collection compartments. Scale bar =  $100\ \mu\text{m}$ . (e) Percentage of trapped worms measured over 30 h ( $n = 46$ ).

parallel channels ( $60\ \mu\text{m}$  high) with 2 distinct compartments for culturing and immobilization of up to 4 individual worms (Fig. 5.1a). YA worms were loaded via the chip inlet and pushed through dedicated on-chip PDMS filters into the culture chambers. For immobilization, worms were relocated and guided via small tapered channels into the on-chip traps. Fig. 5.1b shows the 2-compartment arrangement and an enlarged schematic view with detailed features of the worm trap array. A picture of the whole microfluidic chip is shown in Fig. 5.1c, comprising 4 independent units for assay parallelization, *i.e.* for testing of 4 different experimental conditions independently. Most important features of the worm traps are: (i) 2 passive PDMS trapping pillar structures for secured worm immobilization (highlighted in green in Fig. 5.1b), (ii) an arrangement of side openings (highlighted in red in Fig. 5.1b) for evacuation of embryos into adjacent collection compartments, and (iii) additional lateral openings for adequate worm feeding. To initiate immobilization, the nematode was transferred into the trap and pushed through the constriction formed by the 2



opposite PDMS pillar structures at the entrance of each trap. In this way, trapped worms could be confined for up to 30 h without application of continuous flow. Further to minimizing worm movement, the design of the trapping channels focused on preventing bagging, *i.e.* internal embryo hatching due to prolonged compression of the worm body. For this purpose, the sidewalls of the microtraps have been accommodated with an array of pillars and apertures (40  $\mu\text{m}$  high openings) through which eggs laid during worm immobilization could naturally pass into dedicated collections chambers. A small aperture at the end of these collection channels allowed flushing of embryos and L1 larvae to the chip outlet. Fig. 5.1d shows a brightfield image of a confined gravid adult worm. Eggs can be seen inside the worm body, whereas laid eggs are in the adjacent embryo collection compartments. Possible starving during worm immobilization also had to be considered. Due to the impossibility of controlling the orientation of a worm in the trapping channel, the fluidic design had to be adapted to allow worm feeding in either position and to guarantee a proper amount of suspended bacteria around the mouth region. In Fig. 5.1d the worm was trapped in a head-first position. In this case, specifically shaped openings generate a backflow and redirect bacterial food injected through the embryo collection compartments towards the worm's head (Fig. 5.1b and 5.1d). In case of tail-first trapping, bacterial food was supplied through openings adjacent to the trapping pillars close to the entrance of each trap.

### 5.2.2 Operation of the microfluidic platform

Automated protocols for all fluidic operations were implemented. A brief outline of the platform integration was provided in Chapter 3 (Section 3.4, Fig. 3.4). Before an experiment, each unit of the microfluidic device was flushed with 1 mL of 70 % ethanol for sterilization, rinsed and then filled with S-medium. For worm loading, chip inlets were connected to a dedicated reservoir containing an age-synchronized population of about 30 YA *C. elegans* suspended in S-medium. A pulsed flow sequence was applied for loading the YA worms into a microfluidic unit, thus distributing equally 7 or 8 worms into each on-chip culture chamber through the branched secondary channels (Fig. 5.1a). During this operation the YA worms need to be pushed through the filter lines delimiting the culture chambers (Fig. 5.1b). These V-shaped filters facilitate the passage of the worms during loading and prevent them from escaping when the applied flow is reversed. The filter pore size (minimum width 30  $\mu\text{m}$ ) was adjusted for YA worms. Subsequently, a second pulsed flow sequence with slightly increased flow rate was applied for worm immobilization until most of the traps of a unit were hosting a single worm. At the end of this process, each unit contained approximately 4 x (3-4) immobilized worms, whereas typically 3 to 4 freely moving worms remained in each of the 4 culture chambers. Subsequently, the worm reservoirs were replaced by reservoirs containing bacterial suspensions for worm feeding. Flow pulses were only applied for worm loading, worm transfer for trapping, and for replenishment of the chip with fresh bacteria. Otherwise worms remained confined in the traps without fluidic control. Fig. 5.1e indicates that good long-term trapping efficiency was achieved, with 70% of the worms still being trapped after 30 h.

For experiments involving non-pathogenic *E. coli*, each microfluidic unit on the chip was connected to a computer-controlled V6 Kloehe syringe pump via a rotary valve for selectively actuating feeding protocols of parallel assays (see Chapter 3, Fig. 3.4). An equivalent procedure was applied for experiments involving pathogenic *M. marinum* bacteria. In this case, dedicated 1 ml disposable syringes mounted on a computer-controlled neMESYS syringe pump were used for worm loading and feeding protocols. This setup allowed simplifying the management of contaminated material and minimized the risk of cross-contamination. Bacterial suspensions were injected every 10 min for worm feeding. The time interval between two consecutive injections was selected in order to keep the amount of bacteria in the chambers approximately con-

stant. The bacterial solution was automatically stirred by magnetic stirrers before injection to avoid sedimentation in the syringe reservoir thus improving the control of the amount of food dispensed to the worms. Using fluorescent bacteria as a food source allowed to verify easily the food availability around the head region of the immobilized worms in the traps. The injected bacterial sample volume per pulse was 3  $\mu\text{l}$ . Such low volumes efficiently reduce the risk of bacterial agglomerate formation and consequently of channel clogging, which often compromises the functioning of PDMS microfluidic tools.

### 5.2.3 Imaging protocols of the worm intestine

Details of the hardware configuration of the imaging setup were provided in Chapter 3 (Section 3.4). Depending on the specific assay, low-resolution (Zeiss LD Plan-NEOFLUAR 20 $\times$  NA 0.4 objective) and/or high-resolution imaging (Zeiss 50 $\times$  NA 0.55 objective) was performed. Image processing was done with ImageJ 1.51n software (<https://imagej.nih.gov/ij/>) and Matlab R 2106b software (MathWorks, USA) was used to process data of the intestinal bacterial load in an automated manner. We performed long-term imaging, up to 30 h, for monitoring bacteria accumulation in N2 worms or *eat-2* mutants and of *hsp-6::gfp* expression in the corresponding mutants, respectively. Shorter time-lapse imaging sequences of the gut (up to 180 s) were recorded for assessing bacterial transit, peristaltic motion and the fluorescence decay due to bio-

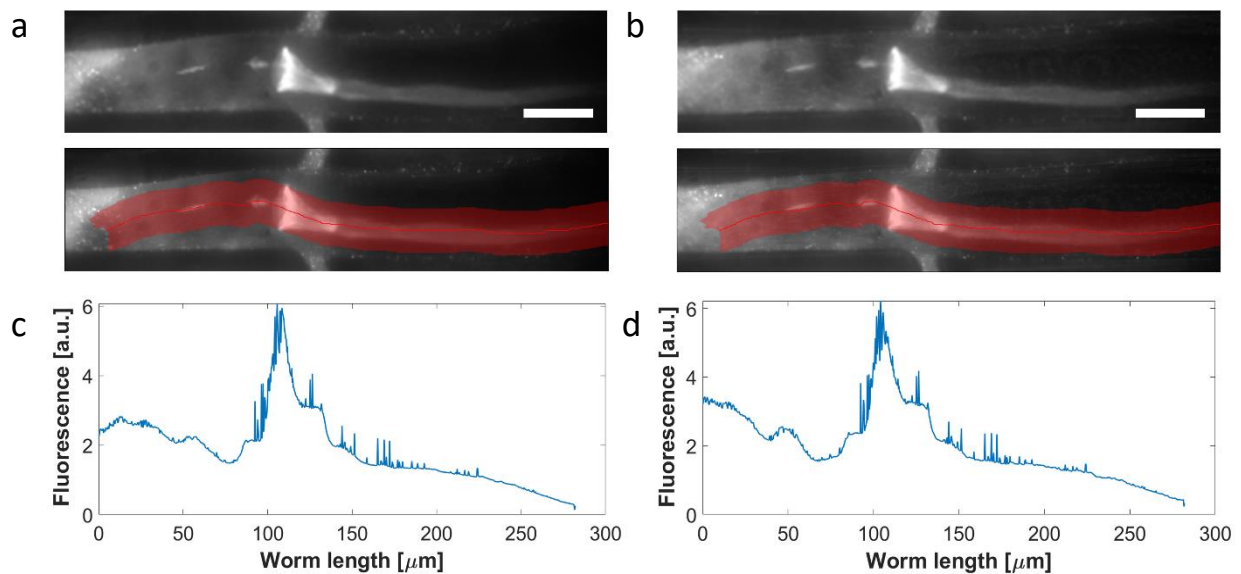


**Figure 5.2** - Fluorescent images of the pharyngeal lumen of an N2 adult worm filled with RFP expressing OP50 *E. coli* bacteria, recorded with double-light exposure (white and 545 nm green light) (a), and with 545 nm green light excitation only (b). The fluorescent signal was measured along the 25  $\mu\text{m}$ -wide red line, indicated in the bottom parts of (a) and (b). (c-d) Comparison between fluorescent signals measured along the red line with double-light exposure (c), and with fluorescence excitation only (d). For low white light power the difference between the two signals was negligible. Scale bar = 40  $\mu\text{m}$ .

chemical digestion. For long-term imaging, brightfield and fluorescence images were recorded successively but quasi-simultaneously, whereas for the short sequences with higher time resolution both images were acquired simultaneously with double-light exposure (*i.e.* white/545 nm for RFP imaging and white/488 nm

for GFP imaging, respectively). Simultaneous acquisition of brightfield/fluorescent images was necessary in order to precisely locate the position of the fluorescent signal of the bacterial load with respect to anatomical structures of the worm. Double-light exposure did not affect the signal originating from fluorescently labeled *E. coli* (Fig. 5.2).

### 5.3 Evaluation of *in vivo* bacterial imaging conditions in the worm intestine

#### 5.3.1 Discriminating intact and disrupted bacteria in the worm gut

Worms mechanically disrupt ingested bacterial food in the pharyngeal grinder. Subsequently, peristaltic action transports bacterial fragments and nutrients into the mid and posterior regions of the gastrointestinal tract for chemical metabolization during the digestive process and finally residues are expelled by activation of a defecation motor program [152]. Expulsion of undigested material takes place approximately every 45 - 50 s for N2 worms [119].

In order to study the specific features and the fate of the bacterial load in more detail, we developed an imaging protocol for discriminating between diffuse and discrete fluorescent signals in the intestinal track. Fig. 5.3a shows a high-resolution brightfield/fluorescent image (50×) of the hindgut of an adult worm, al-

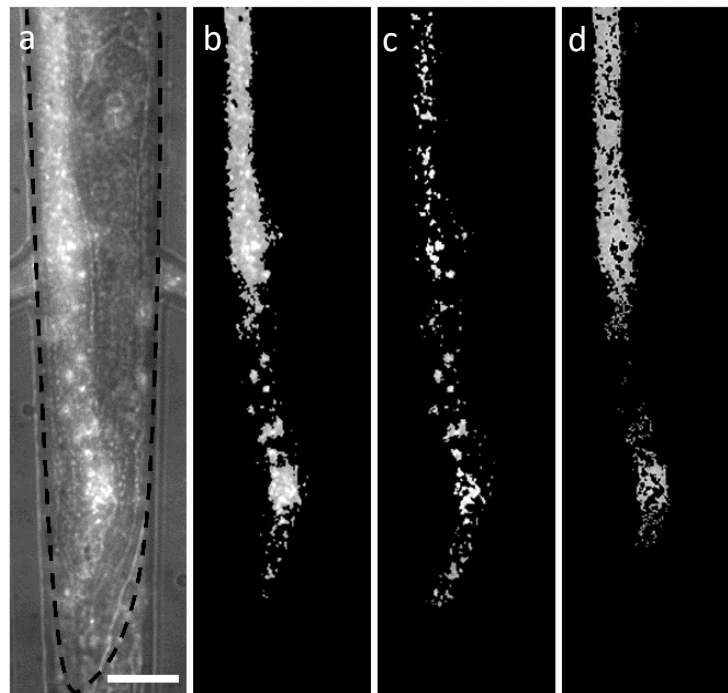


**Figure 5.3** - Automated image analysis for fluorescence measurements of the bacterial load in the worm's gastrointestinal tract. (a) High-resolution (50×) brightfield/fluorescence imaging (hindgut of a N2 adult worm, highlighted by the dashed line) reveals diffuse fluorescence in the gut generated by disrupted bacteria and fluorescent spots related to the presence of intact bacteria/bacterial clusters. (b) The total fluorescence distribution and (c) bright signals related to intact bacteria are discriminated by applying two subsequent thresholding steps. (d) The signal associated with diffuse fluorescence is obtained by subtraction of (c) from (b). Scale bar = 25  $\mu\text{m}$ .

lowing to locate precisely the bacterial load (*E. coli* OP50 RFP). As shown in this example, we generally observed a superposition of diffuse fluorescence distributed in the lumen and brighter spots of small and varying size. As bacteria are mechanically disrupted *in situ* in the worm's grinder, we assume that the diffuse signal may be attributed mainly to the presence of active fluorophores originating from membrane fragments and compounds from the cytoplasm [153], *i.e.* nutritive compounds that can be biochemically transformed in the worm intestine. In the present context, quantification of the diffuse fluorescent signal is therefore important for evaluating the digestive process. On the other hand, depending on the efficacy of the grinding process, also a certain amount of intact single bacteria and bacterial clusters (identified as the brighter spots in Fig. 5.3a) can be found in locations posterior to the grinder. Two subsequent thresholding steps have been applied for extracting the total fluorescent signal intensity  $I_t$  (Fig. 5.3b) and the brighter fluorescent spots  $I_i$  corresponding to intact bacteria that persist in the intestine (Fig. 5.3c). The signal  $I_d$  associated with diffuse fluorescence of disrupted bacteria was obtained by subtraction  $I_d = I_t - I_i$  (Fig. 5.3d). As will be reported later (see Fig. 5.10e and 5.10f), this image processing protocol was particularly useful for evaluating the time constant  $\tau$  of biochemical digestion based on the decay of  $I_d$ .

### 5.3.2 pH sensitivity of different microbial fluorescent markers

The acidic environment in the *C. elegans* intestine, in particular in the mid and posterior sections, may alter signals generated by the fluorescently labeled bacterial load [54]. For this reason, and in particular for a correct and detailed interpretation of the presence, specific features and time dependence of the bacterial load, the pH sensitivity of the fluorophore expressed by the bacteria has to be considered. Similar to the method introduced in Chapter 4, we first used low-magnification (20×) imaging for monitoring the bacterial load of the entire gut of immobilized adult N2 worms. Monitoring of fluorescent bacteria/microbeads accumulation discussed in the present chapter and corresponding color plots for monitoring load dynamics were obtained by adopting the imaging technique already described in Chapter 4. We refer to Fig. 4.6 for a detailed description of bacterial load monitoring and the fluorescent signal processing method.

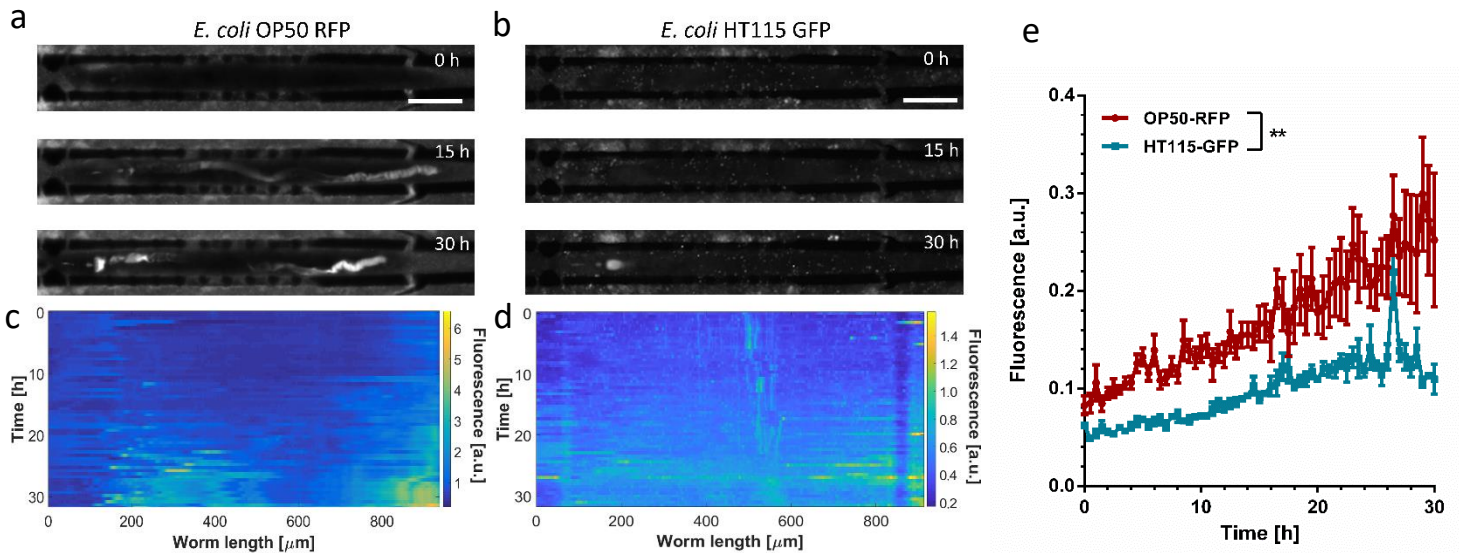


**Figure 5.4** - Analysis of the bacterial load in immobilized adult N2 *C. elegans* worms fed with fluorescently marked *E. coli* bacteria. Fluorophores with different pH sensitivity were used to label the bacterial food. (a) Time-lapse sequence of fluorescence images (20x) over 30 h of a N2 worm fed with *E. coli* OP50 RFP (pH-insensitive), and (b) of a N2 worm fed with *E. coli* HT115 GFP (pH-sensitive). In the ageing worms, an increase of fluorescence in distinct sections of the gut is observed, in particular in the pharyngeal region (for OP50 RFP and HT115 GFP), and in the hindgut (only for OP50 RFP). The strong RFP signal in the posterior region of the intestine is due to the presence of a mixture of intact bacteria and disrupted bacteria. Unlike HT115 GFP, both signals persist due to RFP pH insensitivity. (c-d) Color-coded maps of the fluorescence intensity measured over the whole worm gut, representing the evolution of the bacterial load over 30 h, for the worms fed with OP50 RFP (c) and HT115 GFP (d), respectively. (e) Total fluorescence averaged over the entire worm gut over 30 h for both cases. A general increase over time of the bacterial load is observed, particularly evident in worms fed with the OP50 RFP strain. In HT115 GFP fed worms the overall intensity of fluorescence is lower due to the acidic environment of the hindgut. Values have been normalized with respect to the maximum fluorescence in the pharynx occurring for an event of maximum bacterial intake. Error bars are mean  $\pm$  SD,  $n = 10$  for each condition. Scale bars = 100  $\mu$ m.

In Chapter 4 (Fig. 4.4), we characterized *in vitro* the pH sensitivity of two different *E. coli* strains, OP50 RFP and HT115 GFP, expressing RFP or GFP fluorescent proteins, respectively. We showed that the RFP marker was not affected in the pH range between 3.7 to 6, while the GFP intensity rapidly decreased even in mildly acidic solutions (pH 6) [154]. Here we studied the fate of these two *E. coli* strains *in vivo*. YA N2 nematodes were loaded in the worm microfluidic traps and identical feeding protocols were applied, either using *E. coli* OP50 RFP or HT115 GFP in different assay units of the chip. An example for each condition is shown in Fig. 5.4a and 5.4b, respectively. Representative fluorescence images (20x) of an immobilized N2 worm recorded at 0 h, 15 h and 30 h characterized the long-term evolution of the bacterial load and/or the evolution of the fluorescence signal due to the pH sensitivity of the fluorophore. At the beginning of the observation period (YA worm at  $t = 0$  in Fig. 5.4a and 5.4b), signals were very low along the whole intestinal lumen in both cases. During the YA stage, worms are capable to disrupt and digest ingested bacteria efficiently without significant transient or permanent accumulation. Initial exposure conditions for RFP and GFP recording have been adjusted to the limit of detection of the bacterial load in the pharynx in either cases, thus signal intensities of RFP and GFP raw images may be qualitatively compared. During aging (15 h to 30 h in Fig. 5.4a and 5.4b) a progressive increase of fluorescence was observed in the grinder and the hindgut regions for both cases, whereas the signal remained low in the mid-section of the intestine.

The increase of fluorescence in the pharyngeal region may possibly be explained by the onset of a decreasing efficacy of the grinder function after 30 h. It was shown by analysis of incubated worm lysates that intestinal colonization levels, even for non-pathogenic *E. coli*, already increase at the early adulthood stage [67]. Moreover, pharyngeal swelling by bacterial infection has been identified as a reason for early death in *C. elegans* [106]. Also the hindgut region is particular sensitive to bacterial proliferation fostered by senescent pathologies or genetic causes [67, 143]. As will be discussed below, the strong fluorescent signal visible in the posterior region of the intestine of ageing nematodes fed with the OP50 RFP strain is generated by a mixture of fluorescent reporters originating from disrupted bacterial food and of intact bacteria. Signals from both sources may persist in the hindgut due to the pH insensitivity of RFP.

Color plot panels of the gut fluorescence corresponding to Fig. 5.4a and 5.4b are shown in Fig. 5.4c and 5.4d, respectively. These panels monitor the time evolution of the bacterial load more accurately with a time-lapse resolution of 30 min over 30 h. Overall, the signal intensity in nematodes fed with OP50 RFP is considerably

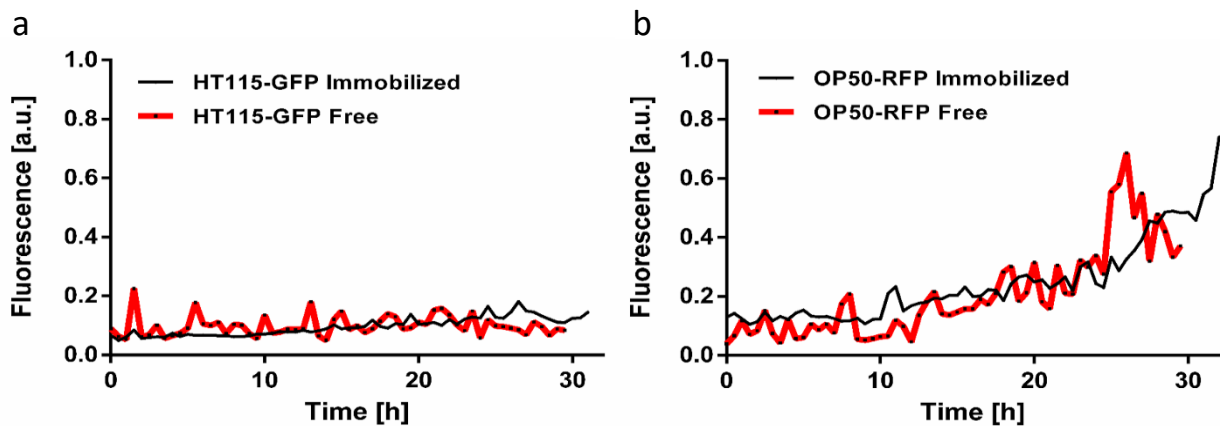


**Figure 5.5** - Comparison between the bacterial load measured by fluorescence of the gut of immobilized and free-swimming worms in adult N2 fed with *E. coli* HT115 GFP (a) and *E. coli* OP50 RFP (b) over 30 h. Fluorescence values were averaged over the whole intestine and normalized with respect to the maximum fluorescence value, measured in the pharynx. Immobilization is not significantly affecting eating and bacterial load in the worm gut in both cases.

higher with respect to the HT115 GFP counterpart. Nevertheless, in both cases an onset of bacterial accumulation can be identified for  $t \geq 20$  h (Fig. 5.4c and Fig. 5.4d). As the worm feeding behavior is not visibly impacted by the two *E. coli* strains, we conclude that the low GFP fluorescence in the hindgut is due to the pH sensitivity of this marker. Actually, only the diffuse GFP signal component related to membrane disruption is affected by the acidic environment (see discussion of Fig. 5.6a), thus we assume that the weak signal observed in this case is generated by a small amount of intact *E. coli* HT115 GFP persisting in the worm gut. The graphs shown in Fig. 5.4e compare the evolution of the apparent average bacterial load over 30 h in worms fed with *E. coli* OP50 RFP and HT115 GFP, respectively. The bacterial load increased over time in both cases, in particular for worms fed with the OP50 RFP strain, reflecting mainly the strong increase of the hindgut signal. Overall, GFP values are below RFP values due to the pH sensitivity of the former. In Fig. 5.4e, values have been normalized with respect to the maximum transient RFP or GFP fluorescent signal recorded in the pharynx, whereby we assume that these signals correspond to a comparable maximum amount of bacterial intake; both graphs in Fig. 5.4e may therefore be compared in a quasi-quantitative way. We also recorded the bacterial load evolution in free-moving (= non-trapped) worms in the dedicated



chambers on the chip. Fig. 5.5 compares both conditions for the two *E. coli* strains and shows that worm immobilization did not affect eating behavior and bacterial load accumulation in the gut, indicating physiological conditions during immobilization.

### 5.3.3 Intact vs disrupted bacteria in the intestine of wild-type *C. elegans* and *eat-2* mutants

In order to verify whether the observed fluorescent signal in the gut reflects accurately the amount of ingested, disrupted and digested bacteria, we investigated the impact of pH in more detail. In particular, as discussed above, for the pH-sensitive GFP reporter, the fluorescent signal may fade in the acidic worm gut, possibly falsely indicating a signal loss caused by chemical digestion. Fig. 5.6a shows a time-lapse sequence of high-resolution images (50 $\times$ ) of the hindgut of an immobilized YA N2 worm fed with *E. coli* HT115 GFP.

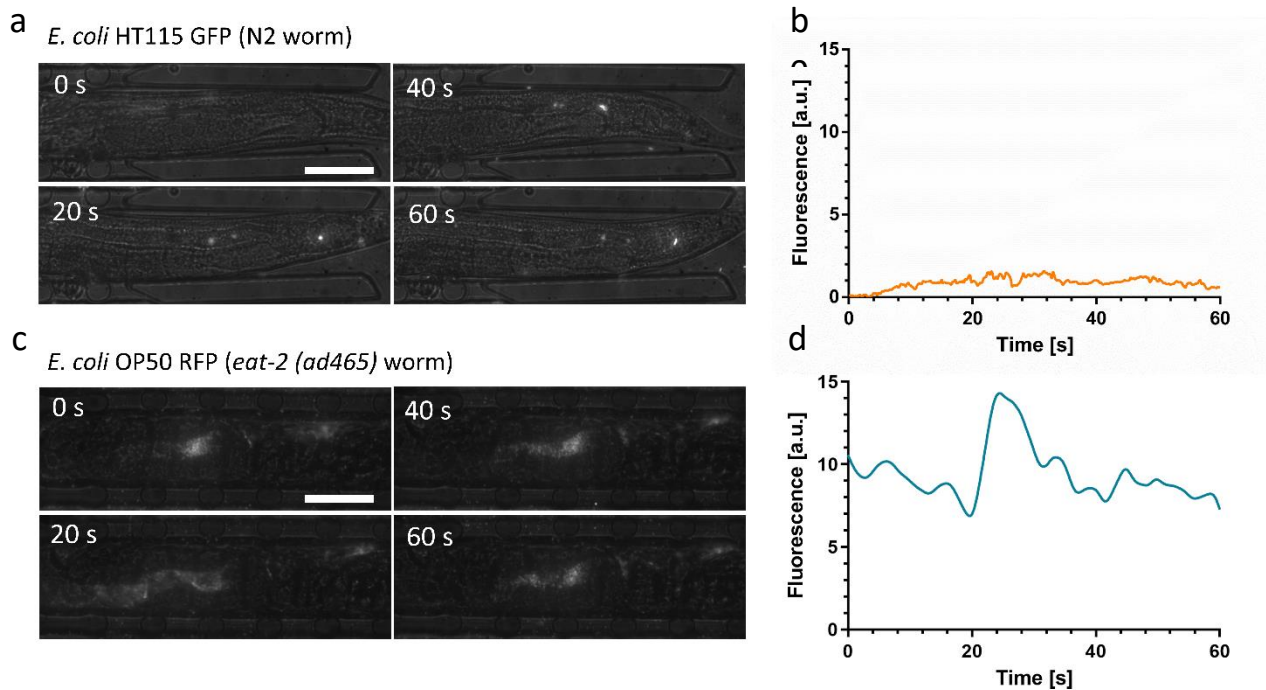


**Figure 5.6** - Intact vs disrupted bacteria in the *C. elegans* intestine. (a) High-resolution brightfield/fluorescence (50 $\times$ ) time-lapse images of an immobilized N2 *C. elegans* worm fed with *E. coli* HT115 GFP. The image sequence shows a few intact bacteria passing through the hindgut region. Despite the pH sensitivity of GFP, fluorescence of intact bacteria is not affected by the acidic environment. Diffuse signals from disrupted bacteria that have lost membrane integrity cannot be observed due to fading of the GFP signal. (b) Fluorescent signal as a function of time measured in the worm in (a), showing a low but relatively constant GFP level originating from intact bacteria. (c) High-resolution time-lapse images of an immobilized *C. elegans* *eat-2* (*ad465*) mutant fed with *E. coli* OP50 RFP. *eat-2* (*ad465*) mutants tend to accumulate intact bacteria in the posterior region of the intestine. The resulting fluorescent signal may be associated to a mixed load of intact and grinded bacteria, as the RFP marker is not affected by the low pH in the hindgut. (d) Time evolution of the fluorescent signal measured in the worm in (c). Overall the fluorescence remains on a constant high level on a time scale relevant for food processing due to the stable presence of intact bacteria in the gut. The peak at  $t \sim 25$  s is due to ingestion and subsequent digestion of a new bacterial aliquot. Scale bars = 50  $\mu$ m.

In this image sequence, we could clearly resolve fluorescent spots generated by a few individual intact bacteria passing through the hindgut region, despite the high intestinal acidity in this region (pH  $\sim$ 3.6). GFP fluorescence of intact bacteria thus appears not to be affected by the acidic environment. This observation indicated that the integrity of the bacterial membrane plays a significant role with respect to fluorescence emitted by the bacterial load during the ingestion and digestion process. On the other hand, no diffuse fluorescence associated to the presence of membrane fragments or other compounds originating from disrupted bacteria was observed in this case. GFP-labeled bacteria thus turn out to be not suitable for monitoring digestion processes in the worm gut, as biochemical decomposition/nutrient absorption and fading of GFP signals due to high pH cannot be discriminated. The average fluorescent signal of the whole worm as a function of time is shown in Fig. 5.6b, reflecting a low but relatively stable signal originating from intact bacteria persisting in the gut.

According to the findings presented above, digestion assays require worm feeding with the pH-insensitive OP50 RFP strain. In this case, we are able to observe strong fluorescent signals in the hindgut, caused by the presence of a mixture of disrupted bacteria and intact bacteria (Fig. 5.4a). In order to confirm this hypothesis, we analyzed the bacterial load in *eat-2 (ad465)* mutants that are characterized by defective pharyngeal pumping, resulting in a conspicuous accumulation of live bacteria in the posterior region of intestine [28]. Fig. 5.6c shows a time-lapse sequence of high-resolution images (50 $\times$ ) of the hindgut of an immobilized *eat-2* mutant fed with *E. coli* OP50 RFP. We detected a mixed load of bacterial fragments and a high amount of intact bacteria generating superposed diffuse and clustered spot-like signals. The corresponding time evolution of the average fluorescent signal in the whole worm is shown in Fig. 5.6d. Overall fluorescence remains on a constant high level on a time scale relevant for food processing cycles due to the stable presence of a considerable number of intact bacteria in the gut of the *eat-2* mutant. The peak in Fig. 5.6d is generated by a new food processing event, *i.e.* ingestion and subsequent digestion of a new bacterial aliquot.

#### 5.3.4 Peristalsis dynamics and biochemical digestion of bacterial food

Based on the imaging protocols and preliminary studies presented above, we were able to evaluate the time constant of nutrient absorption in the worm intestine. We designed an assay for observing simultaneously the fate of *E. coli* OP50 RFP fluorescence due to enzymatic digestion and the intestinal peristaltic action. For the latter, indigestible 1  $\mu$ m-sized rhodamine B-marked melamine microbeads were used for tracking the dynamics and cyclic motion of the intestinal load. In order to obtain real-time recordings of the digestive processes, we performed short time-lapse imaging sequences (60 s to 180 s, frame interval of 250 ms) of confined YA N2 *C. elegans* worms, either at low resolution (20 $\times$ ) for a global view of the entire worm intestine (Fig. 5.7), or at high

resolution (50 $\times$ ) for local and more precise observations, and in particular for the measurement of the decay of the diffuse fluorescent signal in the hindgut (Fig. 5.10). After worm loading and trapping, on-chip microfluidic units were filled either with (i) a mixture of *E. coli* OP50 RFP and red fluorescent microparticles ( $\sim 4 \times 10^9$  beads/mL in S-medium) in equal proportions, (ii) fluorescent microparticles only or (iii) *E. coli* OP50 RFP only, respectively. The chip was refilled with fresh suspension every 10 min in order to maintain the amount of bacteria or particles in the microfluidic chambers.



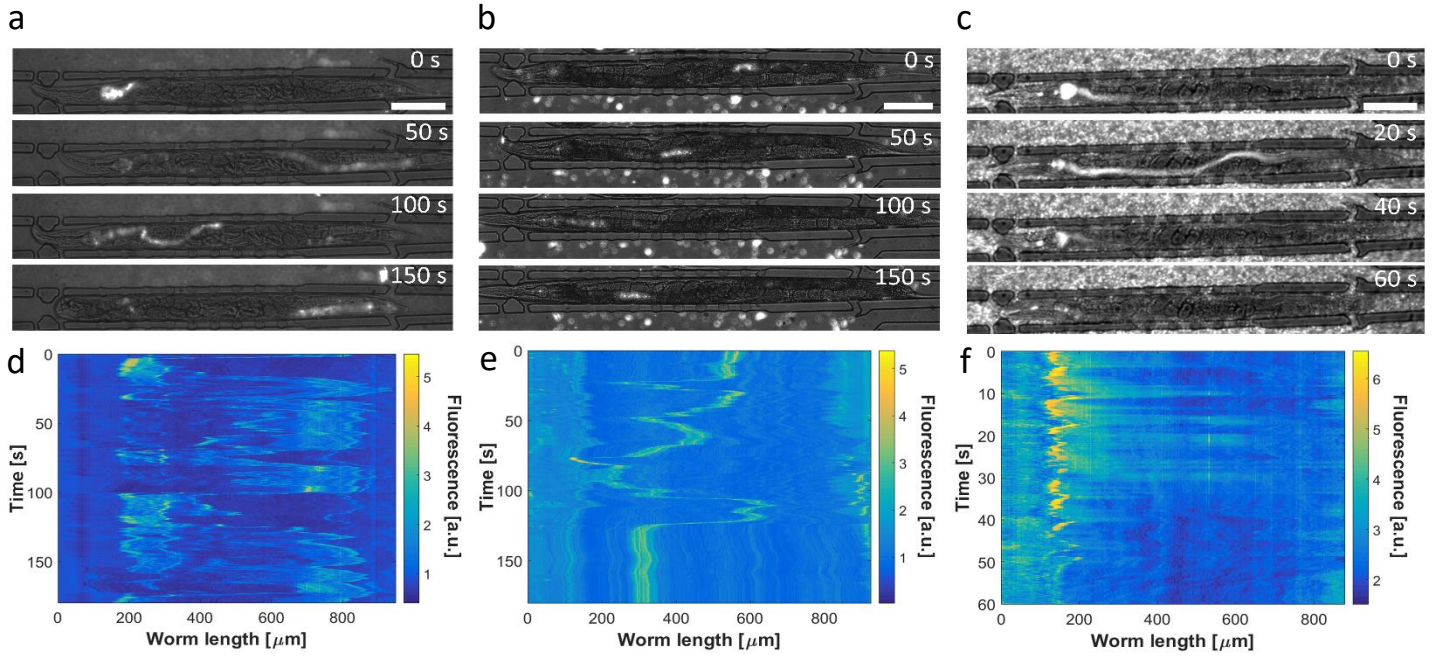


**Figure 5.7** - Analysis of the bacterial digestion and transit of indigestible microbeads in the worm intestine. (a-c) Representative fluorescence time-lapse low-resolution (20×) images of 3 YA N2 *C. elegans* worms immobilized in on-chip traps and fed with *E. coli* OP50 RFP mixed with red fluorescent melamine microbeads (a), red fluorescent microbeads only (b), or *E. coli* OP50 RFP only (c), respectively. In (b) many beads located in the liquid chamber surrounding the worm can be seen. (d-f) Corresponding color plots of time-lapse recordings of the fluorescence intensity of the 3 nematodes in (a-c), showing the evolution and distribution of the bacterial load and/or the fluorescent beads. (d) Superposed diffuse and localized signals related to intact/disrupted bacteria and microbeads, and (e) spatially constraint signal features generated only by microbeads. Microbeads are not digested in the gut and the periodic displacement of the intestinal load by peristaltic action, from the grinder to the hindgut and vice versa, can be tracked in both cases. (f) Fading of the fluorescent signal is observed after feeding the worm with *E. coli* OP50 RFP only. Ingested bacteria initially accumulate in the pharynx and are subsequently pushed towards the posterior region of the gastrointestinal tract. A rapid signal decay occurs in the mid/posterior section of the intestine, starting at  $t > 30$  s after the onset of peristalsis. This decay can be attributed to biochemical digestion, as the RFP label is not sensitive to the acidic environment in the gut. Scale bars = 100  $\mu\text{m}$ .

Representative low-resolution fluorescence images for all 3 conditions are shown in Fig. 5.7a, 5.7b and 5.7c, respectively. Fig. 5.7d, 5.7e and 5.7f are the corresponding color plots. When mixed, intact bacteria and microbeads cannot be distinguished in the worm intestine. In this case, the recorded signal sequences also show extended diffuse regions originating from bacterial membrane fragments. Fluorescent spots and diffuse signals are superposed, resulting in relatively broad features in the intestine (Fig. 5.7a and 5.7d). On the other hand, in the case of mere microbead ingestion, spatially constrained features with stable fluorescence intensity were observed and bright spots generated by single beads and bead clusters can be more clearly identified in the absence of a diffuse signal (Fig. 5.7b and 5.7e). In both cases, resin microbeads cannot be digested and are periodically displaced by peristaltic contractions from the pharyngeal region to the hindgut and vice versa (Fig. 5.7d and Fig. 5.7e, see also Fig. 5.10b). Color panels like Fig. 5.7d were used to evaluate the periodicity of the intestinal load motion. For that, the time evolution of the signal average over the hindgut region was plotted. 4 representative graphs are reported in Fig. 5.8, from which we determined an average period of  $T_p = 71 \pm 5$  s. In Fig. 5.9 multiple peristaltic contractions in the posterior intestinal lumen of a single N2 YA *C. elegans* worm were recorded. Such periodical muscular contractions generate the observed cyclic motion of the intestinal load through the entire worm gut.

On the contrary, when worms are fed only with *E. coli* OP50 RFP bacteria, the transient pattern of the observed fluorescent signals is very different and determined by the rapid biochemical digestion of bacterial food. This dynamic and kinetic behavior is exemplified in the image sequence shown in Fig. 5.7c and with higher time resolution in the color plot panel of Fig. 5.7f. Ingested bacteria, initially intact and concentrated in the worm pharynx, are physically disrupted by mechanical action of the grinder and subsequently, after passing the pharyngeal-intestinal valve, pushed towards the posterior region of the gastrointestinal tract until the pharyngeal lumen is empty. Strongest bacterial transfer from the pharynx to the adjacent intestinal lumen is visible in the time span between 10 s and 30 s on the color plot panel of Fig. 5.7f. This event was also captured in the image at 20 s in Fig. 5.7c. Subsequently a rapid decay of the signal corresponding to the transferred amount of bacteria was observed. Fluorescent signal fading can be mainly identified in the gut section extending from the midgut to the rectum, where already 45 s after a food ingestion event and the onset of peristalsis ( $t = 0$  in the image sequence), the intestine is almost free of fluorescence (Fig. 5.7c and 5.7f for  $t \geq 45$  s). The bacteria-associated fluorescent signal becomes negligible after 60 s. Because of the insensitivity of the RFP marker to the relatively strong acidic pH in the mid and posterior region of the intestine, the observed signal decay has to be attributed to the process of nutrient metabolization and absorption, *i.e.* the activity of digestive enzymes that decompose fluorescent bacterial membrane fragments and nutritive compounds released from the cytoplasm. Defecation did not take place on the time scale of this recording.

For these assays, the examined worms were in the YA stage where notable fluorophore/bacterial accumulation in the hindgut did not occur (as was observed for somewhat older worms in Fig. 5.4a and c). As mentioned above, diffusive fluorescent features can also be identified for the mixed intestinal load monitored in Fig. 5.7d. In principle it should also be possible to detect a decay of fluorescence in this color plot panel. However, relatively strong bead signals impede to a certain extent accurate observation of weaker signal variations due to digestion. Furthermore, recording was carried out over a longer time scale in this case, involving successive ingestion events that replenish the bacterial load in the intestine and cyclic peristaltic motion, eventually screening somewhat a digestive decay.

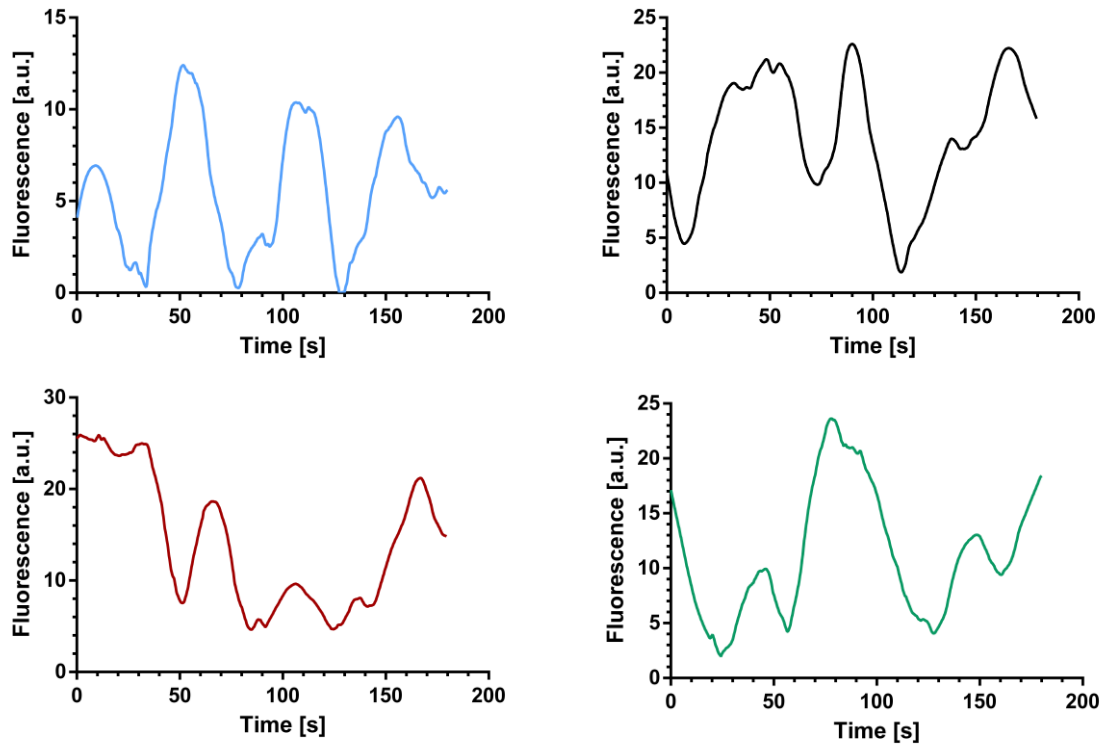


**Figure 5.8** - Evaluation of the periodicity of the intestinal load motion due to peristaltic activity. Color panels like shown in Fig. 5d were used to evaluate the time evolution of the average fluorescent signal corresponding to the hindgut region. Results for 4 representative worms are shown, fed with a mixed suspension of RFP expressing *E. coli* OP50 bacteria and red fluorescent rhodamine B-marked melamine microbeads. We determined an average period of  $T_p = 71 \pm 5$  s.

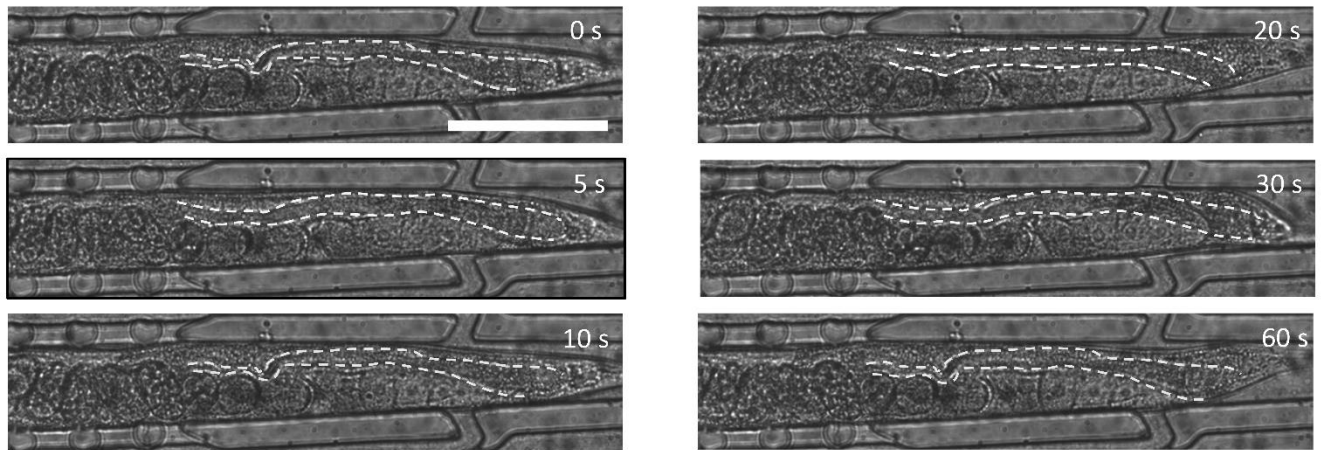


**Figure 5.9** - Brightfield time-lapse recording of the posterior worm section of a gravid N2 *C. elegans* recorded over 60 s, showing multiple peristaltic contractions of the intestinal lumen. Such periodic muscular contractions determine the dynamics of the intestinal transport and may generate, for instance, cyclic motion of the intestinal load through the entire worm gut (as monitored in Fig. 5.7d and 5.7e). An initial contraction of the hindgut is visible at  $t \approx 10$  s, and a second one occurs at  $t \approx 60$  s.

### 5.3.5 Analysis of peristalsis patterns and bacterial absorption by high-resolution imaging

A more detailed investigation of the bacterial transport and digestion processes addressed in Fig. 5.7 is presented in Fig. 5.10 based on high-resolution (50x) time-lapse imaging of the hindgut region of immobilized YA worms. As before, the worms were fed with a mixture of *E. coli* OP50 RFP and red fluorescent melamine microbeads (Fig. 5.10a), fluorescent microbeads only (Fig. 5.10b) or *E. coli* OP50 RFP only (Fig. 5.10c). In the mixed state shown in Fig. 5.10a, single dots and fluorescent clusters, generated by resin microparticles and a small amount of intact bacteria, and diffuse fluorescence associated with grinded bacteria are overlapping and can hardly be discriminated. In this case, the time sequence has been recorded over 180 s in order to focus on the periodicity of motion in the gut due to peristaltic action. The corresponding time evolution of the fluorescent signal in the hindgut region is shown in Fig. 5.10b. The peak at  $t \approx 70$  s and the region extending from  $t \approx 120 - 160$  s (also captured in the image at 150 s in Fig. 5.10a for instance) are caused by the transient localization of clusters of fluorescent microbeads/intact bacteria in the hindgut that are repeatedly pushed back towards the pharynx. The somewhat asymmetric shape of the peaks, due to a slower decay of the peaks with respect to the peak rise, might possibly be related to a digestive process superposing the peristaltic activity (see discussion below and Fig. 5.10f). The cyclic motion of the internal load through the entire worm gut could also be clearly seen in the color plots of Fig. 5.7d and Fig. 5.7e. Provided the time scale of these recordings (180 s), it appears that not-grinded intact bacteria and indigestible beads hinder somehow the defecation process, which normally occurs on a time scale of about 50 s [55].

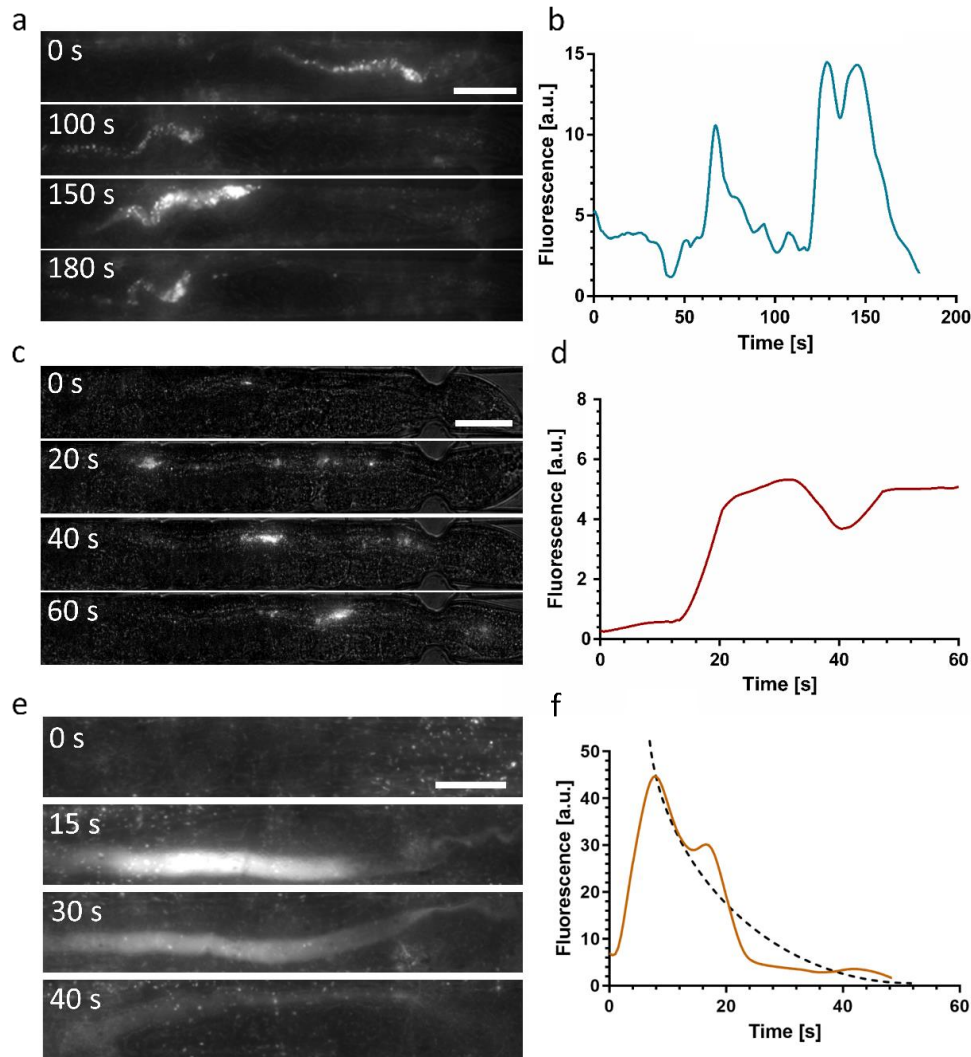


**Figure 5.10** - Analysis of transit patterns and bacterial nutrient absorption in the intestine of N2 *C. elegans* worms by high-resolution brightfield/fluorescence imaging (50x). (a) Time-lapse images of the hindgut region of an immobilized YA worm fed with a mixture of *E. coli* OP50 RFP and red fluorescent microbeads. (b) Average fluorescent signal in the hindgut region corresponding to (a). Peaks at  $t = 70$  s and  $t = 130$  s are caused by transient microbead/intact bacteria clusters (initially located in the proximity of the rectal region, at  $t = 0$  s in this image sequence), which were repeatedly pushed back to the pharynx by peristaltic activity. (c) Images of the hindgut of a YA worm fed with indigestible microbeads only, showing transfer of the beads to the posterior gut region shortly after ingestion. (d) Average fluorescence signal of the hindgut region corresponding to (c). The intensity remained stable over this short initial time period (60 s) after indigestion, since further peristaltic events did not occur yet. (e) Time-lapse images of the hindgut region of an immobilized YA worm fed with *E. coli* OP50 RFP only. An aliquot of disrupted bacteria appearing in the posterior gut section generates strong diffuse fluorescence ( $t = 15$  s). A gradual decay of fluorescence over time was observed ( $t = 30$  s and 40 s), associated to biochemical digestion of membrane fragments and nutritive compounds. (f) Fluorescent signal corresponding to (e) recorded in the hindgut region. Based on additional data (Fig. 5.12,  $n = 5$ ) an exponential decay curve (dashed line) was defined in order to determine the time constant for food digestion ( $\tau = 14 \pm 4$  s). Scale bars = 50  $\mu\text{m}$ .

A closer view on the initial phase after food ingestion is shown in the time-lapse sequence of Fig. 5.10c (50x, 60 s). In this case the immobilized YA N2 worm was fed with red fluorescent microbeads only for visualizing the dynamic behavior of the initial phase after food uptake where beads have been transported to the posterior gut section after passing the grinder without damage. Since digestion of beads does not occur, the fluorescence intensity averaged over the hindgut region is expected to be stable. Fig. 5.10d shows that the time evolution of fluorescence approximates a step-like curve, corresponding to the appearance of the first bead cluster in the hindgut (at  $t \approx 20$  s in this case) and the temporary stability of the signal ( $t \approx 20$  s - 60 s). Subsequently, microbeads are pushed back toward the grinder by a peristaltic contraction, corresponding to the situation shown in Fig. 5.10a and Fig. 5.10b. Defecation may also happen but was not observed in this case. On the other hand, additional transitory accumulation in the posterior intestine could be observed if another consecutive ingestion event occurs rapidly. As shown in two of the graphs in Fig. 5.11, the fluorescence curves feature a 2-step shape in the latter case.

In order to accurately quantify the time constant  $\tau$  associated with the digestive process of enzymatic and biochemical transformation of disrupted bacterial food, we acquired high-resolution images (50x) of the hindgut area of immobilized YA N2 worms fed with *E. coli* OP50 RFP only. Fig. 5.10e shows a representative image sequence visualizing the evolution of the fluorescent signal. The focal plane was adjusted accurately to the mid-height of the gut in order to capture correctly the possible presence of intact bacteria.

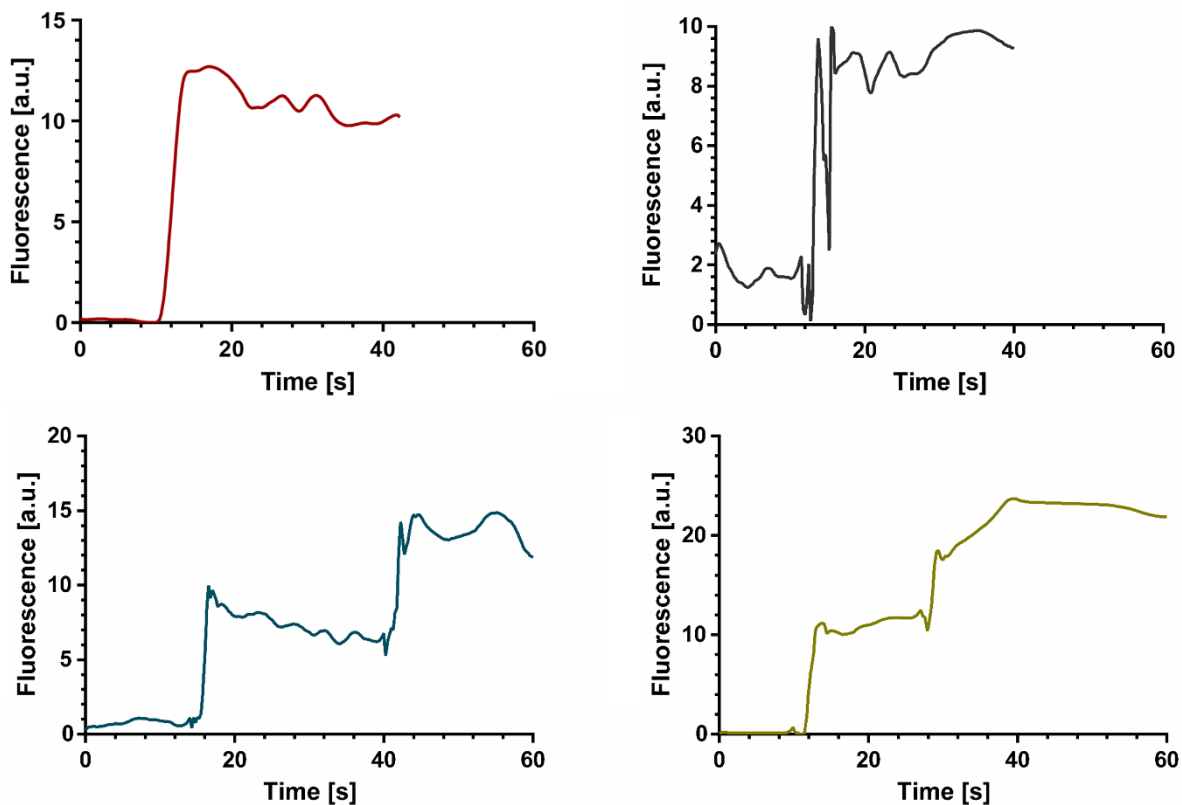


**Figure 5.11** - Fluorescent signal corresponding to the hindgut region for 4 representative worms fed with rhodamine B-marked melamine microbeads. In the two lower graphs, the 2-step shape of the fluorescent signal increase is caused by two consecutive ingestion events of indigestible beads (spaced by  $\sim 20$  s).



The diffuse fluorescence signal was extracted from the raw images according to the image processing protocol described in Fig. 5.3 a-d. At  $t = 0$  food indigestion occurred and no bacteria-related signal could be observed in the gut at this stage. At  $t = 15$  s strong diffuse fluorescence filled the whole intestinal lumen in the posterior region. As was discussed earlier, we assume that this diffuse signal is generated by a mix of small membrane fragments of disrupted bacteria, a significant amount of partly dissociated membrane compounds that still incorporate active RFP markers, and possibly fluorescent cytoplasmic content that was released after disintegration of the bacteria. Subsequent images (Fig. 5.10e,  $t = 30$  s and 40 s) revealed a rapid decay of the fluorescent signal in the intestine.

We attributed the fading of intensity to chemical digestion and absorption of nutrients in the worm gut. Other possible reasons for a loss of signal, in particular pH sensitivity or photobleaching of RFP, relocation of the intestinal load outside the field of view due to peristaltic action (appears only on a longer time scale), and defecation (not observe before the complete fluorescence clearing in this case) can be excluded.

In Fig. 5.10f, we analyzed quantitatively the time dependence of the diffuse fluorescent signal intensity averaged over the hindgut, corresponding to the image sequence in Fig. 5.10e. The initial peak at  $t = 15$  s indicates the arrival of the bacterial load in the hindgut after food uptake and grinding. In the time span of 15 s to 50 s the plot shows the rapid signal decay, which becomes negligible for  $t > 50$  s in this case. The exact features of such graphs are subjected to natural variations of the biological processes and a lack of

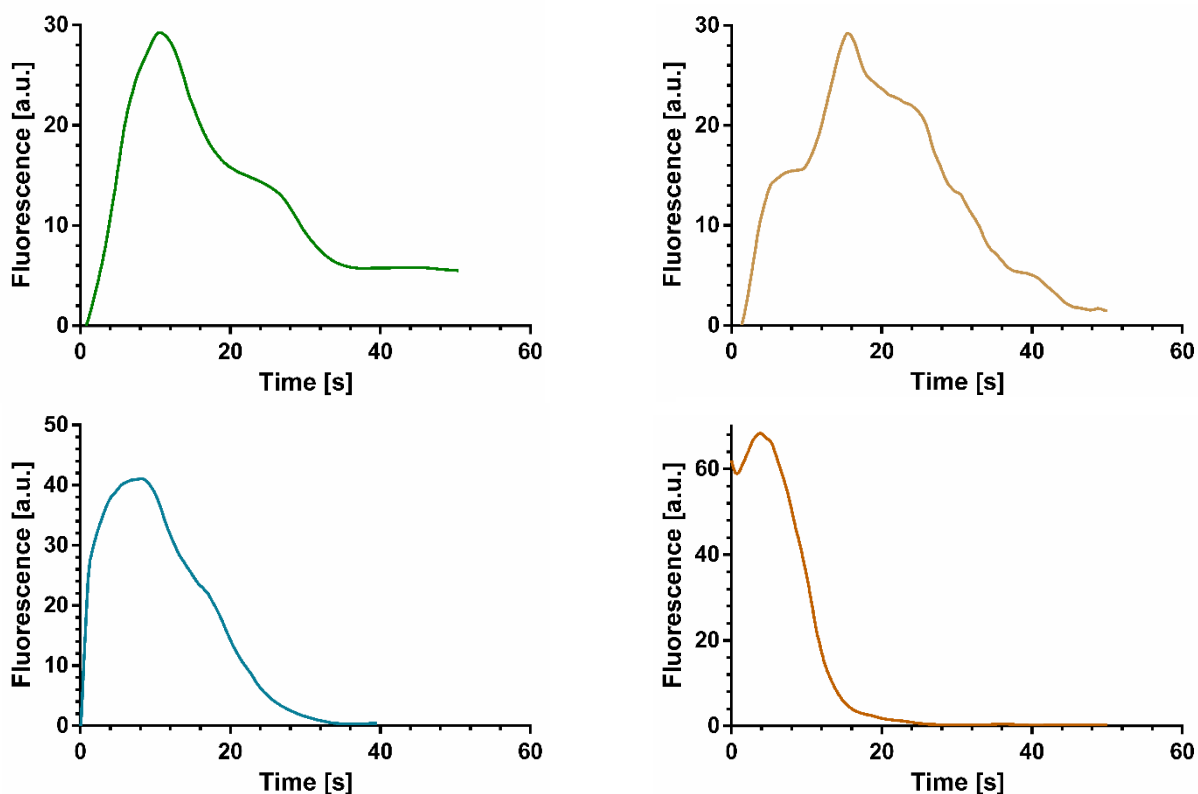


**Figure 5.12** - Fluorescence signal corresponding to the hindgut region for 4 representative worms fed with *E. coli* OP50 RFP. These signals were used to determine the average exponential decay curve in Fig. 6f and to evaluate the absorption time constant  $\tau$  of the digestive process in the worm intestine.

precision of certain assay parameters (e.g. defining the exact time point of food uptake or the transient bacterial accumulation phase in the grinder). Additional typical examples for different worms are reported

in Fig. 5.12. All graphs are clearly different from the step-like shape observed for indigestible beads reflecting a constant fluorescent signal after ingestion (Fig. 5.10d). By averaging the recorded data, we defined an exponentially decaying curve (dashed line in Fig. 5.10f) and estimated a time constant  $\tau = 14 \pm 4$  s ( $n = 5$ ) for biochemical food digestion in the *C. elegans* intestine. This result may also be qualitatively compared to Fig. 5.6d for *eat-2* pharyngeal-pumping defective mutants. In the latter case, the stable baseline of the fluorescent signal, reflecting temporary accumulation of intact bacteria in the hindgut, was superposed by a transient peak due to a new aliquot of grinded bacteria that were rapidly digested.

### 5.3.6 Infection assay on *M. marinum* accumulation and *hsp6::gfp* expression

A wide variety of bacterial species may infect *C. elegans*, which has therefore evolved to an important model for studies of host immunity mechanisms and of pathogen virulence that are analogous to those involved during pathogenesis in humans [138, 139, 140]. In order to validate our microfluidic platform and experimental methods with respect to specific applications, in particular for infection assays involving studies of pathogenic intestine colonization and for monitoring pathogen-induced mitochondrial stress in *C. elegans*, we designed a series of experiments based on the important aquatic pathogen *M. marinum*. *M. marinum* is a slow-growing non-tuberculous mycobacterium that causes a tuberculosis-like illness in fish [155]. In particular, the zebrafish is a natural host to *M. marinum* that was used as model to study tuberculosis pathogenesis, as well as for antitubercular drug discovery [156]. In humans, *M. marinum* is a medically important as it causes cutaneous granulomatous lesions [157]. *M. marinum* is also pathogenic to *C. elegans*. For instance, it was shown that *C. elegans* infected with *M. marinum* displayed a highly increased mortality rate within two days post-infection [158]. Our assays consists in feeding on-chip immobilized worms with the pathogen and measuring (i) the evolution of bacterial accumulation in the worm intestine over several hours, and (ii) to quantify specific fluorescent phenotypic worm features by imaging the time evolution of *hsp-6::gfp* expression, which is an important reporter of mitochondrial stress and the activation of the mitochondrial unfolded protein response (UPR<sup>mt</sup>) in *C. elegans* [148].

For the colonization assays, approximately 16 N2 worms were loaded in each assay unit of the device. Two units were filled with GFP labeled *M. marinum* suspended in S-medium. Considering our discussion above, the pH sensitivity of the GFP fluorophore related to disrupted bacteria is not an issue in the present study, as only accumulation of intact live bacteria is of interest, which are not affected by the acidic environment of the intestine. Non-fluorescent *E. coli* OP50 was used as reference for normal feeding conditions of the worm control groups in the other two on-chip assay units. We acquired high-resolution (50×) fluorescence images of the gut over 15 h, specifically of the pharyngeal and posterior regions, since these sections are most sensitive to bacteria accumulation. Images for both gut sections just after food uptake ( $t = 0$  h) and after on-chip incubation ( $t = 15$  h) are shown in Fig. 5.13a and Fig. 5.13b, respectively. The evolution of the weak autofluorescent signal in a worm fed with *E. coli* is hardly visible with exposure conditions optimized for *M. marinum* (Fig. 5.13a, upper panel). On the other hand, bright spots due to localized accumulation of intact *M. marinum* GFP in the grinder can be seen after 15 h (Fig. 5.13a, lower panel). Likewise, the *M. marinum* bacteria load increased in the hindgut, but the signal is distributed over a larger portion of the intestine, thus relatively weak (Fig. 5.13b, lower panel, same exposure conditions as in Fig. 5.13a).



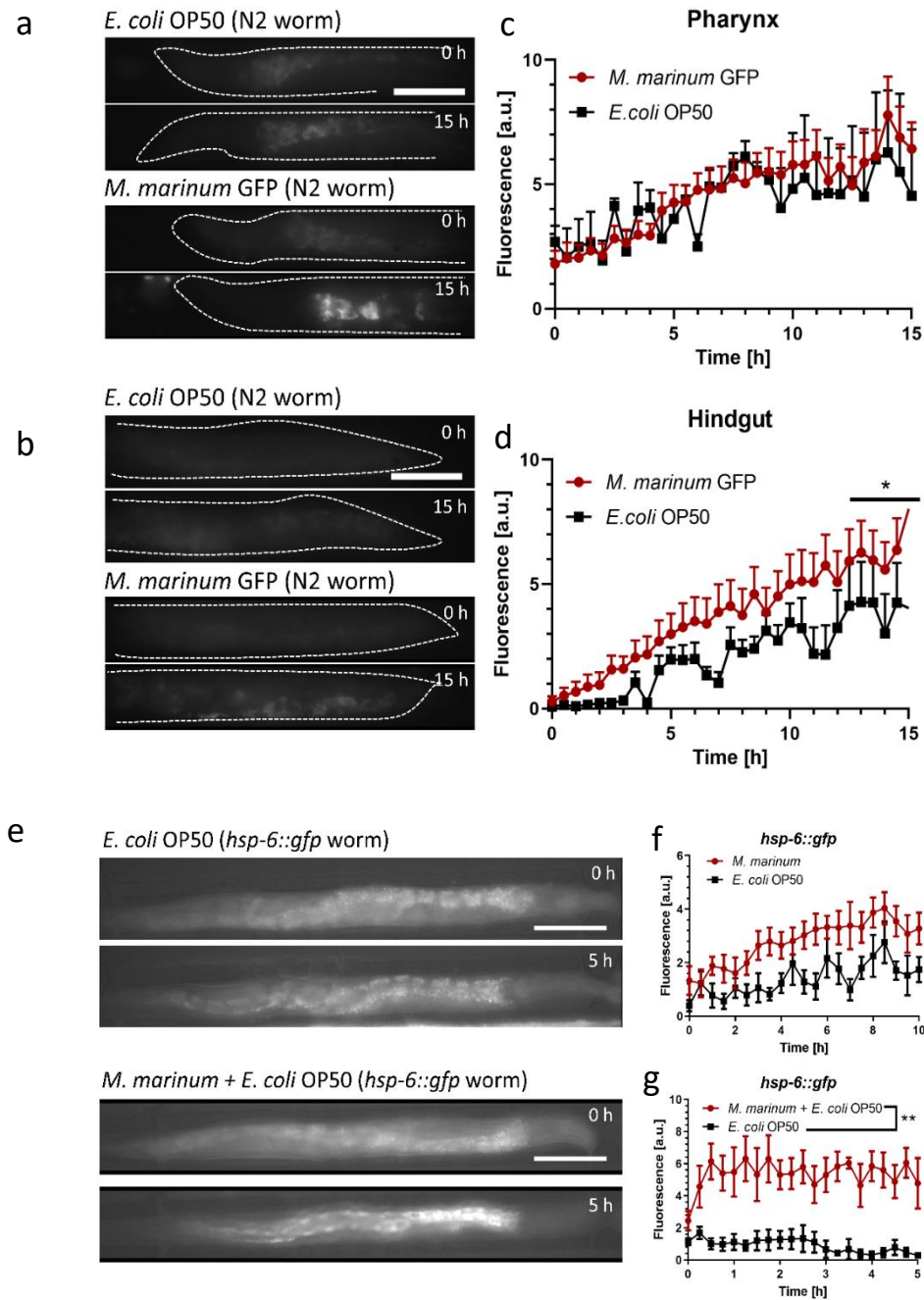


**Figure 5.13** - Analysis of bacterial accumulation and UPR<sup>mt</sup> response in *C. elegans* nematodes induced by pathogenic *M. marinum* bacteria. (a-b) Fluorescence images (50×) of pharynx (a) and hindgut (b) of an immobilized YA N2 *C. elegans*, fed with OP50 *E. coli* bacteria or GFP expressing *M. marinum*, respectively. Worm contours are indicated by dashed lines. Accumulation of *M. marinum* in the grinder and in the hindgut can be identified after 15 h. (c-d) Time evolution of the bacterial load in the pharynx (c) and in the hindgut (d). Average fluorescent signals were normalized with respect to the *E. coli* OP50 value measured in the pharynx for each time point (\* $p \leq 0.5$ ,  $n = 10$ ). (e) Fluorescence images of immobilized YA *hsp-6::gfp* mutants fed with *E. coli* OP50 only (top images) and a mixture of *M. marinum* and *E. coli* OP50 (bottom images). The immobilized worms are oriented with head to the right. Strong fluorescence due to *hsp-6::gfp* expression in the worm fed with *M. marinum* is visible in the anterior region of the intestine adjacent to the pharynx. (f) Average fluorescence signal related to *hsp-6::gfp* expression for nematodes fed with *M. marinum* only and *E. coli* OP50 only, respectively ( $n = 5$ ). (g) Fluorescence signal related to *hsp-6::gfp* expression for nematodes fed with a mixture of *M. marinum* / *E. coli* OP50 and with *E. coli* OP50 only, respectively. *E. coli* OP50 were added to *M. marinum* to verify that the increase of *hsp-6::gfp* expression is not caused by worm starvation (\*\* $p \leq 0.1$ ,  $n = 5$ ). Error bars correspond to mean  $\pm$  SEM. Scale bars = 100  $\mu$ m.

The graphs in Fig. 5.13c and Fig. 5.13d express more clearly the time evolution of the corresponding signal intensities, averaged over the pharyngeal and posterior regions, respectively. The *E. coli* autofluorescence control signal increased over time indicating a progressive accumulation of bacteria in the grinder (Fig. 5.13c, black curve). The observation of this phenomenon was more evident in Fig. 5.4b (at  $t = 30$  h, using *E. coli* HT155 GFP). The evolution of the fluorescent signal associated with *M. marinum* in the pharynx (Fig. 5.13c, red curve) was similar to *E. coli*. For a better comparison, *M. marinum* values have been normalized for each time point with respect to the *E. coli* OP50 intensity determined in the grinder. We deduce therefore from Fig. 5.13c that no specific additional accumulation occurred in the grinder for the present assay conditions. On the other hand, the normalized *M. marinum* signal in the hindgut increased faster than the *E. coli* control (Fig. 5.13d), indicating accumulating and/or colonization possibly due to the pathogenic effect of *M. marinum*. In both cases, a rise of the fluorescent signal in the worms could in principle also be partly be due to increasing autofluorescence in aging worms, however at the early adulthood stage of the worms in the present assays this effect should be negligible [159].

In order to evaluate the feasibility of recording UPR<sup>mt</sup> response with our microfluidic platform, we first measured the mitochondrial stress response in YA *hsp-6::gfp* mutants caused by prolonged exposure to tetracycline. For the assay, an *E. coli* suspension was mixed with tetracycline to a final concentration of 60  $\mu\text{g}/\text{ml}$ . Corresponding brightfield/fluorescence images are shown in Fig. 5.14, where a bright signal generated by *hsp-6::gfp* expression in the pharyngeal region could be observed after tetracycline exposure for 8 h (Fig. 5.14a, lower panel). The increase of *hsp-6::gfp* expression of the treated worms over 15 h is represented in the graph of Fig. 5.14b. For evaluating the mitochondrial stress response induced by pathogenic *M. marinum*, we monitored the fluorescent *hsp-6::gfp* signal in YA mutants for different feeding conditions. Fluorescence images of immobilized *hsp-6::gfp* mutants acquired after the initial filling of the chip with different bacterial suspensions ( $t = 0$  h) and after incubation for 5 h are shown in Fig. 5.13e.

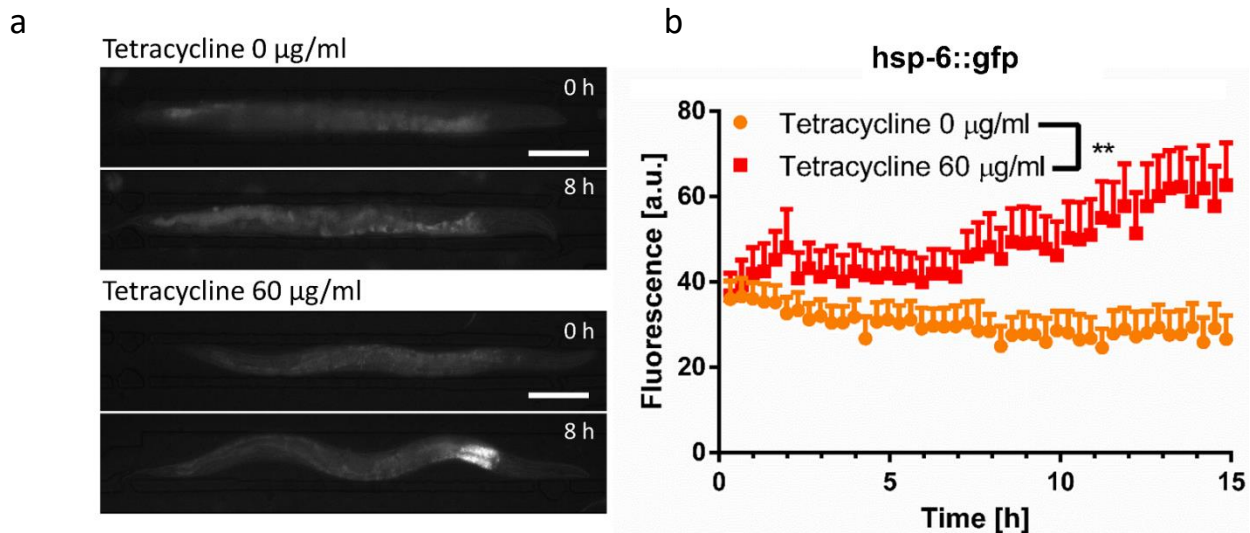


**Figure 5.14** - Analysis of UPR<sup>mt</sup> response in *C. elegans* *hsp-6::gfp* mutants induced by the antibiotic tetracycline. (a) Time-lapse images of immobilized YA *hsp-6::gfp* mutants, without and with tetracycline exposure. Scale bars = 100  $\mu\text{m}$ . (b) Average of fluorescence signal related to *hsp-6::gfp* expression for treated and untreated worms. Error bars correspond to mean  $\pm$  SD, \*\*  $p \leq 0.01$ ,  $n = 10$ .

Images of a *hsp-6::gfp* mutant fed with *E. coli* OP50 only did not show a significant difference over the time interval of 5 h (Fig. 5.13e, top panel). The time evolution of fluorescence intensities for *hsp-6::gfp* mutants fed with *M. marinum* only and the *E. coli* control group is represented in the graph of Fig. 5.13f (averaged over the entire worm). Overall the induced fluorescence response was higher with *M. marinum* compared to *E. coli* only, showing a slight increase over time, similar to the effect of tetracycline (Fig. 5.14b). In order to verify that mitochondrial stress in worms was not induced by food avoidance and starvation, the infection assay was repeated with a mixed suspension of *M. marinum* + *E. coli* OP50, thus delivering the pathogen and providing an adequate food source simultaneously. Fluorescence images of an immobilized *hsp-6::gfp* mutant are shown in Fig. 5.13e (bottom panel). Strong fluorescence due to *hsp-6::gfp* expression in the anterior region of the intestinal track is clearly visible after 5 h. The corresponding fluorescence signal averaged over the whole worm is shown in the graph of Fig. 5.13g (red curve). Like for *M. marinum* only (Fig. 5.13f), the *hsp-6::gfp* induced signal was above the control values for feeding with *E. coli* only. However, in the latter case, we observed a faster onset of stress-related *hsp-6::gfp* expression and a higher overall fluorescent intensity. This could possibly be due to a higher uptake of *E. coli* being a suitable food source, entailing simultaneously ingestion of an enhanced amount of *M. marinum* in the mixed feeding suspension, thus enhanced stress response.

## 5.4 Discussion

Developing new versatile tools for investigating *in vivo* the bacterial load in the *C. elegans* intestinal track appears to be important in the present context, where *C. elegans* is increasingly explored as model organism for the microbiota-gut interaction and for infections assays related to human pathogenesis. Aside from assessing typical worm phenotypes, development and health indicators, imaging bacterial populations and properties directly inside the gut under different pharmacological or microbiological conditions provides important new information. Digestion or food absorption parameters, detecting small amounts of persisting live bacteria, or gut colonization by pathogens are relevant features in this perspective.

Conventional tools and assays, mainly based on bacteria-seeded NGM plates, have been used for the observation and measurement of bacterial colonies in the worm intestine [63, 64, 108]. However, for the time being, a very limited number of related studies was performed by taking advantage of microfluidic approaches, despite the fact that microfluidic tools have been successfully used in *C. elegans* research for a large variety of topics, ranging from behavioral to neurobiological studies [45, 37]. For instance, in microfluidic antimicrobial assays, only representative low-resolution images of the overall bacterial load in infected *C. elegans* have been shown, possibly taken off-chip without worm immobilization [82,85]. Lee *et al.* developed a hexagonal array of micropillars that supported worm motility. The post-infection *P. aeruginosa* bacterial load in the intestine was displayed at low resolution [86]. In another infection assay based on the WormSpa, worms were immobilized and representative low-resolution brightfield images of a single worm fed with *P. aeruginosa* were presented [83]. To our knowledge, the work presented here is the first study that analyzes the bacterial load dynamics, digestion and food absorption in the *C. elegans* gut directly by means of a microfluidic device. Our approach allowed both long-term low-resolution time-lapse imaging of the entire worm body and high-resolution imaging of small sections of the worm intestine for several hours. We identified and characterized dynamic features, in particular cyclic motion of bacteria clusters in the gut due to peristalsis. Detection of single live bacteria, discrimination between intact bacteria and disrupted bacterial fragments in the posterior intestinal lumen, bacterial absorption and bacterial accumulation in different sections of the worm was successfully monitored. Worm response to pathogenic bacteria was also analyzed.

A major challenge of such on-chip assays, is performing *in vivo* long-term immobilization of *C. elegans* nematodes, while maintaining the worms in healthy and physiological conditions. Continuous nutrition supply and frequent egg laying are concomitant factors that are specifically relevant for long-term on-chip culture and observation. Moreover, starting from the YA stage, *C. elegans* are able to exert significantly higher force with respect to the larval stages [160], especially with their mid-body and tail regions, which further complicates stable immobilization of the worms over extended periods. The microfluidic device presented in our work proved to be suitable for *in vivo* bacterial imaging and for measuring the bacterial load in the *C. elegans* gut in a dynamic way. As no active elements are involved for immobilization, device fabrication and operation was simple. Continuous feeding during worm trapping was not impeded. We took advantage of specific features of a microfluidic trap design presented earlier by Kopito *et al.* [81]. In particular, perforating the sidewalls of the traps allowed continuous egg laying, an important requirement for enabling physiological conditions during worm confinement. We adapted and optimized our trap design by introducing dedicated passive structures (trapping pillars) at the entrance of each worm trap, enabling secured worm confinement without applying continuous flow, thus making fluidic protocols more robust. As, on purpose, the worm is not tightly immobilized or compressed, a slight margin of worm movement is allowed during on-chip confinement, *e.g.* small rotations or longitudinal displacements along the trapping channel. Certain limitations might be encountered for tracking of non-fluorescent or not easily identifiable anatomical worm features, however for the present application such issues were not relevant. In any case, the intrinsic limit for high-resolution imaging of the worm gut is set by the internal natural residual motion of the organs and, more importantly, the dynamic behavior of the bacterial load to be studied. Moreover, additional culture chambers have been implemented on the chip, enabling simultaneous measurements of conventional phenotypes related to free-moving worms, *e.g.* thrashing frequency or motility, under identical feeding conditions as for confined worms. Such an approach obviates more complicate reversible immobilization protocols.

Implementing microfluidic approaches for advanced and accurate *in vivo* imaging of bacterial colony dynamics and digestion kinetics opens the way to enhance the information content, throughput and versatility of assays targeting *C. elegans* microbiota-gut interaction. For instance, microfluidic platforms would be especially suitable for parallel on-chip assays based on worm feeding with different bacterial strains and/or the application of different antimicrobial compounds [161]. Likewise a range of *C. elegans* mutants, presenting specific drug-dependent microbial-host interaction features, could be observed simultaneously.

# Chapter 6 Bacteria detection enhanced by dielectric microbeads

Current microscopy systems for imaging of microorganisms are expensive and optimized with respect to resolution and aberration correction. However, such high-end optical systems are not needed in all situations, for instance for merely detecting the presence of pathogens in liquids for on-site analyses. A potential cost-effective approach is to use highly refractive spheres in combination with low-magnification objectives to increase the resolution and the sensitivity of the optical system. Indeed, for point-of-need assays, integration of optical elements on a microfluidic device can bring several advantages, such as test parallelization, automation and low-volume consumption. We report here a study on  $\text{BaTiO}_3$  spheres that are partially embedded in thin polymeric membranes of mismatched refractive index. We computed the optical path of light originating from a sample of interest through this polymeric membrane/dielectric sphere assembly (PMDSA) and showed enhanced detection potential in combination with a low-magnification objective. We then propose a method to easily fabricate custom-designed microfluidic chips and precise positioning of the dielectric spheres for enhanced imaging capabilities. We applied this concept to the detection of living fluorescent bacteria, either flowing in aqueous medium or immobilized in hydrodynamic traps. We quantified the contrast gain provided by the PMDSA for short exposure, also imaging for longer durations could be reliably performed. Since the present PMDSA concept combines optical enhancement of low-magnification objectives with the flexibility of microfluidic handling, it could be highly suitable for portable and cost-effective systems for on-site analysis, with applications ranging from flow cytometry to antibiotic testing.

---

This section was adapted from the following publications:

V. Viri, D. Migliozi, and M. A. M. Gijs, "Integration of polymeric membrane/dielectric sphere assemblies in microfluidic chips for enhanced-contrast imaging with low-magnification systems", *Journal of Optical Microsystems*, 2021, 1(1), 014001.

D. Migliozi, V. Viri, and M. A. M. Gijs, "Integration of highly-refractive spheres in microfluidic chips for high-contrast detection of bacteria with low-magnification systems", *European Conference on Biomedical Optics*, Optical Society of America, 2019.

## 6.1 Introduction

In the past decade, properties of dielectric microspheres ( $\mu\text{Ss}$ ) have been widely studied in view of improving the performance of optical systems in a cost-effective fashion. The effective field of view and the magnification created by the  $\mu\text{Ss}$  were characterized [162,163]. Resolution analysis was performed for  $\mu\text{Ss}$  im-

mersed in liquid media [164] or elastomers [165]  $\mu$ Ss were used for various applications, such as microtopography measurements [166, 167] biological structure imaging [168,169,170,171], single-molecule detection [172], single-nanoparticle detection [173] and fluorescence correlation spectroscopy [174, 175]. Previous examples of technical implementation employed scanning probes [167, 176], arrays [177] or thin polymeric films [178] to perform the imaging. Arraying was also used to enable the detection of nano-objects in a flow [173]. However, handling of microspheres for imaging purposes can be prohibitively cumbersome when aiming to increase throughput and system complexity, while decreasing fabrication costs at the same time. For instance, placing  $\mu$ Ss in precise locations with high yield can be extremely difficult. Moreover, if the  $\mu$ Ss are not well positioned relative to the sample, imaging and detection may be adversely affected [164, 177]. For applications that target the detection of micrometer-size objects (*e.g.* bacteria or cells) compared to nanoscale objects (*e.g.* biomolecules, nanoparticles or subcellular structures), a relatively large depth-of-field is usually required [179, 180]. Additionally, for long-term imaging of living microorganisms, sample handling and immobilization often constitute a significant challenge. Several microfluidic approaches have been proposed to facilitate such analysis, *e.g.* single-cell arraying [181] and single-bacteria immobilization [182]. Existing microfabrication techniques allow integration of optical and fluidic elements in lab-on-a-chip devices [183]. Integrating micro-optical elements with microfluidic platforms can substantially enhance the detection of microorganisms, by adding potential for portability, cost affordability, and eventually automation [184]. Optical waveguides and microfluidic channels have been embedded in polymer-based devices for fluorescence excitation of biological samples, such as fluorescently labeled phospholipids and stained cells [185]. Another work reported a device based on a PDMS 2D optical lens integrated with microfluidic channels to improve the performance of fluorescence spectroscopy performed using optical fibers [186]. An optofluidic system based on a low-refractive index liquid with tuneable biconcave PDMS lenses for focusing light has also been reported [187]. A fluid-based microfabricated lens suitable for integration into a multi-lens optical system for microfluidic flow cytometry was demonstrated [188]. Another work presented microfluidic observation channels combined with solid-state lasers and PIN-based photodetectors for performing flow cytometric measurements of fluorescent microspheres and nucleic acid labeled fungi [189]. However, such approaches mainly employ expensive optical components and fabrication methods, which may seriously compromise the affordability of such systems.

In this work, in order to assess the potential of empowering low-magnification systems for the analysis of microorganisms in a cost-effective way, we integrated dielectric  $\text{BaTiO}_3$  spheres in microstructured PDMS membranes. This PMDSA constitutes a low-cost implementation in microfluidic chip format for potentially enhancing the detection capability of low-end microscopy systems. Our method reduces manual sample preparation steps by integrating the optical elements in a microfluidic tool, which is operated by computer-controlled pumps. The possibility of readily coupling the PMDSA with an optical microscope makes the device suitable for on-site detection of micrometer-size objects and living entities, such as bacteria for instance. Moreover, embedding of dielectric spheres in the PDMS membrane is not limited by a specific microfluidic design and can be adapted to the various applications.

## 6.2 PMDSA modeling, imaging protocols and chip design

### 6.2.1 Analytical modeling of the PMDSA

The procedure to calculate the optical path through a dielectric sphere has been described by our group in [164]. Briefly, to quantitatively calculate the effect of the sphere on the light cone emerging from the sample, we used the property of cylindrical symmetry to reduce the calculation to a 1D problem, as well as

linear wave propagation and Snell's law to compute the relation between the input and output angles relatively to the optical axis of the imaging system. Using the same notation as in [164], the theoretical contrast gain may be calculated as

$$\text{Contrast gain} = \frac{1 - \cos[\theta_s(h)]}{1 - \cos[\theta_{\text{obj}}]}$$

where  $\theta_{\text{obj}}$  is the maximum angle collected by the objective relatively to the optical axis, and  $\theta_s(h)$  is the maximum angle collected in presence of a sphere at a distance  $h$  from the sample.

Based on our previous resolution analysis on dielectric spheres immersed in homogenous media [164], we determined the optimal configuration for a highly refractive sphere (diameter 1 mm, BaTiO<sub>3</sub>, refractive index  $n_s = 1.95$ ) embedded in a PDMS membrane (PDMS, refractive index  $n_{\text{PDMS}} = 1.43$ ). This configuration is shown in Fig. 6.1a. It consists of a sphere that is only partially embedded in PDMS, where the index mismatch between the sphere material, the polymer and the surrounding media increases the overall collection angle of the optical system ( $\theta_{\text{out}}$  with respect to  $\theta_{\text{in}}$  in Fig. 6.1a). This effect can be used to generate resolution and contrast gains for low-magnification objectives. In Fig. 6.1b, we show the presence of an enhanced-detection zone (EDZ) for a  $10 \times / 0.25$  NA objective, which approaches the collection angle of a  $100 \times / 0.75$  NA objective with the same immersion medium (air).

### 6.2.2 Image acquisition and processing

Details of the PMDSA imaging platform have been provide in Chapter 3 (Section 3.4.2). We used *Escherichia coli* expressing red fluorescent protein (DsRed) as sample to assess the PMDSA imaging performance. The following image processing procedure was applied to the time-lapse fluorescence image series recorded from bacteria in liquid flow: (i) the pixel-by-pixel median of the series was subtracted from each image to remove background; (ii) a Gaussian blur with  $\sigma_G = 2$  was applied to each image. This step was performed only for images recorded in the presence of the sphere, where the  $\sim 5.5\times$  magnification increases the variability between adjacent pixels, which may bias the detection of a single bacterium by splitting it into smaller particles; (iii) the standard deviation of the pixels of the entire series was calculated and a threshold was set to 10 times this value; (iv) a threshold was applied to each image and the area and integrated intensity of each particle detected were calculated; (v) for fluorescence images recorded with trapped bacteria, all images of the same sequence were aligned by a custom developed script based on template matching [190] in order to remove artefacts due to possible movement along the xy plane; (vi) subsequently, two regions with the same area were defined, one comprising the immobilized bacterium and an adjacent blank region for background evaluation; (vii) finally, average grayscale values were measured in all slices of the time series for both bacterium and background.



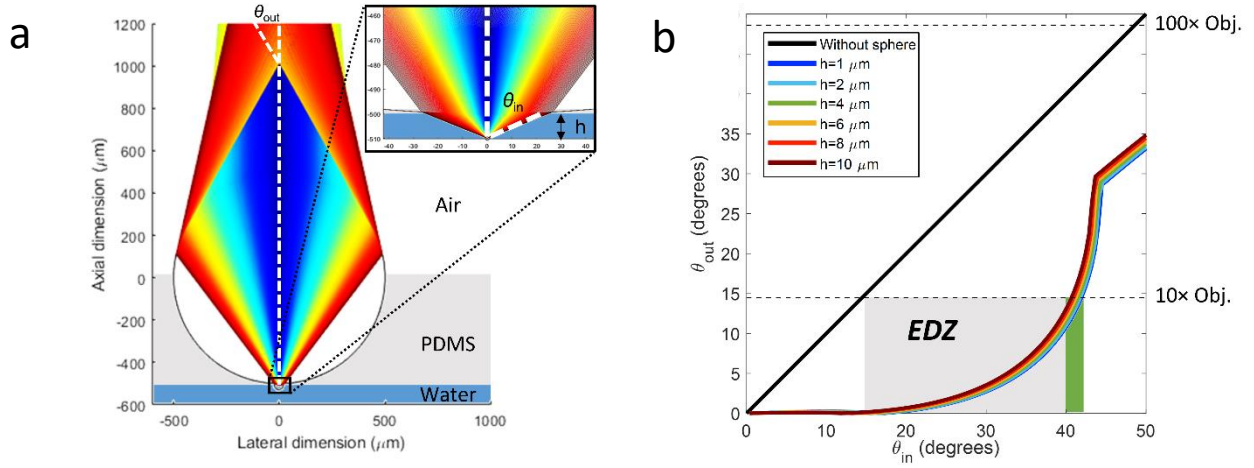


**Figure 6.1** - PMDSA model. (a) Light rays emerge from a point source in a microfluidic channel and propagate upwards through a 1 mm BaTiO<sub>3</sub> sphere partially embedded in PDMS up to the microscope objective (not shown). The sphere-sample distance is marked as  $h$ ;  $\theta_{in}$  denotes the angle of a ray entering the sphere, while  $\theta_{out}$  denotes the angle of the corresponding outgoing ray. The color gradient indicates different propagating rays. (b) Relation between  $\theta_{in}$  and  $\theta_{out}$  for the model shown in (a), for different  $h$  values. The dashed lines mark the acceptance angle for a low-magnification (10 $\times$ ) and a high-magnification (100 $\times$ ) objective, respectively. The grey-shaded area indicates the enhanced-detection zone (EDZ), where the dielectric sphere mediates the collection of light coming from higher angles  $\theta_{in}$  compared to the objective alone. The green-shaded area indicates the maximum angles that are collected by the resulting optical system, which corresponds to an effective objective with NA  $\approx$  0.66.

### 6.2.3 Data Analysis

Only the particles with an area larger than 20 pixels were considered to prevent a potential bias from small particle artefacts. The values of the integrated intensity in the presence of the sphere were divided by  $2\pi\sigma_c$  to correct for the Gaussian blur [191] introduced to ease the identification of the bacteria. All values were then normalized to the highest one for convenient comparison of different conditions. To compute the experimental contrast-to-background ratio (CBR) gain, we divided the respective values corresponding to the same exposure parameters.

### 6.2.4 Microfluidic chip design

We fabricated a PMDSA designed for analyzing bacteria (1 to 2  $\mu\text{m}$  size) in aqueous media (Fig. 6.2a). The device consists of parallel 1 mm wide and 6  $\mu\text{m}$  high channels comprising an array of equally spaced cylindrical pillars (Fig. 6.2b). This large and narrow channel keeps the hydraulic resistance low while confining the bacteria close to the imaging region of the sphere. The pillars (100  $\mu\text{m}$  in diameter) prevent the microchannel ceiling from collapsing (Fig. 6.2ci). The central region of the channel includes a large array of trapping structures for bacteria immobilization and long-term imaging (Fig. 6.2cii). Trapping units have a sieve-like design presenting a tapered opening narrowing from 1.2  $\mu\text{m}$  to 0.8  $\mu\text{m}$ , for tight trapping of *E. coli*. This type of confinement method allows immobilizing a small number of bacteria (down to a single bacterium) in each trapping unit. Once a trap is filled, the flow passing through the sieve stops, preventing additional bacteria from entering the trap [182]. Implementing a densely packed array of traps in the microchannel maximizes the number of detectable bacteria in the field of view of the dielectric sphere and also provides structural stability to the chip.



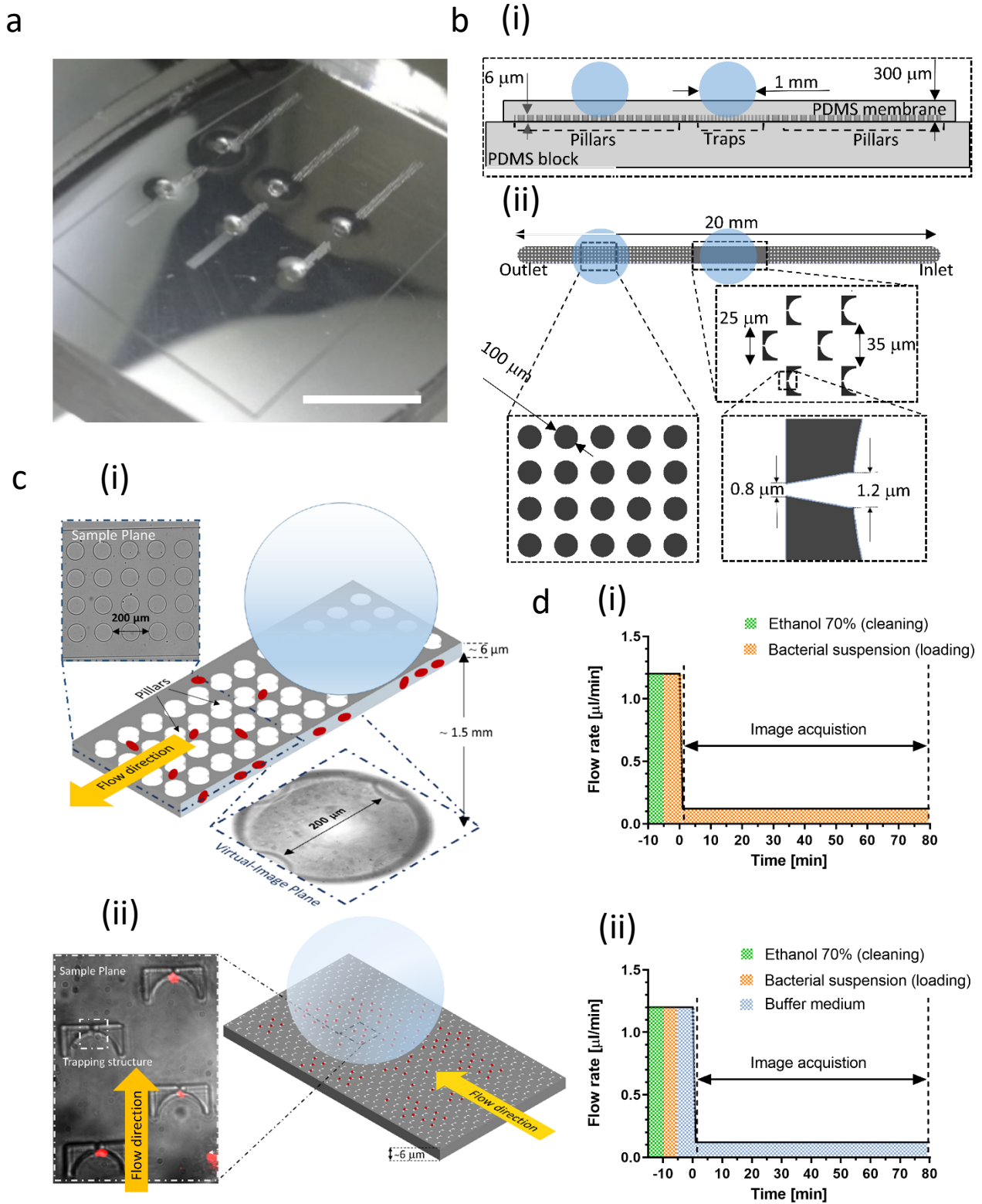


**Figure 6.2** - Structure and operation of the microfluidic PMDSA chip. (a) Picture of the microfluidic device bonded to a thick PDMS block to create 3 parallel channels for imaging of bacteria. Several beads are positioned on top. Scale bar 1 cm. (b) Cross section (i) and top view (ii) schematics of the microfluidic chip with partially embedded  $\text{BaTiO}_3$  spheres and on-chip bacterial traps. (c) Schematics of a microstructured PDMS channel with a partially embedded sphere, for bacterial imaging in a flow (i) or in hydrodynamic traps (ii). In order to avoid collapsing of the top membrane, PDMS pillars are embedded in the microchannel. Dash-dot outlines indicate zooms (bright field images) on the functional chip units. Red fluorescent signals from trapped bacteria are overlapped to the bright field images of the traps. (d) Microfluidic protocols used during imaging of fluorescent bacteria in a flow (i) and in traps (ii).

### 6.3 Optical performance of the PMDSA chip

#### 6.3.1 Contrast enhancement of a low-magnification system

PMDSA chips may be combined with simple optical detection systems thus can possibly be implemented in portable devices, *e.g.* for detecting pathogens in water basins in remote sites. To test the feasibility of this application, we injected red fluorescent bacteria ( $\sim 2000$  bacteria /  $\mu\text{L}$ ) in the chip and recorded image sequences using a low-magnification objective ( $10\times / 0.25$  NA). The fluidic protocol for this application was reported in Fig. 6.2di.

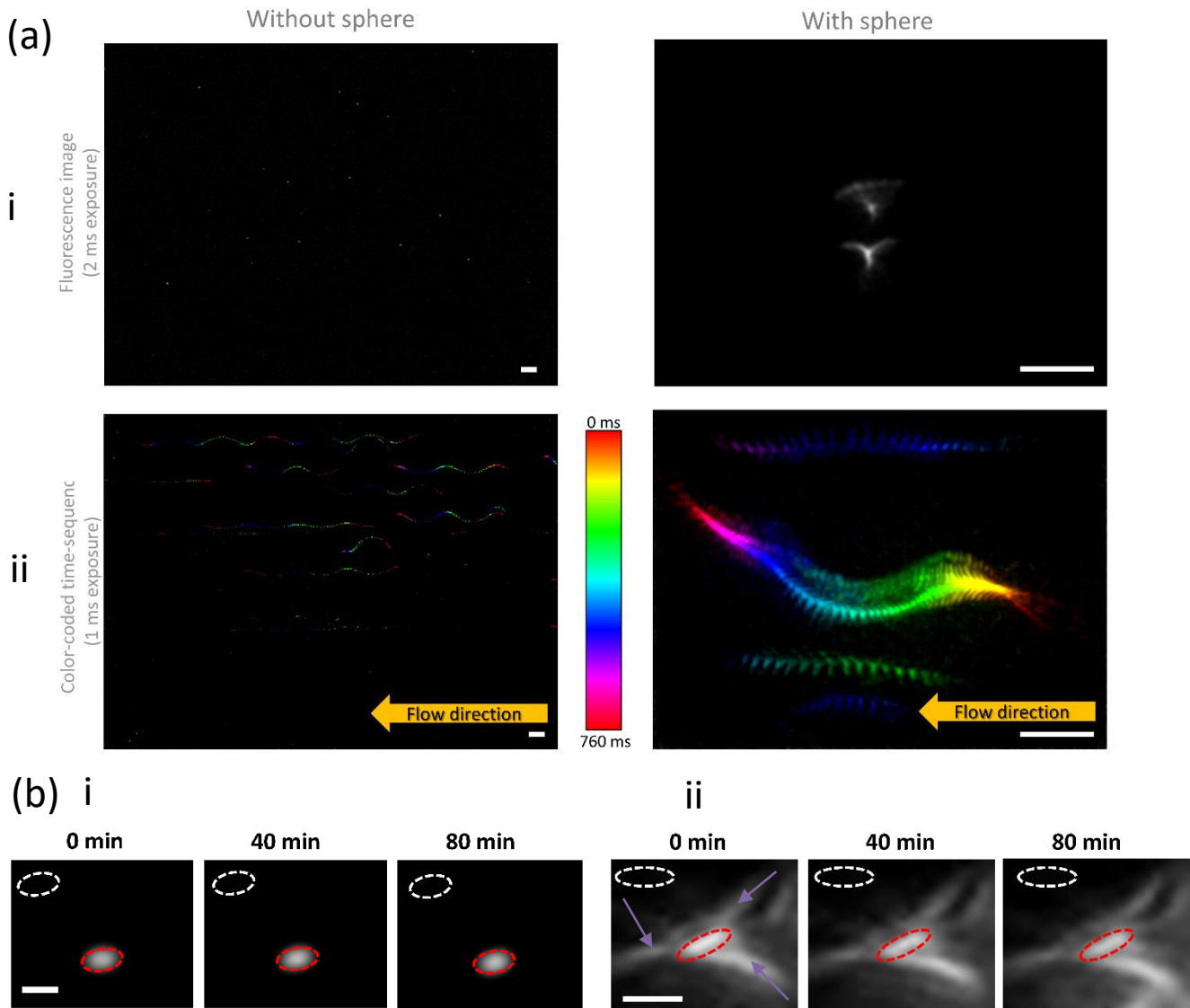


**Figure 6.3** - Imaging of fluorescent bacteria. (a) Fluorescence images (i) and color-coded time sequences (ii) of a flowing suspension of fluorescent bacteria imaged with a low-magnification objective ( $10\times/0.25\text{NA}$ ), either without or with a dielectric sphere. Scale bars  $10\ \mu\text{m}$ . (b) Time-lapse fluorescence of a single trapped bacterium imaged with a high-magnification objective ( $100\times/0.75\ \text{NA}$ ) (i) and with a low-magnification objective ( $10\times/0.25\ \text{NA}$ ) on a PMDSA chip (ii). Scale bars  $2\ \mu\text{m}$ . Red outline: region containing the least-aberrated fluorescent signal of the bacterium. White outline: region containing the reference background. Arrows indicate aberrations introduced by the partially embedded sphere.

To assess the potential for fast image recording, we performed an analysis for short exposure times (1 to 20 ms). Moreover, since we do not require high resolution for such imaging, we used  $2 \times 2$  binning to further decrease the acquisition time. After subtraction of the pixel-by-pixel median of the time series to each frame, we obtained background-free images (Fig. 6.3ai). The PMDSA introduces a  $\sim 5.5\times$  magnification but also some aberrations which distort the expected oval shape of bacteria. By color-coding the different time frames, the trajectories of the bacteria in the channel were obtained (Fig. 6.3aii).

The CBR was quantified as the ratio of the average signal over the average of the background, and finally normalized to its maximum experimental value. In Fig. 6.4a, we report the normalized CBR measured for several exposure times. As expected, in the range of short exposure times, CBR increases for both the conditions, *i.e.* with/without PMDSA (Fig. 6.4a, dark gray area). An additional data point for longer exposure time obtained for immobilized bacteria (as discussed in the next section) indicates a plateau effect for which even a one-order-of-magnitude increase in the exposure time did not result in an increase of the CBR (Fig. 6.4a, light gray area). The CBR gain for the low-magnification objective in the presence of the PMDSA was then calculated and compared to the theoretical gain predicted by the model (Fig. 6.4b).

### 6.3.2 Comparison with a high-magnification system

In order to compare the performance of the PMDSA coupled to a low-magnification objective ( $10\times / 0.25$  NA) and the performance of a high-magnification system ( $100\times / 0.75$  NA), we trapped fluorescent bacteria in a microfluidic channel and imaged them with both systems. For this purpose, we used an array of hydrodynamic traps designed to confine the bacterial cells during the image acquisition (shown in Fig. 6.2c). The imaged trapping section is positioned at the center of each microchannel underneath a dielectric sphere. The fluidic protocol used for the experiment was shown in Fig. 6.2dii. After a cleaning step, a suspension of fluorescent bacteria was injected into the channels. Afterwards, buffer medium was injected to retain only the stably trapped bacteria. Finally, we set a low constant injection flow rate at  $0.12\ \mu\text{L}/\text{min}$  in order to prevent confined bacteria from escaping the immobilization sites during long-term time-lapse imaging over 80 min (Fig. 6.3b). The fluorescence signal was quantified by measuring the average intensity inside the region of interest delimited by the elliptic shape of the bacterium. The background value was quantified as the average intensity inside a region with the same area as the one used for the bacterium, but located away from the trap. A comparison between the CBR measured for the PMDSA coupled with a low-magnification objective ( $10\times / 0.25$  NA) with respect to a high-magnification system ( $100\times / 0.75$  NA) is provided in Fig. 6.4c. Data points have been recorded for a bacteria immobilization time range up to 80 min. The CBR was stable over time for both systems, which shows that the PMDSA structure comprising a thin membrane with embedded spheres does not introduce mechanical instabilities, which could result in drift or oscillations of the focal plane. On the contrary, the CBR of the high-magnification objective remains 3.5 larger than the one obtained with the PMDSA. This observation is not surprising when considering the huge difference in terms of system optimization and corresponding cost. Table 6.1 summarizes the main features of the low- and high-magnification objectives used.

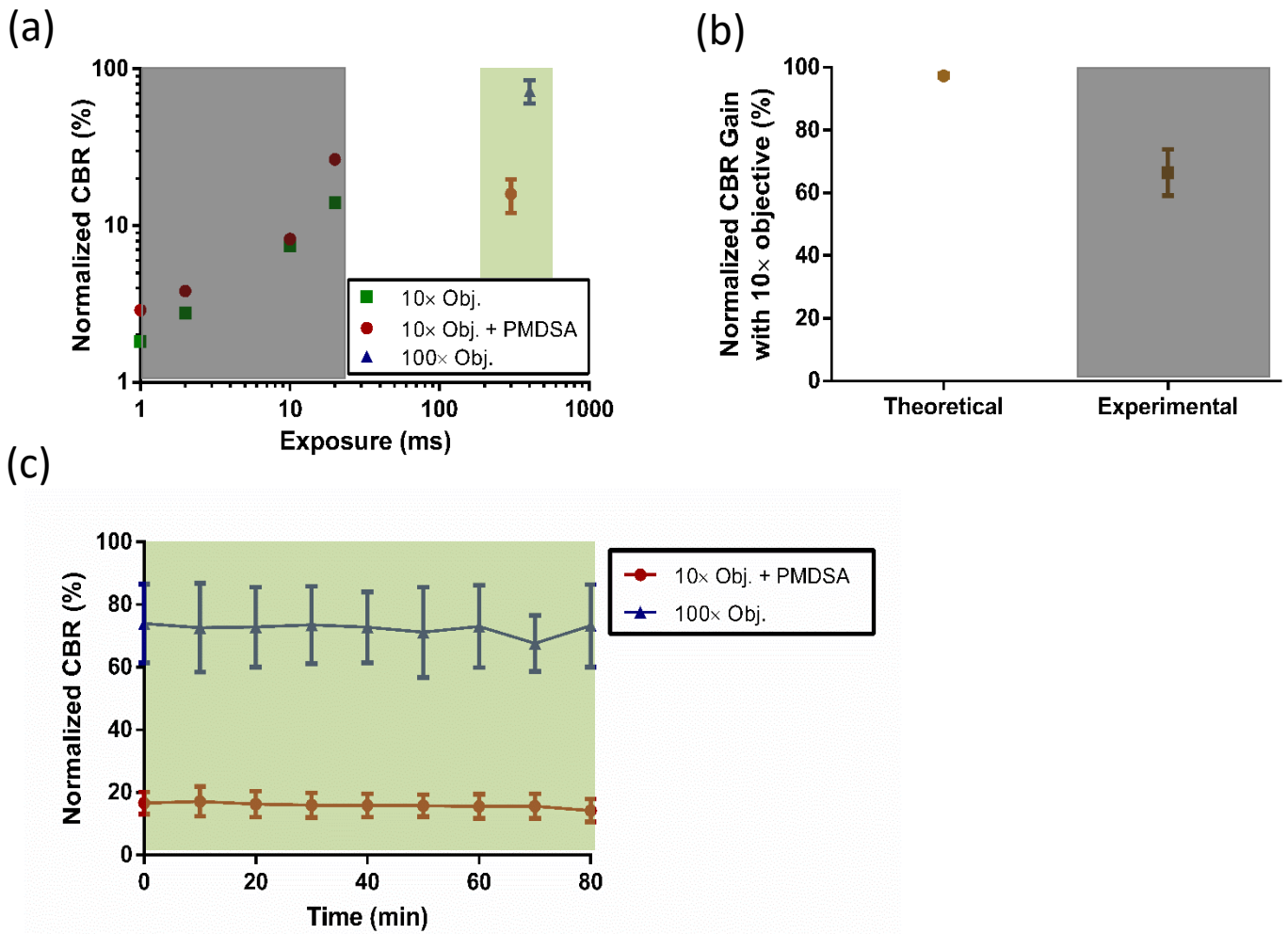


**Figure 6.4** - Quantitative assessment of the optical enhancement with the PMDSA chip. (a) Normalized contrast-to-background ratio (CBR) as a function of exposure time for several optical configurations. Data are plotted as mean  $\pm$  SEM,  $n \geq 3$ . The dark/light grey-shaded areas indicate the corresponding data plotted in (b) and (c). (b) Theoretical and experimental CBR gain for a PMDSA chip/low-magnification objective configuration at low exposure times. (c) Normalized CBR of trapped bacteria over time (PMDSA chip vs high-magnification objective). Data are plotted as mean  $\pm$  SEM,  $n = 3$ .

**Table 6.1** - Summary of the main features of the low- and high-magnification objectives used in this study.

Objective	Magnification	NA	Free working distance [mm]	Immersion	Field of view [mm]	Price [\$]
LD EC Epiplan-Neofluar 100x/0.75 DIC M27	100×	0.75	4	air	25	≈ 6300
EC Epiplan-Neofluar 10x/0.25 DIC M27	10×	0.25	9.3	air	25	≈ 2300

## 6.4 Discussion

We described a method to enhance the contrast in low-magnification optical detection based on highly refractive BaTiO<sub>3</sub> spheres partially embedded in polymeric membranes, which we integrated in microfluidic chip format for imaging of living fluorescent bacteria. The present simple fabrication procedure enables

creating custom designs for the chips and, at the same time, allows to precisely locate the spheres relative to the microfluidic structures. The ability of the PMDSA to enhance the detection of bacteria in a continuous flow with short exposure times (Fig. 6.4a, dark gray area) paves the way for applications where flow cytometry needs to be performed in remote sites, where bulky equipment should be suitably replaced by portable optical and microfluidic systems. Moreover, we demonstrated the opportunity to integrate specific functional microfluidic elements (*e.g.* trapping structures). Such customization can guarantee reliable long-term imaging capabilities (Fig. 6.4c) and thus potentially enable applications such as antibiotic testing directly on-site.

By comparing the experimental CBR results with the theoretical calculation for the PMDSA (Fig. 6.4b), we observe that the system has suboptimal performance ( $\sim 30\%$  lower than the expected theoretical gain). This loss may be due to several factors that can cause a perturbation in the light path from the sample to the objective, such as

- inhomogeneities in the sphere size and material
- aberrations introduced by the sphere (Fig. 6.3bii, arrows)
- reduced depth-of-field in presence of the sphere

The depth-of-field of the microsphere/PMDSA may be estimated as follows (emission wavelength  $\lambda_{em}$ )

$$\frac{\lambda_{em} \cdot n}{NA^2} \approx \frac{(584 \text{ nm} \cdot 1)}{0.66^2} = 1.3 \mu\text{m}$$

Compared to the conventional condition for a low-magnification objective

$$\frac{\lambda_{em} \cdot n}{NA^2} \approx \frac{(584 \text{ nm} \cdot 1)}{0.25^2} = 9.3 \mu\text{m}$$

The depth-of-field of the PMDSA appears to be comparable to the size of a bacterium and thus possibly not all light coming from the sample may be collected by the objective. Moreover, despite the focusing effect of the sphere which increases the contrast gain, excitation through the sphere may also be suboptimal because of sphere inhomogeneities and partial internal reflexion of excitation light at the bottom of the sphere.

Given the nature of the PMDSA proposed here, we expect spherical aberrations because of the presence of the BaTiO<sub>3</sub> sphere, and we cannot exclude other causes for aberrations. Astigmatism or coma for instance can be introduced by imperfections in the shape of the dielectric sphere. To obtain quantitative information about the aberrations introduced by the PMDSA, one may study the aberrated point-spread function in terms of its decomposition with the Zernike polynomials, which analytically describe the different types of aberrations [192]. This may be accomplished by imaging fluorescent nanoparticles, which can be safely approximated as point sources, in contrast to the bacteria in our study. All aberrations introduced by the PMDSA in the optical system degrade the image of the object, which can be certainly detected with higher confidence, but at the price of lowering resolution. Because of the overall increased contrast, this system is more adapted for optical signal detection rather than for complete imaging, which usually requires higher resolution.

Models are also used to analyze and correct distortion [193, 194], which can be especially needed when parts of the imaged object are far from the center of the sphere (total field of view of about  $0.03 \text{ mm}^2$ ). Once the aberrations are more quantitatively described, hardware and software solutions may be used to obtain higher resolution images. From a hardware point of view, the shape of the polymeric membrane could be optimized in order to compensate for some aberrations (flat in the imaging zone for simplicity of fabrication in our study). This method is often used in commercial objectives, where an assembly of several lenses provides much less aberrations than individual ones. From a software point of view, one can apply deconvolution algorithms to the aberrated images. Such methods could highly increase the net resolution of the PMDSA system.

The problem of reducing fabrication costs is well known in microfluidics, a domain which still enormously relies on highly expensive clean-room microfabrication techniques. Assuming that conventional photolithography techniques are used for Si wafer processing, the cost of fabrication of a single mold is of the order of 100 \$ (material + expenses on clean-room equipment only). On the other hand, a Si master can be used multiple times for casting a certain number of PMDSA chips, thus reducing the cost per chip. Other expenses are mainly related to PDMS processing (30 \$/h) and to material costs of PDMS and dielectric spheres (0.5 \$/PMDSA). However, other methods besides clean-room microfabrication are available to obtain reliable chips at low costs. Injection molding or hot embossing [195]), for instance, would be ideal for large-scale production of chips with the design discussed in our study. Given the low cost of the dielectric spheres (0.04 \$/sphere) and the continuously increasing implementation of mass fabrication methods for microfluidic chips, we believe that our proposed fabrication protocol is readily applicable and adaptable to a wide variety of microfluidic chips with integrated optical elements. After initial investment in the creation of a mold for shaping a thermoplastic material (which cost up to tens of k\$), the cost of a single chip may be lowered to 1 \$ or less, depending on the material used. Moreover, with a suitable mold, one may eventually improve the positioning of the dielectric spheres on the chip and decrease the time spent for this operation as well. Together with the potential cost reduction associated to the use of low-end imaging systems, the present approach has high potential for low-resource settings where on-site analytic protocols are most required.

# Chapter 7 Conclusions and outlook

## 7.1 Work and results presented in this thesis

*C. elegans* is a bacterivorous organism that emerged as an interesting and versatile model for studying host-microbiota interactions. *C. elegans* shows significant genetic homology and shares many molecular pathways with higher order animals, and in particular also with humans, enabling more comprehensive studies than with *in vitro* or cell- and tissue-based assays. The relative simplicity of the *C. elegans* nematodes represents a key feature for tackling complex biological processes involved in the worm's interplay with different bacterial species. In fact, the nematode presents a complete digestive apparatus. *C. elegans* intestine functions, which are often fulfilled by several specific organs in more complex organisms, include nutrient processing and absorption, enzymes secretion, defense against pathogens and immune response mechanisms. In addition, multiple phenotypical readouts for assessing of physiological responses, such as expression of specific genes, food consumption and bacterial presence in the intestine, are relatively easily quantifiable parameters in these worms. Microfluidic technology and microfluidic chips specifically designed for *C. elegans* studies substantially increased the overall accuracy of worm monitoring, long-term observation and phenotyping. Fig. 7.1 provides an overview of the three microfluidic platforms for *C. elegans* imaging developed in this thesis, focusing in particular on bacterial load dynamics and absorption kinetics in the worm intestine.

In Chapter 4 we proposed a new method for accurate monitoring of the bacterial intestinal load and transit dynamics in *C. elegans* worms. We made use of a microfluidic approach comprising automated worm handling and culturing protocols enabling observation of both free-swimming and immobilized worms. Our microfluidic platform featured arrays of tapered worm clamps allowing reversible immobilization and high-resolution time-lapse imaging at single-worm resolution (Fig. 7.1a). Two fluorescently marked *E. coli* bacterial strains (HT115 GFP and OP50 RFP) were employed as food source for *C. elegans* in order to characterize the food transit patterns in the worm intestine. On-chip worm culture over several days revealed diminishing gut transit efficiency in aging worms. The dynamics of the microbial load in the gut of free-swimming wild-type N2 worms was characterized by evaluating the frequency of food uptake. The average periodicity of the peristaltic process corresponds approximately to a time interval of 70 s between two intestine contractions. Our analytical technique was further validated by a comparison between the bacterial load patterns in N2 worms and the pharyngeal pumping-defective mutant *eat-2 (ad465)*. We observed accumulation of bacteria in the hindgut region of *eat-2* mutants. As additional validation of our method, we recorded the changes in bacterial transit patterns in YA *C. elegans* nematodes exposed to the neurotransmitter serotonin.



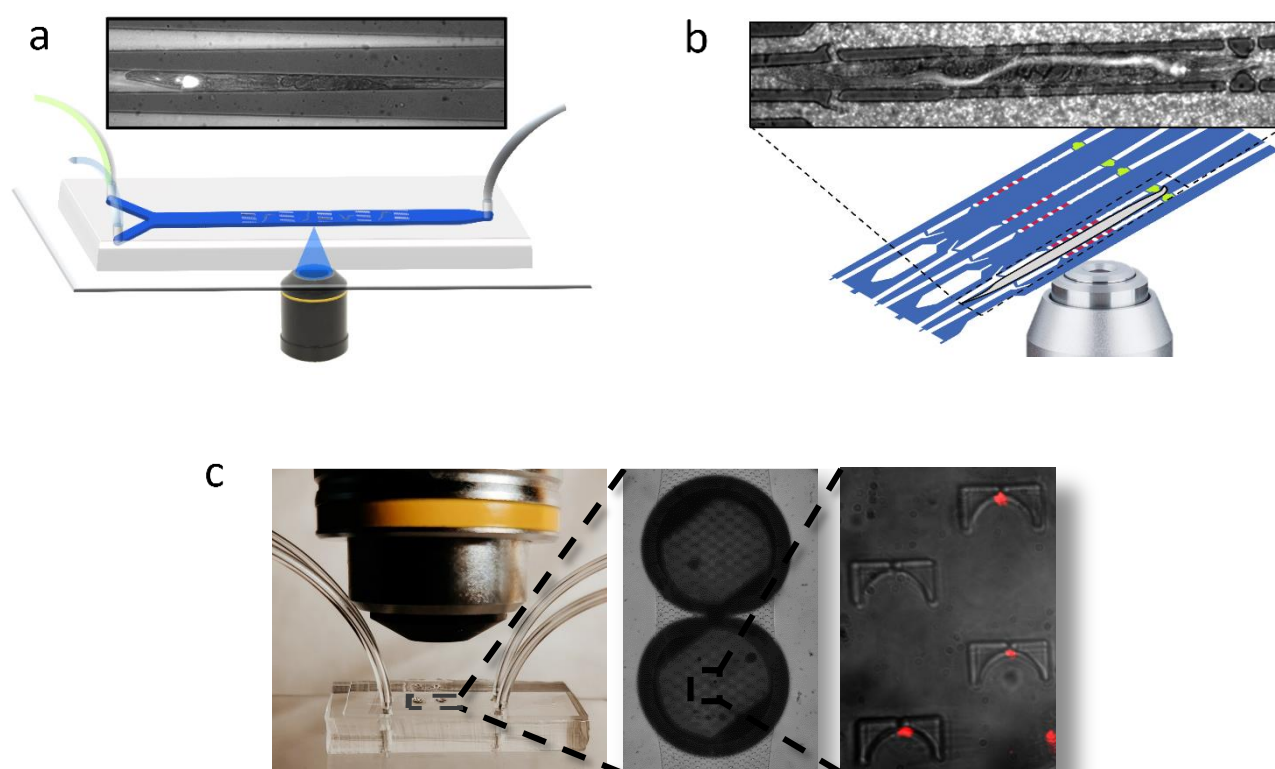


**Figure 7.1** - Microfluidic tools developed in the frame of this thesis for *C. elegans* and bacteria imaging. (a) Microfluidic platform for *in vivo* bacterial transit analysis in *C. elegans*. (b) Microfluidic platform for *in vivo* bacterial load dynamics and food absorption measurements in the *C. elegans* intestine. (c) Microfluidic chip for imaging of fluorescent bacteria with enhanced contrast.

In Chapter 5 we proposed a versatile method for the analysis of the intestinal processing of bacterial food in *C. elegans* nematodes. The microfluidic platform was designed for ergonomic worm confinement over extended periods (Fig. 7.1b). Imaging and tracking of the bacterial load dynamics in the entire worm gut and local high-resolution observations in specific sections were performed, in particular in the pharynx and the hindgut. In order to determine reliable assay protocol conditions, the time evolution of fluorescence patterns were measured in worms fed with *E. coli* bacteria marked either with pH-insensitive (RFP) or pH-sensitive (GFP) reporters, respectively. Ingestion of mixed suspensions of bacteria and indigestible microbeads enabled monitoring dynamic features related to the peristaltic activity of the worm gut. Our imaging protocol allowed discriminating between intact *E. coli* bacteria and diffuse fluorescent signals due to bacterial food disrupted by the grinding process in the pharynx. By recording the decay of the diffuse signal intensity, we could estimate the time constant for enzymatic digestion in N2 YA *C. elegans*, which was of the order of 14 s. As a further validation of our protocols, and in view of possible applications for infection assays, we investigated the bacterial load in the worm intestine in the presence of pathogenic *M. marinum* bacteria and measured the expression of mitochondrial stress response in *C. elegans hsp-6::gfp* mutants. In Chapter 6 we presented a microfluidic-based method for detection of fluorescent bacteria. We combined dielectric millimeter-sized BaTiO<sub>3</sub> microspheres with a micropatterned PDMS membrane and integrated the microfluidic chip into a low-magnification optical microscope (Fig. 7.1c). This polymeric membrane/dielectric microsphere assembly (PMDSA) enabled resolution and contrast gain in a cost-effective optical system. The platform was used for imaging fluorescently marked *E. coli* bacteria. Two modes of op-



eration were assessed, *i.e.* imaging of fluorescent bacteria in solution flow or imaging of immobilized bacteria. For the in-flow application a simple microchannel was used, for the second type of assay dielectric spheres were placed on top of custom-design bacterial PDMS microtraps incorporated in the microchannel. Bacterial imaging contrast obtained by the PDMSA with a low-magnification (10×/0.25 NA) objective was characterized for multiple exposure conditions. Furthermore, we compared the performance of our optical low-magnification/PDMSA system and a high-magnification objective (100×/0.75 NA) by imaging immobilized fluorescently labeled *E. coli* bacteria.

## 7.2 The future of *C. elegans* – microbial assays

In the last years *C. elegans* has been increasingly considered as a valid and versatile alternative model organism with respect to other more complex animal species. In this view, optimized automated systems for worm culture and imaging are needed to foster the impact of *C. elegans* as an accessible and practical tool for fundamental biological studies, biomedical research, eventually for drug screening campaigns in pharmaceutical companies. For instance, recent studies showed promising results relative to the utilization of *C. elegans* in antimicrobial drug screening processes and assessment of drug toxicity [196]. *C. elegans* could be applied in particular in the initial stage of the drug discovery pipeline, thus reducing the amount of expensive and cumbersome tests based on rodents. Reduced costs, high throughput, more accessible generation of large data sets and no ethical limitations are some significant advantages brought by drug screening on *C. elegans*. However, for the time being, mammalian models are still preferred to nematodes in all phases of testing new drug compounds. Mammalian and human cell-derived microtissues are also appearing as a new interesting alternative to the use of animals, as their biology makes them very relevant to understanding drug action in humans. On the other hand, *C. elegans* currently gains increasing popularity as model for research studies on the host-microbiota interconnection. In this respect, microfluidic platforms play a preponderant role, enabling a high degree of system integration with convenient on-chip assay parallelization and multiplexing for a wide range of applications.

In future work related to our platforms, additional features and improved protocol designs can be implemented for more advanced assays. For instance, considering the microfluidic device described in Chapter 4, implementation of pulse chase fluidic protocols would greatly broaden the range of possible experiments achievable by the presented chip. Exposing worms to pulsed chemical stimuli affecting worm's feeding patterns, by following a customizable protocol depending on the type of experimentation, would represent a powerful and accurate tool of analysis of the *C. elegans* response. However, the initial version of the chip presented in the present work was not optimized for fast fluidic exchange, as we intended, as a first approach, to demonstrate the feasibility of monitoring reliably the bacterial load and intestinal transition in immobilized worms. Another potential improvement of the bacterial load analysis consists in the quantification of the amount of viable and dead bacteria in the worm gut after ingestion. This is not feasible with our actual protocol, since it is not possible to assess bacterial viability in the *C. elegans* intestine solely by fluorescence measurements. Possibly, other staining methods or alternative techniques for bacteria labeling have to be implemented to perform this type of analysis on-chip. The platform presented in Chapter 5 was validated with respect to phenotypical analysis and high-resolution imaging of *C. elegans* intestinal colonization. The present method could be further optimized for more exhaustive biological assays, for instance by investigating the correlation between the worm microbiota and worm lifespan. Behavioral studies on *C. elegans* relative to food preference or avoidance can possibly be performed on our chip, by feeding immobilized worms with different bacterial species/strains and monitoring the pharyngeal activity.

Alternatively, by increasing the number of parallel channels on the platform, an effective tool for high-throughput antimicrobial drug screening could be designed. The PDMSA system for bacterial imaging, described in Chapter 6, was based on a simple fabrication procedure enabling the creation of custom designed chips and precise positioning of dielectric spheres relatively to the microfluidic structures. Such features improve the versatility and cost efficiency of the method, thus opening a wide range of applications, comprising flow cytometry or multiplexed testing of antibiotics.

In the frame of this thesis, we presented on-chip techniques for culturing and imaging worms with single-organism resolution that were optimized for *in vivo* studies of bacteria in the worms' intestine. We presented a novel method for the quantification of dynamic features of bacterial presence in the worm gut, allowing spatial and temporal high-resolution imaging. We believe that our approaches provide significant added value for advanced bacteria-based *C. elegans* assays focusing on time-lapse imaging of specific microbia-gut interactions. We envision that the proposed methods for assessing the novel *C. elegans* 'bacterial load dynamics' phenotype will also open the way to a more comprehensive understanding of microbial digestion or infection, nutrient absorption kinetics and other metabolic processes. Moreover, such features may be used for investigating the virulence of different pathogenic strains in the *C. elegans* model organism or for the evaluation of antimicrobial drug efficiency *in vivo*. In conclusion, considering the rapidly increasing number of *C. elegans*-microbia related studies presented in the last years, we think that new effective assays protocols and tools will be needed in near future and that microfluidics approaches, such as developed and discussed in the frame of this thesis, represent a valuable resource for elucidating the *C. elegans* and bacteria interplay. Eventually, the development of advanced commercial platforms, enabling simultaneously high-throughput and high-content analysis, may be envisioned.

# References

- [1] S. Brenner: "The Genetics of *Caenorhabditis Elegans*." *Genetics*. vol. 77, no. 1, pp. 71–94, 1974.
- [2] S. Ogg, S. Paradis, S. Gottlieb, G.I. Patterson, L. Lee, H.A. Tissenbaum, and G. Ruvkun: "The Fork head transcription factor DAF-16 transduces insulin-like metabolic and longevity signals in *C. elegans*." *Nature*. vol. 389, no. 6654, pp. 994–999, 1997.
- [3] N. Perrimon: "Signalling pathways initiated by receptor protein tyrosine kinases in *Drosophila*." *Current Opinion in Cell Biology*. vol. 6, no. 2, pp. 260–266, 1994.
- [4] K.T. Jones and K. Ashrafi: "*Caenorhabditis elegans* as an emerging model for studying the basic biology of obesity." *Disease Models & Mechanisms*. vol. 2, no. 5–6, pp. 224–229, 2009.
- [5] T.C. *elegans* S. Consortium\*: "Genome Sequence of the Nematode *C. elegans*: A Platform for Investigating Biology." *Science*. vol. 282, no. 5396, pp. 2012–2018, 1998.
- [6] T. Kaletta and M.O. Hengartner: "Finding function in novel targets: *C. elegans* as a model organism." *Nat Rev Drug Discov*. vol. 5, no. 5, pp. 387–398, 2006.
- [7] E. Culetto and D.B. Sattelle: "A role for *Caenorhabditis elegans* in understanding the function and interactions of human disease genes." *Hum Mol Genet*. vol. 9, no. 6, pp. 869–877, 2000.
- [8] J. Li and W. Le: "Modeling neurodegenerative diseases in *Caenorhabditis elegans*." *Exp Neurol*. vol. 250, pp. 94–103, 2013.
- [9] H.C. Hrach, S. O'Brien, H.S. Steber, J. Newbern, A. Rawls, and M. Mangone: "Transcriptome changes during the initiation and progression of Duchenne muscular dystrophy in *Caenorhabditis elegans*." *Human Molecular Genetics*. vol. 29, no. 10, pp. 1607–1623, 2020.
- [10] A. Schlotterer, G. Kukudov, F. Bozorgmehr, H. Hutter, X. Du, D. Oikonomou, Y. Ibrahim, F. Pfisterer, N. Rabbani, P. Thornalley, A. Sayed, T. Fleming, P. Humpert, V. Schwenger, M. Zeier, A. Hamann, D. Stern, M. Brownlee, A. Bierhaus, P. Nawroth, and M. Morcos: "*C. elegans* as Model for the Study of High Glucose– Mediated Life Span Reduction." *Diabetes*. vol. 58, no. 11, pp. 2450–2456, 2009.
- [11] C.I. Petersen, T.R. McFarland, S.Z. Stepanovic, P. Yang, D.J. Reiner, K. Hayashi, A.L. George, D.M. Roden, J.H. Thomas, and J.R. Balser: "In vivo identification of genes that modify ether-a-go-go-related gene activity in *Caenorhabditis elegans* may also affect human cardiac arrhythmia." *PNAS*. vol. 101, no. 32, pp. 11773–11778, 2004.
- [12] A. Ray, B.A. Martinez, L.A. Berkowitz, G.A. Caldwell, and K.A. Caldwell: "Mitochondrial dysfunction, oxidative stress, and neurodegeneration elicited by a bacterial metabolite in a *C. elegans* Parkinson's model." *Cell Death & Disease*. vol. 5, no. 1, pp. e984–e984, 2014.
- [13] L.P. O'Reilly, C.J. Luke, D.H. Perlmutter, G.A. Silverman, and S.C. Pak: "*C. elegans* in high-throughput drug discovery." *Advanced Drug Delivery Reviews*. vol. 69–70, pp. 247–253, 2014.
- [14] M. Markaki and N. Tavernarakis: "Modeling human diseases in *Caenorhabditis elegans*." *Biotechnology Journal*. vol. 5, no. 12, pp. 1261–1276, 2010.

- 
- [15] M. Shapira: "Host–microbiota interactions in *Caenorhabditis elegans* and their significance." *Current Opinion in Microbiology*. vol. 38, pp. 142–147, 2017.
- [16] G.L. Simon and S.L. Gorbach: "Intestinal flora in health and disease." *Gastroenterology*. vol. 86, no. 1, pp. 174–193, 1984.
- [17] I. Chiu and A. Rolls: "Editorial overview: Brain, gut and immune system interactions." *Current Opinion in Neurobiology*. vol. 62, pp. iii–v, 2020.
- [18] T. Stiernagle: "Maintenance of *C. elegans*." *WormBook*. 2006.
- [19] Z.F. Altun and D.H. Hall: "Introduction to *C. elegans* anatomy." In *WormAtlas*. 2009.
- [20] N. Fielenbach and A. Antebi: "*C. elegans* dauer formation and the molecular basis of plasticity." *Genes & development*. vol. 22, no. 16, pp. 2149–2165, 2008.
- [21] J.L. Anderson, L.T. Morran, and P.C. Phillips: "Outcrossing and the maintenance of males within *C. elegans* populations." *Journal of heredity*. vol. 101, no. suppl\_1, pp. S62–S74, 2010.
- [22] J.E. Sulston, E. Schierenberg, J.G. White, and J.N. Thomson: "The embryonic cell lineage of the nematode *Caenorhabditis elegans*." *Developmental biology*. vol. 100, no. 1, pp. 64–119, 1983.
- [23] A.J. Bretscher, E. Kodama-Namba, K.E. Busch, R.J. Murphy, Z. Soltesz, P. Laurent, and M. de Bono: "Temperature, oxygen, and salt-sensing neurons in *C. elegans* are carbon dioxide sensors that control avoidance behavior." *Neuron*. vol. 69, no. 6, pp. 1099–1113, 2011.
- [24] B.S. Samuel, H. Rowedder, C. Braendle, M.-A. Félix, and G. Ruvkun: "*Caenorhabditis elegans* responses to bacteria from its natural habitats." *Proceedings of the National Academy of Sciences*. vol. 113, no. 27, pp. E3941–E3949, 2016.
- [25] K. Houthoofd, B.P. Braeckman, I. Lenaerts, K. Brys, A. De Vreese, S. Van Eygen, and J.R. Vanfleteren: "Axenic growth up-regulates mass-specific metabolic rate, stress resistance, and extends life span in *Caenorhabditis elegans*." *Experimental gerontology*. vol. 37, no. 12, pp. 1371–1378, 2002.
- [26] L. Timmons and A. Fire: "Specific interference by ingested dsRNA." *Nature*. vol. 395, no. 6705, pp. 854–854, 1998.
- [27] I. Gusarov, L. Gautier, O. Smolentseva, I. Shamovsky, S. Eremina, A. Mironov, and E. Nudler: "Bacterial nitric oxide extends the lifespan of *C. elegans*." *Cell*. vol. 152, no. 4, pp. 818–830, 2013.
- [28] S. Kumar, B.M. Egan, Z. Kocsisova, D.L. Schneider, J.T. Murphy, A. Diwan, and K. Kornfeld: "Lifespan extension in *C. elegans* caused by bacterial colonization of the intestine and subsequent activation of an innate immune response." *Developmental cell*. vol. 49, no. 1, pp. 100–117. e6, 2019.
- [29] D. Gems and D.L. Riddle: "Genetic, behavioral and environmental determinants of male longevity in *Caenorhabditis elegans*." *Genetics*. vol. 154, no. 4, pp. 1597–1610, 2000.
- [30] D. Garigan, A.-L. Hsu, A.G. Fraser, R.S. Kamath, J. Ahringer, and C. Kenyon: "Genetic analysis of tissue aging in *Caenorhabditis elegans*: a role for heat-shock factor and bacterial proliferation." *Genetics*. vol. 161, no. 3, pp. 1101–1112, 2002.

- [31] R. Pukkila-Worley, A.Y. Peleg, E. Tampakakis, and E. Mylonakis: "Candida albicans hyphal formation and virulence assessed using a Caenorhabditis elegans infection model." *Eukaryotic cell*. vol. 8, no. 11, pp. 1750–1758, 2009.
- [32] S. Mahajan-Miklos, M.-W. Tan, L.G. Rahme, and F.M. Ausubel: "Molecular mechanisms of bacterial virulence elucidated using a Pseudomonas aeruginosa–Caenorhabditis elegans pathogenesis model." *Cell*. vol. 96, no. 1, pp. 47–56, 1999.
- [33] C. Poupet, C. Chassard, A. Nivoliez, and S. Bornes: "Caenorhabditis elegans, a Host to Investigate the Probiotic Properties of Beneficial Microorganisms." *Frontiers in nutrition*. vol. 7, 2020.
- [34] M.W. Pellegrino, A.M. Nargund, N.V. Kirienko, R. Gillis, C.J. Fiorese, and C.M. Haynes: "Mitochondrial UPR-regulated innate immunity provides resistance to pathogen infection." *Nature*. vol. 516, no. 7531, pp. 414–417, 2014.
- [35] C. Darby: "Interactions with microbial pathogens." *WormBook: The Online Review of C. elegans Biology [Internet]*. 2005.
- [36] G.M. Whitesides: "The origins and the future of microfluidics." *nature*. vol. 442, no. 7101, pp. 368–373, 2006.
- [37] N.A. Bakhtina and J.G. Korvink: "Microfluidic laboratories for C. elegans enhance fundamental studies in biology." *Rsc Advances*. vol. 4, no. 9, pp. 4691–4709, 2014.
- [38] M. Cornaglia, T. Lehnert, and M.A. Gijs: "Microfluidic systems for high-throughput and high-content screening using the nematode Caenorhabditis elegans." *Lab on a Chip*. vol. 17, no. 22, pp. 3736–3759, 2017.
- [39] K.N. Le, M. Zhan, Y. Cho, J. Wan, D.S. Patel, and H. Lu: "An automated platform to monitor long-term behavior and healthspan in Caenorhabditis elegans under precise environmental control." *Communications biology*. vol. 3, no. 1, pp. 1–13, 2020.
- [40] M. Cornaglia, L. Mouchiroud, A. Marette, S. Narasimhan, T. Lehnert, V. Jovaisaite, J. Auwerx, and M.A.M. Gijs: "An automated microfluidic platform for C. elegans embryo arraying, phenotyping, and long-term live imaging." *Scientific Reports*. vol. 5, no. 1, pp. 10192, 2015.
- [41] H. Baris Atakan, T. Alkanat, M. Cornaglia, R. Trouillon, and M.A.M. Gijs: "Automated phenotyping of Caenorhabditis elegans embryos with a high-throughput-screening microfluidic platform." *Microsystems & Nanoengineering*. vol. 6, no. 1, pp. 1–14, 2020.
- [42] P. Rezai, A. Siddiqui, P. Ravi Selvaganapathy, and B. P. Gupta: "Electrotaxis of Caenorhabditis elegans in a microfluidic environment." *Lab on a Chip*. vol. 10, no. 2, pp. 220–226, 2010.
- [43] I. de C. Cáceres, N. Valmas, M.A. Hilliard, and H. Lu: "Laterally Orienting C. elegans Using Geometry at Microscale for High-Throughput Visual Screens in Neurodegeneration and Neuronal Development Studies." *PLOS ONE*. vol. 7, no. 4, pp. e35037, 2012.
- [44] G. Aubry, M. Zhan, and H. Lu: "Hydrogel-droplet microfluidic platform for high-resolution imaging and sorting of early larval Caenorhabditis elegans." *Lab on a Chip*. vol. 15, no. 6, pp. 1424–1431, 2015.
- [45] A. San-Miguel and H. Lu: "Microfluidics as a tool for C. elegans research." *WormBook: The Online Review of C. elegans Biology [Internet]*. 2018.

- [46] I. Dimov and M.F. Maduro: "The *C. elegans* intestine: organogenesis, digestion, and physiology." *Cell and tissue research*. pp. 1–14, 2019.
- [47] J. Kimble and W.J. Sharrock: "Tissue-specific synthesis of yolk proteins in *Caenorhabditis elegans*." *Developmental biology*. vol. 96, no. 1, pp. 189–196, 1983.
- [48] H. Schulenburg, C. Léopold Kurz, and J.J. Ewbank: "Evolution of the innate immune system: the worm perspective." *Immunological reviews*. vol. 198, no. 1, pp. 36–58, 2004.
- [49] F. Pauli, Y. Liu, Y.A. Kim, P.-J. Chen, and S.K. Kim: "Chromosomal clustering and GATA transcriptional regulation of intestine-expressed genes in *C. elegans*." *Development*. vol. 133, no. 2, pp. 287–295, 2006.
- [50] J.D. McGhee: "The *C. elegans* intestine (March 27, 2007), WormBook ed." *WormBook. The C. elegans Research Community*. 2007.
- [51] D. Raizen, B. Song, N. Trojanowski, and Y.-J. You: "Methods for measuring pharyngeal behaviors." *WormBook: The Online Review of C. elegans Biology [Internet]*. 2018.
- [52] Z.F. Altun and D.H. Hall: "Alimentary system, intestine." *Herndon LA, editor*. 2009.
- [53] D.E.K. Tarr: "Distribution and characteristics of ABFs, cecropins, nemapores, and lysozymes in nematodes." *Developmental & Comparative Immunology*. vol. 36, no. 3, pp. 502–520, 2012.
- [54] V.M. Chauhan, G. Orsi, A. Brown, D.I. Pritchard, and J.W. Aylott: "Mapping the pharyngeal and intestinal pH of *Caenorhabditis elegans* and real-time luminal pH oscillations using extended dynamic range pH-sensitive nanosensors." *ACS nano*. vol. 7, no. 6, pp. 5577–5587, 2013.
- [55] A. Bender, Z.R. Woydziak, L. Fu, M. Branden, Z. Zhou, B.D. Ackley, and B.R. Peterson: "Novel acid-activated fluorophores reveal a dynamic wave of protons in the intestine of *Caenorhabditis elegans*." *ACS chemical biology*. vol. 8, no. 3, pp. 636–642, 2013.
- [56] L.R. Lapierre, S. Gelino, A. Meléndez, and M. Hansen: "Autophagy and lipid metabolism coordinately modulate life span in germline-less *C. elegans*." *Current Biology*. vol. 21, no. 18, pp. 1507–1514, 2011.
- [57] G.A. Lemieux and K. Ashrafi: "Insights and challenges in using *C. elegans* for investigation of fat metabolism." *Critical reviews in biochemistry and molecular biology*. vol. 50, no. 1, pp. 69–84, 2015.
- [58] D. Palgunow, M. Klapper, and F. Döring: "Dietary restriction during development enlarges intestinal and hypodermal lipid droplets in *Caenorhabditis elegans*." *PLoS one*. vol. 7, no. 11, pp. e46198, 2012.
- [59] N.A. Bishop and L. Guarente: "Two neurons mediate diet-restriction-induced longevity in *C. elegans*." *Nature*. vol. 447, no. 7144, pp. 545–549, 2007.
- [60] S. Gelino, J.T. Chang, C. Kumsta, X. She, A. Davis, C. Nguyen, S. Panowski, and M. Hansen: "Intestinal autophagy improves healthspan and longevity in *C. elegans* during dietary restriction." *PLoS genetics*. vol. 12, no. 7, pp. e1006135, 2016.
- [61] K.K. Brooks, B. Liang, and J.L. Watts: "The influence of bacterial diet on fat storage in *C. elegans*." *PLoS one*. vol. 4, no. 10, pp. e7545, 2009.

- [62] M. Scholz, D.J. Lynch, K.S. Lee, E. Levine, and D. Biron: "A scalable method for automatically measuring pharyngeal pumping in *C. elegans*." *Journal of neuroscience methods*. vol. 274, pp. 172–178, 2016.
- [63] R.L. Gomez-Amaro, E.R. Valentine, M. Carretero, S.E. LeBoeuf, S. Rangaraju, C.D. Broaddus, G.M. Solis, J.R. Williamson, and M. Petrascheck: "Measuring food intake and nutrient absorption in *Caenorhabditis elegans*." *Genetics*. vol. 200, no. 2, pp. 443–454, 2015.
- [64] S.S. Ding, M. Romenskyy, K.S. Sarkisyan, and A.E. Brown: "Measuring *Caenorhabditis elegans* spatial foraging and food intake using bioluminescent bacteria." *Genetics*. vol. 214, no. 3, pp. 577–587, 2020.
- [65] M.-W. Tan, S. Mahajan-Miklos, and F.M. Ausubel: "Killing of *Caenorhabditis elegans* by *Pseudomonas aeruginosa* used to model mammalian bacterial pathogenesis." *Proceedings of the National Academy of Sciences*. vol. 96, no. 2, pp. 715–720, 1999.
- [66] C. Portal-Celhay and M.J. Blaser: "Competition and resilience between founder and introduced bacteria in the *Caenorhabditis elegans* gut." *Infection and immunity*. vol. 80, no. 3, pp. 1288–1299, 2012.
- [67] C. Portal-Celhay, E.R. Bradley, and M.J. Blaser: "Control of intestinal bacterial proliferation in regulation of lifespan in *Caenorhabditis elegans*." *BMC microbiology*. vol. 12, no. 1, pp. 1–17, 2012.
- [68] S. Kwon, E.J.E. Kim, and S.-J.V. Lee: "Mitochondria-mediated defense mechanisms against pathogens in *Caenorhabditis elegans*." *BMB reports*. vol. 51, no. 6, pp. 274, 2018.
- [69] G.V. Mallo, C.L. Kurz, C. Couillault, N. Pujol, S. Granjeaud, Y. Kohara, and J.J. Ewbank: "Inducible anti-bacterial defense system in *C. elegans*." *Current Biology*. vol. 12, no. 14, pp. 1209–1214, 2002.
- [70] M.C. Letizia, M. Cornaglia, G. Tranchida, R. Trouillon, and M.A.M. Gijs: "A design of experiment approach for efficient multi-parametric drug testing using a *Caenorhabditis elegans* model." *Integrative Biology*. vol. 10, no. 1, pp. 48–56, 2018.
- [71] K. Chung, M. Zhan, J. Srinivasan, P.W. Sternberg, E. Gong, F.C. Schroeder, and H. Lu: "Microfluidic chamber arrays for whole-organism behavior-based chemical screening." *Lab on a Chip*. vol. 11, no. 21, pp. 3689–3697, 2011.
- [72] M.A. Unger, H.-P. Chou, T. Thorsen, A. Scherer, and S.R. Quake: "Monolithic microfabricated valves and pumps by multilayer soft lithography." *Science*. vol. 288, no. 5463, pp. 113–116, 2000.
- [73] S.E. Hulme, S.S. Shevkoplyas, J. Apfeld, W. Fontana, and G.M. Whitesides: "A microfabricated array of clamps for immobilizing and imaging *C. elegans*." *Lab on a Chip*. vol. 7, no. 11, pp. 1515–1523, 2007.
- [74] T.V. Chokshi, A. Ben-Yakar, and N. Chronis: "CO<sub>2</sub> and compressive immobilization of *C. elegans* on-chip." *Lab on a Chip*. vol. 9, no. 1, pp. 151–157, 2009.
- [75] J. Krajniak and H. Lu: "Long-term high-resolution imaging and culture of *C. elegans* in chip-gel hybrid microfluidic device for developmental studies." *Lab on a Chip*. vol. 10, no. 14, pp. 1862–1868, 2010.
- [76] M. Cornaglia, G. Krishnamani, L. Mouchiroud, V. Sorrentino, T. Lehnert, J. Auwerx, and M.A. Gijs: "Automated longitudinal monitoring of in vivo protein aggregation in neurodegenerative disease *C. elegans* models." *Molecular neurodegeneration*. vol. 11, no. 1, pp. 1–13, 2016.

- [77] L. Dong, M. Cornaglia, G. Krishnamani, J. Zhang, L. Mouchiroud, T. Lehnert, J. Auwerx, and M.A. Gijs: "Reversible and long-term immobilization in a hydrogel-microbead matrix for high-resolution imaging of *Caenorhabditis elegans* and other small organisms." *PloS one*. vol. 13, no. 3, pp. e0193989, 2018.
- [78] K. Chung, M.M. Crane, and H. Lu: "Automated on-chip rapid microscopy, phenotyping and sorting of *C. elegans*." *Nature methods*. vol. 5, no. 7, pp. 637, 2008.
- [79] C.L. Gilleland, C.B. Rohde, F. Zeng, and M.F. Yanik: "Microfluidic immobilization of physiologically active *Caenorhabditis elegans*." *Nature protocols*. vol. 5, no. 12, pp. 1888–1902, 2010.
- [80] H.B. Atakan, M. Cornaglia, L. Mouchiroud, J. Auwerx, and M.A. Gijs: "Automated high-content phenotyping from the first larval stage till the onset of adulthood of the nematode *Caenorhabditis elegans*." *Lab on a Chip*. vol. 19, no. 1, pp. 120–135, 2019.
- [81] R.B. Kopito and E. Levine: "Durable spatiotemporal surveillance of *Caenorhabditis elegans* response to environmental cues." *Lab on a Chip*. vol. 14, no. 4, pp. 764–770, 2014.
- [82] J. Yang, Z. Chen, P. Ching, Q. Shi, and X. Li: "An integrated microfluidic platform for evaluating in vivo antimicrobial activity of natural compounds using a whole-animal infection model." *Lab on a Chip*. vol. 13, no. 17, pp. 3373–3382, 2013.
- [83] K.S. Lee and E. Levine: "A microfluidic platform for longitudinal imaging in *Caenorhabditis elegans*." *Journal of visualized experiments: JoVE*. no. 135, 2018.
- [84] L. Hu, A. Ge, X. Wang, S. Wang, X. Yue, J. Wang, X. Feng, W. Du, and B.-F. Liu: "Real-time monitoring of immune responses under pathogen invasion and drug interference by integrated microfluidic device coupled with worm-based biosensor." *Biosensors and Bioelectronics*. vol. 110, pp. 233–238, 2018.
- [85] J. Yang, M. Zheng, F. Yang, X. Zhang, W. Yin, X. Liu, G.-J. Zhang, and Z. Chen: "Pseudomonas aeruginosa infected nematode-on-a-chip model array for antibacterials screening." *Sensors and Actuators B: Chemical*. vol. 275, pp. 373–381, 2018.
- [86] K.S. Lee, L.E. Lee, and E. Levine: "HandKAchip-Hands-free killing assay on a chip." *Scientific reports*. vol. 6, no. 1, pp. 1–9, 2016.
- [87] S.E. Hulme and G.M. Whitesides: "Chemistry and the worm: *Caenorhabditis elegans* as a platform for integrating chemical and biological research." *Angewandte Chemie International Edition*. vol. 50, no. 21, pp. 4774–4807, 2011.
- [88] M.B. Gerstein, Z.J. Lu, E.L. Van Nostrand, C. Cheng, B.I. Arshinoff, T. Liu, K.Y. Yip, R. Robilotto, A. Rechtsteiner, and K. Ikegami: "Integrative analysis of the *Caenorhabditis elegans* genome by the modENCODE project." *Science*. vol. 330, no. 6012, pp. 1775–1787, 2010.
- [89] D.D. Shaye and I. Greenwald: "OrthoList: a compendium of *C. elegans* genes with human orthologs." *PloS one*. vol. 6, no. 5, pp. e20085, 2011.
- [90] P. Bercik, S.M. Collins, and E.F. Verdu: "Microbes and the gut-brain axis." *Neurogastroenterology & Motility*. vol. 24, no. 5, pp. 405–413, 2012.
- [91] P.A. Smith: "The tantalizing links between gut microbes and the brain." *Nature News*. vol. 526, no. 7573, pp. 312, 2015.



- [92] Y. Wang and L.H. Kasper: "The role of microbiome in central nervous system disorders." *Brain, behavior, and immunity*. vol. 38, pp. 1–12, 2014.
- [93] M.-W. Tan and M. Shapira: "Genetic and molecular analysis of nematode–microbe interactions." *Cellular microbiology*. vol. 13, no. 4, pp. 497–507, 2011.
- [94] F. Zhang, M. Berg, K. Dierking, M.-A. Félix, M. Shapira, B.S. Samuel, and H. Schulenburg: "Caenorhabditis elegans as a model for microbiome research." *Frontiers in Microbiology*. vol. 8, pp. 485, 2017.
- [95] F. Cabreiro and D. Gems: "Worms need microbes too: microbiota, health and aging in Caenorhabditis elegans. EMBO Mol Med 5: 1300–1310." , 2013.
- [96] M. Shapira: "Gut microbiotas and host evolution: scaling up symbiosis." *Trends in ecology & evolution*. vol. 31, no. 7, pp. 539–549, 2016.
- [97] A. Merckx-Jacques, A. Coors, R. Brousseau, L. Masson, A. Mazza, Y.-C. Tien, and E. Topp: "Evaluating the pathogenic potential of environmental Escherichia coli by using the Caenorhabditis elegans infection model." *Applied and environmental microbiology*. vol. 79, no. 7, pp. 2435–2445, 2013.
- [98] B.B. Shtonda and L. Avery: "Dietary choice behavior in Caenorhabditis elegans." *Journal of experimental biology*. vol. 209, no. 1, pp. 89–102, 2006.
- [99] D.H. Kim: "Bacteria and the aging and longevity of Caenorhabditis elegans." 2013.
- [100] G. Kwon, J. Lee, and Y.H. Lim: "Dairy Propionibacterium extends the mean lifespan of Caenorhabditis elegans via activation of the innate immune system. Sci Rep 6: 31713." , 2016.
- [101] L.C. Clark and J. Hodgkin: "Caenorhabditis microbiota: worm guts get populated." *BMC biology*. vol. 14, no. 1, pp. 1–3, 2016.
- [102] S. Pang and S.P. Curran: "Adaptive capacity to bacterial diet modulates aging in C. elegans." *Cell metabolism*. vol. 19, no. 2, pp. 221–231, 2014.
- [103] S. Srinivasan, L. Sadegh, I.C. Elle, A.G. Christensen, N.J. Faergeman, and K. Ashrafi: "Serotonin regulates C. elegans fat and feeding through independent molecular mechanisms." *Cell metabolism*. vol. 7, no. 6, pp. 533–544, 2008.
- [104] M. Petrascheck, X. Ye, and L.B. Buck: "An antidepressant that extends lifespan in adult Caenorhabditis elegans." *Nature*. vol. 450, no. 7169, pp. 553–556, 2007.
- [105] J. McGhee and S. Ghafouri: "Bacterial residence time in the intestine of Caenorhabditis elegans." *Nematology*. vol. 9, no. 1, pp. 87–91, 2007.
- [106] Y. Zhao, A.F. Gilliat, M. Ziehm, M. Turmaine, H. Wang, M. Ezcurra, C. Yang, G. Phillips, D. McBay, and W.B. Zhang: "Two forms of death in ageing Caenorhabditis elegans." *Nature communications*. vol. 8, no. 1, pp. 1–8, 2017.
- [107] T.I. Moy, A.L. Conery, J. Larkins-Ford, G. Wu, R. Mazitschek, G. Casadei, K. Lewis, A.E. Carpenter, and F.M. Ausubel: "High-throughput screen for novel antimicrobials using a whole animal infection model." *ACS chemical biology*. vol. 4, no. 7, pp. 527–533, 2009.

- [108] M.J. Rodríguez-Palero, A. López-Díaz, R. Marsac, J.-E. Gomes, M. Olmedo, and M. Artal-Sanz: "An automated method for the analysis of food intake behaviour in *Caenorhabditis elegans*." *Scientific reports*. vol. 8, no. 1, pp. 1–10, 2018.
- [109] F. Kamili and H. Lu: "Recent advances and trends in microfluidic platforms for *C. elegans* biological assays." *Annual Review of Analytical Chemistry*. vol. 11, pp. 245–264, 2018.
- [110] S. Mondal, E. Hegarty, C. Martin, S.K. Gökce, N. Ghorashian, and A. Ben-Yakar: "Large-scale microfluidics providing high-resolution and high-throughput screening of *Caenorhabditis elegans* poly-glutamine aggregation model." *Nature communications*. vol. 7, no. 1, pp. 1–11, 2016.
- [111] S.K. Gokce, S.X. Guo, N. Ghorashian, W.N. Everett, T. Jarrell, A. Kottek, A.C. Bovik, and A. Ben-Yakar: "A fully automated microfluidic femtosecond laser axotomy platform for nerve regeneration studies in *C. elegans*." *PloS one*. vol. 9, no. 12, pp. e113917, 2014.
- [112] H. Hwang, D.E. Barnes, Y. Matsunaga, G.M. Benian, S. Ono, and H. Lu: "Muscle contraction phenotypic analysis enabled by optogenetics reveals functional relationships of sarcomere components in *Caenorhabditis elegans*." *Scientific reports*. vol. 6, no. 1, pp. 1–10, 2016.
- [113] L. Dong, M. Cornaglia, T. Lehnert, and M.A. Gijs: "Versatile size-dependent sorting of *C. elegans* nematodes and embryos using a tunable microfluidic filter structure." *Lab on a Chip*. vol. 16, no. 3, pp. 574–585, 2016.
- [114] H. Wen, W. Shi, and J. Qin: "Multiparameter evaluation of the longevity in *C. elegans* under stress using an integrated microfluidic device." *Biomedical microdevices*. vol. 14, no. 4, pp. 721–728, 2012.
- [115] W. Keil, L.M. Kutscher, S. Shaham, and E.D. Siggia: "Long-term high-resolution imaging of developing *C. elegans* larvae with microfluidics." *Developmental cell*. vol. 40, no. 2, pp. 202–214, 2017.
- [116] J.C. Weeks, K.J. Robinson, S.R. Lockery, and W.M. Roberts: "Anthelmintic drug actions in resistant and susceptible *C. elegans* revealed by electrophysiological recordings in a multichannel microfluidic device." *International Journal for Parasitology: Drugs and Drug Resistance*. vol. 8, no. 3, pp. 607–628, 2018.
- [117] A. Ge, L. Hu, X. Wang, J. Zhu, X. Feng, W. Du, and B.-F. Liu: "Logarithmic bacterial gradient chip for analyzing the effects of dietary restriction on *C. elegans* growth." *Sensors and Actuators B: Chemical*. vol. 255, pp. 735–744, 2018.
- [118] B. Song and L. Avery: "The pharynx of the nematode *C. elegans*: a model system for the study of motor control." *Worm*. pp. 1920–31. *Taylor & Francis* (2013).
- [119] C.S. Kwan, R.P. Vázquez-Manrique, S. Ly, K. Goyal, and H.A. Baylis: "TRPM channels are required for rhythmicity in the ultradian defecation rhythm of *C. elegans*." *BMC physiology*. vol. 8, no. 1, pp. 1–11, 2008.
- [120] M.V. Espelt, A.Y. Estevez, X. Yin, and K. Strange: "Oscillatory  $\text{Ca}^{2+}$  signaling in the isolated *Caenorhabditis elegans* intestine: role of the inositol-1, 4, 5-trisphosphate receptor and phospholipases C  $\beta$  and  $\gamma$ ." *The Journal of general physiology*. vol. 126, no. 4, pp. 379–392, 2005.
- [121] T. Teramoto and K. Iwasaki: "Intestinal calcium waves coordinate a behavioral motor program in *C.*

- elegans.” *Cell calcium*. vol. 40, no. 3, pp. 319–327, 2006.
- [122] L. Partridge, M.D. Piper, and W. Mair: “Dietary restriction in *Drosophila*.” *Mechanisms of ageing and development*. vol. 126, no. 9, pp. 938–950, 2005.
- [123] E.L. Greer and A. Brunet: “Different dietary restriction regimens extend lifespan by both independent and overlapping genetic pathways in *C. elegans*.” *Aging cell*. vol. 8, no. 2, pp. 113–127, 2009.
- [124] J.P. McKay, D.M. Raizen, A. Gottschalk, W.R. Schafer, and L. Avery: “eat-2 and eat-18 are required for nicotinic neurotransmission in the *Caenorhabditis elegans* pharynx.” *Genetics*. vol. 166, no. 1, pp. 161–169, 2004.
- [125] D.M. Raizen, R.Y. Lee, and L. Avery: “Interacting genes required for pharyngeal excitation by motor neuron MC in *Caenorhabditis elegans*.” *Genetics*. vol. 141, no. 4, pp. 1365–1382, 1995.
- [126] B. Lakowski and S. Hekimi: “The genetics of caloric restriction in *Caenorhabditis elegans*.” *Proceedings of the National Academy of Sciences*. vol. 95, no. 22, pp. 13091–13096, 1998.
- [127] J.-Y. Hsiao, C.-Y. Chen, M.-J. Yang, and H.-C. Ho: “Live and dead GFP-tagged bacteria showed indistinguishable fluorescence in *Caenorhabditis elegans* gut.” *Journal of microbiology*. vol. 51, no. 3, pp. 367–372, 2013.
- [128] D.L. Chase and M.R. Koelle: “Biogenic amine neurotransmitters in *C. elegans*.” *WormBook: The Online Review of C. elegans Biology [Internet]*. 2007.
- [129] H.R. Horvitz, M. Chalfie, C. Trent, J.E. Sulston, and P.D. Evans: “Serotonin and octopamine in the nematode *Caenorhabditis elegans*.” *Science*. vol. 216, no. 4549, pp. 1012–1014, 1982.
- [130] L. Segalat, D.A. Elkes, and J.M. Kaplan: “Modulation of serotonin-controlled behaviors by Go in *Caenorhabditis elegans*.” *Science*. vol. 267, no. 5204, pp. 1648–1651, 1995.
- [131] N.D. Peterson and R. Pukkila-Worley: “*Caenorhabditis elegans* in high-throughput screens for anti-infective compounds.” *Current opinion in immunology*. vol. 54, pp. 59–65, 2018.
- [132] C. Fang-Yen, L. Avery, and A.D. Samuel: “Two size-selective mechanisms specifically trap bacteria-sized food particles in *Caenorhabditis elegans*.” *Proceedings of the National Academy of Sciences*. vol. 106, no. 47, pp. 20093–20096, 2009.
- [133] G.J. Sarkis, M.R. Kurpiewski, J.D. Ashcom, L. Jen-Jacobson, and L.A. Jacobson: “Proteases of the nematode *Caenorhabditis elegans*.” *Archives of biochemistry and biophysics*. vol. 261, no. 1, pp. 80–90, 1988.
- [134] C.T. Beh, D.C. Ferrari, M.A. Chung, and J.D. McGhee: “An acid phosphatase as a biochemical marker for intestinal development in the nematode *Caenorhabditis elegans*.” *Developmental biology*. vol. 147, no. 1, pp. 133–143, 1991.
- [135] E. Allman, D. Johnson, and K. Nehrke: “Loss of the apical V-ATPase  $\alpha$ -subunit VHA-6 prevents acidification of the intestinal lumen during a rhythmic behavior in *C. elegans*.” *American Journal of Physiology-Cell Physiology*. vol. 297, no. 5, pp. C1071–C1081, 2009.
- [136] J. Zhang, A.D. Holdorf, and A.J. Walhout: “*C. elegans* and its bacterial diet as a model for systems-level

- understanding of host–microbiota interactions.” *Current opinion in biotechnology*. vol. 46, pp. 74–80, 2017.
- [137] N.L. Stuhr and S.P. Curran: “Bacterial diets differentially alter lifespan and healthspan trajectories in *C. elegans*.” *Communications biology*. vol. 3, no. 1, pp. 1–18, 2020.
- [138] E.K. Marsh and R.C. May: “*Caenorhabditis elegans*, a model organism for investigating immunity.” *Applied and environmental microbiology*. vol. 78, no. 7, pp. 2075–2081, 2012.
- [139] C.D. Sifri, J. Begun, and F.M. Ausubel: “The worm has turned—microbial virulence modeled in *Caenorhabditis elegans*.” *Trends in microbiology*. vol. 13, no. 3, pp. 119–127, 2005.
- [140] A. Aballay and F.M. Ausubel: “*Caenorhabditis elegans* as a host for the study of host–pathogen interactions.” *Current opinion in microbiology*. vol. 5, no. 1, pp. 97–101, 2002.
- [141] R. Zhang and A. Hou: “Host-microbe interactions in *Caenorhabditis elegans*.” *International Scholarly Research Notices*. vol. 2013, 2013.
- [142] J. Hodgkin, P.E. Kuwabara, and B. Corneliussen: “A novel bacterial pathogen, *Microbacterium nematophilum*, induces morphological change in the nematode *C. elegans*.” *Current Biology*. vol. 10, no. 24, pp. 1615–1618, 2000.
- [143] M.J. Gravato-Nobre, H.R. Nicholas, R. Nijland, D. O’Rourke, D.E. Whittington, K.J. Yook, and J. Hodgkin: “Multiple genes affect sensitivity of *Caenorhabditis elegans* to the bacterial pathogen *Microbacterium nematophilum*.” *Genetics*. vol. 171, no. 3, pp. 1033–1045, 2005.
- [144] V. Donato, F.R. Ayala, S. Cogliati, C. Bauman, J.G. Costa, C. Lenini, and R. Grau: “*Bacillus subtilis* biofilm extends *Caenorhabditis elegans* longevity through downregulation of the insulin-like signalling pathway.” *Nature communications*. vol. 8, no. 1, pp. 1–15, 2017.
- [145] Y. Liu, B.S. Samuel, P.C. Breen, and G. Ruvkun: “*Caenorhabditis elegans* pathways that surveil and defend mitochondria.” *Nature*. vol. 508, no. 7496, pp. 406–410, 2014.
- [146] J.A. Melo and G. Ruvkun: “Inactivation of conserved *C. elegans* genes engages pathogen-and xenobiotic-associated defenses.” *Cell*. vol. 149, no. 2, pp. 452–466, 2012.
- [147] E.D. Runkel, S. Liu, R. Baumeister, and E. Schulze: “Surveillance-activated defenses block the ROS-induced mitochondrial unfolded protein response.” *PLoS Genet*. vol. 9, no. 3, pp. e1003346, 2013.
- [148] S.A. Broadley and F.U. Hartl: “Mitochondrial stress signaling: a pathway unfolds.” *Trends in cell biology*. vol. 18, no. 1, pp. 1–4, 2008.
- [149] H. Lee, S.A. Kim, S. Coakley, P. Mugno, M. Hammarlund, M.A. Hilliard, and H. Lu: “A multi-channel device for high-density target-selective stimulation and long-term monitoring of cells and subcellular features in *C. elegans*.” *Lab on a Chip*. vol. 14, no. 23, pp. 4513–4522, 2014.
- [150] S.E. Hulme, S.S. Shevkoplyas, A.P. McGuigan, J. Apfeld, W. Fontana, and G.M. Whitesides: “Lifespan-on-a-chip: microfluidic chambers for performing lifelong observation of *C. elegans*.” *Lab on a Chip*. vol. 10, no. 5, pp. 589–597, 2010.
- [151] S. Berger, E. Lattmann, T. Aegerter-Wilmsen, M. Hengartner, A. Hajnal, A. deMello, and X.C. i Solvas:

- “Long-term *C. elegans* immobilization enables high resolution developmental studies in vivo.” *Lab on a Chip*. vol. 18, no. 9, pp. 1359–1368, 2018.
- [152] L. Avery and J.H. Thomas: “Feeding and defecation.” *C. elegans II*. 1997.
- [153] A. Cambré and A. Aertsen: “Bacterial Vivisection: How Fluorescence-Based Imaging Techniques Shed a Light on the Inner Workings of Bacteria.” *Microbiology and Molecular Biology Reviews*. vol. 84, no. 4, 2020.
- [154] V. Viri, M. Cornaglia, H.B. Atakan, T. Lehnert, and M.A. Gijs: “An in vivo microfluidic study of bacterial transit in *C. elegans* nematodes.” *Lab on a Chip*. vol. 20, no. 15, pp. 2696–2708, 2020.
- [155] S.M. Akram and S. Aboobacker: “Mycobacterium Marinum.” StatPearls. *StatPearls Publishing*, Treasure Island (FL) (2021).
- [156] K. Takaki, J.M. Davis, K. Winglee, and L. Ramakrishnan: “Evaluation of the pathogenesis and treatment of Mycobacterium marinum infection in zebrafish.” *Nature protocols*. vol. 8, no. 6, pp. 1114, 2013.
- [157] M.G. Johnson and J.E. Stout: “Twenty-eight cases of Mycobacterium marinum infection: retrospective case series and literature review.” *Infection*. vol. 43, no. 6, pp. 655–662, 2015.
- [158] T. Galbadage, T.F. Shepherd, S.L. Cirillo, T.L. Gumieny, and J.D. Cirillo: “The Caenorhabditis elegans p38 MAPK Gene plays a key role in protection from mycobacteria.” *Microbiologyopen*. vol. 5, no. 3, pp. 436–452, 2016.
- [159] Z. Pincus, T.C. Mazer, and F.J. Slack: “Autofluorescence as a measure of senescence in *C. elegans*: look to red, not blue or green.” *Aging (Albany NY)*. vol. 8, no. 5, pp. 889, 2016.
- [160] S. Sofela, S. Sahloul, C. Stubbs, A. Orozaliev, F.S. Refai, A.M. Esmaeel, H. Fahs, M.O. Abdelgawad, K.C. Gunsalus, and Y.-A. Song: “Phenotyping of the thrashing forces exerted by partially immobilized *C. elegans* using elastomeric micropillar arrays.” *Lab on a Chip*. vol. 19, no. 21, pp. 3685–3696, 2019.
- [161] K. Zhang, S. Qin, S. Wu, Y. Liang, and J. Li: “Microfluidic systems for rapid antibiotic susceptibility tests (ASTs) at the single-cell level.” *Chemical Science*. vol. 11, no. 25, pp. 6352–6361, 2020.
- [162] A. Darafsheh, G.F. Walsh, L. Dal Negro, and V.N. Astratov: “Optical super-resolution by high-index liquid-immersed microspheres.” *Applied Physics Letters*. vol. 101, no. 14, pp. 141128, 2012.
- [163] S. Lee, L. Li, Z. Wang, W. Guo, Y. Yan, and T. Wang: “Immersed transparent microsphere magnifying sub-diffraction-limited objects.” *Applied optics*. vol. 52, no. 30, pp. 7265–7270, 2013.
- [164] D. Migliozi, M.A. Gijs, and G. Huszka: “Microsphere-mediated optical contrast tuning for designing imaging systems with adjustable resolution gain.” *Scientific reports*. vol. 8, no. 1, pp. 1–9, 2018.
- [165] A. Darafsheh, C. Guardiola, A. Palovcak, J.C. Finlay, and A. Cárabe: “Optical super-resolution imaging by high-index microspheres embedded in elastomers.” *Optics Letters*. vol. 40, no. 1, pp. 5–8, 2015.
- [166] B. Yan, Z. Wang, A.L. Parker, Y. Lai, P.J. Thomas, L. Yue, and J.N. Monks: “Superlensing microscope objective lens.” *Applied optics*. vol. 56, no. 11, pp. 3142–3147, 2017.
- [167] M. Duocastella, F. Tantussi, A. Haddadpour, R.P. Zaccaria, A. Jacassi, G. Veronis, A. Diaspro, and F. De

- Angelis: "Combination of scanning probe technology with photonic nanojets." *Scientific reports*. vol. 7, no. 1, pp. 1–7, 2017.
- [168] H. Yang, N. Moullan, J. Auwerx, and M.A. Gijs: "Super-resolution biological microscopy using virtual imaging by a microsphere nanoscope." *Small*. vol. 10, no. 9, pp. 1712–1718, 2014.
- [169] F. Wang, L. Liu, H. Yu, Y. Wen, P. Yu, Z. Liu, Y. Wang, and W.J. Li: "Scanning superlens microscopy for non-invasive large field-of-view visible light nanoscale imaging." *Nature communications*. vol. 7, no. 1, pp. 1–10, 2016.
- [170] J. Li, W. Liu, T. Li, I. Rozen, J. Zhao, B. Bahari, B. Kante, and J. Wang: "Swimming microrobot optical nanoscopy." *Nano Letters*. vol. 16, no. 10, pp. 6604–6609, 2016.
- [171] L. Li, W. Guo, Y. Yan, S. Lee, and T. Wang: "Label-free super-resolution imaging of adenoviruses by submerged microsphere optical nanoscopy." *Light: Science & Applications*. vol. 2, no. 9, pp. e104–e104, 2013.
- [172] J.J. Schwartz, S. Stavrakis, and S.R. Quake: "Colloidal lenses allow high-temperature single-molecule imaging and improve fluorophore photostability." *Nature nanotechnology*. vol. 5, no. 2, pp. 127–132, 2010.
- [173] H. Yang, M. Cornaglia, and M.A. Gijs: "Photonic nanojet array for fast detection of single nanoparticles in a flow." *Nano letters*. vol. 15, no. 3, pp. 1730–1735, 2015.
- [174] P. Ghenuche, J. de Torres, P. Ferrand, and J. Wenger: "Multi-focus parallel detection of fluorescent molecules at picomolar concentration with photonic nanojets arrays." *Applied Physics Letters*. vol. 105, no. 13, pp. 131102, 2014.
- [175] H. Aouani, N. Djaker, J. Wenger, and H. Rigneault: "High-efficiency single molecule fluorescence detection and correlation spectroscopy with dielectric microspheres." *Single Molecule Spectroscopy and Imaging III*. pp. 75710A. *International Society for Optics and Photonics* (2010).
- [176] G. Huszka, H. Yang, and M.A. Gijs: "Microsphere-based super-resolution scanning optical microscope." *Optics express*. vol. 25, no. 13, pp. 15079–15092, 2017.
- [177] G. Huszka and M.A. Gijs: "Turning a normal microscope into a super-resolution instrument using a scanning microlens array." *Scientific reports*. vol. 8, no. 1, pp. 1–8, 2018.
- [178] K.W. Allen, N. Farahi, Y. Li, N.I. Limberopoulos, D.E. Walker Jr, A.M. Urbas, V. Liberman, and V.N. Astratov: "Super-resolution microscopy by movable thin-films with embedded microspheres: resolution analysis." *Annalen der Physik*. vol. 527, no. 7–8, pp. 513–522, 2015.
- [179] Y. Hennequin, C.P. Allier, E. McLeod, O. Mudanyali, D. Migliozi, A. Ozcan, and J.-M. Dinten: "Optical detection and sizing of single nanoparticles using continuous wetting films." *ACS nano*. vol. 7, no. 9, pp. 7601–7609, 2013.
- [180] G. Huang, W. Tian, M. Qi, X. Gong, and G. Zhang: "Improving axial resolution for holographic tracking of colloids and bacteria over a wide depth of field by optimizing different factors." *Optics express*. vol. 26, no. 8, pp. 9920–9930, 2018.
- [181] D. Di Carlo, L.Y. Wu, and L.P. Lee: "Dynamic single cell culture array." *Lab on a Chip*. vol. 6, no. 11, pp.

1445–1449, 2006.

- [182] M.-C. Kim, B.C. Isenberg, J. Sutin, A. Meller, J.Y. Wong, and C.M. Klapperich: “Programmed trapping of individual bacteria using micrometre-size sieves.” *Lab on a Chip*. vol. 11, no. 6, pp. 1089–1095, 2011.
- [183] S.M. Azmayesh-Fard, E. Flaim, and J.N. McMullin: “PDMS biochips with integrated waveguides.” *Journal of Micromechanics and Microengineering*. vol. 20, no. 8, pp. 087002, 2010.
- [184] H. Yang and M.A. Gijs: “Micro-optics for microfluidic analytical applications.” *Chemical Society Reviews*. vol. 47, no. 4, pp. 1391–1458, 2018.
- [185] M. Schelb, C. Vannahme, A. Welle, S. Lenhert, B. Ross, and T. Mappes: “Fluorescence excitation on monolithically integrated all-polymer chips.” *Journal of biomedical optics*. vol. 15, no. 4, pp. 041517, 2010.
- [186] S. Camou, H. Fujita, and T. Fujii: “PDMS 2D optical lens integrated with microfluidic channels: principle and characterization.” *Lab on a Chip*. vol. 3, no. 1, pp. 40–45, 2003.
- [187] C. Song, N.-T. Nguyen, A.K. Asundi, and C.L.-N. Low: “Biconcave micro-optofluidic lens with low-refractive-index liquids.” *Optics letters*. vol. 34, no. 23, pp. 3622–3624, 2009.
- [188] J. Godin, V. Lien, and Y.-H. Lo: “Demonstration of two-dimensional fluidic lens for integration into microfluidic flow cytometers.” *Applied Physics Letters*. vol. 89, no. 6, pp. 061106, 2006.
- [189] Y.-C. Tung, M. Zhang, C.-T. Lin, K. Kurabayashi, and S.J. Skerlos: “PDMS-based opto-fluidic micro flow cytometer with two-color, multi-angle fluorescence detection capability using PIN photodiodes.” *Sensors and actuators B: Chemical*. vol. 98, no. 2–3, pp. 356–367, 2004.
- [190] Q. Tseng: “Template matching and slice alignment–imagej plugins.” , 2015.
- [191] E.S. Gedraite and M. Hadad: “Investigation on the effect of a Gaussian Blur in image filtering and segmentation.” *Proceedings ELMAR-2011*. pp. 393–396. *IEEE* (2011).
- [192] V.N. Mahajan and J.A. Díaz: “Imaging characteristics of Zernike and annular polynomial aberrations.” *Applied optics*. vol. 52, no. 10, pp. 2062–2074, 2013.
- [193] D.C. Brown: “Decentering distortion of lenses.” *Photogrammetric Engineering and Remote Sensing*. 1966.
- [194] J.E. Greivenkamp: “Field guide to geometrical optics.” *SPIE press Bellingham, WA* , 2004.
- [195] V. Faustino, S.O. Catarino, R. Lima, and G. Minas: “Biomedical microfluidic devices by using low-cost fabrication techniques: A review.” *Journal of biomechanics*. vol. 49, no. 11, pp. 2280–2292, 2016.
- [196] P.L. Williams, G.L. Anderson, J.L. Johnstone, A.D. Nunn, M.F. Tweedle, and P. Wedeking: “Caenorhabditis elegans as an alternative animal species.” *Journal of Toxicology and Environmental Health Part A*. vol. 61, no. 8, pp. 641–647, 2000.

# Curriculum Vitae

## Vittorio Viri

Address: Rue de Genève 94, CH-1004 Lausanne Switzerland

Phone: +41 78 665 92 88

E-mail: vittorio.viri@gmail.com, vittorio.viri@epfl.ch

## Education

---

<b>Ecole Polytechnique Fédérale de Lausanne, Switzerland</b>	<b>2017 - 2021</b>
--	--------------------

Ph.D. candidate, LMIS2, Doctoral program of Microsystems and Microelectronics

Thesis Title: "Microfluidic culture platform for *C. elegans* bacterial interaction and digestion studies at single worm resolution"

---

<b>Sapienza Università di Roma, Italy</b>	<b>2014 - 2016</b>
---	--------------------

M.Sc. in Biomedical Engineering

110/110 cum laude

Thesis Title: "Development of an optoelectronic system for detection of DNA based on ruthenium complex"

---

<b>Sapienza Università di Roma, Italy</b>	<b>2011 - 2013</b>
---	--------------------

B.Sc. in Clinical Engineering

110/110

Thesis Title: "Mechanical modeling of twining plants"

## Work and Research Experience

---

<b>Ecole Polytechnique Fédérale de Lausanne, Switzerland</b>	<b>2017- 2021</b>
--	-------------------

Research and teaching assistant, supervised by Prof. Martin Gijs and Dr. Thomas Lehnert

**Research Area:** Microfluidic tools for studies on *C. elegans* nematodes and bacteria.

### Supervision:

1 M.Sc. thesis project



**Teaching:**

Cleanroom theoretical and practical courses for B.Sc. students

MICRO-501 MEMS practicals I

MICRO-332 Manufacturing DLLs

**Technical Skills**

---

**Cleanroom Technologies:**

Photolithography, Dry and wet etching, Mask design and fabrication, Surface treatment, Profilometer devices, PDMS applications

**Programing Languages and Software Skills:**

Matlab, Fiji, ImageJ, CleWin, KLayout, COMSOL, Adobe Illustrator - Photoshop, SolidWorks, C

**Biotechnology:**

*C. elegans* maintenance and handling, bacteria culture, BSL-2 tools and devices, Optical microscopy

**Language Skills**

---

Italian Native

English Fluent (C2)

French Intermediate (B2)